

---

**OXIDATIVE DESULFURIZATION OF FUEL OILS-CATALYTIC  
OXIDATION AND ADSORPTIVE REMOVAL OF  
ORGANOSULFUR COMPOUNDS**

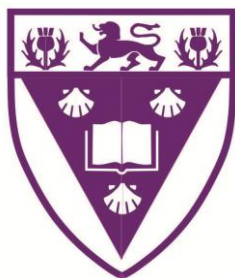
A thesis submitted in fulfilment of the requirements

for the degree of

**DOCTOR OF PHILOSOPHY**

at

Rhodes University



by

**Adeniyi Sunday Ogunlaja**

December 2013

---

---

## Dedication

To my late dad, **Pa Emmanuel Adolphus Ogunlaja**, who sacrificed much to get me through University and passed away during the first year of my PhD research study. I will always remember you for your valuable words of encouragement.

---

### Abstract

The syntheses and evaluation of oxidovanadium(IV) complexes as catalysts for the oxidation of refractory organosulfur compounds in fuels is presented. The sulfones produced from the oxidation reaction were removed from fuel oils by employing molecularly imprinted polymers (MIPs). The oxidovanadium(IV) homogeneous catalyst,  $[V^{IV}O(\text{sal-HBPD})]$ , as well as its heterogeneous polymer supported derivatives,  $\text{poly}[V^{IV}O(\text{sal-AHBPD})]$  and  $\text{poly}[V^{IV}O(\text{allylSB-co-EGDMA})]$ , were synthesized and fully characterized by elemental analysis, FTIR, UV-Vis, XPS, AFM, SEM, BET and single crystal XRD for  $[V^{IV}O(\text{sal-HBPD})]$ . The MIPs were also characterized by elemental analysis, FTIR, SEM, EDX and BET.

The catalyzed oxidation of fuel oil model sulfur compounds, thiophene (TH), benzothiophene (BT), dibenzothiophene (DBT) and 4,6-dimethyldibenzothiophene (4,6-DMDBT), was conducted under batch and continuous flow processes at 40°C by using *tert*-butylhydroperoxide (*t*-BuOOH) as oxidant. The continuous flow oxidation process presented the highest overall conversions and very high selectivity for sulfones. Maximum oxidation conversions of 71%, 89%, 99% and 88% was achieved for TH, BT, DBT and 4,6-DMDBT respectively when  $\text{poly}[V^{IV}O(\text{allylSB-co-EGDMA})]$  was employed at a flow-rate of 1 mL/h with over 90% sulfone selectivity. The process was further applied to the oxidation of hydro-treated diesel containing  $385 \pm 4.6$  ppm of sulfur (mainly dibenzothiophene and dibenzothiophene derivatives), and this resulted to a high sulfur oxidation yield (> 99%), thus producing polar sulfones which are extractible by polar solid phase extractants.

Adsorption of the polar sulfone compounds was carried-out by employing MIPs which were fabricated through the formation of recognition sites complementary to oxidized sulfur-containing compounds (sulfones) on electrospun polybenzimidazole (PBI) nanofibers, cross-linked chitosan microspheres and electrospun chitosan nanofibers. Adsorption of benzothiophene sulfone ( $\text{BTO}_2$ ), dibenzothiophene sulfone ( $\text{DBTO}_2$ ) and 4,6-dimethyldibenzothiophene sulfone ( $\text{4,6-DMDBTO}_2$ ) on the various molecularly imprinted adsorbents presented a Freundlich (multi-layered) adsorption isotherm which indicated interaction of adsorbed organosulfur compounds. Maximum adsorption observed for  $\text{BTO}_2$ ,  $\text{DBTO}_2$  and  $\text{4,6-DMDBTO}_2$  respectively was  $8.5 \pm 0.6$  mg/g,  $7.0 \pm 0.5$  mg/g and  $6.6 \pm 0.7$  mg/g when imprinted chitosan nanofibers were employed,  $4.9 \pm 0.5$  mg/g,  $4.2 \pm 0.7$  mg/g and  $3.9 \pm 0.6$  mg/g on molecularly

---

---

imprinted chitosan microspheres, and  $28.5 \pm 0.4$  mg/g,  $29.8 \pm 2.2$  mg/g and  $20.1 \pm 1.4$  mg/g on molecularly imprinted PBI nanofibers. Application of electrospun chitosan nanofibers on oxidized hydro-treated diesel presented a sulfur removal capacity of 84%, leaving  $62 \pm 3.2$  ppm S in the fuel, while imprinted PBI electrospun nanofibers displayed excellent sulfur removal, keeping sulfur in the fuel after the oxidation/adsorption below the determined limit of detection (LOD), which is 2.4 ppm S. The high level of sulfur removal displayed by imprinted PBI nanofibers was ascribed to hydrogen bonding effects, and  $\pi$ - $\pi$  stacking between aromatic sulfone compounds and the benzimidazole ring which were confirmed by chemical modelling with density functional theory (DFT) as well as the imprinting effect. The home-made pressurized hot water extraction (PHWE) system was applied for extraction/desorption of sulfone compounds adsorbed on the PBI nanofibers at a flow rate of 1 mL/min and at 150°C with an applied pressure of 30 bars. Application of molecularly imprinted PBI nanofibers for the desulfurization of oxidized hydro-treated fuel showed potential for use in refining industries to reach ultra-low sulfur fuel level, which falls below the 10 ppm sulfur limit which is mandated by the environmental protection agency (EPA) from 2015.



---

## Acknowledgements

Firstly, I thank the Almighty God for His mercies and love. He has been my all in all throughout the research work.

I thank my supervisor, Prof. Zenixole R. Tshentu, and my co-supervisor, Prof. Nelson Torto, for their invaluable understanding and guidance during the research work. I am also very grateful for the funding I received through my supervisors so as to attend conferences and also effectively finish up my research thesis.

I thank Mrs Benita Tarr and the office staff who were very helpful and supportive with all administrative things, such as prompt purchase of chemicals and access to funds for conferences.

I also thank the technical staff, in particular Mr Francis Chindeka, who when called upon to fix some laboratory electronic instruments responds promptly and fix it with a constant smile.

I must also acknowledge the DST-Mintek Nanotechnology Innovation centre (DST/MIntek-NIC) for access to BET and for the XPS analysis.

I must also thank all my colleagues in the Inorganic-Analytical Chemistry group (F3 and F12) for the support and the happy work environment you all created made my experience at Rhodes University a memorable one indeed. It has been a privilege to occupy the laboratory with these great individuals. I wish you all the best in your future endeavours.

I must also use this opportunity to thank Nelson Mandela Metropolitan University (NMMU) Chemistry Department for making available some research equipment in order to allow me to complete my research study. My sincere appreciation also goes to my mom, Kehinde Sabina Ogunlaja, who has encouraged me and has also supported me with prayers. I would also like to thank the rest of my family members for support and encouragement.

I would also like to thank someone special to me, Ebunoluwa Ogunfowora, who believed so much in me and listens to my many complaints from the lab.

Finally, I would like to thank Sasol (Pty) Ltd for their financial support during my research studies. I am also grateful to the South African NRF and Rhodes University for funding.

---

## Table of Contents

DEDICATION.....	i
ABSTRACT.....	ii-iii
ACKNOWLEDGEMENTS.....	iv
LIST OF FIGURES.....	xiii-xxv
LIST OF SCHEMES.....	xxvi
LIST OF TABLES.....	xxvii-xxix
<b>Chapter One: Introduction.....</b>	<b>1</b>
1.1 Crude oil.....	1
1.1.1 Origin of crude oils.....	2
1.1.2 Classification of crude oils.....	3
1.1.2.1 Paraffins.....	3
1.1.2.2 Naphthenic.....	3
1.1.2.3 Asphaltenes.....	4
1.1.3 Chemical composition of crude oils.....	4
1.1.3.1 Hydrocarbon compounds.....	4
1.1.3.2 Non-hydrocarbon compounds.....	5
1.1.3.3 Metal complexes.....	9
1.1.4 Physico-chemical properties of the various crude oils.....	10
1.2 Desulfurization of crude oils.....	13
1.2.1 Bio-desulfurization (BDS).....	14
1.2.1.1 Ring destructive pathway.....	14
1.2.1.2 Sulfur-specific (desulfurization) pathway.....	15
1.2.2 Hydro-desulfurization (HDS) process.....	17
1.2.3 Oxidative-desulfurization (ODS) process.....	19
1.2.3.1 General description of the ODS process.....	20
1.3 Catalysis.....	23

---

1.3.1	Some metals employed for catalysed oxidation reactions .....	24
1.3.1.1	Vanadium-catalysed oxidation reactions .....	25
1.3.1.2	Catalytic mechanism of oxidovanadium(IV)-catalysed oxidation reactions .....	29
1.3.2	Polymer-supported catalysts .....	30
1.3.2.1	The basics of polymerization .....	31
1.3.2.2	Polymer microspheres as catalyst support material .....	33
1.3.2.3	Techniques for producing polymer microspheres .....	33
1.3.2.4	Polymer nanofibers as catalyst support materials .....	36
1.4	Adsorptive removal of sulfur/sulfone compounds in fuels .....	39
1.4.1	Molecular imprinting .....	41
1.4.2	Techniques of preparing molecularly imprinted polymers .....	43
1.4.2.1	The covalent approach .....	43
1.4.2.2	Non-covalent approach .....	43
1.4.2.3	The semi-covalent approach .....	43
1.5	Aims and objectives .....	45
<b>Chapter Two: Materials, experimental techniques and methods .....</b>		<b>47</b>
2.1	General reagents .....	47
2.2	Instrumentation and general experimental procedures .....	49
2.2.1	Melting point analysis .....	49
2.2.2	FT-IR .....	49
2.2.3	UV-vis spectroscopy .....	49
2.2.4	NMR (nuclear magnetic resonance) spectroscopy .....	49
2.2.5	Elemental analysis .....	49
2.2.6	Thermogravimetric analysis .....	50
2.2.7	EPR (electron paramagnetic resonance) spectroscopy .....	50
2.2.8	Scanning electron microscopy (SEM) and X-ray energy dispersive spectroscopy (EDS) .....	50
2.2.9	Atomic force microscopy .....	50

---

---

2.2.10	X-ray photoelectron spectroscopy .....	51
2.2.11	Brunauer, Emmett, Teller (BET) surface area analysis .....	52
2.2.12	Inductively coupled plasma – Optical emission spectroscopy .....	52
2.2.13	Gas chromatography .....	53
2.3	<i>Tert</i> -butylhydroperoxide concentration determination .....	55
2.4	Metal content determination on polymer microspheres .....	56
2.5	Catalytic oxidation procedure under batch studies .....	56
2.6	Catalyzed oxidation procedure under continuous flow .....	56
2.7	Adsorption studies using molecularly imprinted chitosan and polybenzimidazole (PBI) as adsorbents ..	58
2.8	Desorption /regeneration condition .....	59
<b>Chapter Three: Characterization, classification and identification of petroleum fuel oils.....</b>		<b>61</b>
3.1	Introduction .....	61
3.2	Experimental work .....	63
3.2.1	Crude oil column separation protocol.....	63
3.2.2	Metal determination and method validation .....	64
3.3	Results and discussion .....	64
3.3.1	Preliminary analysis of the fractions .....	64
3.3.2	FT-IR spectroscopic studies of crude oils.....	65
3.3.3	Metal content determination in crude oils .....	67
3.3.4	Determination of organics .....	70
3.3.5	Relationship of total sulfur content to phenanthrene/dibenzothiophene with derivatives (PHEN/DBT) ratio.....	77
3.4	Conclusions .....	79
<b>Chapter Four: Oxidovanadium(IV)-catalysed oxidation of refractory organosulfur compounds in fuels .....</b>		<b>81</b>
4.1	Introduction .....	81
4.2	Experimental work .....	82
4.2.1	Synthesis of the homogeneous oxidovanadium(IV) complex, [V <sup>IV</sup> O(sal-HBPD)] .....	82

---

---

4.2.1.1	Preparation of <i>N,N</i> -bis( <i>o</i> -hydroxybenzaldehyde)phenylene diamine (sal-HBPD) Schiff base	82
4.2.1.2	Synthesis of V <sup>IV</sup> O(sal-HBPD)	82
4.2.2	Synthesis of heterogeneous Merrified-based oxidovanadium(IV) catalyst, poly[V <sup>IV</sup> O(sal-AHBPD)]	83
4.2.2.1	Nitrosation of <i>N,N</i> -bis( <i>o</i> -hydroxybenzaldehyde)phenylene diamine (sal-HBPD) Schiff base	83
4.2.2.2	Reduction of <i>N,N</i> -bis(4-nitroso- <i>o</i> -hydroxybenzaldehyde)phenylenediamine (sal-NHBPD) Schiff base	83
4.2.2.3	Synthesis of poly[V <sup>IV</sup> O(sal-AHBPD)]	84
4.2.3	Synthesis of poly[V <sup>IV</sup> O(allylsB-co-EGDMA)]	85
4.2.3.1	Synthesis of 3-Allyl-2-hydroxybenzaldehyde	85
4.2.3.2	Synthesis of <i>N,N</i> -bis( <i>o</i> -hydroxybenzaldehyde)phenylenediamine monomer (allylsB)	86
4.2.3.3	Preparation of poly[allylsB-co-EGDMA] microspheres by suspension polymerization	87
4.2.3.4	Synthesis of poly[V <sup>IV</sup> O(allylsB-co-EGDMA)] microspheres	88
4.3	Catalyst characterization and spectroscopic studies	88
4.3.1	Single crystals X-ray analysis of V <sup>IV</sup> O(sal-HBPD)	88
4.3.2	Scanning electron micrograph (SEM) images of poly[(sal-AHBPD)], poly[V <sup>IV</sup> O(sal-AHBPD)], poly[allylsB-co-EGDMA] and poly[V <sup>IV</sup> O(allylsB-co-EGDMA)]	91
4.3.3	Surface area measurements of poly[(sal-AHBPD)], poly[V <sup>IV</sup> O(sal-AHBPD)], poly[allylsB-co-EGDMA] and poly[V <sup>IV</sup> O(allylsB-co-EGDMA)]	93
4.3.4	Atomic force microscopy (AFM) of poly[(sal-AHBPD)], poly[V <sup>IV</sup> O(sal-AHBPD)], poly[allylsB-co-EGDMA] and poly[V <sup>IV</sup> O(allylsB-co-EGDMA)]	94
4.3.5	X-ray photoelectron spectroscopy (XPS) of poly[(sal-AHBPD)], poly[V <sup>IV</sup> O(sal-AHBPD)], poly[allylsB-co-EGDMA] and poly[V <sup>IV</sup> O(allylsB-co-EGDMA)]	96
4.3.6	Thermogravimetric analysis of [V <sup>IV</sup> O(sal-HBPD)], poly[(sal-AHBPD)], poly[V <sup>IV</sup> O(sal-AHBPD)], poly[allylsB-co-EGDMA] and poly[V <sup>IV</sup> O(allylsB-co-EGDMA)]	100
4.3.7	UV-Vis electronic studies of [V <sup>IV</sup> O(sal-HBPD)], poly[V <sup>IV</sup> O(sal-AHBPD)] and poly[V <sup>IV</sup> O(allylsB-co-EGDMA)]	102

---

---

4.3.8	FT-IR spectral studies of poly[(sal-AHBPD)], poly[V <sup>IV</sup> O(sal-AHBPD)], poly[allylsB-co-EGDMA] and poly[V <sup>IV</sup> O(allylsB-co-EGDMA)].....	104
4.3.9	Electron paramagnetic resonance (EPR) studies of V <sup>IV</sup> O(sal-HBPD), poly[V <sup>IV</sup> O(sal-AHBPD)] and poly[V <sup>IV</sup> O(allylsB-co-EGDMA)].....	108
4.3.10	Reactivity of [V <sup>IV</sup> O(sal-HBPD)] with <i>t</i> -BuOOH.....	110
4.4	Catalytic oxidation of organosulfur compounds.....	113
4.4.1	Catalytic oxidation of organosulfur compounds using poly[V <sup>IV</sup> O(sal-AHBPD)] and poly[V <sup>IV</sup> O(allylsB-co-EGDMA)] as catalysts under batch condition.....	113
4.4.1.1	Thiophene.....	113
4.4.1.2	Benzothiophene.....	115
4.4.1.3	Dibenzothiophene.....	115
4.4.1.4	4,6-Dimethyldibenzothiophene.....	116
4.4.2	Catalytic oxidation of organosulfur compounds using [V <sup>IV</sup> O(sal-HBPD)] as catalysts under batch condition.....	122
4.4.3	Summary of the oxidation results .....	124
4.5	Recyclability studies.....	126
4.5.1	Reusability of heterogeneous catalysts poly[V <sup>IV</sup> O(sal-AHBPD)] and poly[V <sup>IV</sup> O(allylsB-co-EGDMA)] under batch process .....	126
4.6	Leaching studies .....	127
4.6.1	Determination of the amount of vanadium ion leached from poly[V <sup>IV</sup> O(sal-AHBPD)] and poly[V <sup>IV</sup> O(allylsB-co-EGDMA)] under batch process.....	127
4.7	Catalysed oxidation of organosulfur compounds using poly[V <sup>IV</sup> O(sal-AHBPD)] and poly[V <sup>IV</sup> O(allylsB-co-EGDMA)] under continuous flow process .....	129
4.7.1	Oxidation of thiophene under a continuous flow process.....	130
4.7.2	Oxidation of benzothiophene under a continuous flow process.....	132
4.7.3	Oxidation of dibenzothiophene under a continuous flow process .....	134
4.7.4	Oxidation of 4,6-dimethyldibenzothiophene under a continuous flow process .....	136

---

---

4.8	Leaching studies of poly[V <sup>IV</sup> O(sal-AHBPD)] and poly[V <sup>IV</sup> O(allylsB-co-EGDMA)] under continuous flow oxidation process.....	139
4.9	General discussion on the catalysed oxidation of organosulfur compounds using [V <sup>IV</sup> O(sal-HBPD)], poly[V <sup>IV</sup> O(sal-AHBPD)] and poly[V <sup>IV</sup> O(allylsB-co-EGDMA)] .....	141
4.10	Characterization of oxidized organosulfur compounds .....	142
4.10.1	Microanalysis of oxidized products.....	142
4.10.2	Nuclear magnetic resonance (NMR) characterization of oxidation products.....	143
4.10.3	FT-IR spectroscopic characterization of oxidation products.....	143
4.11	Catalysed oxidation of model fuel oil.....	146
4.11.1	Catalysed oxidation of model fuel oil using poly[V <sup>IV</sup> O(sal-AHBPD)] and poly[V <sup>IV</sup> O(allylsB-co-EGDMA)] under batch process .....	146
4.11.2	Catalysed oxidation of model fuel oil using p[V <sup>IV</sup> O(sal-AHBPD)] and poly[V <sup>IV</sup> O(allylsB-co-EGDMA)] under continuous flow process .....	149
4.12	Oxidovanadium(IV) catalysed oxidation of hydro-treated diesel (continuous flow and batch process).....	151
4.13	Oxidovanadium(IV) catalysed oxidation of crude oil.....	156
4.14	Conclusions .....	158
<b>Chapter Five: Adsorption of oxidized organosulfur compounds in fuels by using molecularly imprinted polymers .....</b>		<b>160</b>
5.1	Introduction .....	160
5.2	General synthetic route for the fabrication of molecularly imprinted and non-imprinted polymer adsorbents .....	161
5.2.1	Preparation of molecularly imprinted and non-imprinted chitosan microspheres and nanofibers ..	161
5.2.1.1	Preparation of molecularly imprinted and non-imprinted chitosan nanofibers .....	161
5.2.1.2	Preparation of molecularly imprinted and non-imprinted chitosan microspheres.....	162
5.2.2	Preparation of molecularly imprinted and non-imprinted polybenzimidazole (PBI) nanofibers <i>via</i> electrospinning.....	164

---

---

5.3	Adsorbent characterization .....	165
5.3.1	FT-IR spectra of adsorbents.....	167
5.3.2	Energy Dispersive Spectroscopic analysis of adsorbents .....	167
5.3.3	Scanning electron micrographs of adsorbents .....	170
5.3.4	Surface area measurements of adsorbents .....	174
5.3.5	Thermogravimetric analysis of adsorbents .....	177
5.4	Equilibrium swelling ratio of adsorbents.....	180
5.5	Sulfone compounds adsorption studies .....	182
5.5.1	Adsorption studies employing chitosan adsorbents.....	182
5.5.1.1	Adsorbent mass optimization studies .....	182
5.5.1.2	Adsorption selectivity on molecularly imprinted chitosan microspheres and nanofibers .....	184
5.5.1.3	Adsorption kinetics of molecularly imprinted chitosan microspheres and nanofibers.....	185
5.5.1.4	Adsorption isotherms of molecularly imprinted chitosan microspheres and nanofibers.....	191
5.5.1.5	Reusability studies of molecularly imprinted chitosan microspheres and nanofibers .....	197
5.5.2	Adsorption studies employing polybenzimidazole nanofibers .....	198
5.5.2.1	Molecularly imprinted-PBI nanofibers mass adsorption optimization study .....	198
5.5.2.2	Adsorption selectivity on molecularly imprinted polybenzimidazole nanofibers .....	199
5.5.2.3	Adsorption kinetics of molecularly imprinted polybenzimidazole nanofibers.....	201
5.5.2.4	Adsorption isotherms of molecularly imprinted polybenzimidazole nanofibers.....	204
5.5.2.5	Reusability studies on the molecularly imprinted polybenzimidazole nanofibers.....	207
5.5.2.6	Desorption process using pressurized hot water extraction (PHWE).....	208
5.6	Continuous flow adsorption studies.....	210
5.6.1	Adsorption studies on the sulfone compounds using imprinted chitosan and PBI nanofibers .....	210
5.7	Adsorption studies of sulfone compounds on oxidized model fuel and oxidized diesel .....	215
5.7.1	Continuous flow and batch adsorption studies using imprinted chitosan and PBI nanofibers on oxidized model fuel .....	215

---



---

5.7.2	Continuous flow adsorption studies using imprinted chitosan and PBI nanofibers on oxidized hydro-treated diesel.....	217
5.7.3	Continuous flow adsorption studies using imprinted PBI nanofibers on oxidized crude oil.....	222
5.8	Intermolecular interaction studies between adsorbent (chitosan and polybenzimidazole) and sulfone compounds using the density functional theory (DFT).....	224
5.9	Conclusions .....	230
<b>Chapter Six:</b>	<b>Conclusions and future work.....</b>	<b>233</b>
6.1	Conclusions.....	233
6.2	Future work.....	235
	References.....	237

---

**List of Figures**

Figure 1.1	Trends in diesel sulfur fuel specifications from the United States (US), United Kingdom (UK), European Union (EU) and South Africa (SA) over the years.....	2
Figure 1.2	Acidic sulfur and non-acidic sulfur compounds.....	6
Figure 1.3	Sulfur distribution in crude oils in the world (1 wt.% Sulfur = 10000 ppm) .....	7
Figure 1.4	Examples of organic nitrogen compounds (basic and non-basic).....	8
Figure 1.5	Structural examples of organic oxygen compounds (acidic and non-acidic).....	9
Figure 1.6	Chemical structures of nickel porphyrin and vanadium porphyrin.....	10
Figure 1.7	Reactivity of various organic sulfur compounds in hydro desulfurization versus their ring sizes and positions of alkyl substitutions on the ring.....	18
Figure 1.8	Schematics of oxidative-desulfurization ODS process.....	22
Figure 1.9	Overview of the importance of vanadium in supported metal oxide catalysis. The numbers are based on an extensive open literature search in the period 1967-2010.....	25
Figure 1.10	The colour of vanadium in biologically relevant oxidation states. From left to right, $V^{5+}$ , $V^{4+}$ , and $V^{3+}$ .....	27
Figure 1.11	Some typical geometries of vanadium(IV).....	27
Figure 1.12	Molecular orbital scheme for the $VO^{2+}$ species as outlined by Ballhausen.....	29
Figure 1.13	Clustered energy level scheme of OSM for vanadyl(IV) complexes.....	29
Figure 1.14	Schematic descriptions of the stages of precipitation polymerization for porous particle production. (A) Initially, only crosslinker and initiator molecules are in the medium. (B) Oligomers and nuclei begin to form because of radical polymerization. (C) As the reaction continues, nuclei grow by adding monomers and oligomers from the medium.....	35
Figure 1.15	A schematic of a typical suspension polymerization procedure.....	36
Figure 1.16	The electrospinning equipment used for the fabrication of polymer nanofibers.....	37
Figure 1.17	Integrated hydro desulfurization-oxidative desulfurization (HDS-ODS) processes.....	41
Figure 1.18	Highly schematic representation of the molecular imprinting process: The formation of reversible interactions between the template and polymerizable functionality may involve one	

---

	or more of the following interactions: [(A) reversible covalent bond(s), (B) covalently attached polymerizable binding groups that are activated for non-covalent interaction by template cleavage, (C) electrostatic interactions, (D) hydrophobic or van der Waals interactions or (E) co-ordination with a metal centre; each formed with complementary functional groups or structural elements of the template, (a-e) respectively].....	42
Figure 2.1	Simple setup of a continuous flow catalysed oxidation process.....	57
Figure 2.2	A continuous flow set-up used in this study. Imprinted nanofibers are packed into a filter tip compartment, and the sulfone containing compounds (BTO <sub>2</sub> , DBTO <sub>2</sub> and 4,6-DMDBTO <sub>2</sub> ) will be passed through the nanofibers by means of a syringe pump.....	59
Figure 3.1	Structure of phenanthrene and dibenzothiophene.....	61
Figure 3.2	Separation protocol for the crude oil into saturates, aromatics, resins and asphaltenes.....	63
Figure 3.3	FT-IR spectra for aromatics in light, medium, and heavy crude oils.....	66
Figure 3.4	FT-IR spectra for saturates in light, medium, and heavy crude oils.....	66
Figure 3.5	Graph showing the relationship between vanadium-to-nickel (V/Ni) and phenanthrene-to-dibenzothiophene (P/D) to sulfur content of oil (wt%).....	68
Figure 3.6	GC chromatograms of light crude oils showing phenanthrene and dibenzothiophene with their derivatives.....	72
Figure 3.7	GC chromatograms of medium crude oils showing phenanthrene and dibenzothiophene with their derivatives.....	73
Figure 3.8	GC chromatograms of heavy crude oils showing phenanthrene and dibenzothiophene with their derivatives.....	73
Figure 3.9	A graph showing the relationship between sulfur content (wt%) to the ratio of phenanthrene and derivatives to dibenzothiophene.....	77
Figure 3.10	A graph showing the relationship between sulfur content (wt%) to the ratio of phenanthrene with derivatives to 2-methyl-dibenzothiophenes/3-methyl-dibenzothiophene.....	78
Figure 4.1	FT-IR spectra of (A) [sal-HBPD], (B) [sal-NHBPD] and (C) [sal-AHBPD].....	84

---

---

Figure 4.2	FT-IR spectrum of (A) 3-allyl-2-hydroxybenzaldehyde and (B) <i>N,N'</i> -bis( <i>o</i> -hydroxybenzaldehyde) phenylenediamine monomer (allylsB).....	87
Figure 4.3	An ORTEP view of [V <sup>IV</sup> O(sal-HBPD)] Schiff base complex with ellipsoids drawn at 50% probability level, CCDC 872749. ....	89
Figure 4.4	Scanning electron microscopy (SEM) micrograph of microspheres (A) chloromethylated polystyrene microspheres, (B) ligand-anchored microspheres and (C) vanadium incorporated microspheres poly[V <sup>IV</sup> O(sal-AHBPD)].....	92
Figure 4.5	Scanning electron micrographs of (A) poly[allylsB-co-EGDMA], (B) poly[V <sup>IV</sup> O(allylsB-co-EGDMA)] and (C) poly[V <sup>IV</sup> O(allylsB-co-EGDMA)] after use.....	92
Figure 4.6	Nitrogen adsorption-desorption isotherms for (A) poly[sal-AHBPD], (B) poly [V <sup>IV</sup> O(sal-AHBPD)], (C) poly[allylsB-co-EGDMA] and (D) poly[V <sup>IV</sup> O(allylsB-co-EGDMA)].....	94
Figure 4.7	AFM images of (A) poly[sal-AHBPD], (B) poly[V <sup>IV</sup> O(sal-AHBPD)] before use and (C) poly[V <sup>IV</sup> O(sal-AHBPD)] after use. Scale:2x2 μM.....	95
Figure 4.8	AFM images of (A) poly[allylsB-co-EGDMA], (B) poly[V <sup>IV</sup> O(allylsB-co-EGDMA)] and (C) poly[V <sup>IV</sup> O(allylsB-co-EGDMA)] after use. Scale:2x2 μM.....	96
Figure 4.9	Expanded scan for deconvolution of V 2p and N 1s signals for poly[V <sup>IV</sup> O(sal-AHBPD)].....	97
Figure 4.10	High resolution wide scan XPS spectra of (A) poly[(sal-AHBPD)], (B) poly[V <sup>IV</sup> O(sal-AHBPD)] and (C) poly[V <sup>IV</sup> O(sal-AHBPD)] used.....	98
Figure 4.11	Expanded scan for deconvolution of poly[V <sup>IV</sup> O(allylsB-co-EGDMA)], (A) V 2p before use and (B) V 2p after use.....	99
Figure 4.12	High resolution wide scan XPS spectra of (A) poly[allylsB-co-EGDMA], (B) poly[V <sup>IV</sup> O(allylsB-co-EGDMA)] and (C) poly[V <sup>IV</sup> O(allylsB-co-EGDMA)] after use.....	99
Figure 4.13	TG curves of poly[(sal-AHBPD)] , [V <sup>IV</sup> O(sal-AHBPD)] and poly[V <sup>IV</sup> O(sal-AHBPD)].....	101
Figure 4.14	TG profile curve for poly[allylsB-co-EGDMA] and poly[V <sup>IV</sup> O(allylsB-co-EGDMA)].....	102
Figure 4.15	Diffuse reflectance electronic spectra of [V <sup>IV</sup> O(sal-HBPD)], poly[V <sup>IV</sup> O(sal-AHBPD)] and used poly[V <sup>IV</sup> O(sal-AHBPD)] .....	103

---

---

Figure 4.16	Diffuse reflectance electronic spectra of $[V^{IV}O(sal-HBPD)]$ , $poly[V^{IV}O(allylSB-co-EGDMA)]$ and used $poly[V^{IV}O(allylSB-co-EGDMA)]$ .....104
Figure 4.17	FT-IR spectra of (A) Merrified microspheres, (B) $poly[V^{IV}O(sal-AHBPD)]$ and (C) $[V^{IV}O(sal-HBPD)]$ .....105
Figure 4.18	FT-IR spectra of $poly[(sal-AHBPD)]$ and $poly[V^{IV}O(sal-AHBPD)]$ showing $\nu(V-N)$ and $\nu(V-O)$ bands.....106
Figure 4.19	The near-IR and mid-IR spectra of $poly[allylSB-co-EGDMA]$ and $poly[V^{IV}O(allylSB-co-EGDMA)]$ . (A) showing the V-N and V-O range and (B) showing the C=O and V-O range.....107
Figure 4.20	First derivative EPR spectra of $[V^{IV}O(sal-HBPD)]$ in <i>N,N</i> -dimethylformamide (DMF).....108
Figure 4.21	First derivative EPR spectrum of (A) $poly[V^{IV}O(sal-AHBPD)]$ before, and (B) $poly[V^{IV}O(sal-AHBPD)]$ after use.....109
Figure 4.22	First derivative EPR signals of (A) $poly[V^{IV}O(allylSB-co-EGDMA)]$ before, and (B) $poly[V^{IV}O(allylSB-co-EGDMA)]$ after use.....110
Figure 4.23	Spectrophotometric titration of $[V^{IV}O(sal-HBPD)]$ with one drop portions of <i>t</i> -BuOOH ( $5 \times 10^{-2}$ M) in DMF. Inset shows the d-d transition which disappears upon addition of oxidant.....111
Figure 4.24	$^{51}V$ NMR spectrum of (a) solution of 4 mM $[V^{IV}O(sal-HBPD)]$ in 1 equivalent <i>t</i> -BuOOH in MeOH; (b) suspension of $[V^{IV}O(sal-HBPD)]$ after addition of 3 equivalent <i>t</i> -BuOOH in MeOH; and (c) suspension of $[V^{IV}O(sal-HBPD)]$ after addition of 7 equivalent <i>t</i> -BuOOH.....112
Figure 4.25	Percentage conversion for the oxidation of thiophene (TH) and benzothiophene (BT) with time. $[t-BuOOH]_{eq.} = 6.8$ , thiophene = 0.54 g (0.0064 mol), benzothiophene = 0.15 g (0.0011 mol), $poly[V^{IV}O(sal-AHBPD)] = 0.015$ g (0.0135 mmol). <i>Tert</i> -butylammonium bromide (TBAB) = 0.01 g (0.000031 mol), Temp. = 40°C. Toluene/Hexane (1:4) = 10 mL. Blank means in the absence $poly[V^{IV}O(sal-AHBPD)]$ (catalyst) .....117
Figure 4.26	Percentage conversion for the oxidation of thiophene (TH), benzothiophene (BT) dibenzothiophene (DBT) and 4,6-dimethyldibenzothiophene (4,6-DMDBT) with time. Thiophene = 0.54 g (0.0064 mol), benzothiophene = 0.15 g (0.0011 mol), dibenzothiophene =

---

- 
- 0.15 g, (0.00081 mol), 4,6-dimethyldibenzothiophene = 0.15 g (0.00071 mol), poly[V<sup>IV</sup>O(sal-AHBPD)] = 0.015 g (0.0135 mmol), [*t*-BuOOH eq.] = 2.3. *Tert*-butylammonium bromide (TBAB) = 0.01 g (0.000031 mol), Temp. = 40°C. Toluene/Hexane (1:4) = 10 mL.....118
- Figure 4.27 Percentage conversion for the oxidation of thiophene (TH), benzothiophene (BT) dibenzothiophene (DBT) and 4,6-dimethyldibenzothiophene (4,6-DMDBT) with time. Thiophene = 0.54 g (0.0064 mol), benzothiophene = 0.15 g (0.0011 mol), dibenzothiophene = 0.15 g, (0.00081 mol), 4,6-dimethyldibenzothiophene = 0.15 g (0.00071 mol), poly[V<sup>IV</sup>O(allylsB-co-EGDMA)] = 0.024 g (0.0135 mmol), [*t*-BuOOH eq.] = 2.3, *tert*-butylammonium bromide (TBAB) = 0.01 g (0.000031 mol), Temp. = 40°C, toluene/hexane (1:4) = 10 mL.....119
- Figure 4.28 Percentage conversion for the oxidation of thiophene (TH) and benzothiophene (BT) with time. Thiophene = 0.54 g (0.0064 mol), benzothiophene = 0.15 g (0.0011 mol), poly[VO(allylsB-co-EGDMA)] = 0.024 g (0.0135 mmol), *tert*-butylammonium bromide (TBAB) = 0.01 g (0.000031 mol), [*t*-BuOOH]eq.] = 6.8, Temp. = 40°C. Toluene/Hexane (1:4) = 10 mL. Blank means in the absence poly[V<sup>IV</sup>O(allylsB-co-EGDMA)] (catalyst).....120
- Figure 4.29 Graph of % conversion for the oxidation of dibenzothiophene (DBT) and 4,6-dimethyldibenzothiophene (4,6-DMDBT) with time. Dibenzothiophene = 0.15 g (0.00081 mol), 4,6-dimethyldibenzothiophene = 0.15 g (0.00071 mol), poly[V<sup>IV</sup>O(sal-AHBPD)] = 0.015 g (0.0135 mmol), [*t*-BuOOH eq.] = 6.8 and 7.6, Temp. = 40°C. Toluene/Hexane (1:4) = 10 mL. Blank means in the absence of poly[V<sup>IV</sup>O(sal-AHBPD)].....121
- Figure 4.30 Percentage conversion for the oxidation of dibenzothiophene (DBT) and 4,6-dimethyldibenzothiophene (4,6-DMDBT) with time. [*t*-BuOOH eq.] = 6.8 for dibenzothiophene = 0.15 g (0.00081 mol), [*t*-BuOOH eq.] = 7.6 for 4,6-dimethyldibenzothiophene = 0.15 g (0.00071 mol), poly[V<sup>IV</sup>O(allylsB-co-EGDMA)] = 0.024 g (0.0135 mmol), Temp. = 40°C, Toluene/Hexane (1:4) = 10 mL. Blank means in the absence poly[V<sup>IV</sup>O(allylsB-co-EGDMA)].....122
-

- 
- Figure 4.31 Graph of % conversion for the oxidation of thiophene, benzothiophene, dibenzothiophene and 4,6-dimethyldibenzothiophene with time using homogenous catalyst  $[V^{IV}O(\text{sal-HBPD})]$ . Thiophene (TH) = 0.54 g (0.0064 mol), benzothiophene (BT) = 0.15 g (0.0011 mol), dibenzothiophene (DBT) = 0.15 g (0.00081 mol), 4,6-dimethyldibenzothiophene (4,6-DMDBT) = 0.15 g (0.00071 mol),  $[V^{IV}O(\text{sal-HBPD})]$  = 0.0047 g (0.0135 mmol) and Temp. = 40°C, [*t*-BuOOH eq.] for TH, BT and DBT = 6.8 and [*t*-BuOOH eq.] for 4,6-DMDBT is 7.6.....124
- Figure 4.32 Recyclability studies in the oxidation of thiophene (TH), benzothiophene (BT), dibenzothiophene (DBT) and 4,6-dimethyldibenzothiophene (4,6-DMDBT) using poly $[V^{IV}O(\text{sal-AHBPD})]$  as catalyst. Time of reaction = 3 h.....126
- Figure 4.33 Recyclability studies in the oxidation of thiophene (TH), benzothiophene (BT), dibenzothiophene (DBT) and 4,6-dimethyldibenzothiophene (4,6-DMDBT) using poly $[V^{IV}O(\text{allylSB-co-EGDMA})]$  as catalyst. Time of reaction = 6 h.....127
- Figure 4.34 Percentage vanadium leached from the polymer matrix (poly $[V^{IV}O(\text{sal-AHBPD})]$ ) for the various oxidation reactions of organosulfur compounds. The amount of vanadium leached is presented for the 1<sup>st</sup>, 2<sup>nd</sup> and 3<sup>rd</sup> cycles. Time of reaction = 3 h.....128
- Figure 4.35 Percentage vanadium leached from the polymer matrix (poly $[V^{IV}O(\text{allylSB-co-EGDMA})]$ ) for the various oxidation reactions of organosulfur compounds. The amount of vanadium leached is presented for the 1<sup>st</sup>, 2<sup>nd</sup> and 3<sup>rd</sup> cycles. Time of reaction = 6 h.....129
- Figure 4.36 Graph of % conversion for the oxidation of thiophene (TH). [*t*-BuOOH eq.] = 6.8, Temp.: 40°C, Toluene/Hexane (1:4) = 10 mL. Using (A) poly $[V^{IV}O(\text{sal-AHBPD})]$  = 0.015 g (0.0135 mmol) and (B) poly $[V^{IV}O(\text{allylSB-co-EGDMA})]$  = 0.024 g (0.0135 mmol).....131
- Figure 4.37 Graph of % conversion for the oxidation of benzothiophene (BT). [*t*-BuOOH eq.] = 6.8, Temp. = 40°C, Toluene/Hexane (1:4) = 10 mL. Using (A) poly $[V^{IV}O(\text{sal-AHBPD})]$  = 0.015 g (0.0135 mmol) and (B) poly $[V^{IV}O(\text{allylSB-co-EGDMA})]$  = 0.024 g (0.0135 mmol).....133
- Figure 4.38 Graph of % conversion for the oxidation of dibenzothiophene (DBT). [*t*-BuOOH eq.] = 6.8, Temp.: 40°C, Toluene/Hexane (1:4) = 10 mL. Using (A) poly $[V^{IV}O(\text{sal-AHBPD})]$  = 0.015 g (0.0135 mmol) and (B) poly $[V^{IV}O(\text{allylSB-co-EGDMA})]$  = 0.024 g (0.0135 mmol).....135
-

- 
- Figure 4.39 Graph of % conversion for the oxidation of 4,6-dimethyldibenzothiophene (4,6-DMDBT). [*t*-BuOOH eq.] = 7.6, Temp.: 40°C, Toluene/Hexane (1:4) = 10 mL. Using (A) poly[V<sup>IV</sup>O(sal-AHBPD)] = 0.015 g (0.0135 mmol) and (B) poly[V<sup>IV</sup>O(allylsB-co-EGDMA)] = 0.024 g (0.0135 mmol).....137
- Figure 4.40 FT-IR of (A) Thiophene (TH) and bromine-containing thiophene sulfone (THO<sub>2</sub>), (B) Benzothiophene (BT) and benzothiophene sulfone (BTO<sub>2</sub>), (C) Dibenzothiophene (DBT) and dibenzothiophene sulfone (DBTO<sub>2</sub>), (D) 4,6-Dimethyldibenzothiophene (4,6-DMDBT) and 4,6-dimethyldibenzothiophene sulfone (4,6-DMDBTO<sub>2</sub>).....145
- Figure 4.41 GC-FID chromatograms of organosulfur mixture {benzothiophene (BT), dibenzothiophene (DBT) and 4,6-dimethyldibenzothiophene (4,6-DMDBT)} before and after oxidation using poly[V<sup>IV</sup>O(sal-AHBPD)] as catalyst. poly[V<sup>IV</sup>O(sal-AHBPD)] = 0.045 g (0.0405 mmol), Temp.= 40°C. Toluene/Hexane (1:4) = 10 mL. Benzothiophene sulfone (BTO<sub>2</sub>), dibenzothiophene sulfone (DBTO<sub>2</sub>) and 4,6-dimethyldibenzothiophene sulfone (4,6-DMDBTO<sub>2</sub>).....147
- Figure 4.42 GC-FID chromatograms of organosulfur mixture {benzothiophene (BT), dibenzothiophene (DBT) and 4,6-dimethyldibenzothiophene (4,6-DMDBT)} before and after oxidation using poly[VO(allylsB-co-EGDMA)] as catalyst. poly[V<sup>IV</sup>O(allylsB-co-EGDMA)] = 0.072 g (0.0405 mmol), Temp. = 40°C, Toluene/Hexane (1:4) = 10 mL. Benzothiophene sulfone (BTO<sub>2</sub>), dibenzothiophene sulfone (DBTO<sub>2</sub>) and 4,6-dimethyldibenzothiophene sulfone (4,6-DMDBTO<sub>2</sub>).....148
- Figure 4.43 GC-FID chromatograms of organosulfur mixture {benzothiophene (BT), dibenzothiophene (DBT) and 4,6-dimethyldibenzothiophene (4,6-DMDBT)} before and after oxidation using poly[V<sup>IV</sup>O(sal-AHBPD)] and poly[V<sup>IV</sup>O(allylsB-co-EGDMA)] (0.0405 mmol). Temp. = 40°C, toluene/hexane (1:4) = 10 mL, time of reaction = 10 h.....150
- Figure 4.44 GC-MS chromatograms for benzothiophene sulfone (BTO<sub>2</sub>), dibenzothiophene sulfone (DBTO<sub>2</sub>) and 4,6-dimethyldibenzothiophene sulfone (4,6-DMDBTO<sub>2</sub>).....151
-



---

Figure 4.45	GC-AED chromatogram of sulfur standards in diesel using a wavelength of 181 nm (1.5-30.0 ppm S).....	152
Figure 4.46	Calibration plot for instrument response to sulfur concentration (ppm S).....	152
Figure 4.47	GC-AED chromatograms of carbon (A) and sulfur (B) chromatograms of the hydro-treated diesel before oxidation and carbon (C) and sulfur (D) chromatograms of the hydro-treated diesel after oxidation while using poly[V <sup>IV</sup> O(allylSB-co-EGDMA)] as catalyst (continuous flow process). The chromatogram shows the loss of sulfides and the formation of sulfones.....	154
Figure 4.48	GC-AED chromatograms of carbon at 179 nm (A) and sulfur at 181 nm (B) of the hydro-treated diesel before oxidation and carbon at 179 nm (C) and sulfur at 181 nm (D) chromatograms of the hydro-treated diesel fuel after oxidation while using poly[V <sup>IV</sup> O(allylSB-co-EGDMA)] as catalyst (batch process).....	155
Figure 4.49	FT-IR of (A) hydro-treated diesel fuel (385 ± 4.6 ppm S) and (B) oxidized hydro-treated diesel.....	156
Figure 4.50	GC-AED chromatograms of carbon at 179 nm and sulfur at 181 nm for heavy crude oil before oxidation, and carbon and sulfur chromatograms of oxidized heavy crude oil after oxidation while using poly[V <sup>IV</sup> O(allylSB-co-EGDMA)] as catalyst (continuous flow process).....	157
Figure 5.1	Chemical structures of chitosan and polybenzimidazole.....	161
Figure 5.2	FT-IR spectra of chitosan and its modified form (microspheres and electrospun chitosan nanofibers).....	165
Figure 5.3	FT-IR spectrum of (A) pristine PBI, (B) PBI-nanofibers, (C) PBI-BTO <sub>2</sub> nanofibers, (D) PBI-DBTO <sub>2</sub> nanofibers and (E) PBI-4,6-DMDBTO <sub>2</sub> nanofibers.....	167
Figure 5.4	EDS spectra of (A) non-imprinted nanofibers after washing, (B) BTO <sub>2</sub> -imprinted nanofibers after deprotonation and washing, (C) DBTO <sub>2</sub> -imprinted nanofibers after deprotonation and washing and (D) 4,6-DMDBTO <sub>2</sub> -imprinted nanofibers after deprotonation and washing.....	168

---

---

Figure 5.5	EDS spectra of PBI nanofibers (A) non-imprinted PBI after washing, (B) BTO <sub>2</sub> imprinted after washing, (C) DBTO <sub>2</sub> imprinted after washing and (D) 4,6-DMDBTO <sub>2</sub> imprinted after washing.....	169
Figure 5.6	Optimization of chitosan mass before electrospinning (A) 0.1 g in 10 mL (TFA:DCM); (B) 0.2 g in 10 mL (TFA:DCM); (C) 0.4 g in 10 mL (TFA:DCM); (D) 0.5 g in 10 mL (TFA:DCM). NB: TFA to DCM ratio is 7 to 3. Each containing 0.001M sulfone compounds.....	171
Figure 5.7	Micrograph images of wet imprinted chitosan microspheres.....	171
Figure 5.8	Scanning electron microscopy (SEM) of (A) Non-imprinted microspheres, (B) BTO <sub>2</sub> -imprinted microspheres, (C) DBTO <sub>2</sub> -imprinted microspheres, and (D) 4,6-DMDBTO <sub>2</sub> -imprinted microspheres. All images presented were taken after template removal.....	172
Figure 5.9	Scanning electron micrograph (SEM) of (A) Non-imprinted nanofibers, (B) BTO <sub>2</sub> -imprinted nanofibers, (C) DBTO <sub>2</sub> -imprinted nanofibers, and (D) 4,6-DMDBTO <sub>2</sub> -imprinted nanofibers. All images presented were taken after template removal.....	172
Figure 5.10	Scanning electron microscopy (SEM) of PBI-nanofibers in the absence of LiBr (A and B) and electrospinning optimization images in the presence of LiBr (C and D).....	173
Figure 5.11	Scanning electron microscopy (SEM) of (A) PBI-nanofibers, (B) PBI-BTO <sub>2</sub> nanofibers, (C) PBI-DBTO <sub>2</sub> nanofibers, and (D) PBI-4,6-DMDBTO <sub>2</sub> nanofibers showing surface morphology.....	174
Figure 5.12	The BET isotherm linear plot of non-imprinted-chitosan nanofibers (A) BTO <sub>2</sub> -chitosan nanofibers (B), DBTO <sub>2</sub> -chitosan nanofibers (C), and 4,6-DMDBTO <sub>2</sub> -chitosan nanofibers (D).....	175
Figure 5.13	The BET isotherm linear plot of non-imprinted-chitosan microspheres (A) BTO <sub>2</sub> -chitosan microspheres, (B) DBTO <sub>2</sub> -chitosan microspheres (C), and 4,6-DMDBTO <sub>2</sub> -chitosan microspheres (D).....	176
Figure 5.14	The BET isotherm linear plot of NIP-PBI nanofibers (1), BTO <sub>2</sub> -PBI nanofibers (2), DBTO <sub>2</sub> -PBI nanofibers (3), and 4,6-DMDBTO <sub>2</sub> -PBI nanofibers (4).....	177

---

---

Figure 5.15	TG profile curve for (A) pristine chitosan flakes and imprinted nanofibers, and (B) non-imprinted and imprinted chitosan microspheres. ....178
Figure 5.16	TG profile for PBI-nanofibers, PBI-BTO <sub>2</sub> nanofibers, PBI-DBTO <sub>2</sub> nanofibers and PBI-4,6-DMDBTO <sub>2</sub> nanofibers.....179
Figure 5.17	Swelling ratio of adsorbents in CH <sub>3</sub> CN and hexane.....180
Figure 5.18	Scanning electron microscopy (SEM) micrograph of chitosan nanofibers (A) Non-imprinted (B) BTO <sub>2</sub> -imprinted (C) DBTO <sub>2</sub> -imprinted and (D) 4,6-DMDBTO <sub>2</sub> -imprinted, showing surface morphology change after contact with CH <sub>3</sub> CN.....181
Figure 5.19	Swelling ratio of polybenzimidazole nanofibers in CH <sub>3</sub> CN and hexane.....182
Figure 5.20	Effect of microspheres mass variation on the adsorption of benzothiophene sulfone (BTO <sub>2</sub> ), dibenzothiophene sulfone (DBTO <sub>2</sub> ) and 4,6-dimethyldibenzothiophene sulfone (4,6-DMDBTO <sub>2</sub> ).....183
Figure 5.21	Effect of nanofibers mass variation on the adsorption of benzothiophene sulfone (BTO <sub>2</sub> ), dibenzothiophene sulfone (DBTO <sub>2</sub> ) and 4,6-dimethyldibenzothiophene sulfone (4,6-DMDBTO <sub>2</sub> ).....183
Figure 5.22	Effect of selectivity on the adsorption of benzothiophene sulfone (BTO <sub>2</sub> ), dibenzothiophene sulfone (DBTO <sub>2</sub> ) and 4,6-dimethyldibenzothiophene sulfone (4,6-DMDBTO <sub>2</sub> ). Using microspheres (A) employed are NIB: Non-imprinted microspheres; B <sub>B</sub> : benzothiophene sulfone imprinted microspheres; D <sub>B</sub> : dibenzothiophene sulfone imprinted microspheres; D <sub>M-B</sub> : 4,6-dimethyldibenzothiophene sulfone imprinted microspheres and nanofibers (B) are: NIF: Non-imprinted nanofibers; B <sub>F</sub> : benzothiophene sulfone imprinted nanofibers; D <sub>F</sub> : dibenzothiophene sulfone imprinted nanofibers; D <sub>M-F</sub> : 4,6-dimethyldibenzothiophene sulfone imprinted nanofibers.....185
Figure 5.23	Kinetic studies on the various sulfone compounds (A) benzothiophene sulfone (BTO <sub>2</sub> ), (B) dibenzothiophene sulfone (DBTO <sub>2</sub> ) and (C) 4,6-dimethyldibenzothiophene sulfone (4,6-DMDBTO <sub>2</sub> ).....187

---

---

Figure 5.24	Pseudo-first-order plot of the various sulfone compounds (A) benzothiophene sulfone (BTO <sub>2</sub> ), (B) dibenzothiophene sulfone (DBTO <sub>2</sub> ) and (C) 4,6-dimethyldibenzothiophene sulfone (4,6-DMDBTO <sub>2</sub> ).....	189
Figure 5.25	Pseudo-second-order plot of the various sulfone compounds (A) benzothiophene sulfone (BTO <sub>2</sub> ), (B) dibenzothiophene sulfone (DBTO <sub>2</sub> ) and (C) 4,6-dimethyldibenzothiophene sulfone (4,6-DMDBTO <sub>2</sub> ).....	190
Figure 5.26a	Freundlich plot of log q <sub>e</sub> versus log C <sub>e</sub> using chitosan microspheres.....	192
Figure 5.26b	Freundlich plot of log q <sub>e</sub> versus log C <sub>e</sub> using chitosan nanofibers.....	193
Figure 5.27a	Langmuir plot of C <sub>e</sub> /q <sub>e</sub> versus C <sub>e</sub> using chitosan microspheres.....	194
Figure 5.27b	Langmuir plot of C <sub>e</sub> /q <sub>e</sub> versus C <sub>e</sub> using chitosan nanofibers.....	195
Figure 5.28	Reusability adsorption and desorption capacities of the microspheres and nanofibers. NIP: Non-imprinted polymer, MIP: Molecularly imprinted polymer.....	198
Figure 5.29	Effect of imprinted-PBI nanofibers mass variation on the adsorption of benzothiophene sulfone (BTO <sub>2</sub> ), dibenzothiophene sulfone (DBTO <sub>2</sub> ) and 4,6-dimethyldibenzothiophene sulfone (4,6-DMDBTO <sub>2</sub> ).....	199
Figure 5.30	Effect of selectivity on the adsorption of benzothiophene sulfone (BTO <sub>2</sub> ), dibenzothiophene sulfone (DBTO <sub>2</sub> ) and 4,6-dimethyldibenzothiophene sulfone (4,6-DMDBTO <sub>2</sub> ). NIP: Non-imprinted nanofibers; F <sub>B</sub> : benzothiophene sulfone imprinted nanofibers; F <sub>D</sub> : dibenzothiophene sulfone imprinted nanofibers; F <sub>DM</sub> : 4,6-dimethyldibenzothiophene sulfone imprinted nanofibers.....	201
Figure 5.31	Adsorption kinetics of imprinted-PBI nanofibers on their respective sulfone compounds.....	202
Figure 5.32	Pseudo-first-order adsorption plot of log (q <sub>e</sub> -q <sub>t</sub> ) versus t (time).....	203
Figure 5.33	Pseudo-second-order adsorption plot of t/q <sub>e</sub> versus t (time).....	203
Figure 5.34	Freundlich plot the log q <sub>e</sub> versus log C <sub>e</sub> for the imprinted-PBI nanofibers.....	205
Figure 5.35	Langmuir plot the C <sub>e</sub> /q <sub>e</sub> versus C <sub>e</sub> for the imprinted PBI nanofibers.....	206
Figure 5.36	Reusability of the imprinted nanofibers showing the adsorption/desorption capacities.....	208
Figure 5.37	A home-made pressurized hot water extraction (PHWE) system.....	209

---

---

Figure 5.38	Effects of temperature on the amount of sulfone compounds (analyte) extracted from imprinted nanofibers by PHWE method (first cycle). PHWE conditions: flow, 1 mL/min; time for extraction, 40-50 min; solvent, water ( $n = 3$ ).....	211
Figure 5.39	Breakthrough curves for various sulfone compounds (A) benzothiophene sulfone (BTO <sub>2</sub> ), (B) dibenzothiophene sulfone (DBTO <sub>2</sub> ), and (C) 4,6-dimethyldibenzothiophene (4,6-DMDBTO <sub>2</sub> ), using imprinted chitosan nanofibers.....	212
Figure 5.40	Breakthrough curves for various sulfone compounds (A) benzothiophene sulfone (BTO <sub>2</sub> ), (B) dibenzothiophene sulfone (DBTO <sub>2</sub> ), and (C) 4,6-dimethyldibenzothiophene (4,6DMDBTO <sub>2</sub> ), using the various imprinted-PBI nanofibers.....	214
Figure 5.41	GC-FID chromatograms of oxidized model fuel containing benzothiophene sulfone (BTO <sub>2</sub> ), dibenzothiophene sulfone (DBTO <sub>2</sub> ) and 4,6-dimethyldibenzothiophene (4,6-DMDBTO <sub>2</sub> ) before and after adsorption with imprinted-chitosan nanofibers.....	216
Figure 5.42	GC-FID chromatograms of benzothiophene sulfone (BTO <sub>2</sub> ), dibenzothiophene sulfone (DBTO <sub>2</sub> ) and 4,6-dimethyldibenzothiophene (4,6-DMDBTO <sub>2</sub> ) before and after adsorption with imprinted-PBI nanofibers.....	217
Figure 5.43	GC-AED chromatograms of Carbon (A) at 179 nm, and sulfur (B) at 181 nm in hydro-treated diesel after oxidation, and chromatograms of Carbon (C) at 179 nm and sulfur (D) at 181 nm in oxidized hydro-treated diesel after using imprinted-chitosan nanofibers as adsorbent.....	220
Figure 5.44	GC-AED chromatograms showing desorbed sulfones from imprinted-chitosan nanofibers after Soxhlet extraction using a mixture of methanol and acetonitrile (1:1).....	221
Figure 5.45	GC-AED chromatograms of carbon (A) at 179 nm, and sulfur (B) at 181 nm in hydro-treated diesel after oxidation, and chromatograms of carbon (C) at 179 nm and sulfur (D) at 181 nm in oxidized hydro-treated diesel after using imprinted-PBI nanofibers as adsorbent.....	222
Figure 5.46	GC-AED chromatograms of sulfur at 181 nm comparing (A) initial abundance of sulfonated compounds (oxidized sulfur) in hydro-treated diesel before adsorption on imprinted PBI nanofibers to the (B) abundance of desorbed sulfones from the imprinted nanofibers after using methanol and (C) pressurized hot water.....	223

---

---

Figure 5.47	GC-AED chromatograms of carbon (A) at 179 nm, and sulfur (B) at 181 nm in oxidized heavy crude oil, and chromatograms of carbon (C) at 179 nm and sulfur (D) at 181 nm in oxidized heavy crude oil after using imprinted-PBI nanofibers as adsorbent.....	224
Figure 5.48	Molecular modelled stable configurations for the 1:1 adduct of BTO <sub>2</sub> (A), DBTO <sub>2</sub> (B), and 4,6-DMDBTO <sub>2</sub> (C) with chitosan. The dashed lines represent hydrogen bonds.....	226
Figure 5.49	Molecular modelled stable configurations for the 1:1 adduct of BTO <sub>2</sub> (A), DBTO <sub>2</sub> (B), and 4,6-DMDBTO <sub>2</sub> (C) with polybenzimidazole. The dashed lines represent hydrogen bonds.....	228
Figure 6.1	Schematic representation of the catalysed oxidative-desulfurization process.....	235

---

**List of Schemes**

Scheme 1.1	Kodama pathway of dibenzothiophene (DBT) degradation.....	15
Scheme 1.2	The pathway of biological desulfurization of DBT relies on biocatalysts for specificity. NADH is reduced nicotinamide adenosine dinucleotide; FMN is flavin mononucleotide.....	16
Scheme 1.3	Mechanistic routes for the hydro-desulfurization of thiophene.....	19
Scheme 1.4	The ideal reaction in ODS process for dibenzothiophenes and methyl substituted derivatives.....	21
Scheme 1.5	Simplified catalytic mechanism for the oxidation of organosulfur compounds. Here L may refer to donor atom or a solvent molecule.....	30
Scheme 1.6	Radical initiation (a), propagation (b-c) and termination (d).....	31
Scheme 1.7	Basic principle of the S-Zorb sulfur removal technology process developed by Phillips petroleum for sulfur removal from liquid fuel at elevated temperatures under low H <sub>2</sub> pressure.....	40
Scheme 4.1	Synthetic scheme for V <sup>IV</sup> O(sal-HBPD) and poly[V <sup>IV</sup> O(sal-AHBPD)].....	85
Scheme 4.2	Synthetic scheme for [allylsB] ligand and poly[V <sup>IV</sup> O(allylsB-co-EGDMA)] microspheres....	86
Scheme 4.3	Proposed mechanism showing the effect of tetrabutylammonium bromide (TBAB) during conjugation.....	114
Scheme 4.4	Oxidation studies on the different organosulfur compounds ( <i>t</i> -BuOOH) = <i>tert</i> -butylhydroperoxide; TBAB = <i>tert</i> -butylammonium bromide.....	142
Scheme 5.1	Proposed crosslinking of the imprinted chitosan microspheres (possible routes of hydrogen bonding interaction) using glutaraldehyde.....	164

---

**List of Tables**

Table 1.1	Physico-chemical properties of crude oils and hydro-treated diesel oil.....	13
Table 1.2	Comparison of homogeneous and heterogeneous catalysts.....	24
Table 1.3	Overview of the reactions catalysed by supported vanadium oxides and complexes as described in the open literature.....	26
Table 1.4	Some common thermal free radical initiators and photo-initiators for polymerization of vinyl monomers.....	32
Table 1.5	Effect of changing electrospinning conditions/parameters on fiber morphology.....	38
Table 2.1	General reagents used in this study.....	47
Table 2.2	EPR analysis parameters for both the homogeneous [V <sup>IV</sup> O(sal-HBPD)] and heterogeneous poly[V <sup>IV</sup> O(sal-AHBPD)] and poly[V <sup>IV</sup> O(allylSB-co-EGDMA)] catalysts.....	51
Table 2.3	ICP-OES method and operating parameters.....	53
Table 2.4	Chromatographic conditions used in the identification and quantification of the oxidation products and adsorption of organosulfur compounds in model system and hydrotreated diesel.....	54
Table 2.5	Detector conditions used in the identification and quantification of the oxidized compounds...	55
Table 3.1	Weight % of saturates, aromatics, resins and asphaltenes (SARA) in various crude oils.....	65
Table 3.2	Elemental microanalyses of the crude oils, and hydro-treated oil.....	65
Table 3.3	Selected Infra-Red bands of the various crude oils.....	67
Table 3.4	Metal distribution in the aromatic crude oil fractions.....	69
Table 3.5	Validation of certified values of vanadium and nickel on Fuel oil SRM 1634c.....	69
Table 3.6	Some sulfur compounds identified in aromatic fraction of crude oil.....	71
Table 3.7	The distribution ratio of phenanthrene (and derivatives)-to-dibenzothiophene in the crude oil aromatic fractions.....	74
Table 3.8	The distribution ratio of phenanthrene (and derivatives)-to-2,3-methyl-dibenzothiophene in the crude oil aromatic fractions.....	75

---



---

Table 3.9	The distribution ratio of phenanthrene (and derivatives)-to-4-methyl-dibenzothiophene in the crude aromatic oil fractions.....	76
Table 4.1	Summary of crystal data, data collection and structural refinement parameters for the complex.....	90
Table 4.2	Selected bond length (Å) and bond angles (°) for [V <sup>IV</sup> O(sal-HBPD)].....	91
Table 4.3	Elemental binding energies of poly[(sal-AHBPD)] and poly[V <sup>IV</sup> O(sal-AHBPD)] as determined by XPS.....	97
Table 4.4	Elemental binding energies of poly[allylsB-co-EGDMA], poly[V <sup>IV</sup> O(allylsB-co-EGDMA)] and poly[V <sup>IV</sup> O(allylsB-co-EGDMA)] after use as determined by XPS.....	100
Table 4.5	Oxidation of organosulfur compounds using <i>t</i> -BuOOH in the presence of [V <sup>IV</sup> O(sal-HBPD)], poly[V <sup>IV</sup> O(sal-AHBPD)] and using poly[V <sup>IV</sup> O(allylsB-co-EGDMA)]... ..	125
Table 4.6	Catalysed oxidation of organo-sulfur compounds using <i>t</i> -BuOOH in the presence of poly[V <sup>IV</sup> O(sal-AHBPD)] (Cat 1) and poly[V <sup>IV</sup> O(allylsB-co-EGDMA)] (Cat 2).....	138
Table 4.7	The leaching studies on the poly[V <sup>IV</sup> O(sal-AHBPD)] (Cat 1) and poly[V <sup>IV</sup> O(allylsB-co-EGDMA)] (Cat 2) microspheres.....	140
Table 4.8	The ν(C-S) band shifts observed for the various individual oxidation products with respect to their initial starting materials.....	144
Table 5.1	EDS chemical composition of chitosan and polybenzimidazole (PBI)-imprinted and non-imprinted nanofibers.....	170
Table 5.2	Surface area of imprinted and non-imprinted chitosan microspheres and nanofibers.....	175
Table 5.3	Surface area and porosity of imprinted- and non-imprinted-PBI nanofibers.....	176
Table 5.4	Kinetic data of pseudo-first-order and second order for the imprinted-chitosan nanofibers and microspheres.....	196
Table 5.5	Parameters of Langmuir adsorption model and Freundlich adsorption model for the imprinted-chitosan nanofibers and microspheres.....	196
Table 5.6	Kinetic data of pseudo-first-order and second order for the imprinted-PBI nanofibers.....	204
Table 5.7	Parameters of Freundlich adsorption model for the imprinted-PBI nanofibers.....	207

---

---

Table 5.8	Influence of sulfone compounds upon adsorption on imprinted-chitosan and -PBI nanofibers.....	213
Table 5.9	DFT modelling studies on the adducts formed between benzothiophene sulfone (BTO <sub>2</sub> ), dibenzothiophene sulfone (DBTO <sub>2</sub> ) and 4,6-dimethyldibenzothiophene sulfone (4,6-DMDBTO <sub>2</sub> ) with chitosan ( $\Delta\Delta H$ , $\Delta\Delta G$ and $\Delta\Delta S$ complex).....	227
Table 5.10	DFT modelling studies on the adducts formed between benzothiophene sulfone (BTO <sub>2</sub> ), dibenzothiophene sulfone (DBTO <sub>2</sub> ) and 4,6-dimethyldibenzothiophene sulfone (4,6-DMDBTO <sub>2</sub> )with PBI ( $\Delta\Delta H$ , $\Delta\Delta G$ and $\Delta\Delta S$ complex).....	229

# Chapter 1

## Introduction

### 1.1 Crude oil

Crude oil is a complex blend containing thousands of hydrocarbons, non-hydrocarbon compounds and heavy metals.<sup>1</sup> Crude oils are known to mainly comprise of hydrocarbons mixed with variable quantities of sulfur-, nitrogen-, and oxygen-containing compounds. Metals in the forms of inorganic salts or organometallic compounds such as porphyrinate complexes are present in the crude oil mixture in small quantities. The metal content of crude oils varies appreciably from one reservoir to another.<sup>1</sup> Generally, crude oils are not used directly as transportation fuels or raw material in the production of petrochemicals products. Hence, refining of this complex mixture (crude oil) is therefore required to separate the mixture into simpler fractions that can be used as fuels, lubricants, or as intermediate feedstock to the petrochemical industries.<sup>2</sup>

It is predicted that crude oil would be available as a source of energy for several decades to a century.<sup>1</sup> However, there has been crude oil quality degeneration as the remaining contents of the known reservoirs tend to be of heavier and sourer composition and new wells are seldom encountered.<sup>3</sup> With the growing awareness that oil is a finite resource, it is very important to try to utilize it as effectively as possible whilst limiting its environmental impact through processing efficiency, by eliminating sulfur in various fuels. Strict measures to reduce sulfur levels in fuels have been proposed by environmental regulating agencies in some countries of the world (**Figure 1.1**), all aiming at reducing sulfur levels in fuels to an ultra-low level of between 10-15 ppm by 2015.<sup>3</sup>

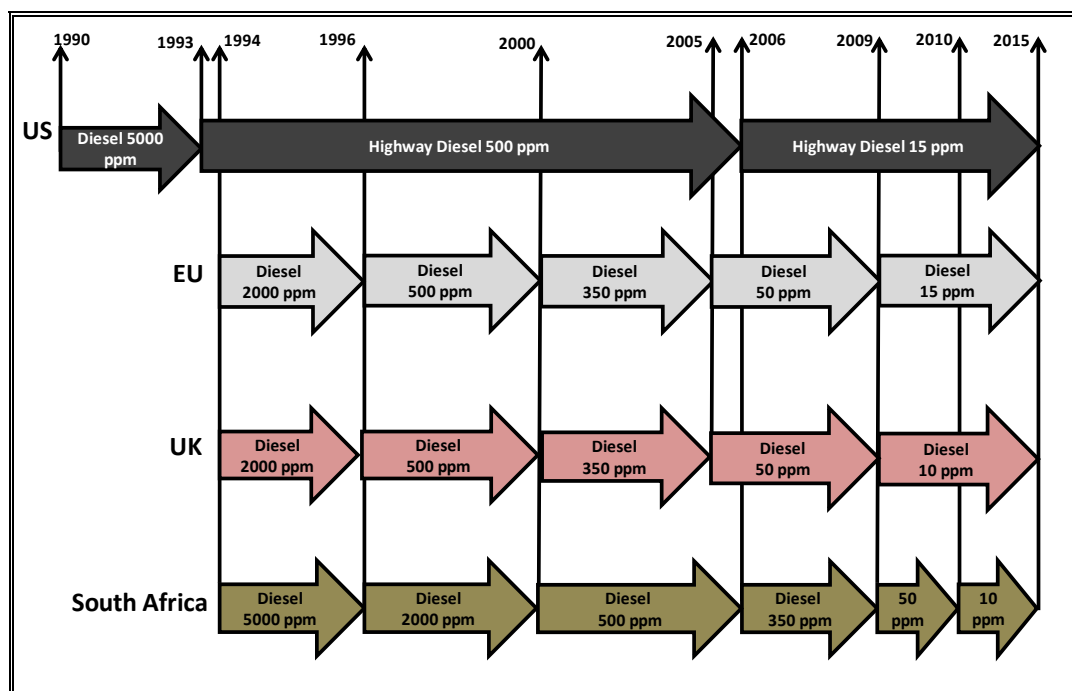


**Figure 1.1** Trends in diesel sulfur fuel specifications from the United States (US), United Kingdom (UK), European Union (EU) and South Africa (SA) over the years.

### 1.1.1 Origin of crude oils

Crude oil is a naturally occurring yellow to black thick liquid. The origin of crude oils has not been clearly established, but it is generally agreed that crude oils are derived from marine animals and plant debris subjected to high temperatures and pressures beneath the earth crust.<sup>1</sup> They are largely found in oil reservoirs associated with sedimentary rocks beneath the earth's surface.<sup>4-6</sup> It is also suspected that a rock constituent catalyses these transformations irrespective of their origin.<sup>5</sup>

According to organic theory, crude oils are derived from animal remains by the putrefactive process which is one of the stages of decomposition. This leaves the tissues and cells to be altered by heat and pressure into hydrocarbon oils. The organic theory, however, does not narrow itself to animal sources alone but brings forward many data that showed possible formation of petroleum from other organic matter as well. It has also been suggested that great masses of organic matter sinks to the bottom of the ocean, thereby decomposing under pressure to yield petroleum.<sup>4</sup>

### 1.1.2 Classification of crude oils

Several criteria have been employed to classify crude oils; these are variations in appearance and viscosity of oils from one oil field to another as well as chemical composition. These variations in appearance range in odour and colour, while the viscosity with respect to gravity can be classified based on American Petroleum Gravity (API) gravity and viscosity. For example, if the API gravity of the crude oil is 20 degrees or less, it is categorized as 'heavy', and those with an API gravity  $\geq 40.1$  degrees are known as 'light' and if the oil ranges between 20 and 40.1 degrees, it is graded as 'intermediate or medium crude'.<sup>5</sup> Classifications can also be based on chemical properties, for example, vanadium-to-nickel ratio, nitrogen and sulfur content. It is known that crude oil with low content of sulfur is referred to as being 'sweet' while the presence of high content sulfur is known as 'sour'. Basically, crude oils can be classified into three predominating hydrocarbon types.<sup>6</sup> These are:

1. Paraffins
2. Naphtha
3. Asphaltenes (resins)

#### 1.1.2.1 Paraffins

These are any saturated hydrocarbons having the general formula  $C_nH_{2n+2}$ . The ratio of paraffinic hydrocarbons in crude oils is high compared to aromatics. Aliphatic saturates are non-polar hydrocarbons without double bonds, but with straight-chain and branched alkanes, as well as cycloalkanes. Cycloalkanes contain one or more rings, which may have several alkyl side chains. The proportion of saturates in a crude oil normally decreases with increasing molecular weight fractions, thus saturates generally are the lightest fraction of the crude oil. Wax is a sub-class of saturates, consisting primarily of straight-chain alkanes, mainly ranging from  $C_{20}$  to  $C_{30}$ . Wax precipitates as a particulate solid at low temperatures, and is known to effect emulsion stability properties of crude oil systems.<sup>7-9</sup>

#### 1.1.2.2 Naphthenic

These are types of alkanes that have one or more rings of carbon atoms in the chemical structure of their molecules. They have higher boiling points, melting points, and densities than paraffins

(alkanes). The higher the naphthenic compounds (aromatics) in fuel the higher the octane number. They are also termed as aromatics, which are usually benzene and its structural derivatives. Aromatics are common to all petroleum, and most of the aromatics contain alkyl chains and cycloalkane rings, along with additional aromatic rings. Aromatics are often classified as mono-, di- and tri-aromatics depending on the number of aromatic rings present in the molecule. Polar, higher molecular weight aromatics may fall in the resin or asphaltene fraction.

### 1.1.2.3 Asphaltenes

Asphaltenes, also grouped alongside resins, contain relatively large quantity of polynuclear aromatics, high asphaltene content, and relatively less paraffins than paraffinic crudes. This fraction is comprised of polar molecules often containing heteroatoms mostly the nitrogen- and oxygen-containing compounds. The resin fraction is defined as the fraction soluble in light alkanes such as pentane and heptane, but insoluble in liquid propane.<sup>10-12</sup> Since the resins are defined as a solubility class, both aromatic and asphaltene fractions is expected. Resins have a higher hydrogen-to-carbon (H/C) ratio (1.2-1.7) as compared to the (0.9-1.2) H/C ratio for asphaltenes.<sup>12</sup> Resins are structurally similar to asphaltenes, but smaller in molecular weight (< 1000 g/mole). Naphthenic acids are commonly regarded as a part of the resin fraction.

## 1.1.3 Chemical composition of crude oils

As much as there are thousands of organic molecules in crude oils, these molecules can be categorized into groups with similar chemical properties as discussed in **Section 1.1.2**. Crude oil mixture is composed of the following groups<sup>1</sup>:

- (a) Hydrocarbon compounds (consist of carbon and hydrogen).
- (b) Non-hydrocarbon compounds.
- (c) Organometallic compounds and inorganic salts.

### 1.1.3.1 Hydrocarbon Compounds

The principal constituents of most crude oils are hydrocarbon compounds. All hydrocarbon straight chain compounds classes are present in crude oil mixture, except the alkenes and alkynes. This may

indicate that crude oils originated under a reducing atmosphere. Hydrocarbon compounds are classified as alkanes (butane, 2-methyl propane and hexane), cycloparaffins (cyclohexane, methyl cyclohexane and cycloheptane) and aromatic compounds (benzene, toluene, naphthalene, 1, 2-benzopyrene and xylenes).<sup>13</sup>

### 1.1.3.2 Non-hydrocarbon Compounds

Non-hydrocarbon compounds occur in crude oils in many forms. The most important and well-known forms are the organic sulfur-, nitrogen-, and oxygen-containing compounds.<sup>13</sup> Most of the non-hydrocarbon compounds are known to be impurities which are harmful and may cause problems to certain catalytic processes.<sup>13</sup> Fuels having high sulfur and nitrogen levels cause pollution problems to the environment in addition to their corrosive nature on catalytic converters.<sup>3</sup>

#### (i) Sulfur compounds

Sulfur in crude oils is mainly present in the form of organosulfur compounds. Organosulfur compounds may generally be classified as acidic and non-acidic. Acidic sulfur compounds when dissolved in water are mildly acidic, for example thiols (mercaptans), while the thiophene, thioethers, and disulfides are examples of non-acidic sulfur compounds found in crude fractions. Organosulfur compounds in fuels produce sulfur oxides ( $\text{SO}_x$ ) during combustion, and these oxides cause severe environmental impacts. Extensive research has been carried out to identify some sulfur compounds in a narrow light petroleum fraction.<sup>13</sup> Examples of some sulfur compounds in crude oils are presented in

**Figure 1.2.**

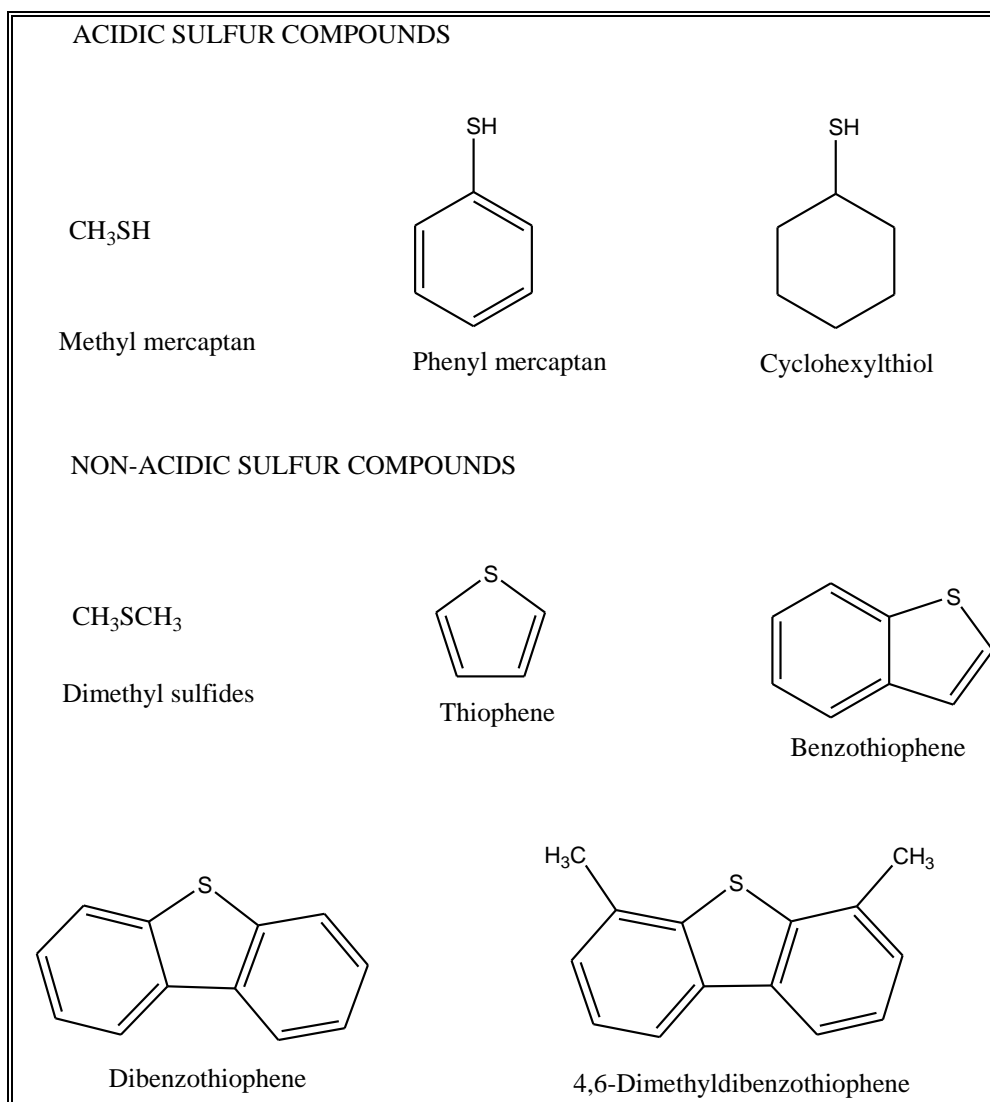


**Figure 1.2** Acidic sulfur and non-acidic sulfur compounds.

Low-sulfur containing crude oils are referred to as sweet oils, while the high-sulfur containing crude oils are referred to as sour crudes and are less desirable due to high cost involved in treating (desulfurizing) the oils. Various crude oils around the world have different sulfur contents (ppm).

**Figure 1.3** presents sulfur distribution in some crude oils reservoirs around the world.



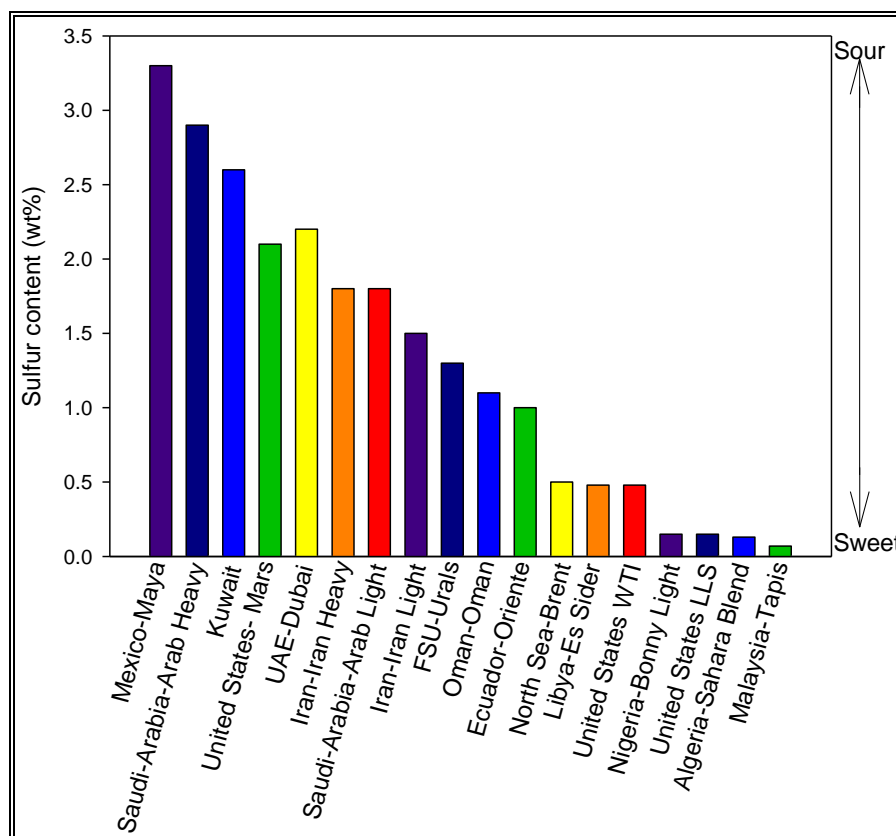


**Figure 1.3** Sulfur distribution in crude oils in the world (1 wt.% Sulfur = 10000 ppm).<sup>14</sup>

The current industrial process employed in the removal of sulfur compounds from crude oils is the hydro-desulfurization process whereby hydrogen gas is passed through a stream of crude oil under high temperature and pressure in the presence of a catalyst. Hydrogen sulfide gas is produced, and it is scrubbed off and converted to elemental sulfur in the Claus process.

## (ii) Nitrogen compounds

Organic nitrogen compounds occur in crude oils either in a simple heterocyclic form as in pyridine ( $C_5H_5N$ ) and pyrrole ( $C_4H_5N$ ), or in a complex structure such as in porphyrin. The nitrogen content in most crude is very low and does not exceed 0.1 wt%. In some heavy crude, however, the nitrogen content may reach up to 0.9 wt%.<sup>7</sup> Nitrogen compounds are more thermally stable than sulfur compounds and accordingly are concentrated in heavier petroleum fractions and residues. Light petroleum streams may contain trace amounts of nitrogen compounds, which should be removed because they poison many processing catalysts, however, the presence of nitrogen compounds in fuel,

maintains fuel stability. During hydro-treatment of petroleum fractions, nitrogen compounds are hydro-denitrogenated to ammonia and the corresponding hydrocarbon.<sup>7</sup>

Nitrogen compounds in crudes may generally be classified into basic and non-basic categories (**Figure 1.4**). Basic nitrogen compounds are mainly those having a pyridine ring, and the non-basic compounds have a pyrrole structure. **Figure 1.4** presents some examples of organic nitrogen compounds found in crude oils.

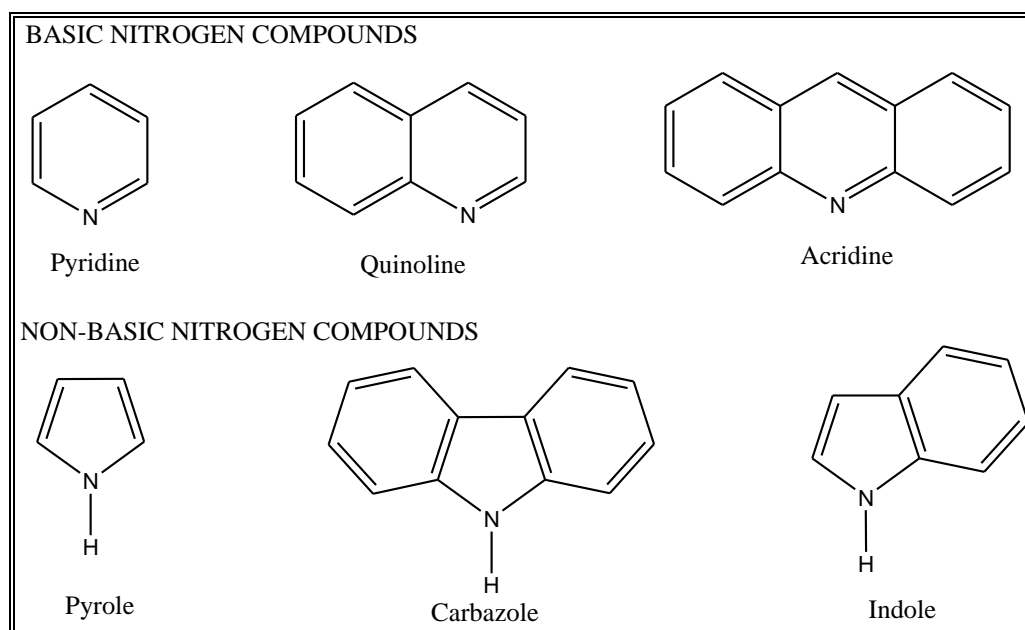


**Figure 1.4** Examples of organic nitrogen compounds (basic and non-basic).

Most of the nitrogen compound species are enriched in resins and asphaltenes, causing them to exhibit polar characteristics.<sup>15</sup> Separation of nitrogen compounds is difficult, and the compounds are susceptible to alteration and loss during handling. Jewell *et al.*<sup>15</sup> extracted basic and acidic nitrogen fractions from fuels by using cation- and anion-exchange resins, respectively, while the non-basic, neutral-nitrogen fractions were obtained by coordination-complex formation with ferric chloride supported on Attapulugus clay. However, the basic low molecular weight nitrogen compounds may be extracted with dilute mineral acids.

### (iii) Oxygen Compounds

Oxygen compounds in crude oils are more complex than the nitrogen and sulfur compounds. However, their presence in petroleum streams is not poisonous to processing catalysts. Many of the

oxygen compounds found in crude oils are weakly acidic and are found in asphaltenes and resin fractions of fuel oils.<sup>15</sup> They are carboxylic acids, cresylic acid, phenol, and naphthenic acid. Naphthenic acids are mainly cyclopentane and cyclohexane derivatives having a carboxyalkyl side chain (**Figure 1.5**). Naphthenic acids in the naphtha fraction have a special commercial importance and can be extracted by using dilute caustic solutions. The total acid content of most crude is generally low, but may reach as much as 3%, for example in some California crudes. Non-acidic oxygen compounds such as esters, ketones, and amides are less abundant than acidic compounds. **Figure 1.5** shows some of the oxygen compounds commonly found in crude oils.<sup>6</sup>

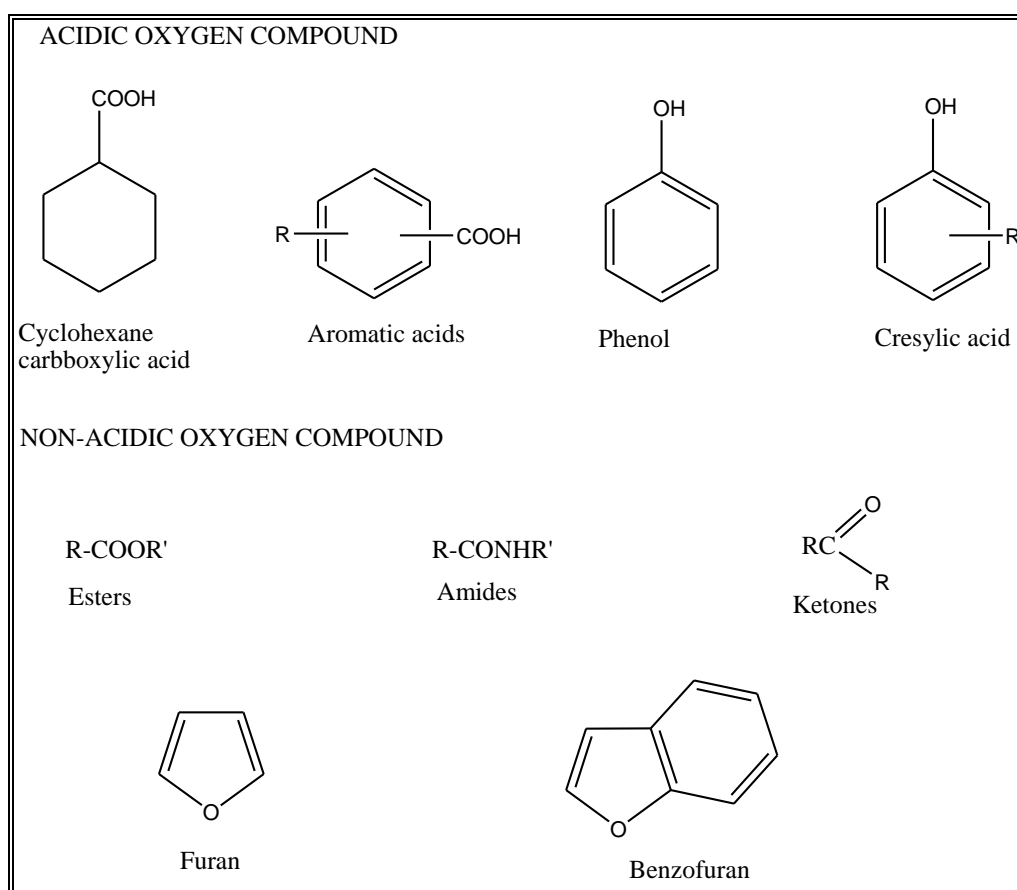


**Figure 1.5** Structural examples of organic oxygen compounds (acidic and non-acidic).

### 1.1.3.3 Metal complexes

Some of the more abundant metals found in crude oils include; sodium, calcium, magnesium, aluminum, iron, vanadium, and nickel.<sup>1</sup> They are present either as inorganic salts, such as sodium and magnesium chlorides, or in the form of organometallic compounds, such as those of nickel and

vanadium (as porphyrinato complexes) (**Figure 1.6**). Calcium and magnesium can form salts or soaps with carboxylic acids in crude oils, and these compounds act as emulsifiers, making their presence undesirable.<sup>6</sup>

When crude oil is processed, sodium and magnesium chlorides produce hydrochloric acid, which is very corrosive. Likewise, vanadium and nickel locked in porphyrins poisons catalysts, hence it should be reduced to very low levels. Desalting crude oils is a necessary step to reduce these salts. Almost all crude oils and bitumens contain detectable amounts of vanadyl and nickel porphyrins. Most of the vanadium and nickel compounds are concentrated in the heavy residues. Solvent extraction processes are used to reduce the concentration of heavy metals in petroleum residues.<sup>6</sup>

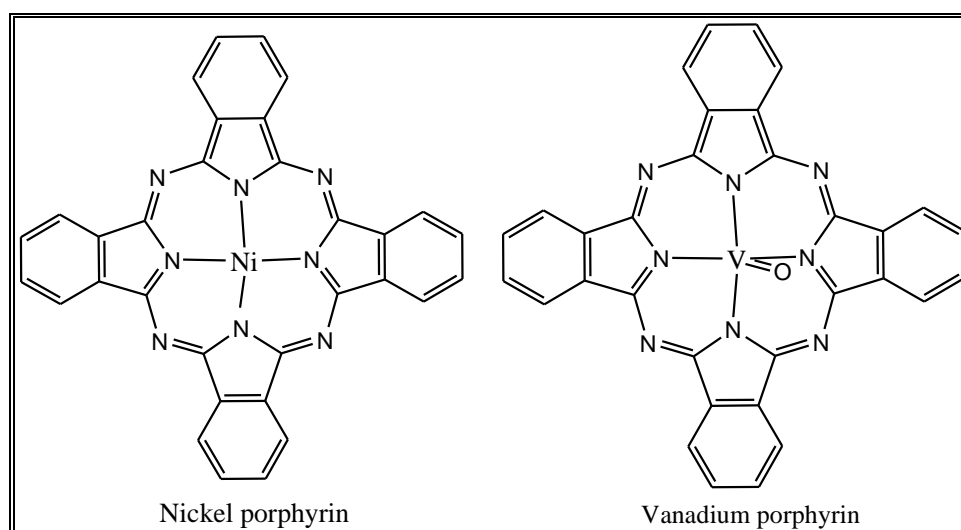


**Figure 1.6** Chemical structures of nickel porphyrin and vanadium porphyrin.

#### 1.1.4 Physico-chemical properties of the various crude oils

Classification of the crude oils is based on the following physico-chemical properties<sup>16,17</sup>;

##### (i) Density, Specific Gravity and API Gravity

Density is defined as the mass per unit volume of a material at specific temperature.<sup>16</sup> The API (American Petroleum Institute) gravity is another way to express the relative masses of crude oils.

The API gravity can be calculated mathematically using **Equation 1.1** below:

$$^{\circ}\text{API} = \frac{141.5}{\text{Sp. gr } 60/60^{\circ}} - 131.5 \quad \mathbf{1.1}$$

A low API gravity indicates a heavier crude oil or a petroleum product, while a higher API gravity means a lighter crude or product. Specific gravities of crude oils roughly range from 0.82 for lighter crudes to 0.976 for heavier crudes (41-10 °API scale).

**(ii) Salt content**

Salts are basically found in crude oils dissolved in water, which mainly exist as an emulsified solution. The salt content expressed in milligrams of sodium chloride per liter oil (or in pounds/barrel) indicates the amount of salt dissolved in water. A high salt content in a crude oil presents serious corrosion problems during the refining process.<sup>6</sup>

**(iii) Sulfur content**

Sulfur, determines the type of treatment required for the distillates and this in turn dictates the price of the refined oils. Sulfur content can be determined by the use of advanced instruments such as gas chromatography fitted to an atomic emission detector (GC-AED) or sulfur chemiluminescence detector (GC-SCD). At present, hydro-desulfurization (HDS) process is being employed in the removal of sulfur from crude oils.<sup>18-23</sup>

**(iv) Pour point**

The pour point of a crude oil is the lowest temperature at which oil is observed to flow under the conditions of the test. Pour point data indicate the amount of long-chain paraffins present in a crude oil. Crude oils with a higher content of paraffins usually have higher wax content than other crude types.<sup>24</sup>

**(v) Ash content**

This test indicates the amount of metallic constituents in a crude oil. The ash left after completely burning an oil sample usually consists of stable metallic salts, metal oxides, and silicon oxide. The ash could be further analyzed for individual elements using spectroscopic techniques.<sup>25</sup> Fuel oils with low contents of metallic constituent are preferable. These components tend to promote mechanical wear, corrosion at high temperature and the formation of deposits in the turbocharger and on the exhaust

valve of engines. The effect of high temperature corrosion and the formation of deposits can be counteracted by the application of ash modifiers.<sup>16</sup>

**(vi) Aniline point**

The aniline point of oil is defined as the lowest temperature at which equal volumes of aniline ( $C_6H_5NH_2$ ) and the oil are miscible, i.e. form a single phase upon mixing. The value gives estimation for the content of aromatic compounds in the oil. The lower the aniline point, the greater is the content of aromatic compounds in the oil.<sup>16</sup>

**(vii) Oxidation stability**

Improved oxidation stability accounts for the slightly higher operating temperatures that oils can accommodate. Oxidation stability is a chemical reaction that occurs with a combination of diesel oil and oxygen. The oxidation rate is usually accelerated by high temperatures, water, acids and catalysts such as copper. This property describes the service life of an oil (diesel or lubricant), as an increase in oil temperature reduces fuel service life, thus increasing oil's viscosity.<sup>16</sup>

**(viii) Cetane number (CN)**

Cetane number (CN) is a measurement of the combustion quality of diesel fuel during compression ignition. It is a significant expression of the quality of a diesel fuel as it measures fuel's ignition delay. A higher fuel cetane number will have shorter ignition delay periods, than fuels with lower cetane number. Di-*tert*-butyl peroxide and *tert*-butyl alcohol are examples of additives to raise the cetane number.<sup>16</sup>

Physico-chemical properties of Nigeria crude oils reported by Odebunmi *et al.*<sup>16</sup> along side diesel oil processed for automotive engines published by South African National Standard (SANS)<sup>17</sup> are presented in **Table 1.1**.

**Table 1.1** Physico-chemical properties of crude oils and hydro-treated diesel oil.

Parameters	Crude oil samples			Diesel oil
	Bonny (Light crude)	Bonny (Medium crude)	Gulf (Heavy crude)	
Density at 37.8°C	0.8404	0.8750	0.8932	0.805
Specific gravity at 37.8°C or 100°F	0.8529	0.8881	0.9065	0.8723
API gravity at 37.8°C	34.4	27.8	24.6	30.7
Viscosity (cP) at 37.8°C	6.10	7.19	7.99	2.0
Kinematic viscosity (cst) at 37.8°C	7.26	8.22	8.95	3.12
Aniline point (°C)	59.5	71.5	85.0	64.5
Pour point (°C)	+3	-3	-5	+2
Water content (%v/v)	0.02	0.01	0.05	0.05
Oxidation stability, mg/100 mL, max.	-	-	-	2.0
Cetane Number, min	-	-	-	45-51

## 1.2 Desulfurization of crude oils

Desulfurization of crude oils (fuels) is a process employed for the elimination of sulfur and/or sulfur-containing compounds in crude oils during the petroleum refining process.<sup>26</sup> Crude oils contain a large variety of sulfur-containing compounds (thiols, thioethers, disulfides and thiophenes), which generate a serious environmental concern because of the emission of sulfur

oxides (SO<sub>x</sub>) and airborne particulate during combustion to the atmosphere.<sup>26</sup> The reduction of these gases in the atmosphere is currently being addressed through the elimination of source compounds (sulfur-containing compounds) present in fuels. The desulfurization process is extremely important in the petroleum-refining industry for the production of cleaner fuels. The three methods of desulfurization are described below.

### 1.2.1 Bio-desulfurization (BDS)

Bio-desulfurization involves the use of micro-organisms (e.g. bacteria) to desulfurize fuels under biological processes. Micro-organisms require sulfur for their growth and biological activities. Dried weight of bacterial cells comprises 0.5-1% sulfur atoms. Sulfur generally occurs in the structure of some enzyme cofactors (such as co-enzyme A, thiamine and biotin), amino acids and proteins (cysteine, methionine, and disulfide bonds).<sup>27</sup> Depending on their metabolic pathways, micro-organisms may have the ability to obtain the sulfur they need from different sources. Some micro-organisms consume the sulfur in thiophenic compounds such as dibenzothiophene (DBT), thus reducing the sulfur content in fuel. Energy BioSystems Corporation (EBC) was initially the only commercial venture dedicated to the development of bio-desulfurization technology. EBC's concept for a bio-desulfurization process was to treat diesel, but also to produce a value-added surfactant by-product to achieve a more economical process.<sup>28,29</sup> Bacteria converting dibenzothiophene and alkyl sulfides are relatively well known while fewer bacteria are found for benzothiophene, and only a few bacteria detected for thiophene.<sup>27</sup>

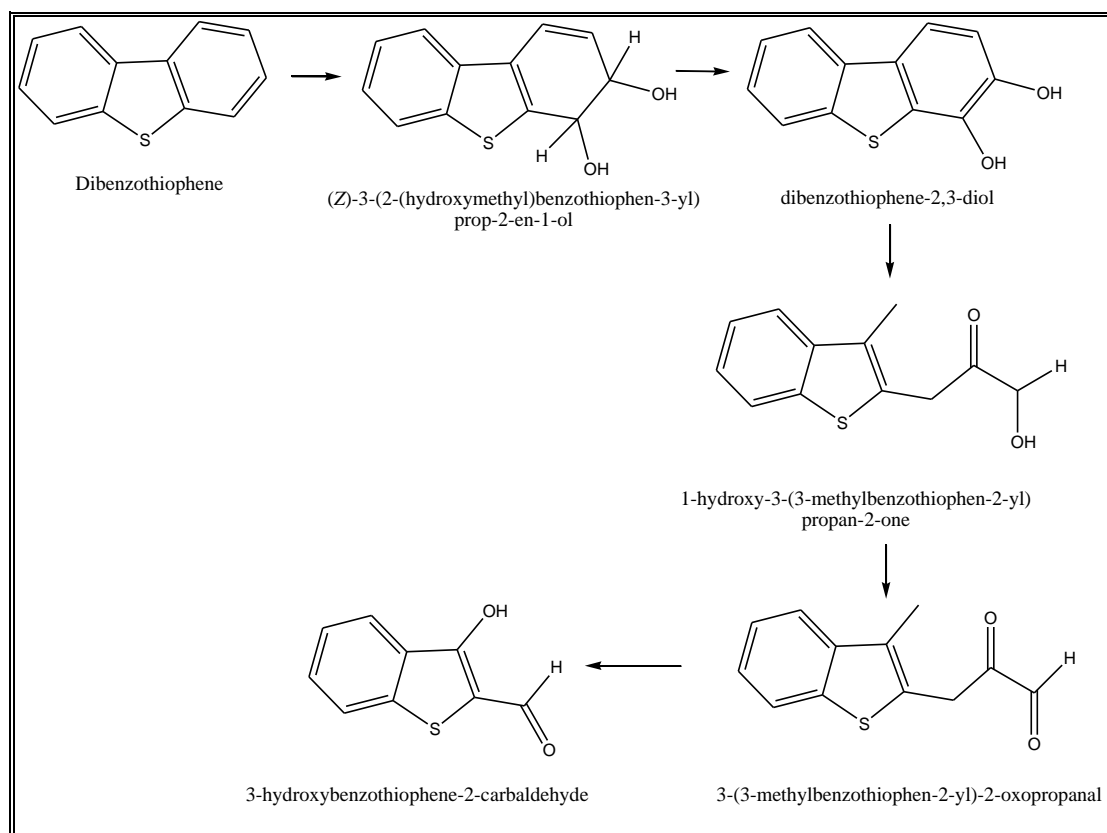
The two main pathways known for the utilization of dibenzothiophene by bacteria are: destructive (degradation) pathway and sulfur-specific (desulfurization) pathway.

#### 1.2.1.1 Ring destructive pathway

The ring destructive mechanistic process, also known as the 'Kodama pathway' (**Scheme 1.1**),<sup>30</sup> involves the initial dioxygenation of the peripheral aromatic ring of dibenzothiophene, followed by cleavage of the ring which finally leads to the accumulation of 3-hydroxybenzothiophene-2-carbaldehyde as a water-soluble end product with lower carbon content than dibenzothiophene. In this



pathway, no desulfurization occurs; the dibenzothiophene (organosulfur compound) is converted to a more polar compound which can be stripped off.

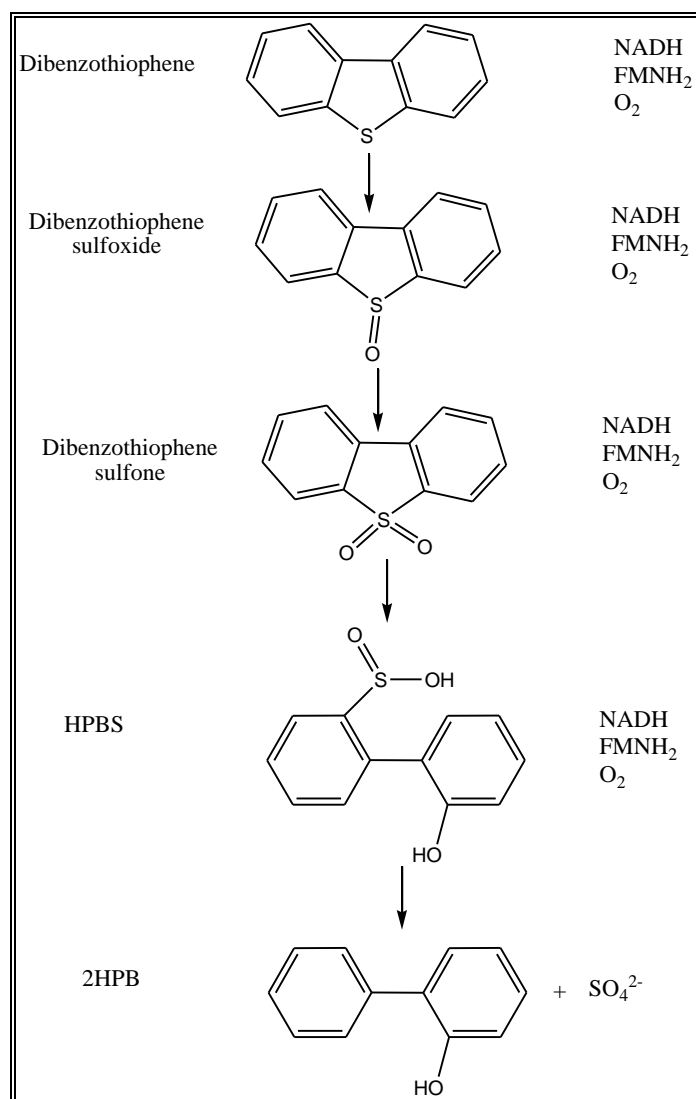


**Scheme 1.1** Kodama pathway of dibenzothiophene (DBT) degradation.

### 1.2.1.2 Sulfur-specific (desulfurization) pathway

The sulfur-specific desulfurization pathway involves the oxidation of dibenzothiophene to dibenzothiophene sulfoxide (DBTO), dibenzothiophene sulfone (DBTO<sub>2</sub>), sulfinate (HPBS) and hydroxybiphenyl (HBP) in the presence of oxygen and water under ambient temperature and pressure conditions (**Scheme 1.2**). NADH-FMN oxidoreductase, is an accessory component of the desulfurization pathway and allows the regeneration of the cofactors needed for the monooxygenase reactions catalyzed by dibenzothiophene monooxygenase (DszC) and dibenzothiophene-5,5-dioxide monooxygenase (DszA) that catalyzes the conversion of DBTO<sub>2</sub> into 2-hydroxybiphenyl-2-sulfinate (HBPS) and 2-hydroxybiphenyl (HPB) (**Scheme 1.2**). This bacterial strain therefore transform DBT to DBTO and then to DBTO<sub>2</sub>. Sulfur in DBTO<sub>2</sub> was removed to form SO<sub>3</sub><sup>2-</sup> and SO<sub>4</sub><sup>2-</sup> consecutively.

With the removal of sulfur, DBTO<sub>2</sub> was converted to benzoate and then was mineralized to water and carbon dioxide.



**Scheme 1.2** The pathway of biological desulfurization of DBT relies on biocatalysts for specificity. NADH is reduced nicotinamide adenosine dinucleotide; FMN is flavin mononucleotide.

In general, the bio-desulfurization process does not show very deep desulfurization, the maximum sulfur content limit of 50-200 ppm sulfur at best has been achieved. However, the bio-desulfurization process suffers the following limitations: (i) production of active resting cells (biocatalysts) with a high specific activity; (ii) preparation of a biphasic system containing oil fraction, aqueous phase and biocatalyst; (iii) bio-desulfurization of a wide range of organosulfur compounds at a suitable rate; (iv)

separation of desulfurized oil fraction, and recovery of the biocatalyst and its return to the bioreactor; and (v) efficient wastewater treatment.<sup>26</sup>

### 1.2.2 Hydro-desulfurization (HDS) process

The hydro-desulfurization (HDS) process has been employed for the removal of sulfur compounds from as early as the 1930's. In the HDS process, crude oil is heated, mixed with hydrogen, and fed to a reactor packed with a pelleted CoMo/Al<sub>2</sub>O<sub>3</sub> catalyst. Temperatures of the reactor range from 300 to 350°C at a pressure range of 15 to 90 bars to generate a mixture of the treated/desulfurized crude oil, hydrogen sulfides (H<sub>2</sub>S) and hydrogen gas. H<sub>2</sub>S is further recycled through a Claus process to recover the elemental sulfur.<sup>31,32</sup>

The addition of hydrogen to sulfur compounds at higher temperatures activates carbon-sulfur (C-S) bond cleavage as shown in the reaction **Scheme 1.3** for the hydro-desulfurization of thiophene. Two mechanistic routes are presented in **Scheme 1.3**, and in the first route, hydrogenation of thiophene precedes C-S bond scission, and in the second route, C-S bond scission occurs, before hydrogenation takes place. Both mechanistic routes produce carbon and sulfur which can easily be absorbed onto mesoporous aluminosilicate molecular sieves.<sup>31-33</sup>

HDS process is however limited in treating refractory sulfur compounds such as dibenzothiophenes (DBTs) and 4,6-dimethyldibenzothiophene<sup>31,33-36</sup> which are the main non-reactive organosulfur compounds to the hydrogenation process. **Figure 1.7** presents the order of reactivity of some sulfur compounds found in crude oils in the HDS process. The order of reactivity is governed by electron density of sulfur in the compounds which tends to increase as the bulkiness of the compounds decreases, and as bulkiness increases HDS reactivity decreases (**Figure 1.7**). Electron density is a representation of the probability of finding an electron in a specific location around an atom or molecule. In general, an electron is likely to be found in regions with high electron density than region low electron density, in so doing influencing the reactivity of sulfur in the compounds.<sup>31</sup> Hence, the higher electron density results in decreased HDS activity.

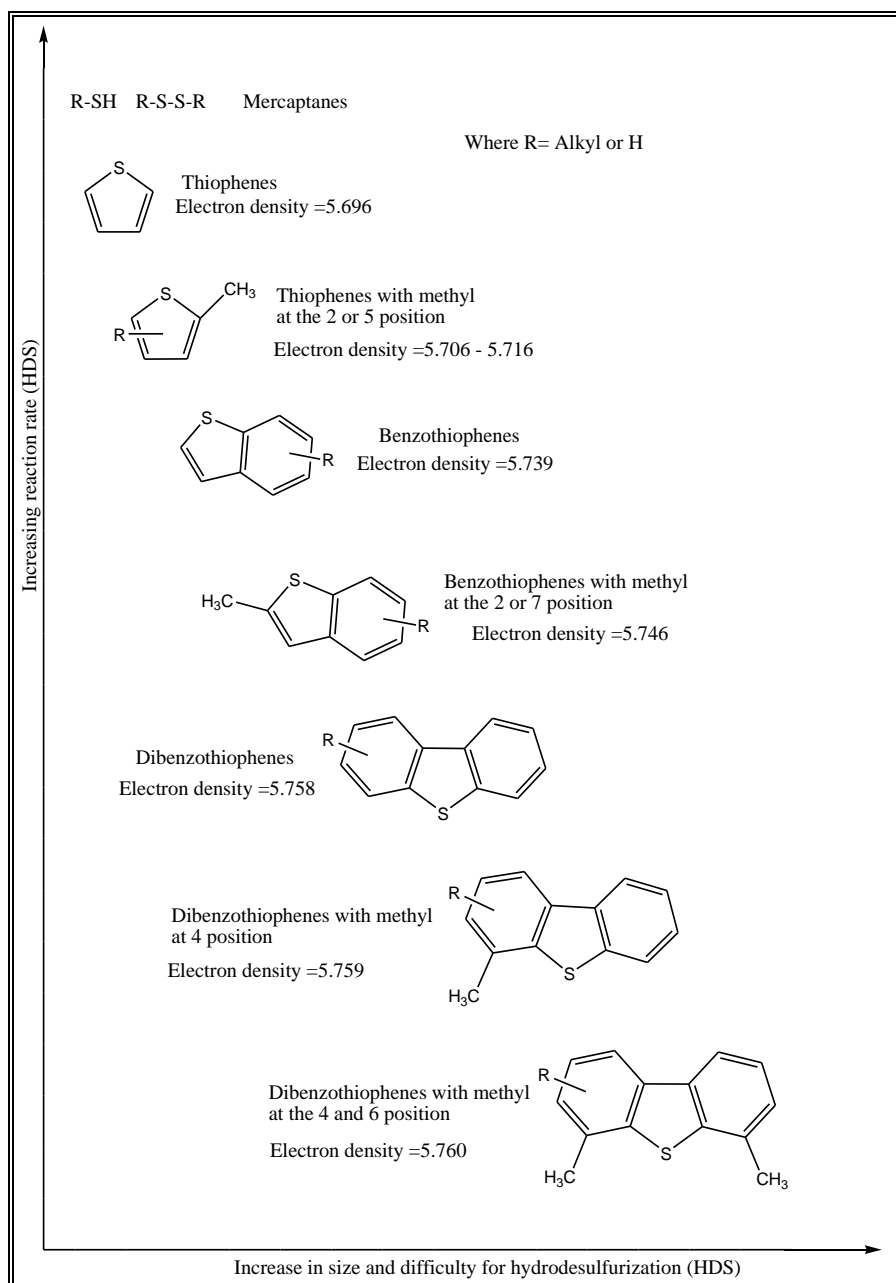
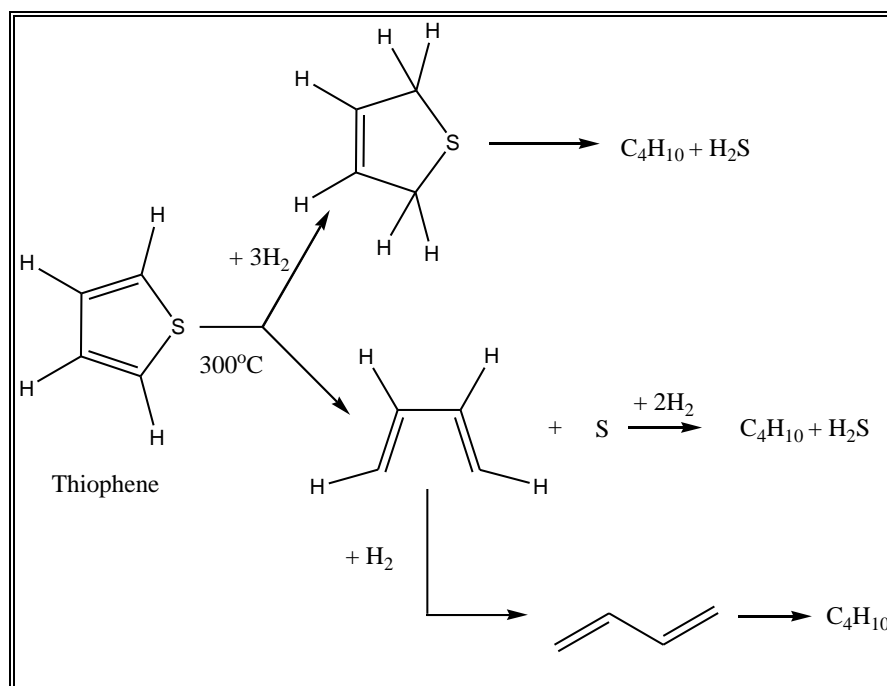


**Figure 1.7** Reactivity of various organic sulfur compounds in hydro-desulfurization versus their ring sizes and positions of alkyl substitutions on the ring.<sup>31</sup>



**Scheme 1.3** Mechanistic routes for the hydro-desulfurization of thiophene.

The production of ultra-low sulfur fuels (10-50 ppm) using HDS process will therefore require the application of extreme operating conditions, i.e., high temperatures and high pressures, and the use of highly active catalysts at slow velocity pace, since most HDS process reduces the sulfur content in fuels to a range of 200-300 ppm.<sup>31-34, 37-41</sup> Under these extreme conditions (high temperatures and high pressures), to produce ultra-low sulfur fuels, the aromatics and polynuclear aromatics content would fall outside the requisite specification as they tend to be hydrogenated. The other fuel requirements such as oxygen content, vapor pressure, aromatics and olefin content for petrol, and cetane number, density and T95 point for diesel would also be compromised. Also the high cost involved in such extreme conditions such as the use of excess hydrogen gas and energy therefore makes the end-product expensive. An alternative process which can complement the HDS process under mild conditions to achieve ultra-low sulfur fuels is therefore essential, and oxidative-desulfurization shows potential.

### 1.2.3 Oxidative-desulfurization (ODS) process

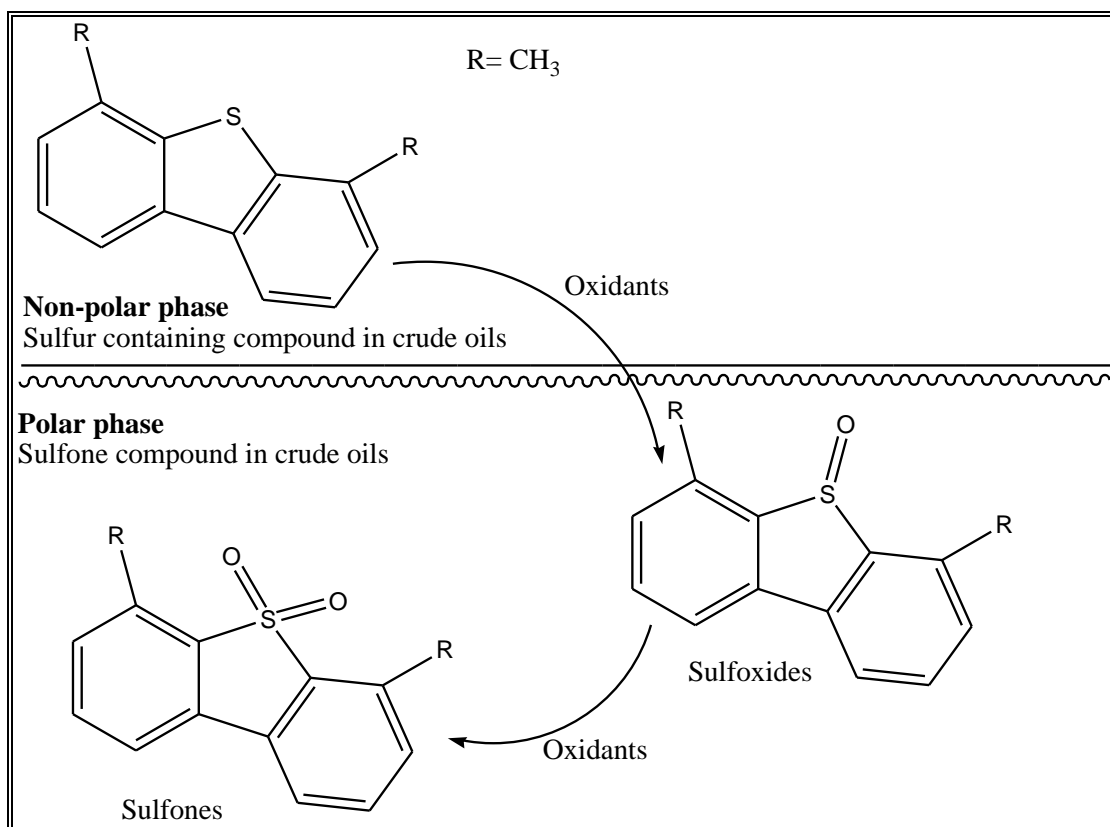
Oxidative-desulfurization (ODS) has been considered as a new technology for desulfurization of fuel oils. The ODS process includes two stages: (i), oxidation of the sulfur atoms in the first step; and (ii),

liquid extraction of the polar products at the final step. The utmost advantages of the ODS process is that the refractory sulfur-containing compounds can be oxidized and it operates at a low reaction temperature, and pressure, and in the absence of hydrogen which is expensive. With HDS being able to desulfurize thiophene and acidic sulfur compounds at relatively moderate conditions and the ODS process being capable of desulfurizing refractory sulfur compounds, then the ODS process has great potential to be a complementary process to HDS for producing deeply desulfurized crude oil.

### 1.2.3.1 General description of the ODS process

In the ODS process, sulfur-containing compounds in crude oils are oxidized using selective oxidants such as nitric acid,<sup>42-44</sup> nitrogen oxides,<sup>42,45-46</sup> organic hydroperoxides,<sup>47-51</sup> peroxyacids,<sup>52-53</sup> hydrogen peroxide,<sup>54-55,57</sup> and/or ozone<sup>56,58</sup> in the presence of a catalyst to produce sulfone compounds that can be preferentially extracted due to their increased relative polarity.

For oxidation to take place, the oxidant needs to be in contact with fuel oils under optimum conditions, and the oxidant donates oxygen atoms to the sulfur in benzothiophenes, dibenzothiophenes and its derivatives to form sulfoxides and/or sulfones (**Scheme 1.4**). Some of the by-products generated by oxidant influence the quality of the fuels; for example *tert*-butyl alcohol which is a potential octane booster for fuels is generated as by-product of *tert*-butylhydroperoxide.<sup>48,51</sup>



**Scheme 1.4** The ideal reaction in ODS process for dibenzothiophenes and methyl substituted derivatives.

A practical industrial flow system for oxidative desulfurization of hydro-treated crude oil (**Figure 1.8**), where catalyst in the crude oils are extracted and washed, un-used oxidant are also separated in the separator section before further oil processing can take place.

Liquid-liquid extraction of the oxidized compounds (sulfones and sulfoxides) was carried out by contacting oxidized crude oil with a non-miscible solvent which is selective for the polar oxidized sulfur compounds.<sup>59-64</sup> The desulfurized crude oil is water washed to recover any traces of dissolved extraction solvent and then polished either by absorption using silica gel and alumina to produce high quality clean sulfur free oil.<sup>65</sup>

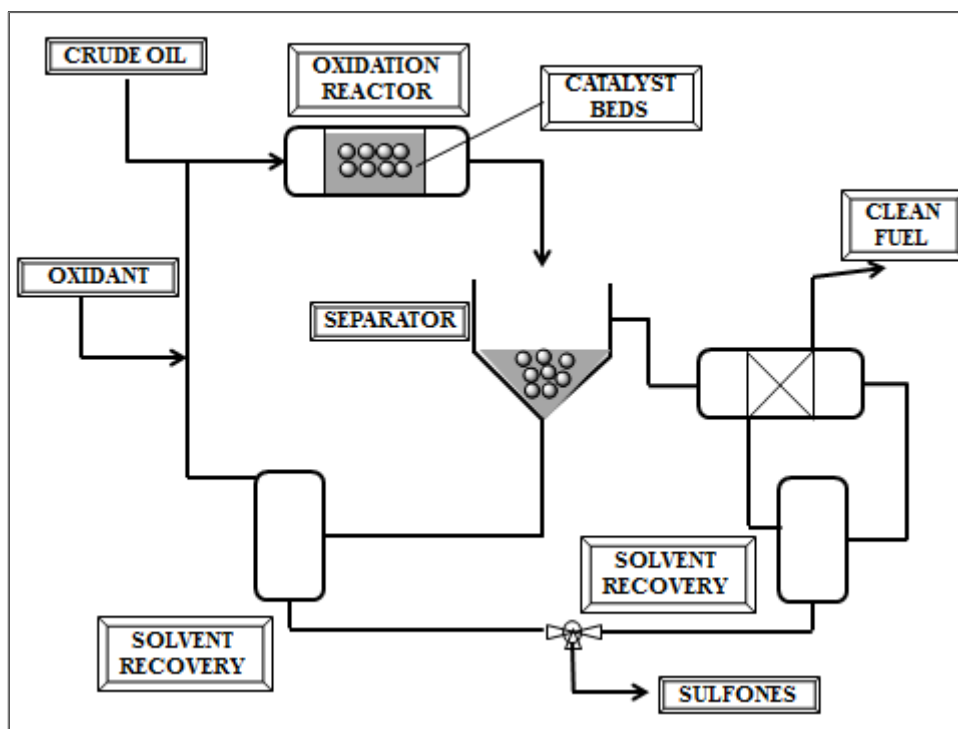


**Figure 1.8** Schematics of oxidative-desulfurization ODS process.<sup>65</sup>

The choice of solvent for the extraction of sulfone in crude oils is critical. A solvent must be thermodynamically compatible with the compound to be extracted. Water-soluble polar solvents such as *N,N*-dimethylformamide (DMF), dimethylsulfoxide (DMSO), and acetonitrile are usually employed for the desulfurization of crude oils. The former two solvents have a high extractability for sulfones but have a high boiling point (above 200°C), which is close to the boiling point of the sulfones, and thus may not be re-used for further extraction based on the solvent recovery by distillation. Acetonitrile was, however, a preferred solvent for the extraction of sulfones despite its high cost because of its relatively low boiling point (82°C) making solvent recovery by distillation possible. However, it extracts a large quantity of aromatics along with sulfones, thereby giving rise to a low quality fuel.<sup>65</sup> Several solid adsorbent materials have also been developed for the adsorption of sulfone compounds in order as to eliminate the limitations posed by the liquid extractants.<sup>66-72</sup> The adsorbents for organosulfur compounds are discussed in details in **Section 1.4**. Oxidative-desulfurization demonstrates that it is possible to remove sulfur compounds from fuels to meet strict regulation limits,<sup>42-51</sup> though a high oxidant-to-sulfur (O/S) ratio is required to oxidize sulfur



compounds to their corresponding sulfoxides and sulfones. However, this drawback (i.e. high oxidant constraint) can be avoided by use of suitable catalysts.<sup>65</sup>

### 1.3 Catalysis

A catalyst is a substance which in minimal amounts will bring about the transformation of large quantities of the reacting substances, and which will be found unchanged in its chemical composition at the end of the reaction. The entire process is termed catalysis, and was first coined in 1836 by Berzelius.<sup>73</sup> The initiation of a reaction by a catalyst is referred to as positive catalysis, that is when the reaction velocity is accelerated. When the reaction itself develops substances which themselves accelerate the reaction, the process is referred to as auto-catalysis. Negative catalysis (or retardation) may be readily understood as denoting the reverse of the positive catalysis process. Poisons are grouped under the negative catalysis. Catalytic poisons are substances which reduce the activity of solid catalysts.<sup>74</sup>

In summary, the functions which a catalyst may perform depend upon the nature and complexity of the reactions involved. These functions may be broadly divided into two:

- (a) To increase the rate of a given reaction or, as is usually the case, to lower the activation energy at which a reaction will occur at a desirable rate, and
- (b) To direct a reaction along a particular path when several pathways are possible.

Catalysts are being employed for catalytic reactions in the production of various chemicals by the manufacturing industries.<sup>75</sup> They are subdivided into two main types namely; homogeneous and heterogeneous catalysts. Heterogeneous catalysts are catalysts which exist in a different phase as compared to the reactants, while the homogeneous catalysts are in the same phase with the reactants. Industrial applications of homogeneous catalysts are limited due to difficulties associated with the separation of the catalysts from reaction solution. However, heterogeneous catalyst can be easily recovered from reaction solution which thus promotes catalyst reusability and recyclability thereby reducing production costs.<sup>76</sup> A table comparing these two types of catalysts has been included (**Table 1.2**).

**Table 1.2** Comparison of homogeneous and heterogeneous catalysts.<sup>75,77</sup>

Heterogeneous Catalysts	Homogeneous Catalysts
Simple separation and recyclability	Often difficult to separate
Diverse process applicability	Limited process applicability (batch only)
Diffusion controlled	Diffusion limitations practically absent
Thermally stable	Lower thermal stability
Well defined structure	Structure can be difficult to identify

### 1.3.1 Some metals employed for catalysed oxidation reactions

The oxidation of organosulfur compounds with organic hydroperoxides occurs in the presence of metal catalyst(s) mostly transition metals in high oxidation states. Such metals include: Mo(IV), Ti(IV), V(V), W(V) and others. Molybdenum oxide was among the first catalyst utilised in the catalysed oxidation of hydro-treated fuels.<sup>78-83</sup> The catalyst is usually employed as a heterogeneous catalyst, by incorporating molybdenum (Mo) onto alumina (Mo/Al<sub>2</sub>O<sub>3</sub>). Molybdenum however tends to be leached into the reaction medium, thereby resulting to loss in the activity of the heterogeneous catalyst since the main part of the catalytic activity is due to the solubilized/leached molybdenum, and catalyst recovery becomes difficult.<sup>40</sup> Alternative heterogeneous catalysts which are more stable during use have been investigated; some examples of such catalysts include cobalt/manganese (Co/Mn),<sup>80</sup> titanium (Ti),<sup>85,86</sup> gold (Au)<sup>87</sup> and rhenium (Re).<sup>88</sup>

Titanium catalysts gave the best results in catalysed oxidation step during oxidative-desulfurization.<sup>47</sup> However, titanium (Ti) is known to be expensive and the use of titanium in catalysed reactions industrially, generally, would result to an increase in cost of production. Hence, the search for a cheaper and more robust catalyst that can be applied industrially led to the use of vanadium which is relatively cheap and readily available.

### 1.3.1.1 Vanadium-catalyzed oxidation reactions

Vanadium is one of the most abundant and widely distributed metals in the earth's crust.<sup>89-93</sup> The major sources of vanadium are titaniferrous magnetite ores from mines in South Africa, Australia, China and Russia.<sup>92,93</sup> Some industrial processes now employ vanadium metal ion over other metal ions as catalysts for the manufacture of some important chemicals.<sup>92,93</sup> A survey comparing the use of vanadium for catalysis over other metals is presented in **Figure 1.9**, and reviews of some industrial catalytic oxidative processes based on vanadium oxides are shown in **Table 1.2**.<sup>95</sup>

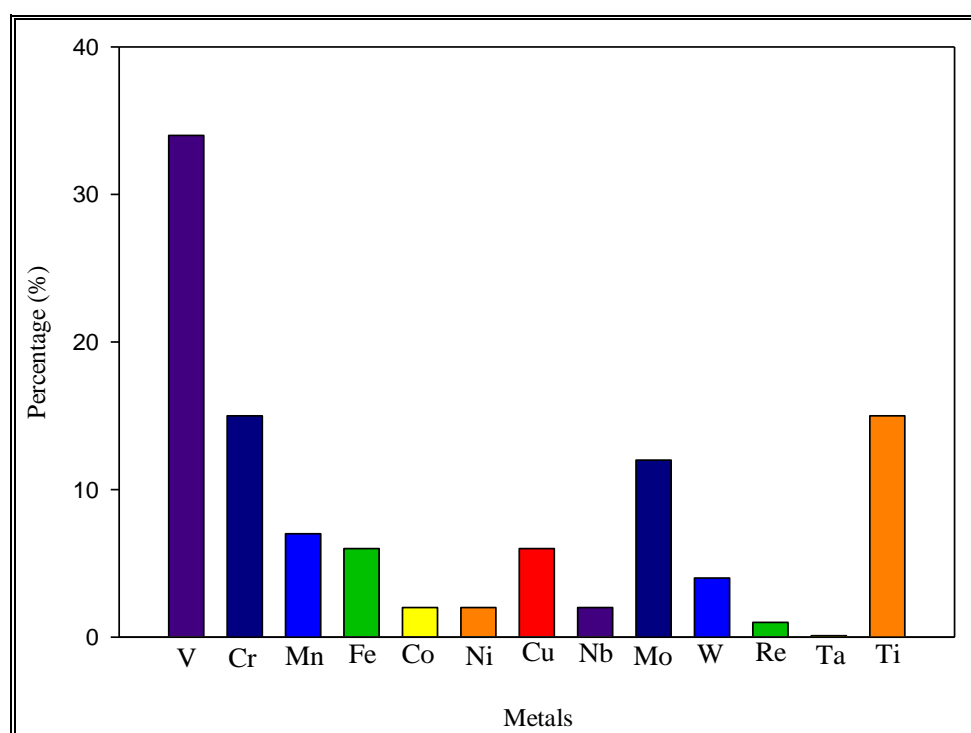


**Figure 1.9** Overview of the importance of vanadium in supported metal oxide catalysis. The numbers are based on an extensive open literature search in the period 1967-2010.

Many of these processes utilize the heterogeneous forms of vanadium catalysts, where vanadium oxides are deposited on the surface of an oxide support such as  $\text{SiO}_2$ ,  $\text{Al}_2\text{O}_3$ ,  $\text{TiO}_2$  and  $\text{ZrO}_2$ . Other than the oxide supports, vanadium oxides and complexes are also deposited on the surfaces of polymers, zeolites and carbon and employed as catalyst in the oxidation of several substrates (**Table 1.3**). The chemistry and spectral information of vanadium are important factors to be considered when designing oxidovanadium(IV) complexes, and these are briefly discussed below.

**Table 1.3** Overview of the reactions catalysed by supported vanadium oxides and complexes as described in the open literature.<sup>95</sup>

Catalytic reaction	References
Selective oxidation of alkanes and alkenes	96-97
Selective catalytic reduction of NO <sub>x</sub> with NH <sub>3</sub>	98-100
Oxidation of o-xylene to phthalic anhydride	101-102
Ammoxidation of aromatics and methylaromatics	103-105
Selective oxidation of methanol to formaldehyde	106
Oxidation of SO <sub>2</sub>	107-109
Oxidation of aliphatic and aromatic hydrocarbons	110-111
Oxidation of H <sub>2</sub> S	112-113
Oxidative dehydrogenation of alkanes	114-116
Decomposition of isopropylalcohol	117
Total oxidation of benzene	118
Selective oxidation of 4-methylanisole	119
Photo-oxidation of CO	120
Oxidative coupling of methane	121
Partial oxidation of methane to formaldehyde	122-124
Polymerization of olefins	125
Direct conversion of methane to aromatics	116-117
Oxidation of organosulfur compounds	126-133

### (a) Vanadium chemistry

Vanadium has an electron configuration of [Ar]4s<sup>2</sup>3d<sup>3</sup>. Vanadium can be found in a variety of oxidation states which comprises +2 (lilac), +3 (green), +4 (blue) and +5 (yellow) as presented in **Figure 1.10**. V<sup>5+</sup> (d<sup>0</sup>) can be present in tetrahedral (VO<sub>4</sub>), pentahedral (VO<sub>5</sub>) and octahedral (VO<sub>6</sub>) coordination environment and tends to form polyoxoanions. V<sup>4+</sup> (d<sup>1</sup>) is also stable and mostly present in square pyramidal or pseudo-octahedral coordination. Five-membered coordination is also observed

with  $V^{3+}$  ( $d^2$ ). Vanadium in the oxidation states of +3, +4 and +5 are relatively stable, while the +2 is less stable and only present under reducing conditions.<sup>77</sup>

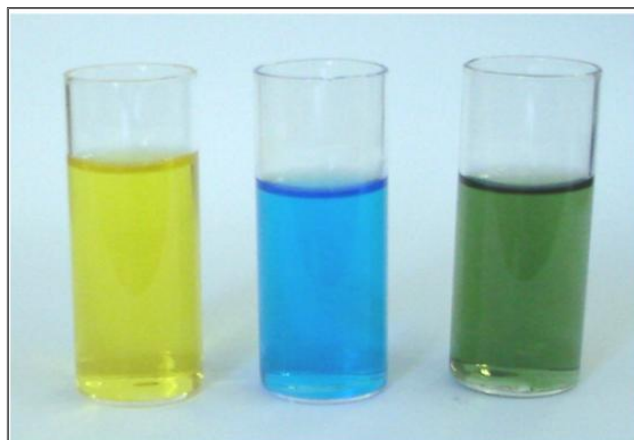


**Figure 1.10** The colour of vanadium in biologically relevant oxidation states. From left to right,  $V^{5+}$ ,  $V^{4+}$ , and  $V^{3+}$ .<sup>77</sup>

Vanadium(IV) and (V) forms complexes with ligands containing oxygen, nitrogen and sulfur donor functionalities, thereby exhibiting several stereochemical arrangements (**Figure 1.11**).<sup>77</sup> Vanadium(V) and (IV) complexes are been found as tetrahedral, octahedral, trigonal bipyramidal, pentagonal bipyramidal and square pyramidal geometries, while vanadium(III) exhibits fewer geometries due to its rigidity.<sup>77</sup> V(III) is found mainly in square pyramidal, or distorted octahedral (if a sixth position is occupied).

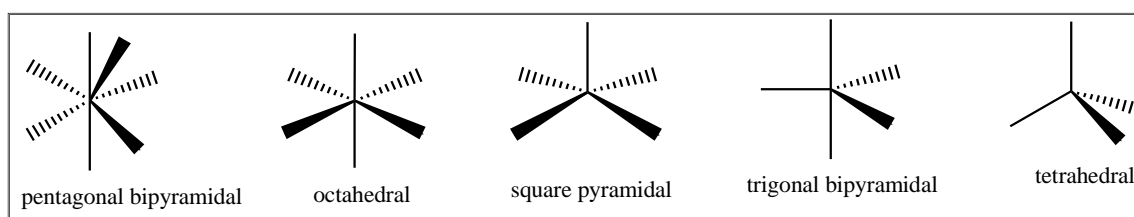


**Figure 1.11** Some typical geometries of vanadium(IV).

### (b) Structure and spectra of oxidovanadium(IV) complexes

Ballhausen and Gray,<sup>134</sup> considered  $VO^{2+}$  in an aqueous solution as the  $VO(H_2O)_5^{2+}$  ion to elucidate the molecular orbital description of the vanadyl ion. They proposed that the vanadium 3d, 4s, and 4p orbitals, along with the 2s,  $2p_\sigma$  ( $2p_z$ ) and  $2p_\pi$  ( $2p_x$ ,  $2p_y$ ) oxide oxygen orbitals, and the  $sp^3_\sigma$  hybrid

oxygen (from water) orbitals were involved in bonding. The bonding strengths were arranged in the order (V–O) > (four square planar waters) > (axial water). Taking this in consideration, one can predict the following (symmetry in parenthesis):

1. A strong  $\sigma$  bond between the  $sp^3_\sigma$  hybrid orbital of oxygen and the  $(4s + 3d_z^2)$  vanadium hybrid orbitals ( $a_1$ )
2. Two  $\pi$ -bonds between the oxygen  $2p_x$  and  $2p_y$  orbitals and the vanadium  $3d_{xz}$  and  $3d_{yz}$  ( $e$ )
3. Four  $\sigma$  bonds between the  $sp^3_\sigma$  hybrid orbitals of the equatorial water oxygens and the vanadium  $(4s-3d_z^2)$  ( $a_1$ ),  $4p_x$  and  $4p_y$  ( $e$ ), and  $3d_{x^2-y^2}$  ( $b_1$ ) orbitals
4. The  $sp^3_\sigma$  hybrid orbital of the axial water oxygen is bonded to the remaining  $4p_z$  ( $a_1$ ) orbital of vanadium
5. The vanadium  $3d_{xy}$  ( $b_2$ ) is non-bonding

From this information, the energy level scheme was predicted and is shown in **Figure 1.12**. This model allowed for the prediction and interpretation of magnetic, electron spin resonance (ESR) and optical properties.

The Ortolano, Selbin and McGlynn (OSM) scheme predicts three possible transitions from the ground state,  $b_2$  ( $d_{xy}$ ). These include;  $d_{xy} \rightarrow (d_{xz}, d_{yz})$ ;  $d_{xz} \rightarrow (d_{x^2-y^2})$  and  $d_{xz} \rightarrow (d_z^2)$ . The first two transitions may invert depending on the  $\sigma$ -donor strength of the ligands. The third transition may overlap or be completely masked by charge transfer bands. Insertion of a fifth or sixth (polar) ligand would not be expected to lead to any noticeable effects (**Figure 1.13**).<sup>134,77</sup>

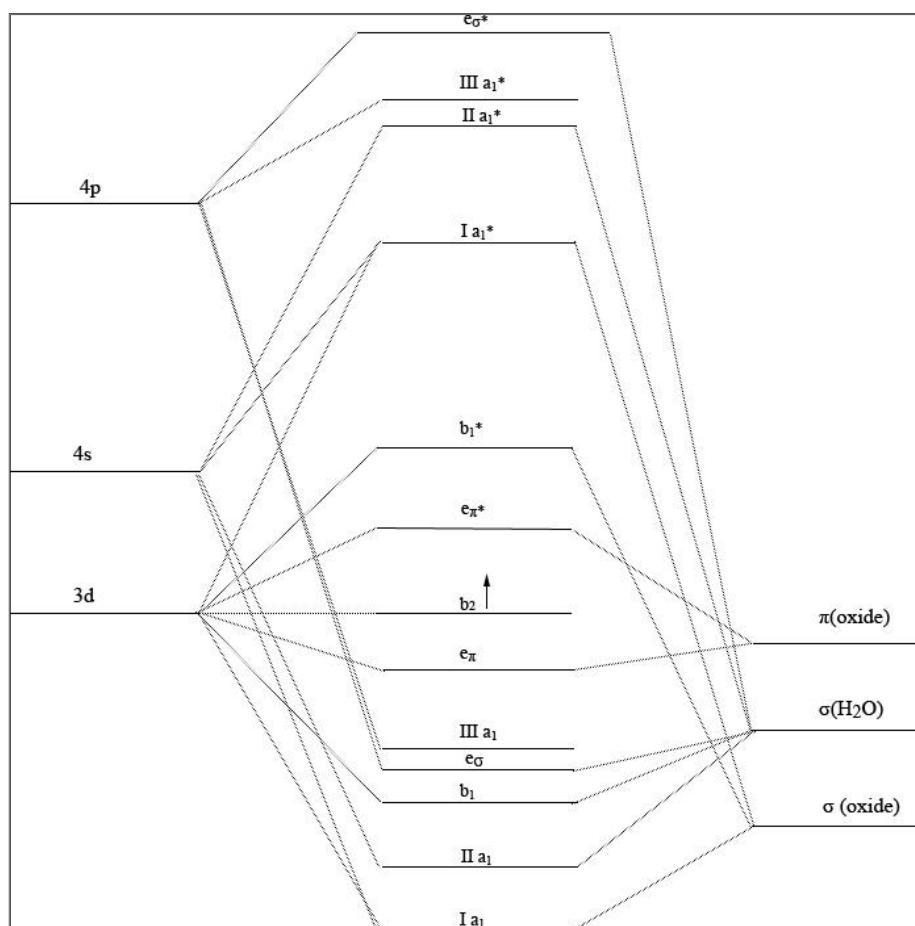


**Figure 1.12** Molecular orbital scheme for the  $\text{VO}^{2+}$  species as outlined by Ballhausen.<sup>134</sup>

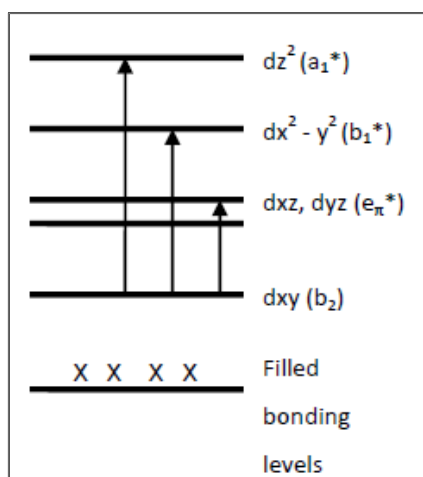
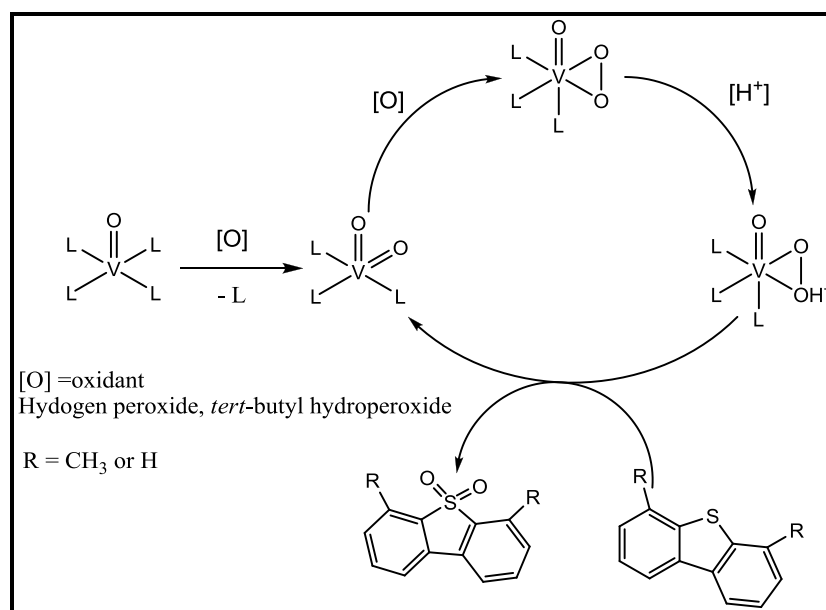


**Figure 1.13** Clustered energy level scheme of OSM for vanadyl(IV) complexes.<sup>134,77</sup>

### 1.3.1.2 Catalytic mechanism of oxidovanadium(IV)-catalysed oxidation reactions

Spectroscopic techniques such as  $^{51}\text{V}$  NMR,<sup>135</sup> UV/Vis and EPR<sup>70</sup> have been employed to investigate the catalytic mechanism of oxidation of oxidovanadium(IV) and to also explore the possibility of

interaction of a substrate with neat vanadium complexes. These studies indicated that intermediate species were formed during the catalytic cycle. Oxidovanadium(IV) was initially oxidized to dioxidovanadium(V) followed by addition of the peroxide to form the oxidoperoxido species (**Scheme 1.5**). Furthermore, in an acidic medium, the peroxy may protonate to form the hydroxylperoxidovanadium(V) species.<sup>136</sup> It is proposed that these reactive oxoperoxido-vanadium species react with the substrate to give the oxidation product.<sup>137</sup>



**Scheme 1.5** Simplified catalytic mechanism for the oxidation of organosulfur compounds. Here L may refer to donor atom or a solvent molecule.<sup>77</sup>

### 1.3.2 Polymer-supported catalysts

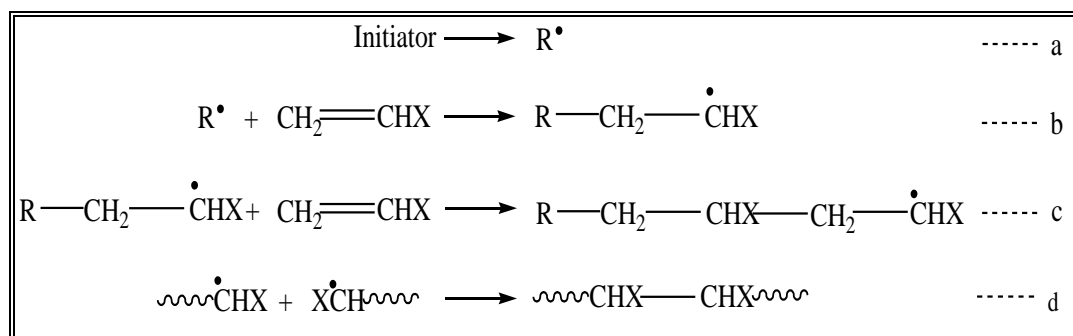
Support material for metal ion catalysts enhances their performance significantly. It helps to influence catalyst activity, stability, selectivity, and recyclability.<sup>138</sup> The principal catalyst-preparation technique involves two stages. First, rendering a metal-salt component into a more evenly distributed catalyst sites on a support and secondly; conversion of the supported metal salt to a metallic or oxide state. The first stage is known as dispersion and is achieved by impregnation, adsorption from solution, co-precipitation, or deposition, while the second stage is called calcination or reduction.<sup>139</sup> A desirable catalyst support should be chemically, mechanically and thermally stable, and also possess a large surface area which thus enhances the dispersion of incorporated catalytically active component such



as metal salts.<sup>76</sup> Zeolites and silica-based resins have been employed more often as a very popular choice of catalyst support due to their stability and high porosity.<sup>140-146</sup> Polymers as catalyst supports show similar properties, and extensive studies have been reported on the use of polymers as catalyst support.<sup>128,147-149</sup> This thesis focused on the synthesis and use of polymers as support materials.

### 1.3.2.1 The basics of polymerization

Polymerization is the process in which monomer units are linked by chemical reaction to form long chains known as polymer. Generally, monomers are unsaturated compounds, commonly containing allyl or vinyl groups. Monomer purity is of the highest important factor to be considered when looking at the requirements for chain-growth processes. For polymerization to take place there must be an initiator. Polymerization process is classified as anionic, cationic, or free radical due to the way in which polymerization is initiated and thus the nature of the propagating chain. Free radical polymerization is known to be the most popular way of producing polymer materials. It involves the continuous addition of monomer units to a growing free radical chain.<sup>150</sup> The general mechanism of this process in relation to the polymerization of a vinyl monomer is shown in **Scheme 1.6**.



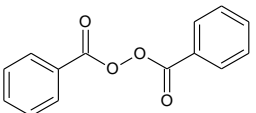
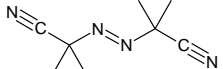
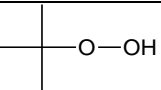
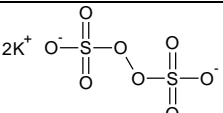
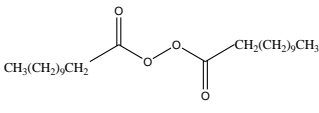
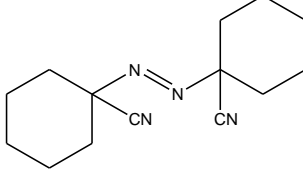
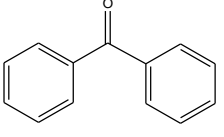
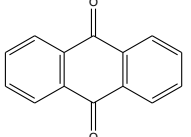
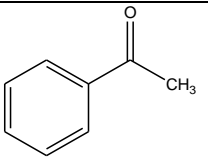
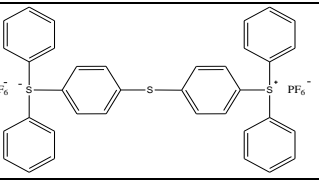
**Scheme 1.6** Radical initiation (a), propagation (b-c) and termination (d).

The above mechanism showed that initiation is a two-stage process (a and b), at first a free radical is formed, and second this radical adds on to a monomer unit. The propagation step (c) is the core of the process, but as in all chain growth processes it is the number of monomer units that are added for each initiator molecule that determines the molecular weight of the final material. In the case of free-radical polymerization this is controlled by considering the processes involved in terminating the growing chain. Often these involve radical-radical combinations and high molecular weights are favoured by keeping the concentration of free radicals low. The final step (d) is known as the

termination step, this is the step where polymer growth terminates due to the exhaustion of free radicals. As stated earlier, for polymerization to take place, an initiator in the presence or absence of heat is required. These initiators provide the initial radical which then reacts with the allylic or vinylic monomer. Radical initiators may be divided into thermal free radical initiator and photo-initiator as shown in **Table 1.4**. A co-copolymer can also be produced by introducing a second monomer into a free-radical polymerization; the polymerization mechanism is similar to the mechanism under **Scheme 1.6**. Introducing a co-monomer helps in modifying the properties of the resultant polymer.<sup>151-</sup>

<sup>153</sup> For suitable polymerization to take place, a choice of solvent (porogen) is important as it influences the nature of the end polymer.<sup>154-156</sup>

**Table 1.4** Some common thermal free radical initiators and photo-initiators for polymerization of vinyl monomers.

Name	Structure	Name	Structure
Thermal free radical initiators			
<b>Benzoyl-peroxide</b>		<b>2,2-Azobisisobutyronitrile</b>	
<b>Tert-butylhydroperoxide</b>		<b>Potassium persulfate</b>	
<b>Dodecanoyl peroxide</b>		<b>1,1-Azobis(cyclohexane-carbonitrile)</b>	
Photo-initiator			
<b>Benzophenone</b>		<b>Anthraquinone</b>	
<b>Acetophenone</b>		<b>Triarylsulfonium hexafluorophosphate salts</b>	

### 1.3.2.2 Polymer microspheres as catalyst support material

The development of polymer particles (microspheres) that can be utilized as catalyst support for industrial applications has necessitated the tailoring of suspension and emulsion polymerization processes to suit particular needs.<sup>157-159</sup> These polymer particles can be classified as macro- (>50 nm), meso- (50-2 nm) and micro-porous (< 2 nm) depending on the size of the pores they possess. For a polymer support to be effective, it must possess a large surface area, high porosity and must have the ability to take up various solvents with different polarity without been dissolved or reacting. Crosslinking of polymer microspheres enhances their mechanical stability and also prevents them from dissolving in solvents of similar polarity, thereby preserving the porous nature of the support. For these reasons, polymer microspheres were employed as catalyst support for the experiments reported in this thesis.

### 1.3.2.3 Techniques for producing polymer microspheres

Polymer particles (microspheres) are produced by heterogeneous polymerizations, i.e. using two or more immiscible liquids in the presence of an initiator and heat. The main techniques used in making polymer particles (microspheres) are suspension, dispersion, precipitation, multistage, membrane/microchannel emulsification and microfluidic polymerizations.<sup>160-165</sup> For this section we shall discuss the common techniques which are suspension, precipitation and emulsion polymerizations. Emulsion polymerization typically gives uniform sized particles with diameters of less than 1  $\mu\text{m}$  while dispersion and suspension polymerization produce larger microspheres but with a broad particle size distribution.<sup>166</sup> Synthesizing an insoluble polymer requires the addition of a crosslinking agent. Crosslinkers typically contains two or more sites for polymerization thereby linking different polymer chains to make a highly branched network. The most commonly used crosslinkers are divinylbenzene, *N,N*-methylenebisacrylamide and ethylene glycol dimethacrylate.

#### (a) Emulsion polymerization

In 1912, chemists realized that polymer particles can be produced from an emulsion.<sup>167</sup> In emulsion polymerization; a hydrophobic monomer is dispersed in an aqueous phase by use of a surfactant, often known as an emulsifier. Emulsion can also be simply explained as liquid/liquid dispersion. Emulsion

polymerization involves a multistage heterogeneous polymerization process; firstly, non-porous polymer particles are produced, which are relatively small and mono-disperse in the reaction vessel. These particles are subsequently enlarged in a second stage so as to be easily recovered. These particles can be regular non-spherical or spherical in shape depending on the need. It has been reported that emulsion polymerization is not readily used to form porous particles.<sup>168</sup>

#### **(b) Dispersion and precipitation polymerization**

Dispersion and precipitation polymerizations start as completely homogeneous (liquid) solutions. A phase separation that takes place at the early stage of the polymerization reaction makes it to be regarded as part of the class of heterogeneous polymerizations. Dispersion and precipitation polymerizations are similar in mechanism except for two main differences: (1) a stabilizer is used in dispersion polymerization but not in precipitation polymerization and (2) a crosslinker is necessary and used in large proportions in precipitation polymerization, while the use of crosslinkers in dispersion polymerization is always avoided. Precipitation polymerization is more suitable for highly crosslinked and porous particles, in many cases divinylbenzene (DVB) is polymerized alone.<sup>169-171</sup> Dispersion polymerization is generally used to obtain non-crosslinked and non-porous polymer particles.<sup>172-176</sup> A schematic description of precipitation polymerization is presented in **Figure 1.14**, where oligomers and nuclei are formed due to radical polymerization. These oligomers grow to form the desired polymer in the presence of a monomer.

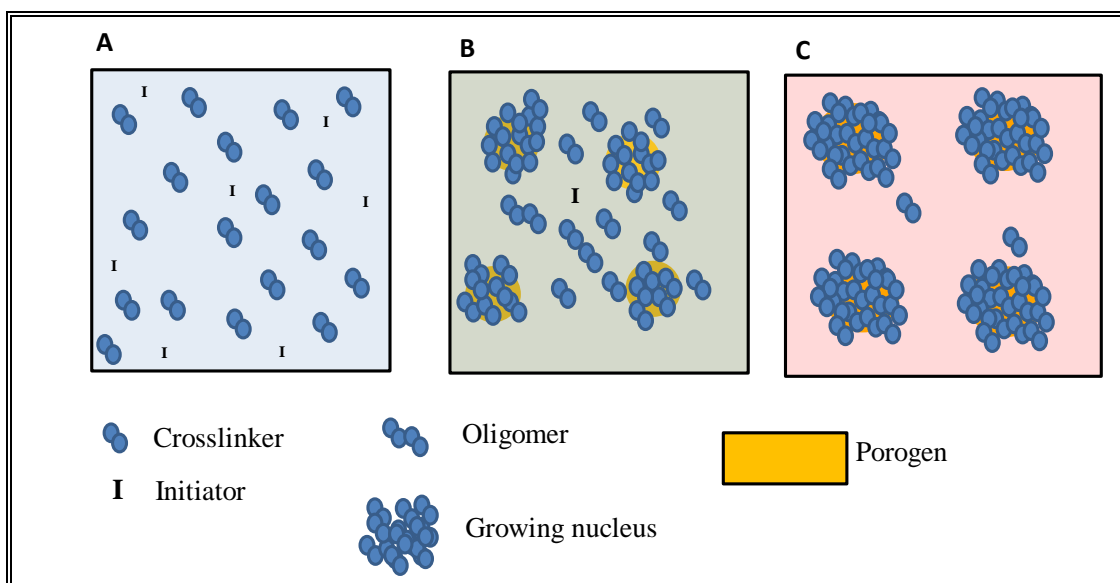


**Figure 1.14** Schematic descriptions of the stages of precipitation polymerization for porous particle production. (A) Initially, only crosslinker and initiator molecules are in the medium. (B) Oligomers and nuclei begin to form because of radical polymerization. (C) As the reaction continues, nuclei grow by adding monomers and oligomers from the medium.

### (c) Suspension polymerization

Suspension polymerization is quite different from emulsion, precipitation and dispersion polymerization in that it starts with the dispersion monomer droplets into a continuous phase with the aid of surfactants and also the initiator which is not soluble in the aqueous phase. For a typical suspension polymerization, a mixture of monomer, soluble initiator (organic soluble) and porogen is added to the continuous aqueous phase to form oil droplets in which both initiation and chain growth occur inside the monomer droplets. As shown in **Figure 1.15**, there is a separate phase with monomeric species (monomers and crosslinkers), initiator and porogen on one hand and there is the aqueous continuous phase with stabilizers on the other hand. Monomer droplets in the aqueous continuous phase begin to form on stirring. Continuous mechanical agitation with a constant speed keeps the monomer droplets well dispersed. Two parameters are of utmost importance in suspension polymerization: (1) monomer solubility in the continuous aqueous phase and (2) the role of

surfactants and stabilizers.<sup>177, 178</sup> The bead size depends on several factors including; stirring speed, ratio of water to monomer, concentration and type of stabilizer and solution viscosities.<sup>77</sup>

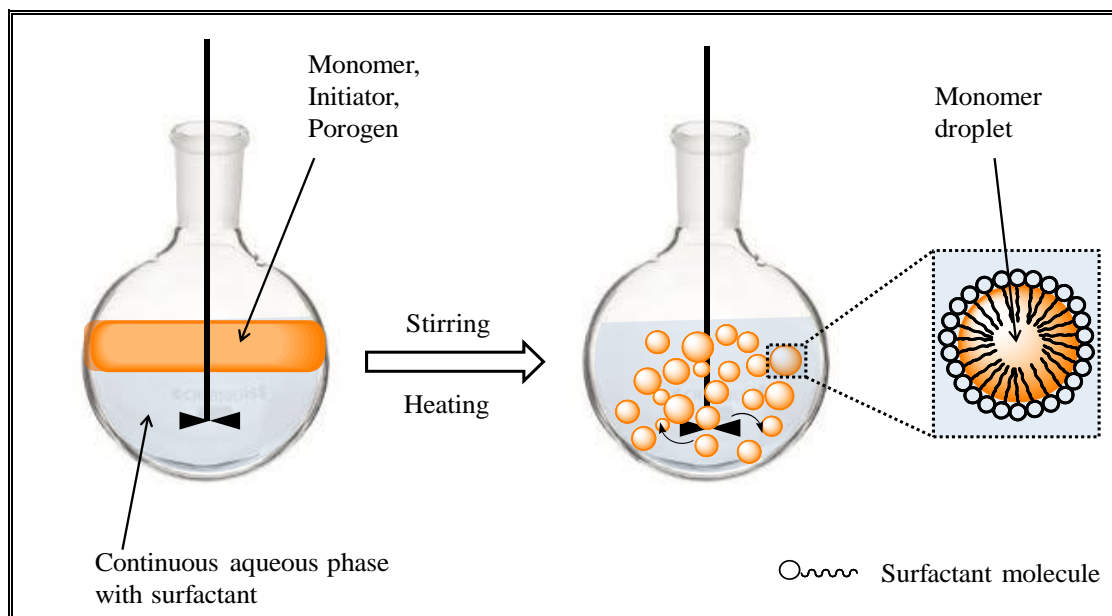


**Figure 1.15** A schematic of a typical suspension polymerization procedure.

#### 1.3.2.4 Polymer nanofibers as catalyst support materials

Polymer fibers may be produced by a variety of methods including; drawing,<sup>179</sup> template synthesis,<sup>180, 181</sup> deposition on a substrate,<sup>182, 183</sup> thermally induced phase separation and spinning. Of all the fiber fabrication routes, electrospinning allows for fabrication of fine polymer fibers with diameters varying from 30 nm to greater than 5  $\mu\text{m}$  thereby increasing their surface areas.<sup>184, 185</sup> Potential applications of electrospun fibers include filtration membranes, adsorption sorbents, fiber-based sensors, tissue engineering scaffolds and catalytic nanofibers.<sup>185–187</sup>

Electrospinning apparatus was first developed over a century ago by Cooley.<sup>188</sup> A modern electrospinning set-up consist of a syringe pump, a high voltage and a collector (**Figure 1.16**), and it is relatively simple and inexpensive to set up. During the electrospinning process, a polymer solution in a syringe is pumped to a needle tip attached to the syringe *via* tubing; the solution is held at the needle tip by surface tension. The application of an electric field using the high-voltage source causes a positive charge to be induced within the polymer, resulting in charge repulsion within the solution. This results in an electrostatic force, which opposes and eventually overcomes the surface tension of the polymer solution, causes the initiation of polymer jets. As the jets travels down to the collector

that is negatively charged collector, the polymer solvent evaporates leaving the polymer fibers on the collector.

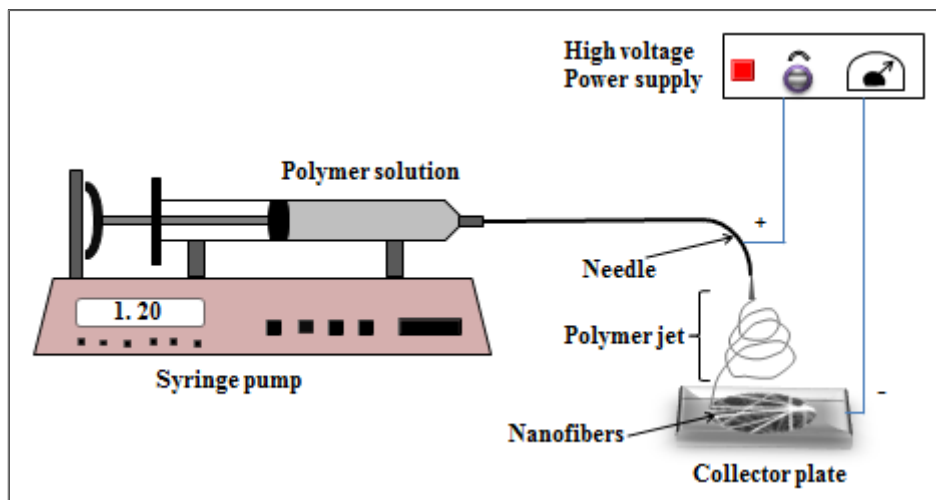


**Figure 1.16** The electrospinning equipment used for the fabrication of polymer fibers.

A stable electrospinning jet is known to be comprised of four regions,<sup>189</sup> these are: the base, the jet, the splay, and the collection. In the base region, the jet emerges from the needle to form a cone known as the Taylor cone. The shape of the base depends upon the surface tension of the liquid and the force of the electric field. Jets can be ejected from surfaces that are essentially flat if the electric field is strong enough, and the solution spreads out evenly and it is collected on a grounded surface. Several parameters are known to influence the formation of stable fibers in electrospinning. Doshi and Reneker,<sup>190</sup> classified these parameters as (i) solution properties (viscosity, conductivity, surface tension, polymer molecular weight, dipole moment, and dielectric constant), (ii) controlled variables (distance between the needle tip and collector, voltage and flow-rate) and (iii) ambient parameters (temperature, humidity and others).<sup>191,192</sup> An adapted summary of the above mentioned parameters on fiber morphology reviewed by Quynh *et al.*<sup>193</sup> is presented in **Table 1.5**.

**Table 1.5** Effect of changing electrospinning conditions/parameters on fiber morphology.<sup>193</sup>

Process parameter	Effect on fiber morphology	References
Viscosity/concentration	<ul style="list-style-type: none"> <li>• Low concentrations/viscosities yielded defects in the form of microspheres and junctions; increasing concentration/viscosity reduced the defects.</li> <li>• Fiber diameters increased with increasing concentration/viscosity.</li> </ul>	194-206
Conductivity/solution charge density	<ul style="list-style-type: none"> <li>• Increasing the conductivity aided in the production of uniform bead-free fibers.</li> <li>• Higher conductivities yielded smaller fibers in general (exceptions were PAA and polyamide-6).</li> </ul>	195, 196, 199, 207-211
Surface tension	<ul style="list-style-type: none"> <li>• No conclusive link established between surface tension and fiber morphology.</li> </ul>	198, 199, 204, 212
Polymer molecular weight	<ul style="list-style-type: none"> <li>• Increasing molecular weight reduced the number of microspheres and droplets.</li> </ul>	205, 206, 213, 214
Dipole moment and dielectric constant	<ul style="list-style-type: none"> <li>• Successful spinning occurred in solvents with a high dielectric constant.</li> </ul>	211, 215, 216
Flow-rate	<ul style="list-style-type: none"> <li>• Lower flow-rates yielded fibers with smaller diameters.</li> <li>• High flow-rates produced fibers that were not dry upon reaching the collector.</li> </ul>	200, 212, 216-218
Field strength/voltage	<ul style="list-style-type: none"> <li>• At too high voltage, beading or stretching of fibers may occur.</li> <li>• Correlation between voltage and fiber diameter was ambiguous.</li> </ul>	201, 204, 206, 207, 215, 219
Distance between tip and collector	<ul style="list-style-type: none"> <li>• A minimum distance was required to obtain dried fibers.</li> <li>• At distances either too close or too far, beading was observed.</li> </ul>	194, 200, 201, 208, 218
Collector composition and geometry	<ul style="list-style-type: none"> <li>• Smoother fibers resulted from metal collectors.</li> <li>• More porous fiber structure was obtained using porous collectors.</li> <li>• Aligned fibers were obtained using a conductive frame, rotating drum, or a wheel-like bobbin collector.</li> <li>• Yarns and braided fibers were also obtained.</li> </ul>	186, 198, 203, 220-224
Ambient parameters	<ul style="list-style-type: none"> <li>• Increased temperature caused a decrease in solution viscosity, resulting in smaller fibers.</li> <li>• Increasing humidity resulted in the appearance of circular pores on the fibers.</li> </ul>	189, 205, 225



Both the polymer microspheres and fibers have been employed as catalyst support for metal ions used during catalysed reactions.<sup>135,187</sup> While these fibrous catalyst supports showed great promise in terms of higher oxidation yield as a result of its higher surface area, certain aspects including solubility and mechanical strength of the fibers require attention.<sup>187</sup> The fibers are known not to be able to withstand higher temperatures, thus limiting its use in the industries for catalysis. Another concern with the fibers is catalyst leaching.<sup>220</sup> Higher concentration of metal ions are leached from polymer fibers. As mentioned above, fibers are also sensitive to solvents, and tend to dissolve or change morphology in most organic solvents and acids, and these result in lowering the activity of the catalysts within the polymer-fiber support. The polymer microspheres on the other hand are stable and do not easily dissolve in solvents due to the higher level of crosslinking. Depending on the level of metal ion coordination to the polymer support, leaching of metal ions has been reported to be generally low on the polymer microspheres as compared to the fibers.<sup>128,129</sup>

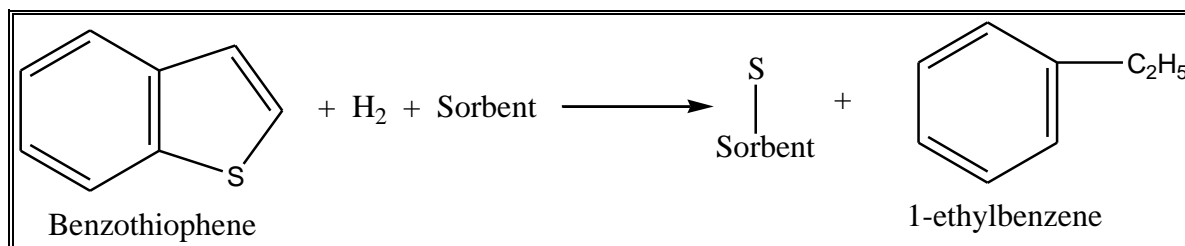
From the above observations, fibers are not the best support for use when working with a complex matrix such as fuels due to its mechanical stability and solubility concerns. For this thesis the focus will be on the potential use of the fibers as adsorption sorbents, i.e. to remove the oxidation products from the oil matrix.

#### **1.4 Adsorptive removal of sulfur/sulfone compounds in fuels**

Sulfur in the form of organosulfur compounds present in fuels can be eliminated through desulfurization as discussed earlier in **Section 1.2**. Hydro-desulfurization (HDS) process produces hydrogen sulfide as one of its main products which is scrubbed off with steam and converted to elemental sulfur via the Claus process.

On the other hand, oxidative-desulfurization (ODS) technique produces sulfone compounds as the main products in the treatment of fuels. As mentioned earlier (**Section 1.2.3**), liquid extractant of sulfones from fuel show limitations, thus leading to the motivation for the development of solid adsorbent materials. In 2001, Phillips petroleum licenced a process called “S-Zorb” for the selective removal of sulfur. The adsorbent is based on zinc oxide, silica, alumina and nickel.<sup>66</sup> The S-Zorb process is carried out in the presence of hydrogen and modified zinc oxide. Sulfur compounds are

carried over to hydrogen sulfide, and the sulfur is bound by zinc oxide as zinc sulfide by the process known as chemisorption (**Scheme 1.7**).



**Scheme 1.7** Basic principle of the S-Zorb sulfur removal technology process developed by Phillips petroleum for sulfur removal from liquid fuel at elevated temperatures under low H<sub>2</sub> pressure.

Velu *et al.*<sup>67</sup> also developed zeolites-based adsorbents for sulfur compounds. However both adsorbents (S-Zorb and zeolite-based adsorbent) have their limitations as they allow only the elimination of thiophenic compounds such as thiophenes, benzothiophenes and their alkyl derivatives present in fuels, and the absorption process is only applied in the hydro-desulfurization (HDS) process. Hence, the other refractory sulfur compounds such dibenzothiophenes and their alkyl derivatives remain un-removed in the fuel. Recently, Campos *et al.*<sup>71</sup> reported the use of metal organic framework (MOF) C300 for the adsorption of some organosulfur compounds in diesel fuel, and this showed great potential, however the adsorbents (MOFs) are expensive, hence discouraging its application for fuel treatment on an industrial scale. A combination of the HDS and ODS process is however proposed as a possible way for the reduction of sulfur in fuels to ultra-low level as shown in the integrated HDS-ODS process (**Figure 1.17**).

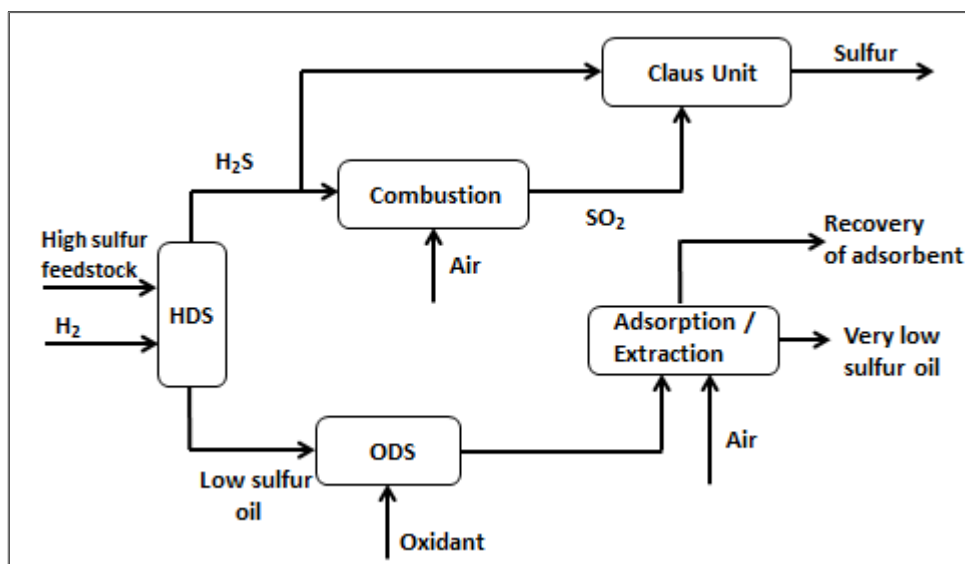


**Figure 1.17** Integrated hydro desulfurization-oxidative desulfurization (HDS-ODS) processes.

Liquid extraction of sulfone compounds formed during the ODS process also presents its own limitations as other aromatic compounds that influence the properties of fuels are extracted in the process.<sup>65</sup> This development has prompted the fabrication, design and synthesis of stimuli-response materials that allow for bonding interactions with sulfone compounds in the presence of other aromatic compounds in the oxidative desulfurization process which can eliminate refractory organosulfur compounds present in fuels.<sup>68-72</sup> The development of a stimuli-response material which recognises compounds can be fabricated through the use of a technique known as molecular imprinting.

For this thesis, the focus will be designing a new class of molecularly imprinted polymer materials which will allow for selective adsorption of oxidized refractory sulfur compounds in fuels. An overview on molecular imprinting and the techniques of imprinting on a polymer are discussed in **Sections 1.4.1 and 1.4.2.**

### 1.4.1 Molecular imprinting

Molecular imprinting is a technique employed for the introduction of recognition sites into matrices, *via* the formation of an assembly between the imprinting template (atom, ion, molecule, complex and micro-organisms) and functionalized group within the network (adsorbent). After which removal of some or the entire template from the adsorbent creates molecular recognition sites on the

spaces vacated within the adsorbent as shown in **Figure 1.18**. Molecular imprinting dates back to the 1930s, where Polyakov employed the concept of imprinting on silica matrices.<sup>226-228</sup> The use of other matrices especially polymer for imprinting is extensive in the literature.<sup>229-282</sup> A molecularly imprinted polymer (MIP) is prepared by mixing a template molecule with functional monomers, cross-linking monomers and a radical initiator in a proper solvent (porogen), and polymerization is initiated by subjecting the mixture to heat or irradiated by UV light. In synthesizing a molecularly imprinted polymer, the radical initiator,<sup>283, 284</sup> porogen effect,<sup>284-287</sup> and polymer stability,<sup>288-292</sup> has to be seriously considered.

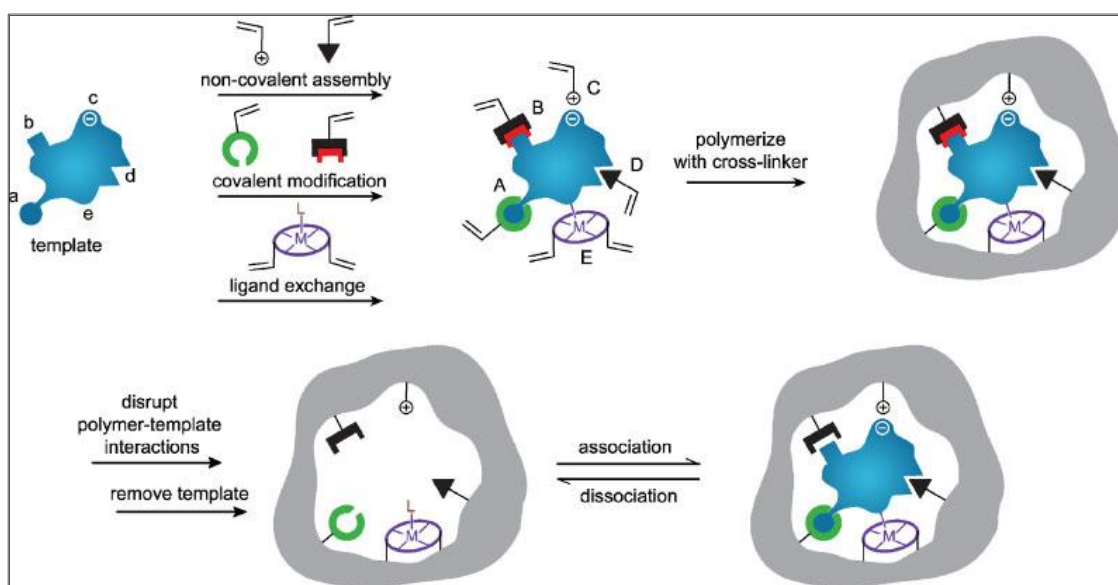


**Figure 1.18** Highly schematic representation of the molecular imprinting process: The formation of reversible interactions between the template and polymerizable functionality may involve one or more of the following interactions: [(A) reversible covalent bond(s), (B) covalently attached polymerizable binding groups that are activated for non-covalent interaction by template cleavage, (C) electrostatic interactions, (D) hydrophobic or van der Waals interactions or (E) co-ordination with a metal centre; each formed with complementary functional groups or structural elements of the template, (a-e) respectively].<sup>293</sup>

## 1.4.2 Techniques of preparing molecularly imprinted polymers

There are three principal methodologies for assembling recognition site on polymers. These techniques are (a) covalent binding approach, (b) non-covalent approach and (c) semi-covalent approach.

### 1.4.2.1 The covalent approach

Covalent bonding between molecules includes of interactions such as  $\sigma$ -bonding,  $\pi$ -bonding or metal-metal bonding. In the covalent approach, templates (molecules) which can covalently bound to one or more groups in the polymer matrices are utilized.<sup>294-296</sup> After imprinting, the template is cleaved and the functionality left in the binding site is capable of binding target molecule by re-establishment of the covalent bond. Compounds such as alcohols (diols), aldehydes, ketones, amines, carboxylic acids<sup>297, 298</sup> and carboxylic ester linkage<sup>299-301</sup> can be imprinted with this approach. The advantage of this approach is that functional groups within the polymer matrix are only associated with the template site making site recognition possible.

### 1.4.2.2 Non-covalent approach

This method was first introduced in organic polymers by Mosbach research group.<sup>302</sup> Interactions such as hydrogen bonding, ion pairing and dipole-dipole interactions occur between the functional polymer and templates under a non-covalent approach. Non-covalent imprinting approach is important for two reasons: the methodology is far easier than covalent methods, and it produces higher affinity binding sites. Non-covalent imprinting interactions between functional monomer and template during polymerization is the same as those between polymer and template in the re-binding step, thus, making this method of imprinting most widely employed due to its simplicity.<sup>303-306</sup>

### 1.4.2.3 The semi-covalent approach

Semi-covalent imprinting produces a more uniform distribution in binding site affinities on the polymer groups by combining the technique of covalent and the non-covalent approach. In this approach, templates are covalently bound initially to a polymer group with known functionalities which is recovered after cleavage of the template.<sup>307</sup> Re-binding of the template on the polymer takes

place *via* non-covalent interactions without restrictions. In the semi-covalent imprinting approach, templates and the monomer are connected using a spacer group. Glyceric acid (template) was imprinted to a boronic acid and to 4-vinylaniline through an amide bond. The re-binding process indicated that the initial covalent bond between was transformed to an ion pair formation (a non-covalent bond).<sup>308, 309</sup>

## 1.5 Aims and objectives

The principle aim of this study was to prepare a polymer supported ligand and its oxidovanadium(IV) complex as catalyst for the oxidation of organosulfur compounds, and also to fabricate molecularly imprinted polymers (MIPs) for adsorption of the oxidized organosulfur compounds. Methods for the production of polymer supports for catalyst and molecularly imprinted polymers (MIPs) will be investigated and the performance of the catalytic materials and adsorbents will be evaluated on model compounds. The research objectives are as follows:

1. Synthesis of salen-functionalized Merrifield resins and the corresponding polymer-bound oxidovanadium(IV) catalysts and assess their catalytic activity.
2. Synthesis of salen-functionalized polymer microspheres *via* suspension polymerization and assess the catalytic activity of the oxidovanadium(IV) functionalized microspheres.
3. Fabrication of imprinted electrospun chitosan nanofibers and microspheres using oxidized organosulfur compounds as templates and assess their adsorption activity and selectivity.
4. Fabrication of imprinted electrospun polybenzimidazole nanofibers using oxidized organosulfur compounds as templates and assess their adsorption activity and selectivity.

Finally, the optimized oxidation and adsorption processes will be applied on real systems, i.e. on an HDS-processed fuel oil (hydrotreated oil) as well as heavy crude oil.

*This page is kept blank*



# Chapter 2

## Materials, experimental techniques and methods

### 2.1 General reagents

**Table 2.1** General reagents used in this study

Chemical name	Purity/concentration	Supplier
Acetone	Analytical grade	Merck Chemicals, South Africa
Acetonitrile	99.9% HPLC grade	Merck Chemicals, South Africa
Allyl bromide	97%	Sigma-Aldrich, South Africa
Ammonium hydroxide	28% NH <sub>3</sub> in H <sub>2</sub> O	Merck Chemicals, South Africa
Azobis(isobutyronitrile) (AIBN)	98%, refrigerated at 4°C	Sigma-Aldrich, South Africa
Benzothiophene	99%	Merck Chemicals, Germany
Chitosan	90% degree of deacetylation	Sigma Aldrich, South Africa
Dibenzothiophene	99%	Merck Chemicals, USA
Dichloromethane	Analytical grade	Merck Chemicals, South Africa
Ethyleneglycol dimethacrylate (EGDMA)	98% and contains 90-110 ppm monomethyl ether hydroquinone as inhibitor	Sigma-Aldrich, South Africa
Ethanol	Analytical grade	Merck Chemicals, South Africa
Glutaraldehyde	~50% in H <sub>2</sub> O (5.6 M)	Sigma-Aldrich, Germany
Hexane	≥ 97% HPLC grade	Merck Chemicals, South Africa
Methanol	Analytical grade	Merck Chemicals, South Africa
Merrifield microspheres	5% crosslinked	Sigma-Aldrich, South Africa
<i>N,N</i> -Dimethylacetamide (DMAc)	Analytical grade	Merck Chemicals, South Africa

<i>N,N</i> -Dimethylformamide (DMF)	Analytical grade	Merck Chemicals, South Africa
<i>o</i> -Phenylenediamine	99.5%	Sigma-Aldrich, South Africa
Polyvinyl alcohol	88% hydrolyzed, $M_w = 130,000$	Sigma-Aldrich, Germany
Polybenzimidazole (PBI)	Intrinsic viscosity of $0.8 \text{ dL g}^{-1}$	PBI performance products (Charlotte, NC), USA
Potassium carbonate	99.9%	BJH Chemicals, Germany
Salicylaldehyde	98%	Merck Chemicals, USA
Silver nitrate	98%	Merck, South Africa
Tetrabutylammonium bromide (TBAB)	98%	Sigma-Aldrich, USA
<i>Tert</i> -butylhydroperoxide ( <i>t</i> -BuOOH)	5.0-6.0 M solution in decane, < 4% water	Sigma-Aldrich, Germany
Thiophene	99%	Merck Chemicals, Germany
Trifluoroacetic acid (TFA)	Reagent plus® 99%	Sigma-Aldrich, Germany
Triton X-114 {(1,1,3,3-Tetramethylbutyl)phenyl-polyethylene glycol, Polyethylene glycol <i>tert</i> -octylphenyl ether}	Laboratory grade	Sigma Aldrich, Germany
Total sulfur standards in diesel	0.2-500 ppm S	Matheson Tri-Gas, Texas, USA
Toluene	99.9% HPLC grade	Merck Chemicals, South Africa
Ultrapure TraceSelect nitric acid	65%	Sigma-Aldrich, South Africa
Vanadium(IV) oxide sulfate trihydrate [ $V^{IV}OSO_4 \cdot 3H_2O$ ]	97%	Sigma-Aldrich, Germany
Vanadium for ICP calibration	1002 ppm ( $\pm 2 \text{ mg.L}^{-1}$ ) stock solution	Teknolab, South Africa
4,6-Dimethyldibenzothiophene	98%	Sigma-Aldrich, South Africa

## 2.2 Instrumentation and general experimental procedures

### 2.2.1 Melting point analysis

Melting points were determined using Gallenkamp melting point apparatus equipped with a thermometer (0-400 °C).

### 2.2.2 FT-IR

The infrared spectra were recorded on either a Perkin Elmer 2000 FT-IR spectrometer in the far-IR range ( $700\text{-}50\text{ cm}^{-1}$ ) as Nujol mull or as neat compounds using KBr or on a Perkin Elmer 100 ATR-IR ( $4000\text{-}650\text{ cm}^{-1}$ ).

### 2.2.3 UV-vis spectroscopy

The solution electronic spectra were recorded on a Perkin Elmer Lambda 25 UV-Vis spectrophotometer using 1 cm quartz cells. The solid reflectance spectra of the metal complexes were recorded on a Shimadzu UV-VIS-NIR Spectrophotometer UV-3100 with an MPCF-3100 sample compartment with samples mounted between two quartz discs which fit into a sample holder coated with barium sulfate. The spectra were recorded over the wavelength range of 1200-250 nm, and the scans were conducted at medium speed using a 20 nm slit width.

### 2.2.4 NMR (nuclear magnetic resonance) spectroscopy

The structures of all ligands were determined by  $^1\text{H}$  NMR spectroscopy on a Bruker AMX 400 NMR MHz spectrometer and reported relative to tetramethylsilane (TMS)  $\delta$  0.00.

### 2.2.5 Elemental analysis

Elemental analysis was carried out with a Vario Elementary ELIII Microcube CHNS elemental analyser.<sup>310</sup> Calibration of the instrument was done with the use of the following standards in a linear curve adjustment within the total working range.

Standard 1: Sulfanilamide - C; 41.81, H; 4.65, N; 16.25, S; 18.62%

Standard 2; Acetanilide - C; 71.09, H; 0.67, N; 10.36%

### 2.2.6 Thermogravimetric analysis

Thermogravimetric analysis was performed using a Perkin-Elmer TGA 7 thermogravimetric analyser (TGA). Typically, the samples were heated at a rate of  $10\text{ }^{\circ}\text{C}\cdot\text{min}^{-1}$  under a constant stream of nitrogen gas. The temperature range differed depending on the sample used. The samples were contained in platinum pans. The onset of decomposition or mass loss ( $T_{\text{onset}}$ ) was determined from the normal TG-curve.

### 2.2.7 EPR (electron paramagnetic resonance) spectroscopy

EPR spectra were recorded with a Bruker ESP 300E X-band spectrometer, and the spin hamiltonian parameters were obtained by using the computer program of Rockenbauer and Korecz.<sup>311</sup> The analysis parameters are presented in **Table 2.2**.

### 2.2.8 Scanning electron microscopy (SEM) and X-ray energy dispersive spectroscopy (EDS)

Samples were prepared for scanning electron microscopy (SEM) by coating them in gold using a Balzers' Sputtering device. The samples were viewed using a TESCAN Vega TS 5136LM typically operated at 20 kV at a working distance of 20 mm. Elemental analysis of samples using energy dispersive spectroscopy (EDS) was determined by using the same procedure as described for SEM analysis, except that no sample surface coating was needed.

### 2.2.9 Atomic force microscopy

Atomic force microscopy (AFM) imaging was performed using a CP-11 Scanning Probe Microscope from Veeco Instruments (Carl Zeiss, South Africa) in non-contact mode at a scan rate of 1 Hz using a MP11123 cantilever. The images were obtained using a spring constant range of 20-80  $\text{N}\cdot\text{m}^{-1}$ , and resonant frequency range of 217-276 Hz.

**Table 2.2** EPR analysis parameters for both the homogeneous [V<sup>IV</sup>O(sal-HBPD)] and heterogeneous poly[V<sup>IV</sup>O(sal-AHBPD)] and poly[V<sup>IV</sup>O(allylsB-co-EGDMA)] catalysts.

	poly[V <sup>IV</sup> O(sal-AHBPD)] and poly[V <sup>IV</sup> O(allylsB-co-EGDMA)]	[V <sup>IV</sup> O(sal-HBPD)]
<b>Fields</b>		
Center Field	3500 G	3500 G
Sweep Width	1500 G	2000 G
Resolution	5000 points	5000 points
<b>Microwave</b>		
Frequency	9.840 GHz	9.750 GHz
Power	0.200 mW	0.399 mW
<b>Receiver</b>		
Receiver Gain	1.00e+003	1.00e+004
Mod. Phase	0.00 deg	0.00 deg
Harmonic	1	1
Mod. Frequency	100.00 kHz	100.00 kHz
Mod. Amplitude	16.25 G	16.25 G
<b>Signal Channel</b>		
Conversion	5.120 ms	20.000 ms
Time Constant	20.480	40.960
Sweep Time	25.600 s	100.000 s

### 2.2.10 X-ray photoelectron spectroscopy

X-ray photoelectron spectroscopy (XPS) measurements were performed with a Kratos Axis Ultra X-ray Photoelectron Spectrometer equipped with a monochromatic Al K<sub>α</sub> source (1486.6 eV). The base pressure of the system was below 3 x 10<sup>-7</sup> Pa. XPS experiments were recorded with 75 W power

source using a hybrid-slot spectral acquisition mode and an angular acceptance angle of  $\pm 20^\circ$ . The analyzer axis made an angle of  $90^\circ$  with the specimen surface, with the specimen surface making an angle of  $45^\circ$  with the X-ray angle. A charge neutraliser was used due to the insulating surface used to prepare the sample. The elemental analysis and metal core level were recorded with a step of 1 eV and pass energy of 160 eV. XPS data analysis was performed with Kratos version 2 programs.<sup>312</sup>

### 2.2.11 Brunauer, Emmett, Teller (BET) surface area analysis

Adsorption/desorption isotherms were measured using a Micromeritics ASAP 2020 Surface Area and Porosity Analyzer. Prior to each measurement, samples were degassed for a minimum of one week to ensure complete removal of adsorbed impurities. Degassing was performed at  $40^\circ\text{C}$  for chitosan fibers and microspheres,  $70^\circ\text{C}$  for PBI and imprinted-PBI fibers and  $120^\circ\text{C}$  for the heterogeneous catalysts (poly[V<sup>IV</sup>O(sal-AHBPD)] and poly[V<sup>IV</sup>O(allylsB-co-EGDMA)]), unless mentioned otherwise. Approximately 0.2 g of sample was used and an equilibration interval of 30 seconds was allowed during the run. The surface area (BET), total pore volume and pore size distribution (BJH method) were calculated from the BET isotherms. For the analysis, N<sub>2</sub> gas was employed for adsorption/desorption isotherm of PBI and imprinted-PBI fibers at 77 K, while CO<sub>2</sub> was used for chitosan microspheres and fibers at 273 K.

### 2.2.12 Inductively coupled plasma – Optical emission spectroscopy

The vanadium content was determined using a Thermo Electron (iCAP 6000 Series) inductively coupled plasma (ICP) spectrometer equipped with an Optical Emission Spectrometer (OES) as detector. Four wavelengths were chosen for vanadium detection (290.88 nm, 292.40 nm, 309.31 nm, and 311.07 nm). These wavelengths were the most sensitive and had the minimum amount of interferences. Three runs were performed at each wavelength. Additional operating parameters have been listed in **Table 2.3**. Calibration was performed using six standards typically; 1 ppm, 2 ppm, 5 ppm, 10 ppm, 15 ppm and 20 ppm. The standards were prepared by appropriate dilution of a 1000 ppm stock solution. All solutions were filtered through 0.45  $\mu\text{M}$  Millipore® filters to prevent nebulizer blockages.

**Table 2.3** ICP-OES method and operating parameters

Parameter	Setting
Plasma Ar gas flow rate	5.0 L.min <sup>-1</sup>
Auxiliary Ar gas flow rate	1.00 L.min <sup>-1</sup>
Nebulizer Ar gas flow rate	0.90 L.min <sup>-1</sup>
Sampling depth	8.5 mm
Pump rate	100 rpm
N <sub>2</sub> addition flow rate	0.5 L.min <sup>-1</sup>
Cooled spraying chamber temperature	4°C
Selected wavelengths (Vanadium)	290.88 nm 292.40 nm 309.31 nm 311.07 nm
Sample flush time	30 s
Points per peak	3
Time scan acquisition	50 ms/point
RF power	1150 Watts

### 2.2.13 Gas chromatography

Progress of the catalysed reactions was monitored using either an Agilent gas chromatograph (7890A or 6890N), fitted with a Flame Ionization Detector (FID), Agilent G2350A Atomic Emission Detector (AED) and Agilent gas chromatograph (7890A) fitted with an electron impact ionization Mass Selective triple-axis Detector (5975C VL MSD). The GC parameters are summarized in **Table 2.4**, while the detector conditions are summarized in **Table 2.5**. It is to be noted that all the gas chromatographs (GC-FID, GC-AED and GC-MS) were fitted with DB-5 or HP-5 columns of the following dimensions (30 m x 0.25 mm x 0.25 µm).

**Table 2.4** Chromatographic conditions used in the identification and quantification of the oxidation products and adsorption of organosulfur compounds in model system and hydro-treated diesel.

		Hydro-treated diesel and crude oil	Model organosulfur compounds	
		Oxidation and adsorption.	Oxidation.	Adsorption.
<b>GC</b>	Volume ( $\mu\text{L}$ )	1	1	1
	Mode	split	Split	Split
	Temperature ( $^{\circ}\text{C}$ )	250	250	250
	Inlet pressure (kPa)	60.24	60.24	60.24
	Av. velocity (mL/sec)	30.16	30.16	30.16
<b>Oven</b>	Split ratio	20:1	5:1	5:1
	Initial temperature ( $^{\circ}\text{C}$ )	45	80	50
	Ramp ( $^{\circ}\text{C}/\text{min}$ )	10	20	15
	Intermediate temperature ( $^{\circ}\text{C}$ )	150	100	80
	Hold time (min)	5	0	0
	Ramp ( $^{\circ}\text{C}/\text{min}$ )	20	30	20
	Final temperature ( $^{\circ}\text{C}$ )	320	320	300
	Hold time (min)	2	0	1
	Final time (min)	26	9.33	13
<b>Signal</b>		50 Hz/0.004 min	50 Hz/0.004 min	50 Hz/0.004 min



**Table 2.5** Detector conditions used in the identification and quantification of the oxidized compounds.

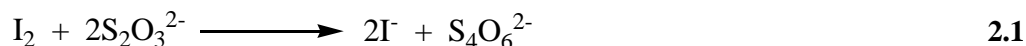
<b>FID</b>		
Temperature	Heater (°C)	300
Reagent gases	H <sub>2</sub> flow (mL/min)	30
	He flow (mL/min)	1.63
	Air flow (mL/min)	400
	N <sub>2</sub> (make up) (mL/min)	25
<b>MS</b>		
Temperature	Heater (°C)	250
Reagent gases	H <sub>2</sub> flow (mL/min)	100
<b>AED</b>		
Wavelength	Sulfur (nm)	181
	Carbon (nm)	179
Temperature	Transfer line (°C)	350
	Cavity block (°C)	320
Reagent gases	H <sub>2</sub> reagent (kPa)	300
	O <sub>2</sub> reagent (kPa)	380
Frequency	H <sub>2</sub> make up flow (mL/min)	100

### 2.3 *Tert*-butylhydroperoxide concentration determination

A known amount of *tert*-butylhydroperoxide (*t*-BuOOH) was contacted with 10 mL of 1 M potassium iodide (KI) solution in an acidic medium (10 mL, 2 M HCl) in a 250 mL conical flask. Under this condition, *tert*-butylhydroperoxide (*t*-BuOOH) is reduced by KI to liberate iodine.<sup>313</sup>

The equivalent amount of iodine liberated was titrated against 0.1 M sodium thiosulphate. When the colour of the iodine had almost disappeared, 1-2 mL of the starch suspension (0.2%) was added, followed by the dropwise addition of thiosulphate solution until the blue colour disappears.<sup>313</sup> The

equation below (**Equation 2.1**) was used to calculate the amount of iodide ions that reacts with each mole of peroxide ions.



#### 2.4 Metal content determination on polymer microspheres

Vanadium(IV) content on poly[V<sup>IV</sup>O(sal-AHBPD)] and poly[V<sup>IV</sup>O(allylsB-co-EGDMA)] microspheres were determined by weighing out a known mass into a vial, and 10 mL of TraceSelect HNO<sub>3</sub> (69%) was added.<sup>314</sup> This mixture was heated up to a temperature of 40°C for 12 h to leach out the vanadium. The acid-leached solution was then diluted with deionized-distilled water to 100 mL, filtered through 0.45 μM filters and analysed by ICP-OES.

#### 2.5 Catalytic oxidation procedure under batch studies

The catalytic oxidation of known quantities of thiophene (TH), benzothiophene (BT), dibenzothiophene (DBT) and 4,6-dimethyldibenzothiophene (4,6-DMDBT) were carried out using unsupported catalyst, [V<sup>IV</sup>O(sal-HBPD)] and supported polymer catalysts, poly[V<sup>IV</sup>O(sal-AHBPD)] and poly[V<sup>IV</sup>O(allylsB-co-EGDMA)] and *tert*-butylhydroperoxide (*t*-BuOOH) as oxidant. In a typical 50 mL round bottom flask, 10 mL of a toluene/hexane (1:4) solvent mixture, organosulfur compound and catalyst were mixed and then heated to 40°C under continuous stirring at 500 rpm in an oil bath. The catalysed oxidation reaction was considered to begin on addition of the required volume of *t*-BuOOH (oxidant). The oxidation reaction for the various organosulfur compounds were carried out separately, and mixed when studies were carried out on model fuel organosulfur compounds. The progress of the reaction was monitored using GC-FID. For the catalysed oxidation of hydro-treated diesel, progress of the reaction was followed with GC-AED.

#### 2.6 Catalyzed oxidation procedure under continuous flow

The catalytic oxidation of thiophene (TH), benzothiophene (BT), dibenzothiophene (DBT) and 4,6-dimethyldibenzothiophene (4,6-DMDBT) were carried out in a 25 mL syringe by employing both supported catalysts poly[V<sup>IV</sup>O(sal-AHBPD)] and poly[V<sup>IV</sup>O(allylsB-co-EGDMA)], separately. The catalyzed oxidation reaction for each of the substrates and catalysts were carried out separately. An

aqueous solution of *tert*-butylhydroperoxide (*t*-BuOOH) and each of the organosulfur compounds {thiophene (TH), benzothiophene (BT), dibenzothiophene (DBT) and 4,6-dimethyldibenzothiophene (4,6-DMDBT)} were dissolved in 10 mL solution of toluene/hexane (1:4), after which the homogeneous solution was transferred to a syringe attached to a compartment containing a known mass of catalyst as presented in **Figure 2.1**. The reaction mixture was heated to 40°C with the aid of a heating blanket, after which an applied flow rate was used to pump the solution through the catalyst in order for oxidation to occur. Flow-rates of 1 mL/h, 3 mL/h, 5 mL/h, 7 mL/h and 10 mL/h were employed in the continuous flow catalyzed oxidation reaction, respectively. The residence time required while employing the various flow-rates was calculated by using **Equation 2.2**.

$$\text{Rate} = \text{Volume (mL)} / \text{Time (h)} \quad 2.2$$

Continuous flow catalysed oxidation processes for hydro-treated diesel was monitored by using a gas chromatography fitted with an atomic emission detector (GC-AED).

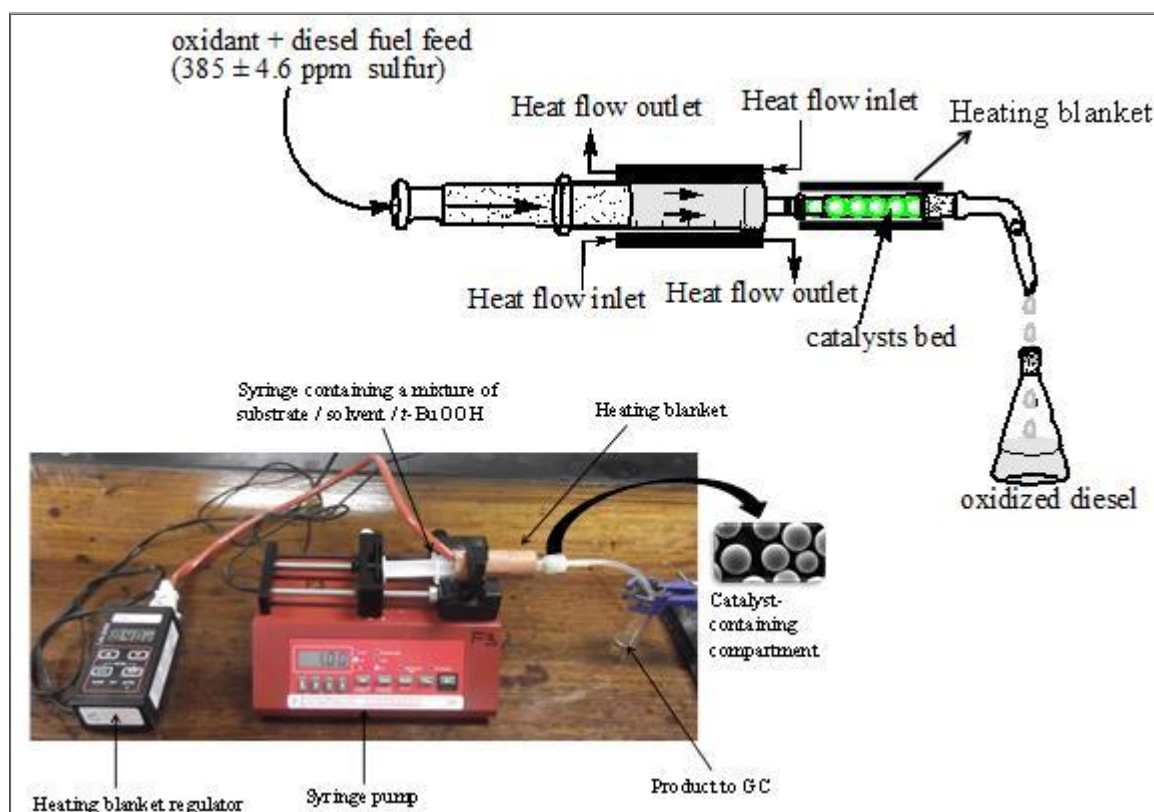


**Figure 2.1** Simple setup of a continuous flow catalysed oxidation process.

## 2.7 Adsorption studies using molecularly imprinted chitosan and polybenzimidazole (PBI) as adsorbents

Batch and continuous flow adsorption studies were performed for optimizing sulfone adsorption from fuels. The batch adsorption study was performed by weighing out a known mass of adsorbent (imprinted and non-imprinted microspheres and nanofibers) in vials containing 2 mL of 0.005 M sulfone compounds {benzothiophene sulfone (BTO<sub>2</sub>), dibenzothiophene sulfone (DBTO<sub>2</sub>) and 4,6-dimethyldibenzothiophene sulfone (4,6-DMDBTO<sub>2</sub>)}. The screw-capped vials containing sulfone suspensions were left under mechanical agitation (150 rpm) for 24 h, after which the adsorbents were removed from the solutions by filtration and the resulting solutions analysed by the gas chromatography fitted with a flame ionization detector (GC-FID). Rate of adsorption with time (adsorption kinetics) was also carried out using the above mentioned conditions. The adsorption capacity,  $q_e$  (mg/g), for each sulfone compound was calculated using **Equation 2.3**.

$$q_e = \frac{V(C_o - C_e)}{W} \quad 2.3$$

where  $C_o$ ,  $C_e$ ,  $W$  and  $V$  are the initial concentration (mg/L), equilibrium concentration (mg/L), dry weight of nanofibers (g) and solution volume (L) respectively.

Continuous flow adsorption technique was also employed for the adsorption of sulfone compounds, and breakthrough volumes were evaluated. A breakthrough volume represents the evolution of the concentration of a solution as a function of adsorption parameters like contact time between liquid and solid phase (adsorbent), solvent concentration and temperature. For continuous flow adsorption, a known mass of imprinted polymer was packed into a cylindrical tube attached to the tip of a syringe containing a 5 mM sulfone compound acetonitrile solution (5 mL) as shown in **Figure 2.2**. Adsorption was assumed to begin as soon as the respective sulfone compounds were pumped through the conditioned imprinted adsorbent. A flow rate of 1 mL/h was employed for the continuous flow studies. Conditioning of adsorbents was carried-out by pre-wetting adsorbents with solvents employed in dissolving the sulfone compounds.

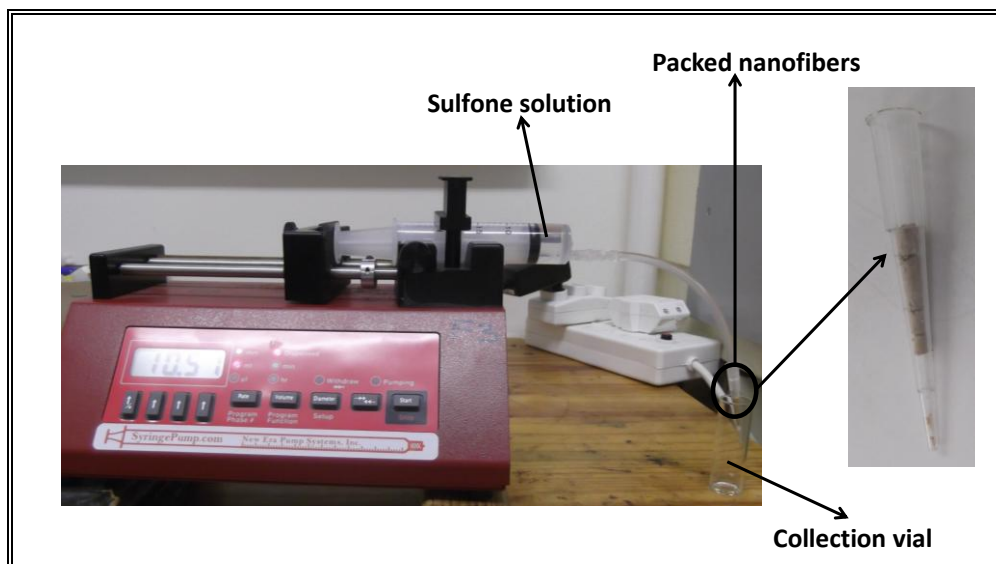


**Figure 2.2** A continuous flow set-up used in this study. Imprinted nanofibers are packed into a filter tip compartment, and the sulfone containing compounds (BTO<sub>2</sub>, DBTO<sub>2</sub> and 4,6-DMDBTO<sub>2</sub>) will be passed through the nanofibers by means of a syringe pump.

Adsorption studies on the oxidized hydro-treated diesel were monitored by using a gas chromatography fitted with an atomic emission detector (GC-AED).

## 2.8 Desorption /regeneration condition

The nanofibers and microspheres containing the sulfone compounds after adsorption studies were regenerated to test their reusability by the use of these methods:

- (i) Soxhlet extraction using a 50 mL solvent mixture of acetonitrile and methanol (1:1). The Soxhlet extraction process was allowed to proceed for 12 h.
- (ii) Home-made pressurized hot water extraction (PHWE) system. The principle of desorption is discussed in **Chapter 5, Section 5.5.2.6**.

*This page is kept blank*

# Chapter 3

## Characterization, classification and identification of petroleum fuel oils

### 3.1 Introduction

The determination of organic and trace metals constituents in crude oils is important to predict crude oil source. Organics such as phenanthrene and dibenzothiophene (**Figure 3.1**) are molecular indicators found in crude oils.<sup>315-318</sup>

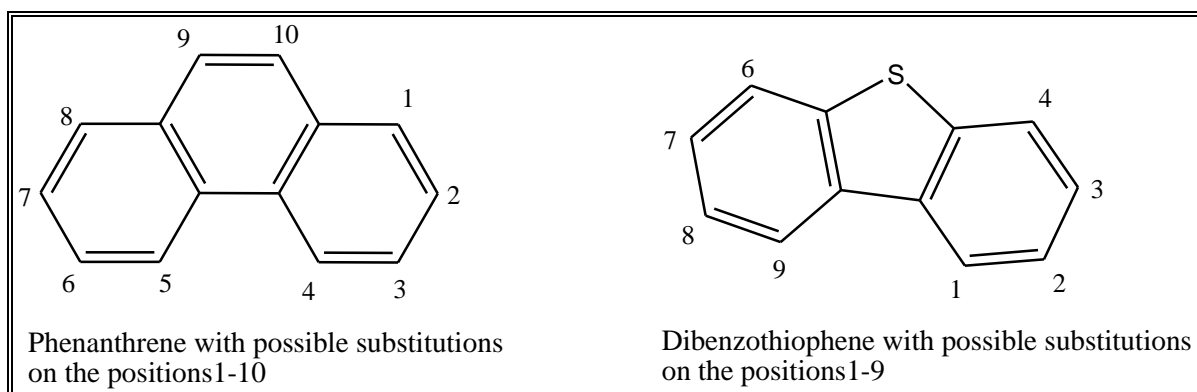


**Figure 3.1** Structure of phenanthrene and dibenzothiophene.

In identifying and classifying the organics in crude oil, several techniques have been traditionally employed, such as infrared (IR) spectroscopy, ultraviolet fluorescence (UVF) spectroscopy, and gas chromatography (GC).<sup>319</sup> A gas chromatograph coupled to a mass spectrometer (GC-MS) has been found to give more positive identification for organic compounds in crude oils.<sup>320</sup> Christopher *et al.*<sup>321</sup> reported the classification and identification of oil source rock by evaluating the phenanthrene/dibenzothiophene ratio (P/D) in the various oils by employing a GC-MS. This technique was also employed by Douglas *et al.*<sup>322</sup> and it revealed that the aromatic fractions of oil contain more toxic and more persistent compounds than the aliphatic fraction.

Likewise, trace metal ion concentrations and ratios in crude oils have also been reported to give information on the origin and environment of deposition of petroleum as well as regional geochemical prospecting.<sup>323-325</sup> Barwise *et al.*<sup>326</sup> reported that low V/Ni ratios (< 0.5) are expected for petroleum or crude oil derived from marine organic matter with high to moderate sulfur content, while crude oil or

petroleum from lacustrine and terrestrial organic matter has V/Ni ratios ranging from 1 to 10. Henry *et al.*<sup>327</sup> used atomic adsorption spectrometer (AAS) to determine some heavy metals in crude oils and petroleum products, and Al Swaidan<sup>328</sup> determined vanadium in crude oil by inductively coupled plasma-mass spectrometry. Akinlua *et al.*<sup>329</sup> determined some rare earth elements in Nigeria, Niger-Delta crude oils by inductively coupled plasma-mass spectrometry. Odebunmi *et al.*<sup>330</sup> and Olajire *et al.*<sup>331</sup> also determined trace metals in Nigeria crude oil using AAS and from their report trace metal contents in Nigeria crude oils were present in relatively moderate to low concentrations.

Column chromatography has been employed to separate crude oils into fractions for better identification of target compounds (phenanthrene and dibenzothiophene).<sup>332</sup> Boukir and his co-worker<sup>332</sup> reported that crude oil can be fractionated into saturates, aromatics, resins and asphaltenes by using SARA (saturates-aromatics-resins-asphaltenes) fractionation. For all the maltenic fractions, *n*-heptane was used to elute saturates; *n*-heptane/toluene was used to elute the aromatic fractions while dichloromethane/methanol mixture in equal volume was used to elute resins in the crude oil. The fractionation was achieved by using silica/alumina column chromatography. Li *et al.*<sup>333</sup> reported the separation of the interfacial active fractions of crude oils by the precipitation and adsorption chromatography procedure, where the resin fraction from crude oil was extracted by 2.5 L of benzene/methanol (50/50 v/v).

In this chapter, fractionation of crude oil into saturates, aromatics, resins and asphaltenes (SARA) are reported, and also molecular indicators such as the ratio of phenanthrene-to-dibenzothiophene from the aromatic fraction and the ratio of vanadium-to-nickel in the crude oils were employed to classify crude oils. The determination of trace metal elements in crude oils was carried out using inductively coupled plasma-optical emission spectrometer (ICP-OES), while the identification and quantification of the organic aromatic compounds in the crude oil fractions was carried on the gas chromatography-mass spectrometry (GC-MS). Refractory organosulfur compounds found in hydro-treated fuel were also discussed.



## 3.2 Experimental work

### 3.2.1 Crude oil column separation protocol

Separation of the various crude oil samples (Nigeria bonny light, medium and heavy crude oil) into (asphaltenes, resins, aromatics and saturates) was carried out in a column packed with silica gel as reported by Jewell *et al.*<sup>334</sup>, Tshentu *et al.*<sup>335</sup> and Shi *et al.*<sup>336</sup> as shown in **Figure 3.2**.

0.5 g of crude oil was dissolved in 10 mL of pentane and allowed to stand for 4 h, then centrifuged at 10 000 rpm for 30 min to separate the pentane soluble fraction from the asphaltenes. The fractionation was carried out in a column (about 2-3 cm diameter) packed with 14 g of silica gel. For this purpose, the column was pre-wet with 5 mL hexane. Elution was carried out by using 25 mL of *n*-hexane for saturates, 25 mL of dichloromethane for aromatics and 25 mL mixture of dichloromethane:methanol (1:1) was used to elute the resins. Drying of the various fractions was done in the fumehood by bubbling nitrogen gas in the sample vials. The weight percentage of each fraction eluted is presented in **Table 3.1**. The two main fractionated products of interest (saturates and aromatics) were analyzed by using FT-IR and GC-MS.

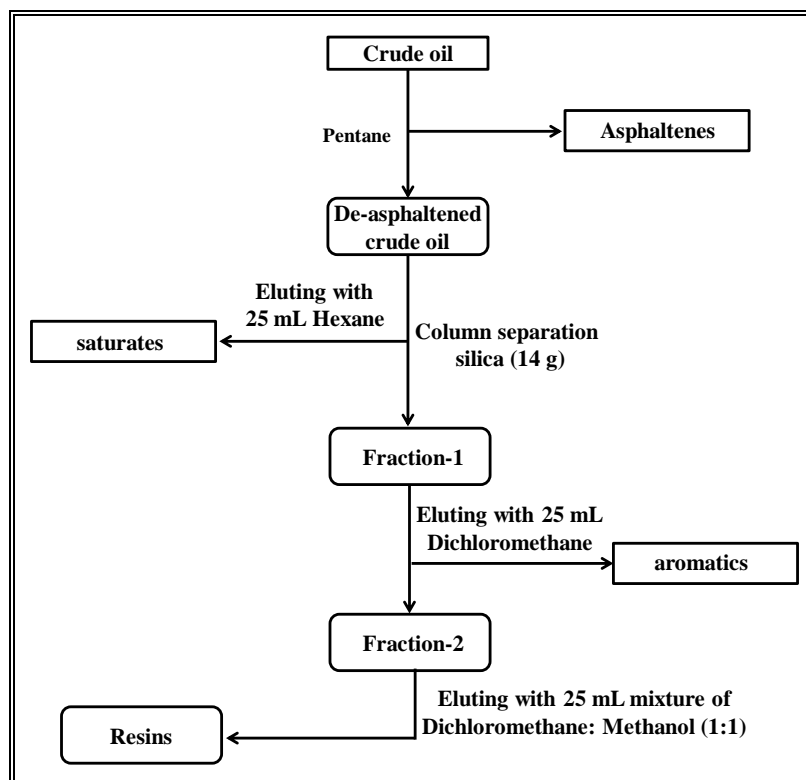


**Figure 3.2** Separation protocol for the crude oil into saturates, aromatics, resins and asphaltenes.

### 3.2.2 Metal determination and method validation

3 mL of deionized water was added to 2.0 g of the oil sample and shaken in a centrifuge to extract water soluble metal salts (aqueous phase) from the oils (organic phase). To 0.2 g of the organic phase (oil), 3 mL of HNO<sub>3</sub> was added for digestion of the oil which charred, and the addition of 4 mL of 30% hydrogen peroxide completely decomposed the sample. The resultant colourless aqueous solution was made up to 100 mL with deionized water. This resulting aqueous matrix was compatible for ICP-OES. The same procedure as described above was also adopted for the fuel oil standard reference material SRM 1634c. National institute of standards and technology (NIST) fuel oil standard reference material (SRM 1634c), with a nickel of  $17.54 \pm 0.21$  mg/kg and a vanadium content of  $28.19 \pm 0.40$  mg/kg was purchased from NIST (USA) and used to validate the method for element determination.

## 3.3 Results and discussion

### 3.3.1 Preliminary analysis of the fractions

The fractionated SARA weight percentages and microanalysis data are presented in **Tables 3.1** and **3.2** respectively. The summation of all the fractions in each crude oil showed that the separation protocol was effective. Heavy crude oil contains a higher proportion of asphaltenes and resins as compared to medium and light crude oils. From the elemental analysis result, the total sulfur concentration of 2 540 ppm was found to be present in light crude oil, 5 080 ppm S in medium crude oil and 17 920 ppm S in heavy crude oil. Carbon-to-sulfur ratio (C/S) decreased as the sulfur contents in the crude oils increased from light crude oil to the heavy oil. This showed the presence of higher concentration of sulfur compounds in heavy crude oil as compared to the medium and light crude oil.

**Table 3.1** Weight % of saturates, aromatics, resins and asphaltenes (SARA) in various crude oils.

Family	Light crude oil (w/w %)	Medium crude oil (w/w %)	Heavy crude oil (w/w %)
Saturates	37.13	31.02	16.10
Aromatics	43.14	40.21	44.32
Asphaltenes	3.46	7.32	12.03
Resins	15.54	20.41	27.00

**Table 3.2** Elemental microanalyses of the crude oils, and hydro-treated oil.

Crude oils	Fractions	wt (%)				ratios	
		C	H	N	S	C/N	C/S
Light	Saturates	84.87	16.26	0.05	-	1697	-
	Aromatics	86.59	11.88	0.15	0.254	577	341
Medium	Saturates	86.74	15.74	0.03	-	2891	-
	Aromatics	82.96	11.22	0.38	0.508	218	163
Heavy	Saturates	83.17	16.26	-	-	-	-
	Aromatics	84.50	12.61	0.43	1.792	196	47
Hydro-treated oil		85.95	17.72	0.56	-	153	-

### 3.3.2 FT-IR spectroscopic studies of crude oils

Similar vibrational bands were observed for aromatic and saturate fractions of the light, medium and heavy crude oils, however variations in band intensities of  $\nu(\text{O-H})$  and  $\nu(\text{R-NH-R})$  bands in aromatic fractions (**Figure 3.3**) and saturates fraction is provided in **Figure 3.4**. The existence of one or more aromatic rings in the oil matrix is confirmed by C-H and C=C-C vibrations (**Figures 3.3** and **3.4**).

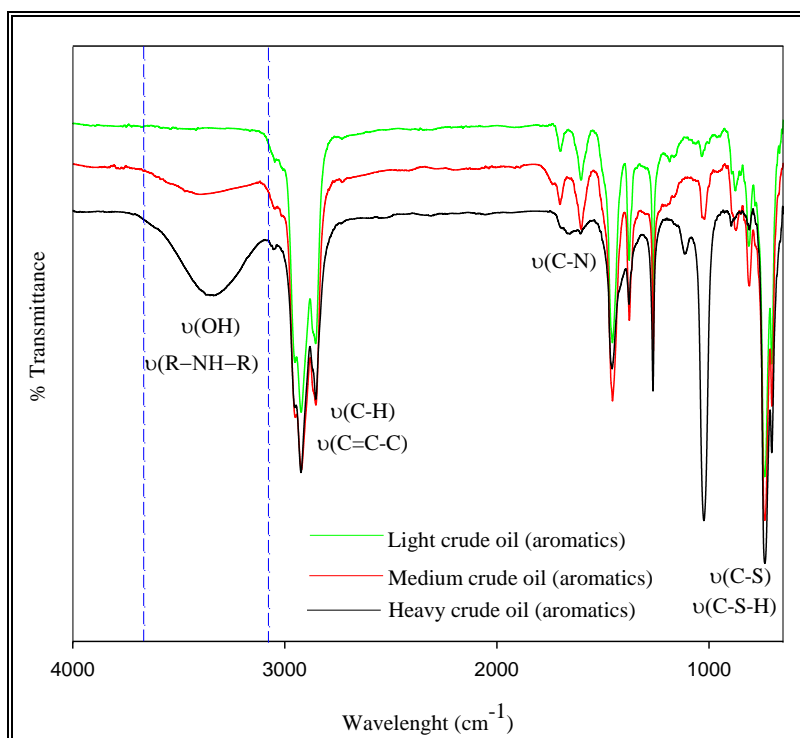


**Figure 3.3** FT-IR spectra for aromatics in light, medium, and heavy crude oils.

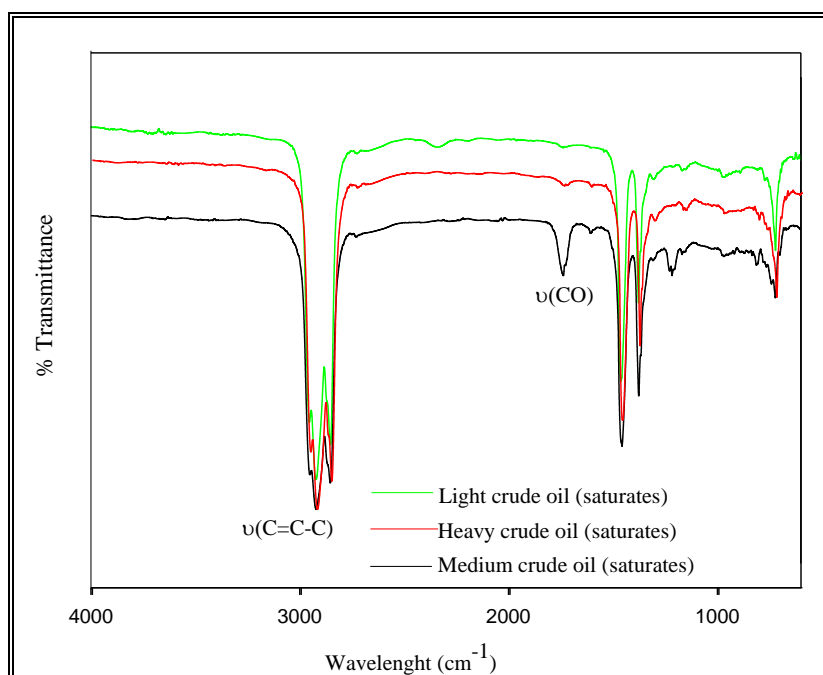


**Figure 3.4** FT-IR spectra for saturates in light, medium, and heavy crude oils.

A broad band around  $3330\text{-}3420\text{ cm}^{-1}$  in the aromatics was assigned to  $\nu(\text{O-H})$  and  $\nu(\text{R-NH-R})$  group.

These bands were observed in the medium and heavy crude oils, with the peaks in the spectrum of the

heavy crude oil far broader than those in the spectrum of the medium crude oil. The high intensity of the bands signifies the presence of more bonded hydroxyl and amino containing compounds. Thiols (C-S) and (C-S-H) stretching vibrations occurred between the vibrational frequencies of 720-800  $\text{cm}^{-1}$  in all the crude oil aromatic fractions. The C-N stretching frequencies attributed to the aromatic amine (as well as primary, secondary and tertiary amine) occurred in the region 1150-1380  $\text{cm}^{-1}$ .<sup>337</sup> The vibrational frequencies for various crude oils are represented in **Table 3.3**.

**Table 3.3** Selected Infra-Red bands of the various crude oils.

Crude oils	Fractions	Colors	IR- Bands ( $\text{cm}^{-1}$ )			
			v(O-H)	v(C-H) stretch	v(C=C-C) aromatics	v(C-S)
<b>Light</b>	Saturates	Light yellow	-	2921	-	726
	Aromatics	Light brown	-	2923	1605	738
<b>Medium</b>	Saturates	Light yellow	-	2921	-	719
	Aromatics	Brown	3401	2923	1603	738
<b>Heavy</b>	Saturates	Light yellow	-	2954	-	726
	Aromatics	Dark brown	3335	2924	1655	740

### 3.3.3 Metal content determination in crude oils

Thirteen (13) elements were analysed in crude oil samples (**Table 3.4**). Light crude oil has the highest concentration of the following metals; Mg (72 to 167 ppm), Ni (26 to 37 ppm), Pd (61 to 198 ppm) and Ca (62 to 200 ppm). Heavy crude oil has the highest concentration of the following metals; Cu (18 to 32 ppm), V (17 to 74 ppm) and Zn (28 to 53 ppm). The metal concentrations of the medium crude oil fall in between the range of both the light and heavy crude oils. Nickel and vanadium are the two most common transition metals in crude oils and are largely present as porphyrin complexes which are mainly derived from chlorophyll precursors,<sup>338</sup> hence vanadium-to-nickel ratio (V/Ni) provides possible information about the likely source of oil.<sup>326</sup> From the results obtained, the light crude oil had a V/Ni ratio of 0.47, and the medium crude oil had a V/Ni ratio of 1.36 while the heavy

crude oil had a V/Ni ratio of 2.77. The low V/Ni ratio of bonny light crude oil indicated that the oil was derived from marine organic matter, while the high V/Ni ratio for the heavy oil indicated that the oil was derived from terrestrial organic matter. The medium crude oil was classified as being originated from a mixture of the marine and terrestrial organic matter, owing to the migration of hydrocarbon.<sup>339</sup> The V/Ni ratio also increased as the sulfur content (wt%) of the oil decreased (**Figure 3.5**). The metal determination method validation results for the analysis of vanadium and nickel in fuel (NIST, SRM 1634c) are presented in **Table 3.5**. Errors of 0.51% and 2.23% were obtained when nickel and vanadium concentrations were determined respectively. It can be concluded from the method validation results that the sample preparation method detailed under **Section 3.2.2** can be used reliably for the determination of metals in crude oils.

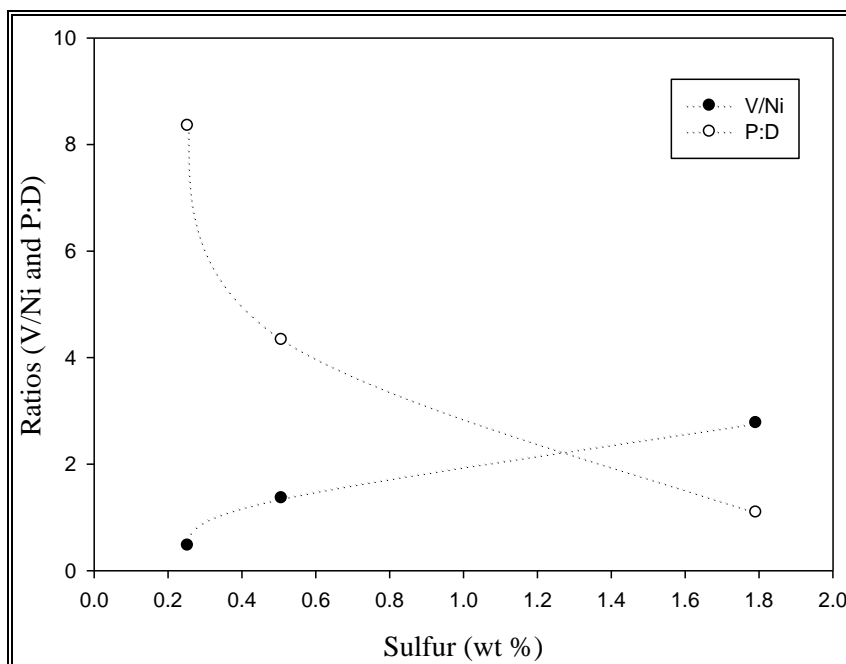


**Figure 3.5** Graph showing the relationship between vanadium-to-nickel (V/Ni) and phenanthrene-to-dibenzothiophene (P/D) to sulfur content of oil (wt%).

**Table 3.4** Metal distribution in the aromatic crude oil fractions.

Crude oil Fractions	Metals (ppm)														
	Co	Mn	Cu	V	Mg	Ni	Pt	Pd	Rh	Ir	Fe	Ca	Cd	Zn	V/Ni
Light crude	ND	ND	18.4 (6.3)	17.1 (2.3)	167.5 (6.1)	36.4 (1.0)	ND	198.7 (1.2)	ND	ND	ND	200.4 (5.6)	ND	28.4 (2.8)	0.47
Medium crude	ND	ND	28.7 (5.1)	40.4 (2.3)	112.8 (0.6)	29.2 (1.6)	ND	197.5 (1.7)	ND	ND	ND	168.2 (0.7)	ND	36.9 (1.1)	1.36
Heavy crude	ND	ND	32.3 (3.2)	74.5 (1.4)	72.2 (2.8)	26.1 (2.2)	ND	61.6 (1.8)	ND	ND	ND	62.6 (1.9)	ND	53.1 (1.6)	2.77

ND: %RSD presented in parenthesis. The values are at a level of confidence of approximately 95% for light, medium and heavy crude oils respectively.

**Table 3.5** Validation of certified values of vanadium and nickel on Fuel oil SRM 1634c.

Elements	Certified value (mg/kg)	ICP-OES value (mg/kg)	% error
Nickel	17.54 ± 0.21	17.45 ± 0.41	0.51
Vanadium	28.19 ± 0.40	28.82 ± 0.36	2.23

### 3.3.4 Determination of organics

Compositional information on the thousands of species found in the saturate and aromatic fractions of crude oil were characterized by using the GC-MS.<sup>340</sup> For this thesis, the focus was on the identification of compounds of interest in the aromatics of the various crude oil, namely phenanthrene and dibenzothiophene with derivatives. GC chromatograms for light crude oil showing phenanthrene and dibenzothiophene with their derivatives is presented in **Figure 3.6**, medium crude oil showing phenanthrene and dibenzothiophene with their derivatives is presented in **Figure 3.7** and heavy crude oil showing phenanthrene and dibenzothiophene with their derivatives is presented in **Figure 3.8**. It was observed that the amount of phenanthrene and its derivatives decreased from the light crude oil to the heavy crude oil, while an increase in quantity of dibenzothiophene and its derivatives was detected from the light crude oil to the heavy crude oil, with 4,6-dimethyldibenzothiophene identified in only the heavy crude oil. Some sulfur-containing compounds with derivatives found in the analysed crude oil fractions are presented in **Table 3.6**, and it can be seen that most of the compounds identified are similar to the sulfur-containing compounds reported by Ma and his co-workers.<sup>341-343</sup>



**Table 3.6** Some sulfur compounds identified in aromatic fraction of crude oil

Proposed identification	Molecular ion	Proposed identification	Molecular ion
C3-benzothiophene	176	C5-dibenzothiophene*	254
Dibenzothiophene*	184	C8-benzothiophene	260
4-methyldibenzothiophene	198	C3-dibenzothiophene*	226
C6-benzothiophene	218	C4-dibenzothiophene*	240
C7-benzothiophene	232	C12-benzothiophene	302
C2-dibenzothiophene	212	C5-phenanthrothiophene	278
4,6-dimethyldibenzothiophene*	212	C2-phenanthrothiophene*	236
2,6- and/or 2,7-dimethyldibenzothiophene*	212	C4- benzonaphthothiophene	290
3,6-dimethyldibenzothiophene	212	benzo[ <i>b</i> ]naphtho[2,1- <i>d</i> ]thiophene	234
C12-benzothiophene	302	C1-benzonaphthothiophene	248
C3-phenanthrothiophene	250	C14-benzothiophene	330
C1-benzonaphthothiophene	248	C15-benzothiophene	344
C4-phenylbenzothiophene	266	C4-benzonaphthothiophene	294
3,7- and/or 3,8-dimethyldibenzothiophenes	212	C16-benzothiophene	358
2 and/or 3-dimethyldibenzothiophene*	198	C13-benzothiophene*	316
1,4 and/or 1,6-dimethyldibenzothiophene*	212	1-methyldibenzothiophene*	198

**ND:** C represents methyl groups (-CH<sub>3</sub>), \* represents the compounds found in both crude oils and hydro-treated diesel.

The higher abundance of the sulfur-containing compounds in the GC chromatogram of heavy crude oil as compared to light and medium crude oil aromatic fractions complimented the microanalysis data which also gave higher sulfur content (wt%). The ratio of phenanthrene-to-dibenzothiophene decreased from the light crude oil to the heavy crude oil (**Table 3.7**). A high ratio of phenanthrene and its derivatives-to-dibenzothiophene and its derivatives was observed for the light crude oil. This indicated that there is less of sulfur containing compounds in the oil. The ratio of phenanthrene and its derivatives-to-dibenzothiophene and its derivatives were observed to be low for the heavy crude oils (**Table 3.8**), and therefore more sulfur-containing compounds are present in the heavy oils. A similar trend was also observed in phenanthrene (and derivatives)-to-4-methyldibenzothiophene (**Table 3.9**). From all ratios presented in **Tables 3.7, 3.8** and **3.9**, the values of medium crude oil falls in between the heavy and light crude oil. This variation was attributed to the origin of the oil (mixture of marine and terrestrial organic matter as a result of migration). The method is a simple, yet powerful method for determining the source rock depositional environment and lithology of crude oils.<sup>344</sup>

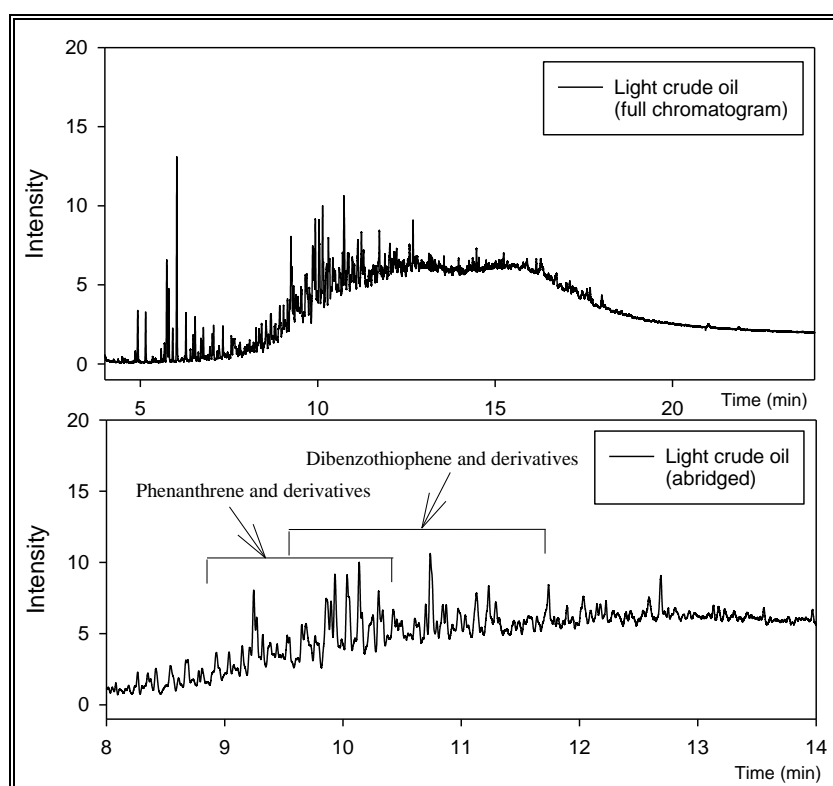


**Figure 3.6** GC chromatograms of light crude oils showing phenanthrene and dibenzothiophene with their derivatives.

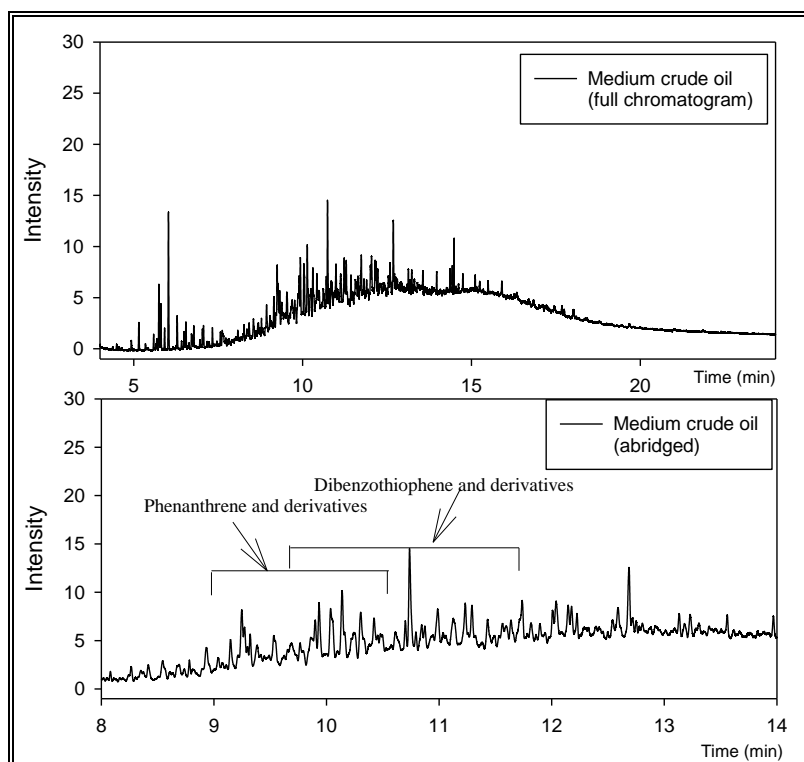


**Figure 3.7** GC chromatograms of medium crude oils showing phenanthrene and dibenzothiophene with their derivatives.

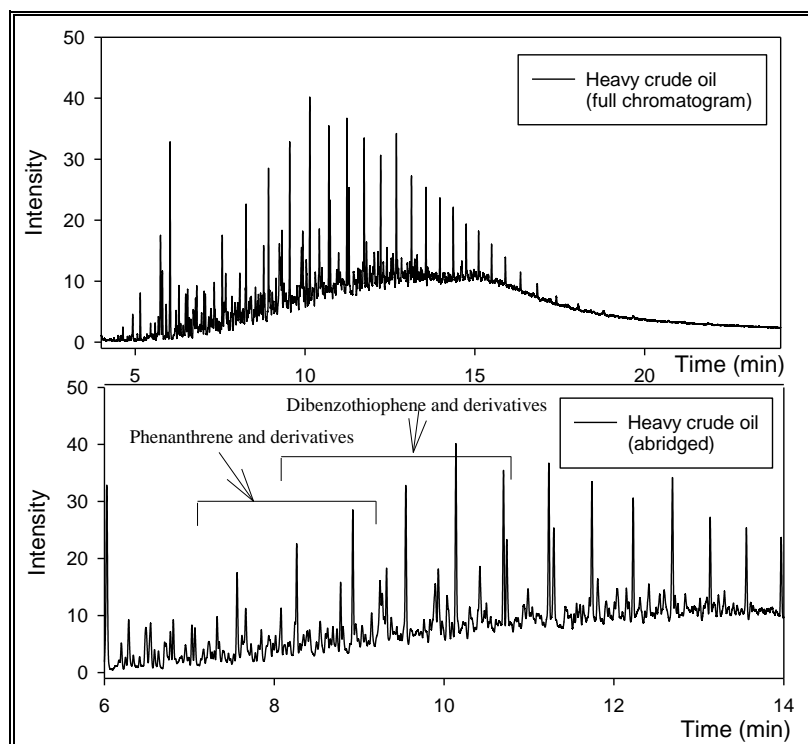


**Figure 3.8** GC chromatograms of heavy crude oils showing phenanthrene and dibenzothiophene with their derivatives

**Table 3.7** The distribution ratio of phenanthrene (and derivatives)-to-dibenzothiophene in the crude oil aromatic fractions.

Crude oil Fractions (aromatic)	ratio													
	P:D	1P:D	2P:D	3P:D	9P:D	2EtP/ 9EtP/ 3,6P:D	1EtP/ 2,6P/ 3,5P:D	2,7P:D	2,3P:D	1,7P:D	1,9P/ 4,9P/ 4,10P:D	1,3P/ 2,10P/ 3,9P/ 3,10P:D	1,6P/ 2,5P/ 2,9P:D	1,8P:D
Light crude	8.35	3.85	6.23	6.04	5.96	2.48	3.02	1.62	1.34	3.38	1.46	8.31	4.10	0.70
Medium crude	4.33	2.71	2.66	2.96	3.49	1.60	1.61	0.76	0.77	2.87	1.17	5.44	2.69	0.58
Heavy crude	1.09	0.68	0.37	0.41	0.49	0.33	0.39	0.19	0.16	0.60	0.25	1.32	0.64	0.14

**P:** Phenanthrene; **D:** Dibenzothiophene; **2D:** 2-methyl-dibenzothiophene; **3D:** 3-methyl-dibenzothiophene; **4D:** 4-methyl-dibenzothiophene; **Et:** Ethyl; **1P:** 1-Methyl-phenanthrene; **2P:** 2-Methyl-phenanthrene; **3P:** 3-Methyl-phenanthrene; **9P:** 9-Methyl-phenanthrene; **3,5P:** 3,5-Dimethyl-phenanthrene; **1,3P:** 1,3-Dimethyl-phenanthrene; **1,6P:** 1,6-Dimethyl-phenanthrene; **2,5P:** 2,5-Dimethyl-phenanthrene; **2,10P:** 2,10-Dimethyl-phenanthrene; **3,9P:** 3,9-Dimethyl-phenanthrene; **1,9P:** 1,9-Dimethyl-phenanthrene; **4,9P:** 4,9-Dimethyl-phenanthrene; **1EtP:** 1-Ethyl-phenanthrene; **2EtP:** 2-Ethyl-phenanthrene; **9EtP:** 9-Ethyl-phenanthrene; **3,6P:** 3,6-Dimethyl-phenanthrene; **2,7P:** 2,7-Dimethyl-phenanthrene; **2,3P:** 2,3-Dimethyl-phenanthrene; **1,7P:** 1,7-Dimethyl-phenanthrene; **4,10P:** 4,10-Dimethyl-phenanthrene; **3,10P:** 3,10-Dimethyl-phenanthrene; **2,9P:** 2,9-Dimethyl-phenanthrene; **1,8P:** 1,8-Dimethyl-phenanthrene.

**Table 3.8** The distribution ratio of phenanthrene (and derivatives)-to-2,3-methyl-dibenzothiophene in the crude oil aromatic fractions.

Crude oil Fractions (aromatic)	ratio													
	P:2/3D	1P:2,3D	2P: 2/3D	3P: 2/3D	9P: 2/3D	2EtP/ 9EtP/ 3,6P: 2/3D	1EtP/ 2,6P/ 3,5P: 2/3D	2,7P: 2/3D	2,3P: 2/3D	1,7P: 2/3D	1,9P/ 4,9P/ 4,10P: 2/3D	1,3P/ 2,10P/ 3,9P/ 3,10P: 2/3D	1,6P/ 2,5P/ 2,9P: 2/3D	1,8P: 2/3D
<b>Light crude</b>	8.35	3.85	6.23	6.04	5.95	2.48	3.02	1.62	1.34	3.38	1.46	8.31	4.02	0.70
<b>Medium crude</b>	5.34	3.32	3.26	3.62	4.27	1.95	1.97	0.93	0.94	3.51	1.43	6.66	3.28	0.71
<b>Heavy crude</b>	0.98	0.61	0.74	0.63	0.88	0.30	0.35	0.17	0.14	0.54	0.22	1.18	0.57	0.13

**P:** Phenanthrene; **D:** Dibenzothiophene; **2D:** 2-methyl-dibenzothiophene; **3D:** 3-methyl-dibenzothiophene; **4D:** 4-methyl-dibenzothiophene; **Et:** Ethyl; **1P:** 1-Methyl-phenanthrene; **2P:** 2-Methyl-phenanthrene; **3P:** 3-Methyl-phenanthrene; **9P:** 9-Methyl-phenanthrene; **3,5P:** 3,5-Dimethyl-phenanthrene; **1,3P:** 1,3-Dimethyl-phenanthrene; **1,6P:** 1,6-Dimethyl-phenanthrene; **2,5P:** 2,5-Dimethyl-phenanthrene; **2,10P:** 2,10-Dimethyl-phenanthrene; **3,9P:** 3,9-Dimethyl-phenanthrene; **1,9P:** 1,9-Dimethyl-phenanthrene; **4,9P:** 4,9-Dimethyl-phenanthrene; **1EtP:** 1-Ethyl-phenanthrene; **2EtP:** 2-Ethyl-phenanthrene; **9EtP:** 9-Ethyl-phenanthrene; **3,6P:** 3,6-Dimethyl-phenanthrene; **2,7P:** 2,7-Dimethyl-phenanthrene; **2,3P:** 2,3-Dimethyl-phenanthrene; **1,7P:** 1,7-Dimethyl-phenanthrene; **4,10P:** 4,10-Dimethyl-phenanthrene; **3,10P:** 3,10-Dimethyl-phenanthrene; **2,9P:** 2,9-Dimethyl-phenanthrene; **1,8P:** 1,8-Dimethyl-phenanthrene.

**Table 3.9** The distribution ratio of phenanthrene (and derivatives)-to-4-methyl-dibenzothiophene in the crude aromatic oil fractions.

Crude oil Fractions (aromatic)	ratio													
	P:4D	1P:4D	2P:4D	3P:4D	9P:4D	2EtP/ 9EtP/ 3,6P:4D	1EtP/ 2,6P/ 3,5P:4D	2,7P:4D	2,3P:4D	1,7P:4D	1,9P/ 4,9P/ 4,10P:4D	1,3P/ 2,10P/ 3,9P/ 3,10P:4D	1,6P/ 2,5P/ 2,9P:4D	1,8P:4D
Light crude	5.06	2.33	3.77	3.66	3.61	1.51	1.83	0.98	0.81	2.05	0.88	5.03	2.43	0.42
Medium crude	4.27	2.65	2.61	2.89	3.42	1.56	1.58	0.74	0.75	2.81	1.14	5.33	2.63	0.56
Heavy crude	0.61	0.38	0.46	0.39	0.55	0.18	0.22	0.11	0.09	0.34	0.14	0.73	0.36	0.08

**P:** Phenanthrene; **D:** Dibenzothiophene; **2D:** 2-methyl-dibenzothiophene; **3D:** 3-methyl-dibenzothiophene; **4D:** 4-methyl-dibenzothiophene; **Et:** Ethyl; **1P:** 1-Methyl-phenanthrene; **2P:** 2-Methyl-phenanthrene; **3P:** 3-Methyl-phenanthrene; **9P:** 9-Methyl-phenanthrene; **3,5P:** 3,5-Dimethyl-phenanthrene; **1,3P:** 1,3-Dimethyl-phenanthrene; **1,6P:** 1,6-Dimethyl-phenanthrene; **2,5P:** 2,5-Dimethyl-phenanthrene; **2,10P:** 2,10-Dimethyl-phenanthrene; **3,9P:** 3,9-Dimethyl-phenanthrene; **1,9P:** 1,9-Dimethyl-phenanthrene; **4,9P:** 4,9-Dimethyl-phenanthrene; **1EtP:** 1-Ethyl-phenanthrene; **2EtP:** 2-Ethyl-phenanthrene; **9EtP:** 9-Ethyl-phenanthrene; **3,6P:** 3,6-Dimethyl-phenanthrene; **2,7P:** 2,7-Dimethyl-phenanthrene; **2,3P:** 2,3-Dimethyl-phenanthrene; **1,7P:** 1,7-Dimethyl-phenanthrene; **4,10P:** 4,10-Dimethyl-phenanthrene; **3,10P:** 3,10-Dimethyl-phenanthrene; **2,9P:** 2,9-Dimethyl-phenanthrene; **1,8P:** 1,8-Dimethyl-phenanthrene.

### 3.3.5 Relationship of total sulfur content to phenanthrene/dibenzothiophene with derivatives (PHEN/DBT) ratio

The phenanthrene/dibenzothiophene (PHEN/DBT) with derivatives ratios also assist in the classification of oils due to variations in some important organic constituent. The relationship between the sulfur content and the PHEN/DBT with derivatives ratio is more complex than a simple one-to-one correspondence owing to the fact that derivatives of phenanthrene are also considered in this classification. **Figure 3.9** shows that light oil which has higher PHEN/DBT with derivatives ratio has low sulfur content, while the heavy oil which has a lower PHEN/DBT with derivatives ratio has higher total sulfur content. The medium crude oil PHEN/DBT with derivatives ratio is in between the light and heavy crude oil ratios. Group I (heavy crude oil) has high sulfur content ( $> 1\%$ ) with low PHEN/DBT with derivative ratios (0.1-1.3). Group II (medium crude oil) has moderate sulfur content ( $\sim 0.5\%$ ) and moderate-high PHEN/DBT ratios (0.6-5.7). Group III (light crude oil) has a low sulfur content ( $\sim 0.3\%$ ) and moderate to relatively higher PHEN/DBT with derivatives ratios (0.7-8.3).

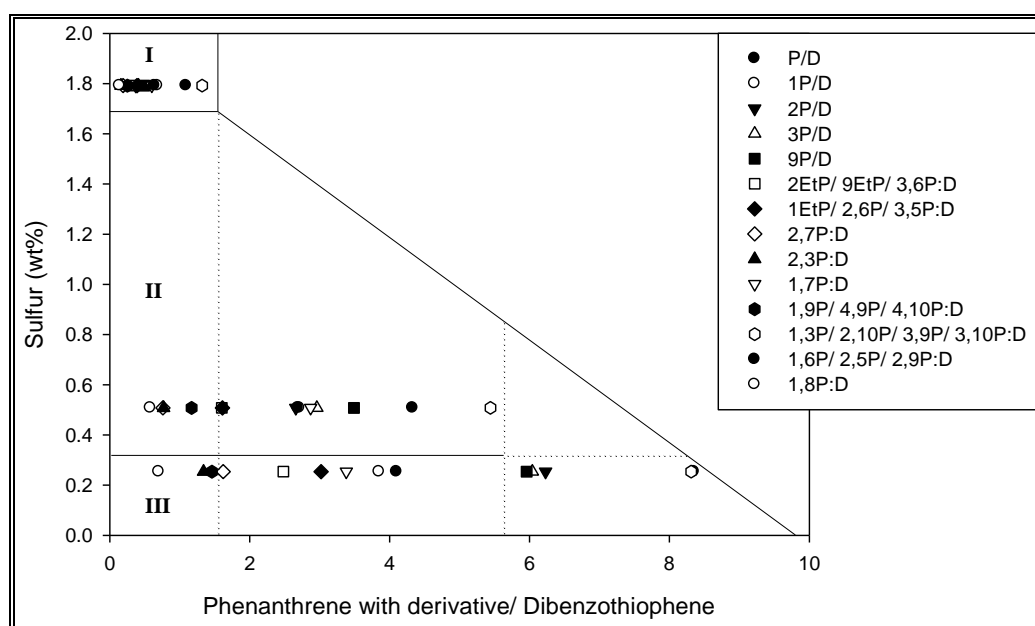


**Figure 3.9** A graph showing the relationship between sulfur content (wt%) to the ratio of phenanthrene and derivatives to dibenzothiophene.

Similar trends were observed when the relationship between sulfur content (wt%) and PHEN/2:3DBT with derivatives ratio were employed (**Figure 3.10**), with the heavy crude oil having low

PHEN/2:3DBT with derivative ratios (0.1-1.1), medium crude oil having moderate PHEN/2:3DBT with derivative ratios (0.6-6.7) and the light crude oil having relatively higher PHEN/2:3DBT with derivative ratios (0.7-8.4). These trends were in agreement with the work of William *et al.*<sup>344</sup> The oils were classified to originate from the marine and non-marine carbonate rocks.

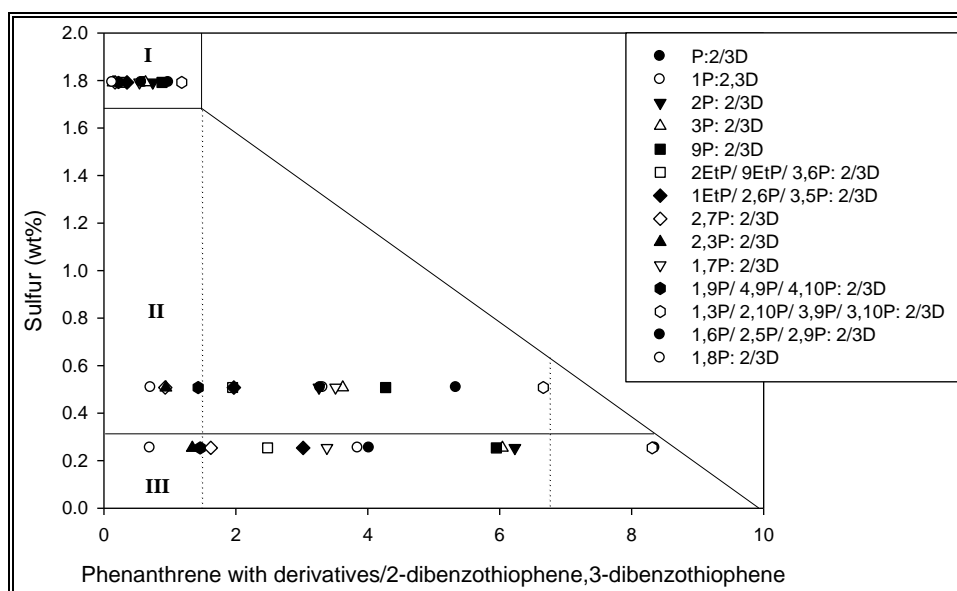


**Figure 3.10** A graph showing the relationship between sulfur content (wt%) to the ratio of phenanthrene with derivatives to 2-methyl-dibenzothiophenes/3-methyl-dibenzothiophene.



### 3.4 Conclusions

- (1) The ratios of vanadium-to-nickel (V/Ni) and phenanthrene/dibenzothiophene (PHEN/DBT) with derivatives have proven informative in the classification and in the identification of the source of the crude oils from Nigeria.
- (2) Similarities in the relationship between the sulfur content (wt%)-to-PHEN/DBT and PHEN-derivatives ratio-to-DBT with derivatives are capable of distinguishing oil based on their geographic origin.
- (3) Based on the ratios of vanadium-to-nickel (V/Ni) and phenanthrene/dibenzothiophene (PHEN/DBT) with derivatives of the oils, the light crude oil can be classified as being originated from marine organic matter due to its low sulfur content, the heavy crude oil originated from the terrestrial organic matter due to the high sulfur content and the medium crude oil was assumed to be formed due to the migration of the composition of petroleum hydrocarbon of the light and heavy crude oil.
- (4) Refractory organosulfur compounds such as dibenzothiophene, 2,3-dimethyldibenzothiophene, 2,6-dimethyldibenzothiophene, C4-benzothiophene, C5-benzothiophene, 1-methyldibenzothiophene, etc, were identified in hydro-treated diesel fuels.

*This page is kept blank*

# Chapter 4

## Oxidovanadium(IV)-catalysed oxidation of refractory organosulfur compounds in fuels

### 4.1 Introduction

The oxidation of organosulfur compounds have been catalysed by various metals, such as V(IV) and (V)<sup>144,133,345-347</sup>, Mo(IV)<sup>348</sup>, Co/Mn<sup>349</sup>, Mn(II)<sup>350</sup> and Ag(I)<sup>351</sup>. Metal centers are either employed as homogeneous catalysts or incorporated into supports such as silica, alumina or Merrifield polymer microspheres,<sup>135, 352-354</sup> and applied as heterogeneous catalysts.<sup>355</sup> Oxidation oxidants such as *tert*-butylhydroperoxide (*t*-BuOOH) has been reported as a suitable organic oxidant for the oxidation of sulfur compounds in a hydrocarbon matrix<sup>78</sup> unlike H<sub>2</sub>O<sub>2</sub> which requires the use of polar co-solvents.<sup>59</sup> The heterogeneous catalysts activities are greatly influenced by the porosity and morphology of catalyst supports.<sup>187</sup>

The focus of this chapter was to;

1. Synthesise a homogeneous tetradentate oxidovanadium(IV) metal complex, [V<sup>IV</sup>O(sal-HBPD)], and also to synthesize of heterogeneous polymer-anchored oxidovanadium(IV) metal complexes, poly[V<sup>IV</sup>O(sal-AHBPD)] and poly[V<sup>IV</sup>O(allylsB-co-EGDMA)].
2. Carry out an oxidation study of thiophene, benzothiophene, dibenzothiophene and 4,6-dimethyldibenzothiophene (model organosulfur compounds) using [V<sup>IV</sup>O(sal-HBPD)] and polymer-anchored oxidovanadium(IV) metal complexes, poly[V<sup>IV</sup>O(sal-AHBPD)] and poly[V<sup>IV</sup>O(allylsB-co-EGDMA)], as catalysts under batch process.
3. Carry out an oxidation study of thiophene, benzothiophene, dibenzothiophene and 4,6-dimethyldibenzothiophene (model organosulfur compounds) using poly[V<sup>IV</sup>O(sal-AHBPD)] and poly[V<sup>IV</sup>O(allylsB-co-EGDMA)], as catalysts under continuous flow process.
4. Apply the optimum oxidation catalyst and reaction process to the oxidation of hydro-treated diesel and crude oils.

Under all catalytic oxidation process, *tert*-butylhydroperoxide (*t*-BuOOH) was employed as oxidant, as partial oxidations with H<sub>2</sub>O<sub>2</sub> were observed as a result of solvent immiscibility. Leaching studies

were carried-out to confirm the stabilization of vanadium(IV) in the polymer-anchored support. Catalyst re-usability studies under batch oxidation process were also carried-out.

## 4.2 Experimental work

Synthesis and development of homogeneous catalyst,  $[V^{IV}O(\text{sal-HBPD})]$ , and polymer-anchored heterogeneous catalysts,  $\text{poly}[V^{IV}O(\text{sal-AHBPD})]$  and  $\text{poly}[V^{IV}O(\text{allylSB-co-EGDMA})]$ , are described below.

### 4.2.1 Synthesis of the homogeneous oxidovanadium(IV) complex, $[V^{IV}O(\text{sal-HBPD})]$

#### 4.2.1.1 Preparation of *N,N*-bis(*o*-hydroxybenzaldehyde)phenylene diamine (sal-HBPD) Schiff base

To a solution of *o*-phenylenediamine (10.81 g, 0.1 mol) dissolved in 100 mL of absolute ethanol, 26.6 mL of salicylaldehyde (0.25 mol) was added and the mixture stirred while heating at 60°C for 30 min. After cooling to room temperature, the yellow precipitate of sal-HBPD was filtered, washed with methanol to remove impurities and then dried in the oven (**Scheme 4.1**). Yield: 94%, mp: 154-157°C (yellow crystals). FT-IR ( $\text{cm}^{-1}$ ): 1609  $\nu(\text{C}=\text{N})$ , 1158  $\nu(\text{C}-\text{O})$ , 3357  $\nu(\text{O}-\text{H})$ .  $^1\text{H}$  NMR ( $\delta$ , ppm in DMSO): 13.10 (s, 2H, OH), 8.92 (s, 2H,  $-\text{HC}=\text{N}-$ ), 7.44 (d, 2H, aromatic), 7.41-7.48 (m,  $J = 8.2$ , 6H, aromatic), and 6.81-6.98 (m,  $J = 7.4$ , 4H, aromatic) see **Figure 4.1**. *Anal.* Calcd (found) for  $\text{C}_{20}\text{H}_{16}\text{N}_2\text{O}_2$  (%): C, 75.93(75.00); H, 5.10(5.78); N, 8.86(8.94).

#### 4.2.1.2 Synthesis of $V^{IV}O(\text{sal-HBPD})$

Unsupported vanadium complex  $[V^{IV}O(\text{sal-HBPD})]$  was synthesized by dissolving  $[VOSO_4]$  (0.16 g, 0.001 mol) into a solution of sal-HBPD Schiff base (1.28 g, 0.004 mol) in 25 mL of methanol. The reaction was allowed to proceed for 6 h at 50°C. The green precipitate formed was filtered and washed with excess methanol and ethanol. The product  $[V^{IV}O(\text{sal-HBPD})]$  was then dried in a desiccator over silica gel. Yield: 93.1%, mp: > 300°C. FT-IR ( $\text{cm}^{-1}$ ): 1627  $\nu(\text{C}=\text{N})$ , 1161  $\nu(\text{C}-\text{O})$ , 990  $\nu(\text{V}=\text{O})$ . *Anal.* Calcd (found) for  $\text{C}_{40}\text{H}_{34}\text{N}_4\text{O}_9\text{V}_2$  (%): C, 58.83(59.19); H, 4.20(3.93); N, 6.86(6.87).

## 4.2.2 Synthesis of heterogeneous Merrified-based oxidovanadium(IV) catalyst, poly[V<sup>IV</sup>O(sal-AHBPD)]

### 4.2.2.1 Nitrosation of *N,N*-bis(*o*-hydroxybenzaldehyde)phenylene diamine (sal-HBPD) Schiff base

Ligand synthesis for Merrified-based support was synthesized by employing the synthetic route reported by Gupta *et al.*<sup>356</sup> with minor modifications. The nitrosation of sal-HBPD Schiff base synthesised under **Section 4.2.1.1**, was carried out by reacting sal-HBPD Schiff base (3.88 g, 0.02 mol) with sodium nitrite (3.40 g, 0.05 mol) in 1 M HCl (40 mL) at a temperature of approximately 0°C for 12 h. *N,N*-Bis(4-nitroso-*o*-hydroxybenzaldehyde)phenylenediamine (sal-NHBPD) produced was filtered and washed thoroughly with hot distilled water to remove reaction impurities (**Scheme 4.1**). Yield: 86.7%, mp: 108-110°C (yellow powder). FT-IR (cm<sup>-1</sup>): 1603 ν(C=N), 1154 ν(C-O), 3357 ν(O-H), 1704 ν(NO). <sup>1</sup>H NMR (δ, ppm in DMSO): 10.40, 9.41 (s, 2H, OH), 8.12 (s, 2H, -HC=N-), 7.44 (d, 2H, aromatic), 7.41-7.48 (m, 6H, aromatic), and 6.81-6.98 (m, *J* = 10.4, 4H, aromatic). *Anal.* Calcd (found) for C<sub>20</sub>H<sub>15</sub>N<sub>4</sub>O<sub>4</sub> (%): C, 64.17(64.22); H, 3.77(4.01); N, 14.97(15.14).

### 4.2.2.2 Reduction of *N,N*-bis(4-nitroso-*o*-hydroxybenzaldehyde)phenylenediamine (sal-NHBPD) Schiff base

The reduction of *N,N*-bis(4-nitroso-*o*-hydroxybenzaldehyde)phenylenediamine (sal-NHBPD) was carried out using nitrosated sal-NHBPD Schiff base (3.74 g, 0.01 mol) in 1 M HCl (30 mL) in presence of metallic iron (2 g) at 60°C for 24 h, this produced *N,N*-bis(4-amino-*o*-hydroxybenzaldehyde)phenylenediamine (sal-AHBPD) Schiff base (**Scheme 4.1**). Yield: 80.2%, mp: 101-105°C (brown powder). FT-IR (cm<sup>-1</sup>): 1610 ν(C=N), 1161 ν(C-O), 3352 ν(O-H). <sup>1</sup>H NMR (δ, ppm in DMSO): 10.20, 9.41 (s, 2H, OH), 8.12 (s, *J* = 8.2, 2H, -HC=N-), 7.52 (d, *J* = 6.1, 2H, aromatic), 7.72-7.31 (m, *J* = 7.7, 8H, aromatic), and 7.11-6.98 (m, *J* = 7.9, 31.7, 4H, aromatic). *Anal.* Calcd (found) for C<sub>20</sub>H<sub>17</sub>N<sub>4</sub>O<sub>2</sub> (%): C, 68.35(68.34); H, 5.24(4.90); N, 16.17(16.32). The FT-IR spectra of sal-HBPD, sal-NHBPD and sal-AHBPD are presented in **Figure 4.1**.

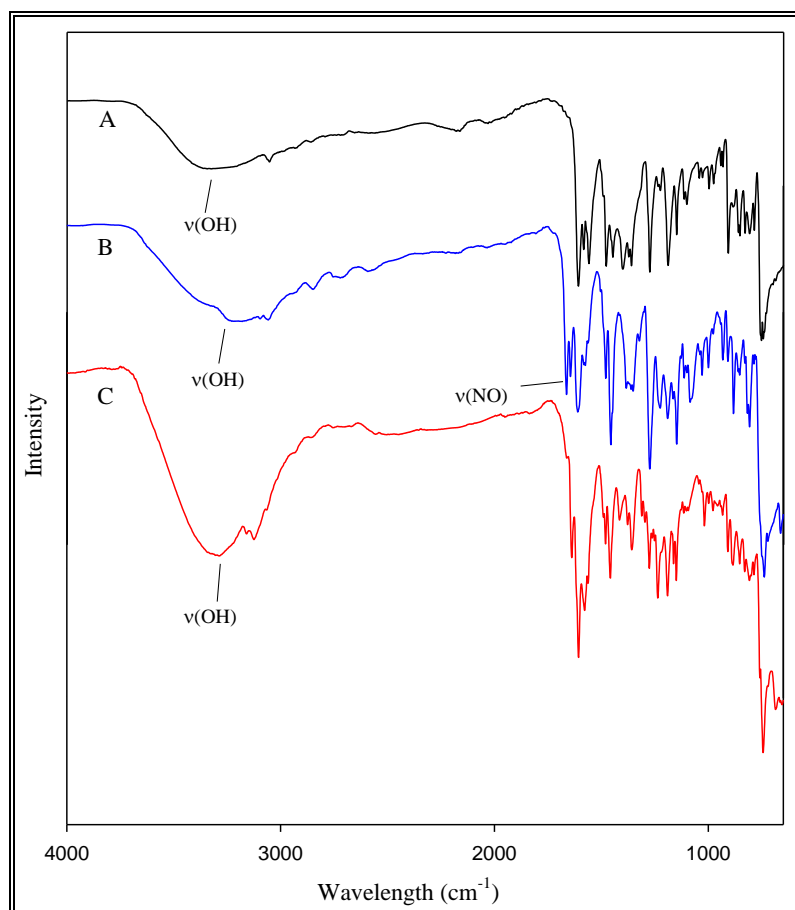
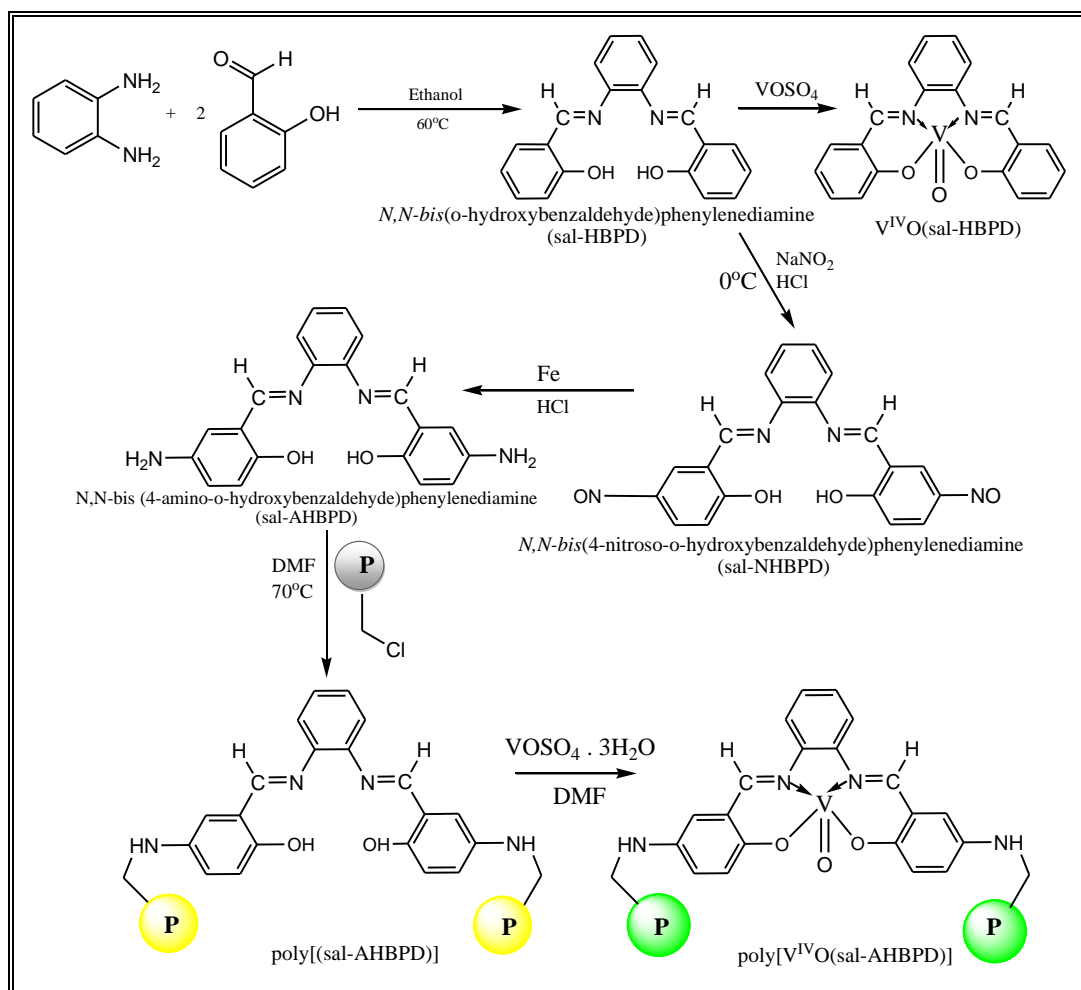


**Figure 4.1** FT-IR spectra of (A) [sal-HBPD], (B) [sal-NHBPD] and (C) [sal-AHBPD].

#### 4.2.2.3 Synthesis of poly[V<sup>IV</sup>O(sal-AHBPD)]

Sal-AHBPD Schiff base (1.2 g) and chloromethylated polystyrene Merrified microspheres (1.5 g) were mixed in *N,N*-dimethylformamide (DMF) and the reaction was heated in an oil bath with stirring under reflux at 70°C for 48 h. The resulting microspheres were filtered and then Soxhlet extracted with methanol for 12 h to remove unreacted ligand and further washed with hot DMF followed by hot methanol. The microspheres were further suspended into a DMF solution containing [VOSO<sub>4</sub>·3H<sub>2</sub>O] (1 g, 0.0061 mol) while stirring at 60°C for 6 h. The resulting microspheres were filtered and washed with methanol for 12 h using Soxhlet extraction to remove excess [VOSO<sub>4</sub>]. A light green colouration was observed indicating the presence of vanadium(IV) on the microspherical microspheres (**Scheme 4.1**). FT-IR (cm<sup>-1</sup>): 1627  $\nu$ (C=N), 1161  $\nu$ (C–O), 990  $\nu$ (V=O). *Anal* found (%): C, 71.22; H, 7.231; N, 4.99; V, 5.64.



**Scheme 4.1** Synthetic scheme for  $\text{V}^{\text{IV}}\text{O}(\text{sal-HBPD})$  and  $\text{poly}[\text{V}^{\text{IV}}\text{O}(\text{sal-AHBPD})]$ .

### 4.2.3 Synthesis of polymer-anchored oxidovanadium(IV) metal complex, $\text{poly}[\text{V}^{\text{IV}}\text{O}(\text{allylSB-co-EGDMA})]$

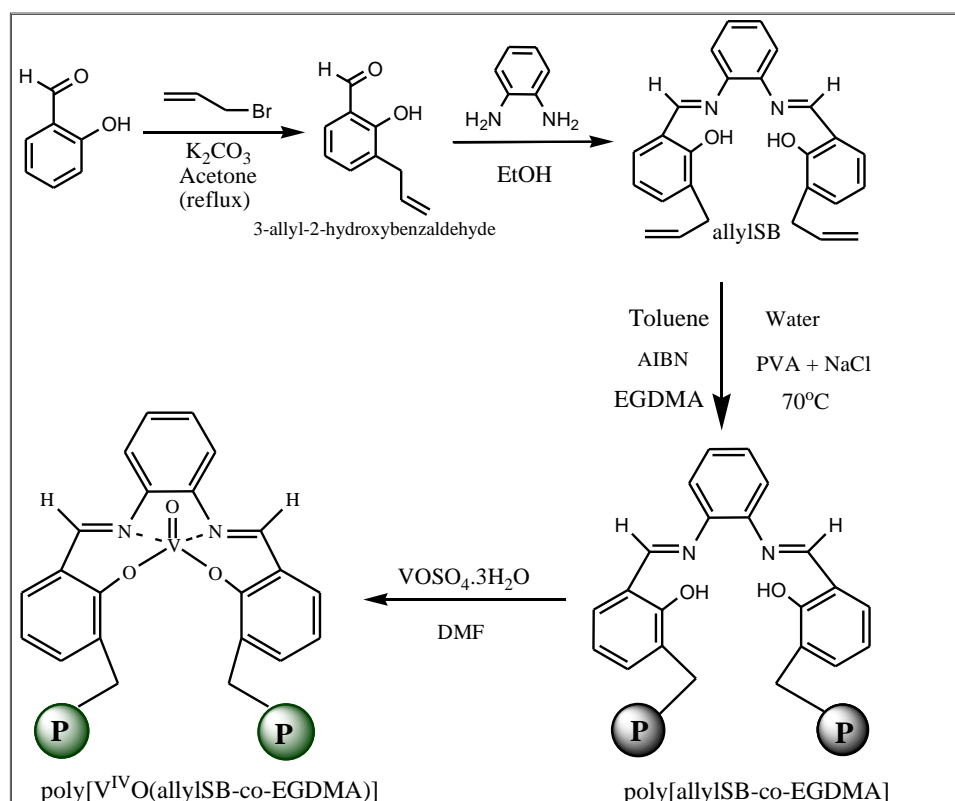
#### 4.2.3.1 Synthesis of 3-Allyl-2-hydroxybenzaldehyde

3-Allyl-2-hydroxybenzaldehyde was prepared according to a reported literature method.<sup>357</sup>  $\text{K}_2\text{CO}_3$  (1.38 g, 0.01 mol) and allylbromide (0.86 mL, 0.01 mol) were added to a solution of salicylaldehyde (0.65 mL, 0.01 mol) in acetone (30 mL), and the mixture was heated under reflux for 6 h. Upon refluxing, Claisen rearrangement takes place,<sup>358</sup> and the intermediate product 2-(allyloxy)benzaldehyde observed by Tobiasz<sup>357</sup> is transferred to the desired product (**Scheme 4.2**). After 6 h, the yellow resultant solution was filtered and distilled under high vacuum to give light yellow oil. Yield: 89%. *Anal. Calcd* (found) for  $\text{C}_{10}\text{H}_{10}\text{O}_2$ (%): C, 74.06(74.09); H, 6.21(6.96).  $^1\text{H}$  NMR ( $\delta$ , ppm in DMSO): 10.42 (s,  $J = 54.5$ , 1H), 7.71 (d,  $J = 7.8$ , 1H), 7.61 (t,  $J = 7.8$ , 1H), 7.18 (d,

1H), 7.06 (t, 1H), 6.09 (m, 1H), 5.46 (d, 1H), 5.30 (d, 1H), 4.71(s, 2H). FT-IR ( $\text{cm}^{-1}$ ): 3430  $\nu(\text{O-H})$ , 1683  $\nu(\text{C=N})$ , 1620  $\nu(\text{C=C})$  (**Figure 4.2**).

#### 4.2.3.2 Synthesis of *N,N*-bis(*o*-hydroxybenzaldehyde)phenylenediamine monomer (allylSB)

3-allyl-2-hydroxybenzaldehyde (1.0 g, 0.0062 mol) and *o*-phenylenediamine (0.33 g, 0.0081 mol) were dissolved in 20 mL of absolute ethanol. The mixture was heated with stirring at 50°C for 3 h. After cooling to 0°C overnight, formation of yellowish needle-like crystals of *N,N*-bis(*o*-hydroxybenzaldehyde)phenylenediamine monomer (allylSB) was observed (**Scheme 4.2**), and the needles were collected by filtration and dried in the fumehood. Yield: 68%, mp: 151-153°C. *Anal.* Calcd (found) for  $\text{C}_{26}\text{H}_{24}\text{N}_2\text{O}_2$  (%): C, 78.76(78.78); H, 6.10(5.90); N, 7.07(7.43).  $^1\text{H}$  NMR ( $\delta$ , ppm in DMSO): 12.99 (s, 1H), 8.95 (s, 1H), 7.68 (d,  $J = 7.6$ , 1H), 7.44 (m,  $J = 1.5$ , 2H), 7.19 (d, 1H), 6.98 (t, 1H), 5.98 – 5.85 (m, 1H), 5.20 (s, 1H), 4.60 (s, 1H), 4.18 (d,  $J = 5.3$ , 2H). FT-IR ( $\text{cm}^{-1}$ ): 3320  $\nu(\text{O-H})$ , 1663  $\nu(\text{C=N})$ , 1632  $\nu(\text{C=C})$ , 1158  $\nu(\text{C-O})$  (**Figure 4.2**).



**Scheme 4.2** Synthetic scheme for [allylSB] ligand and poly[V<sup>IV</sup>O(allylSB-co-EGDMA)] microspheres.



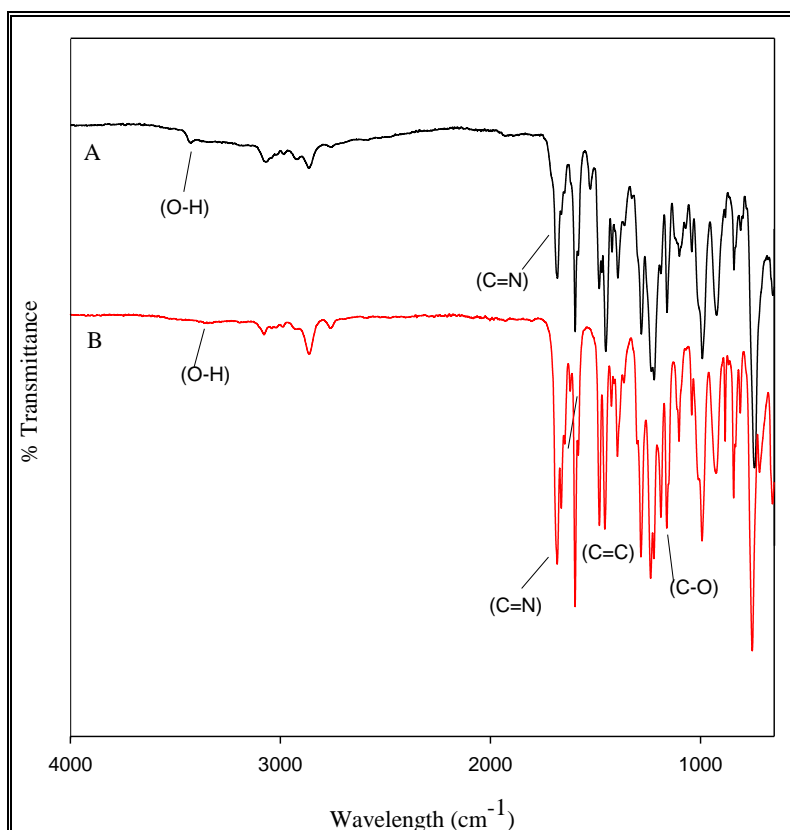


**Figure 4.2** FT-IR spectrum of (A) 3-allyl-2-hydroxybenzaldehyde and (B) *N,N'*-bis(*o*-hydroxybenzaldehyde)phenylenediamine monomer (allylsB).

#### 4.2.3.3 Preparation of poly[allylsB-co-EGDMA] microspheres by suspension polymerization

The functional monomer *N,N'*-bis(*o*-hydroxybenzaldehyde)phenylenediamine (4 g, 0.01 mol), crosslinker ethyleneglycol dimethacrylate (EGDMA) (2 mL, 0.0075 mol) and azobis(isobutyronitrile) (AIBN) (0.2 g, 0.001 mmol) were stirred in 5 mL of toluene. In a separate 250 mL round bottom flask an aqueous solution containing polyvinylalcohol (PVA) (0.025 g) and NaCl (0.07 g) in 100 mL of water was stirred at 280 rpm. The solution was warmed up to 70°C to allow the dissolution of PVA and NaCl. The organic solution was added dropwise to the aqueous solution under constant stirring, and the reaction was allowed to proceed for 24 h under an argon atmosphere (**Scheme 4.2**). The mixture was cooled to room temperature and the resultant microspheres were collected by filtration, washed with hot DMF and methanol and then dried at 50°C overnight. The microspheres were then sieved with a mesh sieve of diameter  $\leq 300 \mu\text{m}$  to attain the required microspheres diameter. *Anal. found* (%): C, 56.66; H, 7.47; N, 5.29. FT-IR ( $\text{cm}^{-1}$ ): 3410  $\nu(\text{O-H})$ , 1722  $\nu(\text{C=O})$ , 1645  $\nu(\text{C=N})$ .

#### 4.2.3.4 Synthesis of poly[V<sup>IV</sup>O(allylsB-co-EGDMA)] microspheres

Poly[allylsB-co-EGDMA] microspheres (2 g) were swollen in 30 mL of DMF for 2 h. To this was added VOSO<sub>4</sub>·3H<sub>2</sub>O, (1 g, 4.6 mmol) in DMF (**Scheme 4.2**). The mixture was heated to 60°C and stirred overnight. The resultant blue-green microspheres were filtered and washed several times with DMF and MeOH, and then dried at 50°C overnight. *Anal.* found (%): C, 48.44; H, 6.99; N, 4.20; V, 2.83. FT-IR (cm<sup>-1</sup>): 1723 ν(C=O), 1659 ν(C=N), 957 ν(V=O), 419 ν(V-O), 351 ν(V-N).

### 4.3 Catalyst characterization and spectroscopic studies

#### 4.3.1 Single crystals X-ray analysis of V<sup>IV</sup>O(sal-HBPD)

Single crystals of [V<sup>IV</sup>O(sal-HBPD)] suitable for X-ray analysis were grown by slow evaporation of the complex in a acetone–methanol (1:1) mixture. Intensity data were collected on a Bruker APEX II CCD area detector diffractometer with graphite monochromated Mo K<sub>α</sub> radiation (50 kV, 30 mA) using the APEX 2 data collection software.<sup>359a</sup> The collection method involved ω-scans of width 0.5° and 512x512 bit data frames. Data reduction was carried out using the program SAINT+<sup>359b</sup> and face indexed absorption corrections were made using XPREP.<sup>359b</sup> The crystal structure was solved by direct methods using SHELXTL.<sup>360</sup> Non-hydrogen atoms were first refined isotropically followed by anisotropic refinement by full matrix least-squares calculations based on F<sup>2</sup> using SHELXTL. Hydrogen atoms were first located in the difference map then positioned geometrically and allowed to ride on their respective parent atoms. Diagrams and publication material were generated using SHELXTL and PLATON.<sup>361</sup> Crystal data, data collection and structural refinement parameters for the complex are presented in **Tables 4.1**.

Selected bond lengths and bond angles are given in **Tables 4.2**. There are two crystallographically independent molecules in the asymmetric unit of the compound (**Figure 4.3**). The structure of the compound showed a square pyramidal geometry with the vanadium atom lying ~0.59 Å above the N<sub>2</sub>O<sub>2</sub> plane in each molecule. The N(1)N(2)O(1)O(2) and N(3)N(4)O(4)O(5) planes from the two molecules bisect each other at an angle of 43.35°. The geometric parameter (τ) was found to be 0.31 thereby confirming a slightly distorted square pyramidal geometry.<sup>362, 363</sup> This slight distortion was evidenced by the following bond angles: for the first molecule; O(1)-V(1)-O(2) = 85.74(7)°, O(1)-

$V(1)-N(1) = 87.55(7)^\circ$ ,  $O(2)-V(1)-N(2) = 87.77(7)^\circ$ ,  $O(2)-V(1)-N(1) = 77.83(8)^\circ$ ,  $O(1)-V(1)-N(2) = 145.13(8)^\circ$  and  $O(2)-V(1)-N(1) = 143.80(8)^\circ$ . For the second molecule;  $O(5)-V(2)-O(4) = 85.61(7)^\circ$ ,  $O(4)-V(2)-N(3) = 88.21(8)^\circ$ ,  $O(5)-V(2)-N(4) = 88.03(7)^\circ$ ,  $N(3)-V(2)-N(4) = 78.41(7)^\circ$ ,  $O(4)-V(2)-N(2) = 146.99(8)^\circ$  and  $O(5)-V(2)-N(3) = 144.4(8)^\circ$ . The V-N and V-O bond lengths are:  $V(1)-N(1)$ ,  $2.0707(2) \text{ \AA}$ ,  $V(1)-N(2) = 2.0642(2) \text{ \AA}$ ,  $V(1)-O(1) = 1.9198(2) \text{ \AA}$  and  $V(1)-O(2) = 1.9249(2) \text{ \AA}$  (first molecule);  $V(2)-N(3) = 2.0423(2) \text{ \AA}$ ,  $V(2)-N(4) = 2.0601(1) \text{ \AA}$ ,  $V(2)-O(4) = 1.9209(1) \text{ \AA}$  and  $V(2)-O(5) = 1.9197(1) \text{ \AA}$  (second molecule). This implies slightly stronger V-O bonds compared to V-N bonds, which could be expected for the interaction of vanadyl with a phenolate group.

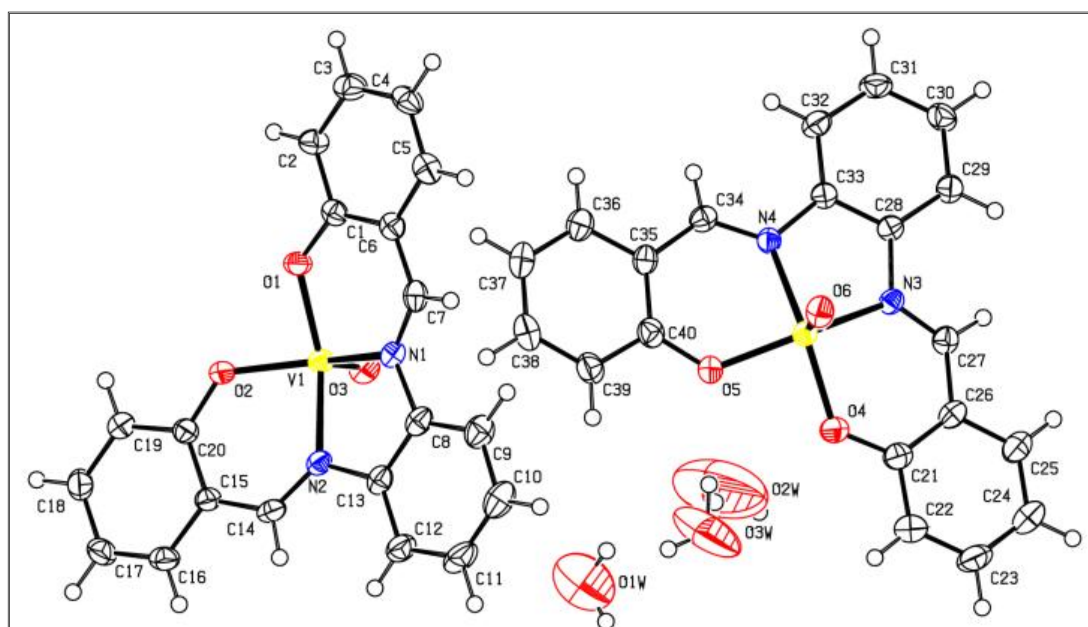


**Figure 4.3** An ORTEP view of  $[V^{IV}O(\text{sal-HBPD})]$  Schiff base complex with ellipsoids drawn at 50% probability level, CCDC 872749.

**Table 4.1** Summary of crystal data, data collection and structural refinement parameters for the complex

Parameters	[V <sup>IV</sup> O(sal-HBPD)]
Empirical formula	C <sub>40</sub> H <sub>34</sub> N <sub>4</sub> O <sub>9</sub> V <sub>2</sub>
Formula weight (M)	816.59
Temperature, <i>T</i> (K)	173(2) K
Wavelength, Mo K $\alpha$ (Å)	0.71073
Crystal system	Monoclinic
Space group	<i>P</i> 2(1)/ <i>c</i>
<i>a</i> (Å)	19.8921(5)
<i>b</i> (Å)	6.8805(2)
<i>c</i> (Å)	27.6507(7)
$\alpha$ (°)	90.00
$\beta$ (°)	108.493(2)
$\gamma$ (°)	90.00
Volume, <i>V</i> (Å <sup>3</sup> )	3589.06(17)
<i>Z</i>	4
Calculated density, $\rho$ (Mg m <sup>-3</sup> )	1.511
Absorption coefficient, $\mu$ (mm <sup>-1</sup> )	0.585
F(000)	1680
Index ranges	-26 ≤ <i>h</i> ≤ 26, -9 ≤ <i>k</i> ≤ 9, -36 ≤ <i>l</i> ≤ 35
Reflections collected	33940
Independent reflections	8648 [ <i>R</i> <sub>(int)</sub> = 0.0734]
Completeness to Theta= 28.00°	99.9 %
Max. and min. transmission	0.9657 and 0.8394
Data/restraints/parameters	8648/0/496
Goodness-of-fit on <i>F</i> <sup>2</sup>	0.914
Final <i>R</i> indices [ <i>I</i> > 2 $\sigma$ ( <i>I</i> )]	<i>R</i> <sub>1</sub> = 0.0438, <i>wR</i> <sub>2</sub> = 0.0871
<i>R</i> indices (all data)	<i>R</i> <sub>1</sub> = 0.0870, <i>wR</i> <sub>2</sub> = 0.0993
Largest diff. peak and hole (eÅ <sup>-3</sup> )	0.552 and -0.355 e.Å <sup>-3</sup>

**Table 4.2** Selected bond length (Å) and bond angles (°) for [V<sup>IV</sup>O(sal-HBPD)]

Bond lengths	(Å)	Bond angles	(°)
C(1)-O(1)	1.325(3)	O(2)-V(1)-N(1)	143.80(8)
C(20)-O(2)	1.323(3)	O(1)-V(1)-N(2)	145.13(8)
V(1)-O(1)	1.9198(2)	C(7)-N(1)-V(1)	125.97(1)
V(1)-O(2)	1.9249(2)	C(8)-N(1)-V(1)	125.58(1)
V(1)-O(3)	1.5887(2)	O(3)-V(1)-N(2)	104.31(8)
V(1)-N(1)	2.0707(2)	O(3)-V(1)-N(1)	107.98(8)
V(1)-N(2)	2.0652(2)	N(2)-V(1)-N(1)	143.80(8)
C(7)-N(1)	1.301(3)	O(2)-V(1)-N(1)	77.83(8)
C(8)-N(1)	1.423(3)	O(1)-V(1)-O(2)	85.74(7)
C(13)-N(2)	1.436(3)	O(2)-V(1)-N(2)	87.77(7)
C(14)-N(2)	1.303(3)	O(1)-V(1)-N(1)	87.55(7)
C(40)-O(5)	1.328(3)	O(4)-V(2)-N(2)	146.99(8)
C(21)-O(4)	1.327(3)	O(5)-V(2)-N(3)	144.4(8)
V(2)-O(4)	1.9209(2)	C(34)-N(4)-V(2)	113.70(1)
V(2)-O(5)	1.9197(2)	C(33)-N(4)-V(2)	130.18(2)
V(2)-O(6)	1.5939(2)	O(6)-V(2)-N(3)	106.36(8)
V(2)-N(3)	2.0423(2)	O(5)-V(2)-N(3)	144.40(8)
V(2)-N(4)	2.0601(2)	O(4)-V(2)-N(4)	146.99(8)
C(27)-N(3)	1.295(3)	O(5)-V(2)-O(4)	85.61(7)
C(28)-N(3)	1.426(3)	O(4)-V(2)-N(3)	88.21(8)
C(33)-N(4)	1.425(3)	O(5)-V(2)-N(4)	88.03(7)
C(34)-N(4)	1.309(3)	N(3)-V(2)-N(4)	78.41(7)

#### 4.3.2 Scanning electron micrograph (SEM) images of poly[(sal-AHBPD)], poly[V<sup>IV</sup>O(sal-AHBPD)], poly[allylsB-co-EGDMA] and poly[V<sup>IV</sup>O(allylsB-co-EGDMA)]

The scanning electron micrographs (SEM) of Merrified microspheres (5% crosslinked), ligand-anchored microspheres and poly[V<sup>IV</sup>O(sal-AHBPD)] are presented in **Figure 4.4**. Significant changes in average microspheres diameter from 178-254 μm to 286-308 μm was observed after functionalization of the microspheres with the ligand and oxidovanadium(IV).

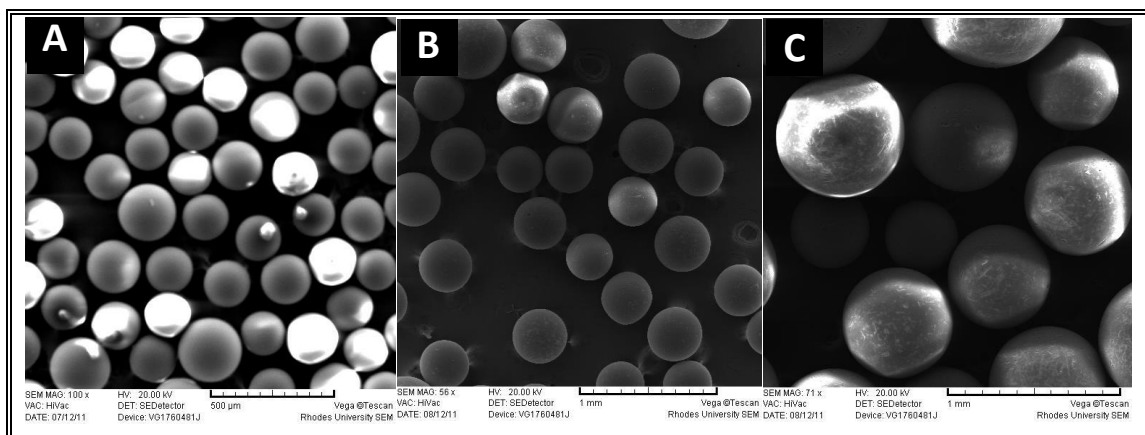


**Figure 4.4** Scanning electron microscopy (SEM) micrograph of microspheres (A) chloromethylated polystyrene microspheres, (B) ligand-anchored microspheres and (C) vanadium incorporated microspheres poly[V<sup>IV</sup>O(sal-AHBPD)].

Poly[allylSB-co-EGDMA] and poly[V<sup>IV</sup>O(allylSB-co-EGDMA)] images are presented in **Figure 4.5**. From the images, spherical microspheres were successfully synthesised *via* suspension polymerization. A diameter range of 252-272 µm and 262-306 µm for poly[allylSB-co-EGDMA] and poly[V<sup>IV</sup>O(allylSB-co-EGDMA)] respectively was observed. In both SEM images (**Figure 4.3** and **4.4**), the morphology of the microspheres were preserved after functionalization with VOSO<sub>4</sub>.

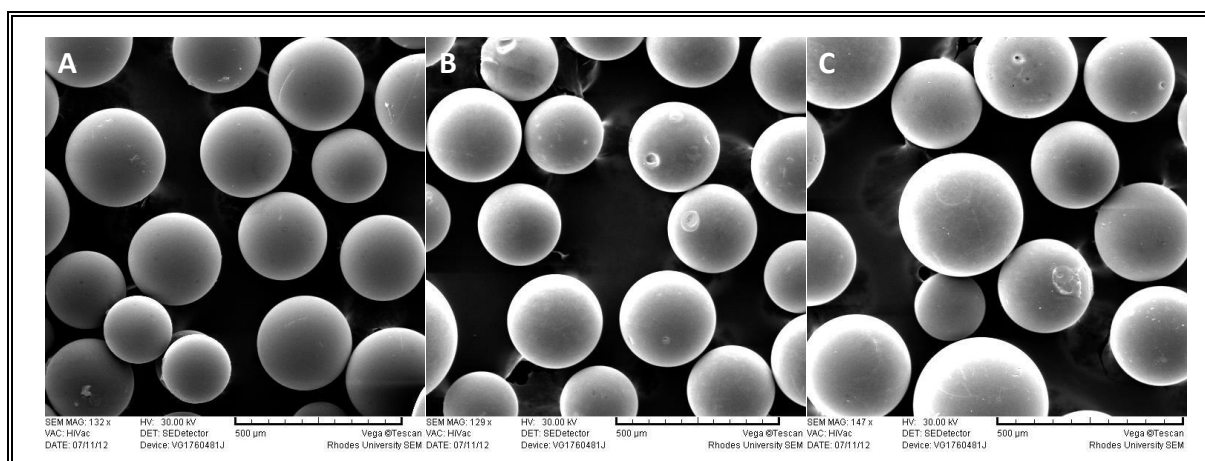


**Figure 4.5** Scanning electron micrographs of (A) poly[allylSB-co-EGDMA], (B) poly[V<sup>IV</sup>O(allylSB-co-EGDMA)] and (C) poly[V<sup>IV</sup>O(allylSB-co-EGDMA)] after use.

### 4.3.3 Surface area measurements of poly[(sal-AHBPD)], poly[V<sup>IV</sup>O(sal-AHBPD)], poly[allylsB-co-EGDMA] and poly[V<sup>IV</sup>O(allylsB-co-EGDMA)]

The BET surface area and porosity of Merrifield microspheres were found to be  $10 \text{ m}^2 \cdot \text{g}^{-1}$ , while its pore size was  $197 \text{ \AA}$  (**Figure 4.6**). Upon functionalization to poly[V<sup>IV</sup>O(sal-AHBPD)], the surface area and porosity reduced to  $7 \text{ m}^2 \cdot \text{g}^{-1}$  and  $181 \text{ \AA}$  respectively (**Figure 4.6**). The drop in surface area and porosity can be attributed to the ligand and vanadium(IV) occupying the pores thereby reducing the surface area and porosity.

The surface area and porosity of poly[allylsB-co-EGDMA] were found to be  $27 \text{ m}^2 \cdot \text{g}^{-1}$  and  $194 \text{ \AA}$  respectively (see isotherm **Figure 4.6**). On anchoring vanadium(IV) to poly[allylsB-co-EGDMA] to form poly[V<sup>IV</sup>O(allylsB-co-EGDMA)], the surface area and porosity decreased to  $23 \text{ m}^2 \cdot \text{g}^{-1}$  and  $135 \text{ \AA}$  (**Figure 4.6**), respectively. The drop in surface area and porosity was attributed to vanadium(IV) occupying the pores. After use, a further fall in the surface area of poly[V<sup>IV</sup>O(allylsB-co-EGDMA)] to  $9 \text{ m}^2 \cdot \text{g}^{-1}$  was observed, while the porosity of the microspheres increased to  $214 \text{ \AA}$ . poly[V<sup>IV</sup>O(sal-AHBPD)] also recorded a reduced surface area and porosity of  $3 \text{ m}^2 \cdot \text{g}^{-1}$  and  $203 \text{ \AA}$  respectively after use. The increase in porosity may be linked to a number of factors amongst which are the collisions experienced between the microspheres which could result to pore size modification.<sup>128,129</sup> From the two polymer-supported catalysts, poly[V<sup>IV</sup>O(sal-AHBPD)] and poly[V<sup>IV</sup>O(allylsB-co-EGDMA)], it can be noted that the latter had the highest surface area.

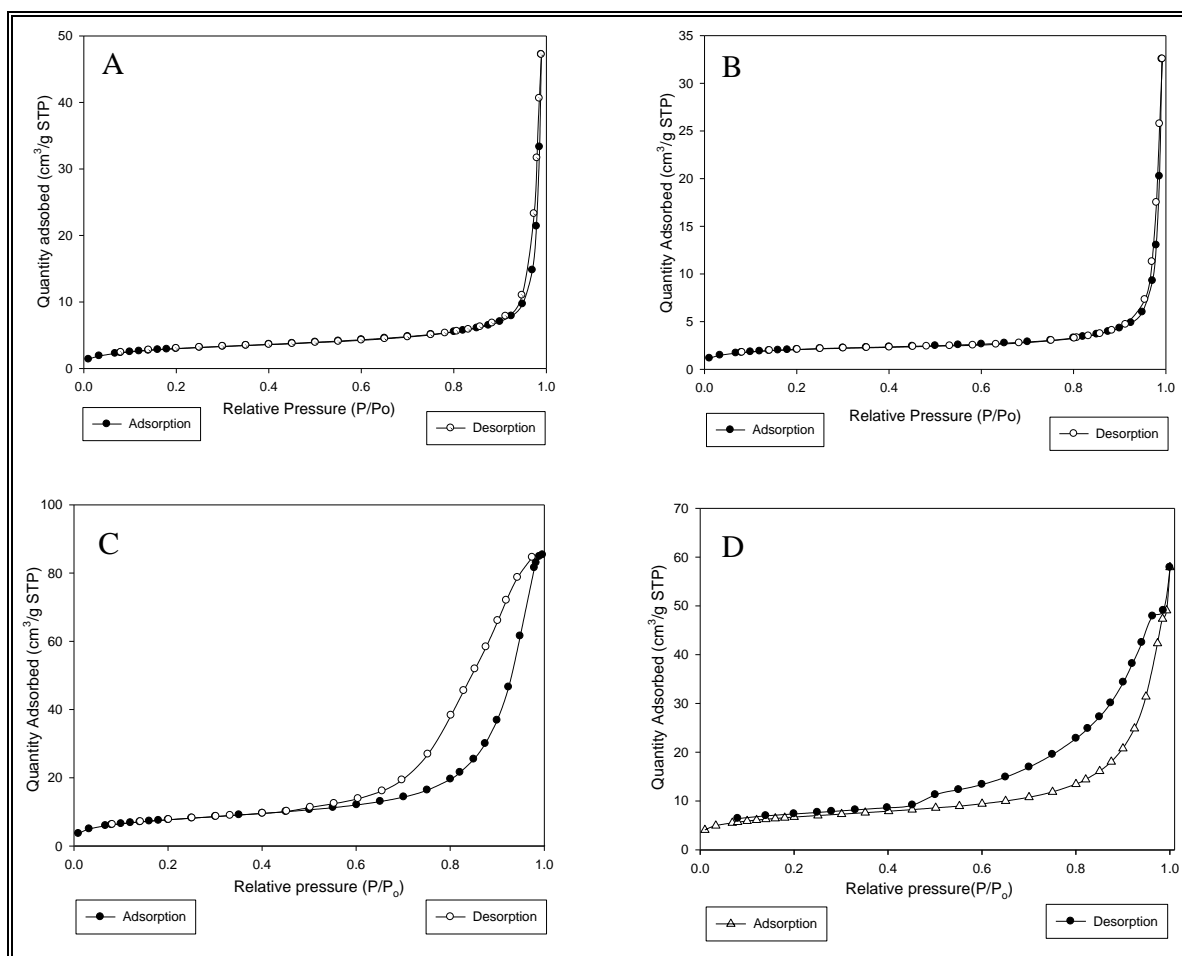


**Figure 4.6** Nitrogen adsorption-desorption isotherms for (A) poly[sal-AHBPD], (B) poly[V<sup>IV</sup>O(sal-AHBPD)], (C) poly[allylsB-co-EGDMA] and (D) poly[V<sup>IV</sup>O(allylsB-co-EGDMA)].

#### 4.3.4 Atomic force microscopy (AFM) of poly[(sal-AHBPD)], poly[V<sup>IV</sup>O(sal-AHBPD)], poly[allylsB-co-EGDMA] and poly[V<sup>IV</sup>O(allylsB-co-EGDMA)]

The surface roughness and mean height for poly[(sal-AHBPD)] were observed to be 4.18 Ra.nm<sup>-1</sup> and 21.31 nm respectively. On reacting poly[(sal-AHBPD)] with vanadyl sulfate [VOSO<sub>4</sub>] to form poly[V<sup>IV</sup>O(sal-AHBPD)], the surface roughness and mean height decreased to 1.29 Ra.nm<sup>-1</sup> and 8.63 nm respectively. This showed that V(IV) has been locked within the ligands in the microspheres pores thereby reducing its porosity, this phenomenon was also confirmed by the BET surface measurement. Surface roughness and morphology of poly[(sal-AHBPD)], poly[V<sup>IV</sup>O(sal-AHBPD)] and poly[V<sup>IV</sup>O(sal-AHBPD)] after use are presented in **Figure 4.7**. However, after one cycle of the



oxidation studies the surface roughness and mean height of poly[V<sup>IV</sup>O(sal-HBPD)] increased to 20.57 Ra.nm<sup>-1</sup> and 58.66 nm respectively. This signifies that some changes in the surface morphology of the microspheres occurred at the different stages.

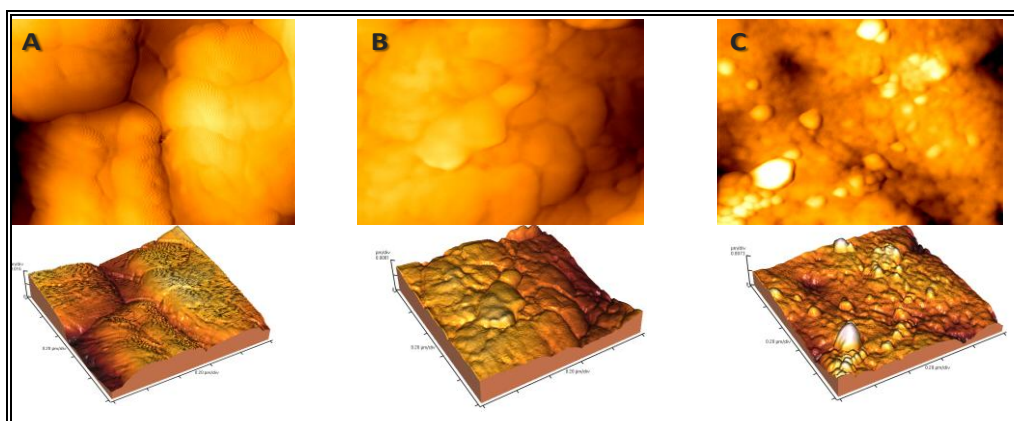


**Figure 4.7** AFM images of (A) poly[sal-AHBPD], (B) poly[V<sup>IV</sup>O(sal-AHBPD)] before use and (C) poly[V<sup>IV</sup>O(sal-AHBPD)] after use. Scale:2x2  $\mu$ M.

The surface roughness and mean height for poly[allylsB-co-EGDMA] microspheres were observed to be 12 Ra.nm<sup>-1</sup> and 38 nm respectively, signifying that the synthesized microspheres were more porous than poly[sal-AHBPD]. Upon reacting poly[allylsB-co-EGDMA] with vanadyl sulfate [VOSO<sub>4</sub>] to form poly[V<sup>IV</sup>O(allylsB-co-EGDMA)] the surface roughness and mean height decreased to 3 Ra.nm<sup>-1</sup> and 19 nm respectively. The reduction of the surface roughness could be attributed to vanadyl anchored to the ligand within the pores. This observation was in agreement with the BET result. However, after one cycle of the oxidation studies the surface roughness of poly[VO(allylsB-co-EGDMA)] microspheres (Fig. 4c) increased slightly to 4 Ra.nm<sup>-1</sup> while the mean height (18 nm) remained similar to that of poly[V<sup>IV</sup>O(allylsB-co-EGDMA)] before use, signifying that the surface morphology was preserved. Poly[allylsB-co-EGDMA], poly[V<sup>IV</sup>O(allylsB-co-EGDMA)] and poly[V<sup>IV</sup>O(allylsB-co-EGDMA)] after use are depicted in **Figure 4.8**.

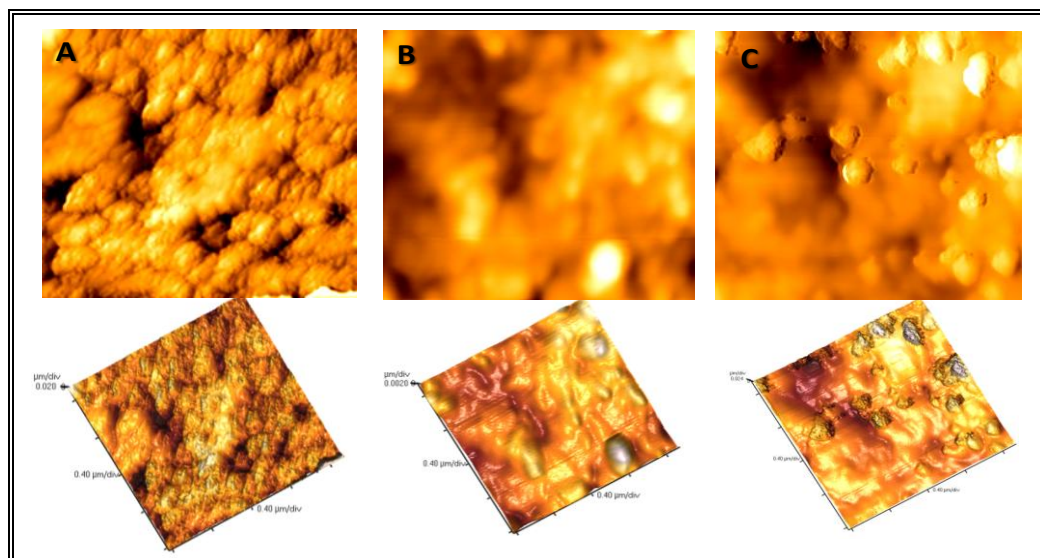


**Figure 4.8** AFM images of (A) poly[allylSB-co-EGDMA], (B) poly[V<sup>IV</sup>O(allylSB-co-EGDMA)] and (C) poly[V<sup>IV</sup>O(allylSB-co-EGDMA)] after use. Scale: 2x2 μM.

#### 4.3.5 X-ray photoelectron spectroscopy (XPS) of poly[(sal-AHBPD)], poly[V<sup>IV</sup>O(sal-AHBPD)], poly[allylSB-co-EGDMA] and poly[V<sup>IV</sup>O(allylSB-co-EGDMA)]

XPS was employed to investigate the surface chemistry (expected elements) of the polymer-supported catalyst. The XPS spectra of poly[(sal-AHBPD)] and poly[V<sup>IV</sup>O(sal-AHBPD)] complimented the microanalysis results, showing all the expected atoms. On functionalizing poly[(sal-AHBPD)] with [VOSO<sub>4</sub>], the O 1s peak intensity increased significantly, due to the V=O as well as possibly the presence of some residual solvent (methanol and ethanol).

The V 2p peaks although low in intensity were present at 522.1 eV (V 2p<sub>1/2</sub>) and 514.5 eV (V 2p<sub>3/2</sub>) (**Figure 4.9**), confirming the +4 oxidation state of vanadium. There were two N 1s peaks for poly[(sal-AHBPD)], appearing at 398 and 396 eV (**Figure 4.9**) corresponding to the C=N (imine) and -NH nitrogen. Wide scan XPS spectra of poly[(sal-AHBPD)], poly[V<sup>IV</sup>O(sal-AHBPD)] and poly[V<sup>IV</sup>O(sal-AHBPD)] after use are presented in **Figure 4.10**. The summary of the peaks are presented in **Table 4.3**.

**Table 4.3** Elemental binding energies of poly[(sal-AHBPD)] and poly[V<sup>IV</sup>O(sal-AHBPD)] as determined by XPS.

Polymer	Binding Energy (eV)				
	O 1s	N 1s	C 1s	V 2p <sub>3/2</sub>	V 2p <sub>1/2</sub>
poly[(sal-AHBPD)]	531.2	398.2	283.0	-	-
poly[V <sup>IV</sup> O(sal-AHBPD)]	531.4	398.0	283.2	514.5	522.1
poly[V <sup>IV</sup> O(sal-AHBPD)] used	531.3	399.0	283.0	515.0	522.1

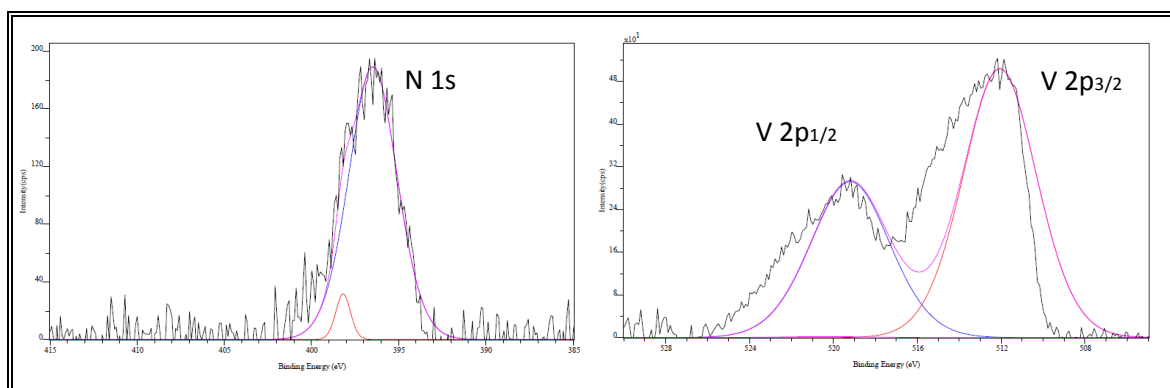


**Figure 4.9** Expanded scan for deconvolution of V 2p and N 1s signals for poly[V<sup>IV</sup>O(sal-AHBPD)].

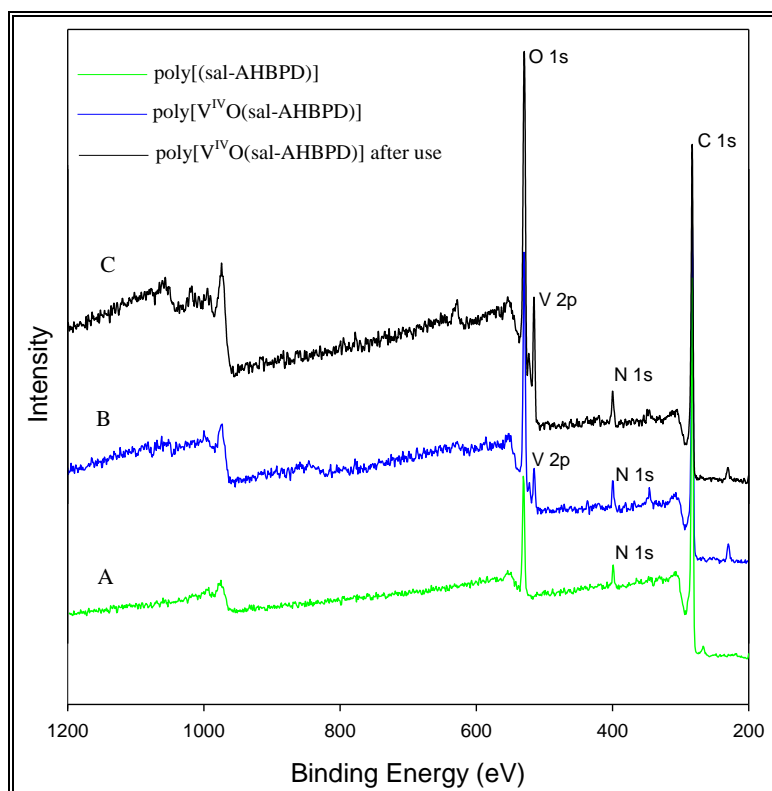


**Figure 4.10** High resolution wide scan XPS spectra of (A) poly[(sal-AHBPD)], (B) poly[V<sup>IV</sup>O(sal-AHBPD)] and (C) poly[V<sup>IV</sup>O(sal-AHBPD)] used.

Carbon (C 1s), hydrogen (H 1s), oxygen (O 1s) and nitrogen (N 1s) peaks were also detected for poly[allylsB-co-EGDMA] and upon anchoring VOSO<sub>4</sub> onto poly[allylsB-co-EGDMA], to form poly[V<sup>IV</sup>O(allylsB-co-EGDMA)], V 2p peaks appeared. The N 1s for poly[V<sup>IV</sup>O(allylsB-co-EGDMA)] gave a signal peak appearing at 398.5 corresponding to the C=N (imine) groups on the microspheres. The expanded V 2p peaks were observed at 520.0 eV (V 2p<sub>1/2</sub>) and 515.5 eV (V 2p<sub>3/2</sub>) on the initial and used microspheres confirming vanadium(IV) (**Figure 4.11, Table 4.4**). Wide scan XPS spectra of poly[allylsB-co-EGDMA], poly[V<sup>IV</sup>O(allylsB-co-EGDMA)] and poly[V<sup>IV</sup>O(allylsB-co-EGDMA)] after use is presented in **Figure 4.12**. It was noticed that both catalysts, poly[V<sup>IV</sup>O(sal-AHBPD)] and poly[V<sup>IV</sup>O(allylsB-co-EGDMA)], retained their functionalities after they have been used for three oxidation cycles due to availability of vanadium(IV) on the polymer support.

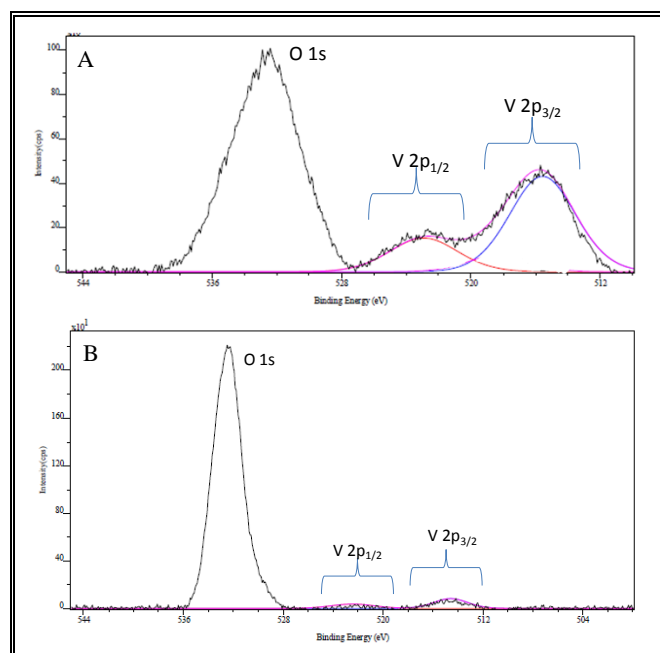


**Figure 4.11** Expanded scan for deconvolution of poly[V<sup>IV</sup>O(allylSB-co-EGDMA)], (A) V 2p before use and (B) V 2p after use.

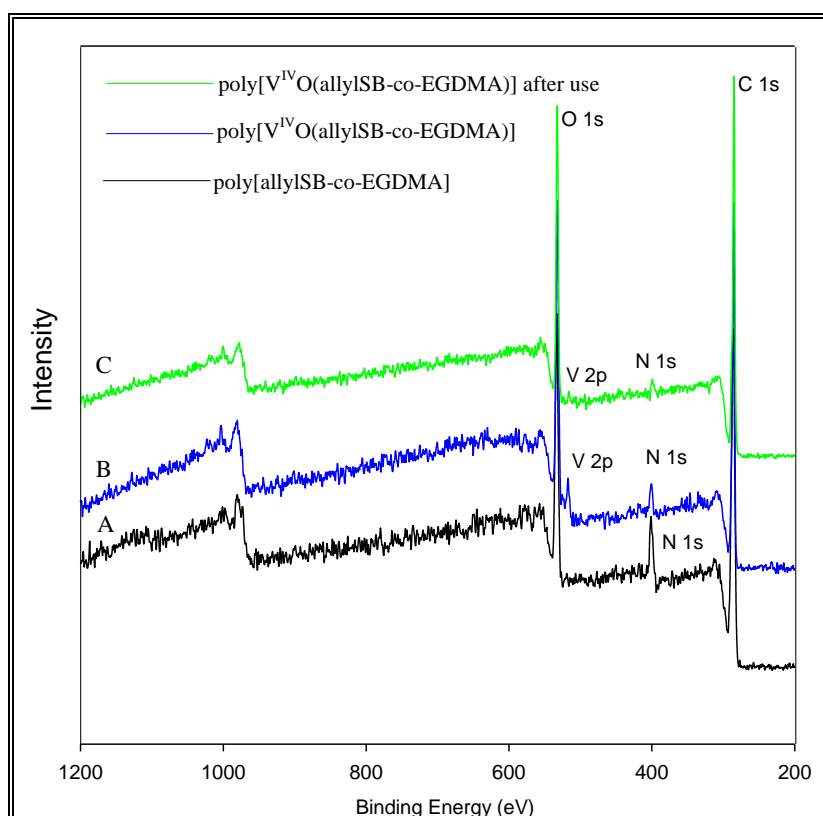


**Figure 4.12** High resolution wide scan XPS spectra of (A) poly[allylSB-co-EGDMA], (B) poly[V<sup>IV</sup>O(allylSB-co-EGDMA)] and (C) poly[V<sup>IV</sup>O(allylSB-co-EGDMA)] after use.

**Table 4.4** Elemental binding energies of poly[allylsB-co-EGDMA], poly[V<sup>IV</sup>O(allylsB-co-EGDMA)] and poly[V<sup>IV</sup>O(allylsB-co-EGDMA)] after use as determined by XPS.

MICROSPHERES	Binding Energy (eV)				
	O 1s	N 1s	C 1s	V 2p <sub>3/2</sub>	V 2p <sub>1/2</sub>
poly[allylsB-co-EGDMA]	531.7	398.5	285.2	-	-
poly[V <sup>IV</sup> O(allylsB-co-EGDMA)]	532.0	398.5	285.3	515.5	520.0
poly[V <sup>IV</sup> O(allylsB-co-EGDMA)] after use	531.9	398.5	285.3	515.4	521.1

#### 4.3.6 Thermogravimetric analysis of [V<sup>IV</sup>O(sal-HBPD)], poly[(sal-AHBPD)], poly[V<sup>IV</sup>O(sal-AHBPD)], poly[allylsB-co-EGDMA] and poly[V<sup>IV</sup>O(allylsB-co-EGDMA)]

The thermal analysis profiles of the metal complex, [V<sup>IV</sup>O(sal-HBPD)], alongside polymer-supported catalysts, poly[V<sup>IV</sup>O(sal-AHBPD)] and poly[V<sup>IV</sup>O(allylsB-co-EGDMA)], are fully discussed in this section. For the TG thermogram of V<sup>IV</sup>O(sal-HBPD), a step wise decomposition of the structure was observed. Initial weight loss of about 4.6% occurred over the temperature range of 130-340°C due to the loss of hydrated water molecules. After which an overall stepwise decomposition of 75.3% of the complex was observed between 340-530°C. Vanadium oxide residue was produced afterward (**Figure 4.13**).

The thermogram of poly[sal-AHBPD] showed three degradation steps; which are loss of trapped solvents and intra-particle water in the range 100-350°C to a total of ca. 4.7%, and structural collapse at the temperature range 300-680°C with a weight loss of ca. 94.2% (**Figure 4.13**). For poly[V<sup>IV</sup>O(sal-AHBPD)], surface-trapped water/solvents were removed at a temperature of around 100°C while the intra-particle waters were volatilized in the range of 200-300°C with a total weight loss of about 9.73%. The rapid collapse of the poly[V<sup>IV</sup>O(sal-AHBPD)] with a weight loss of ca. 70.55% occurred in a temperature range of 350-650°C (**Figure 4.13**).

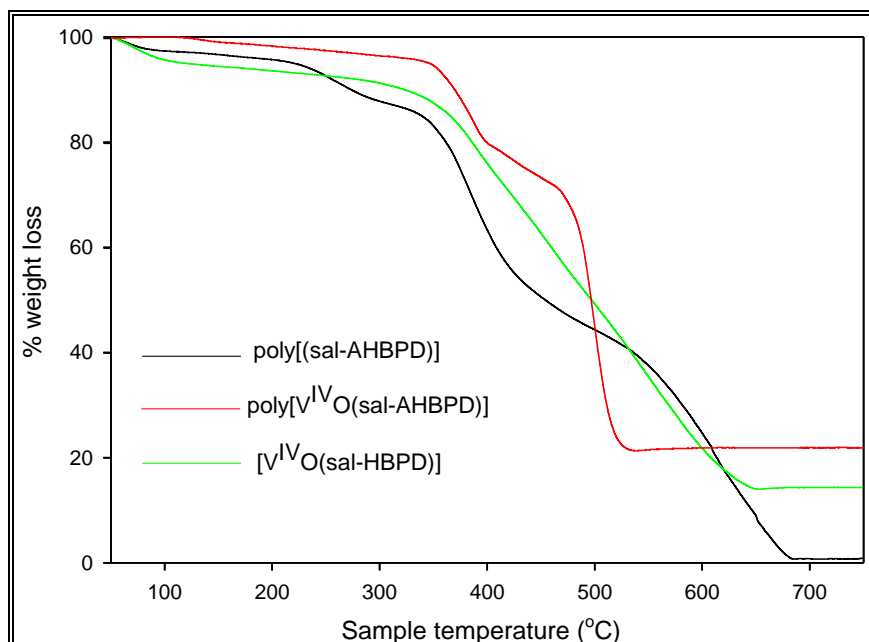


**Figure 4.13** TG profile curves of poly[(sal-AHBPD)], [V<sup>IV</sup>O(sal-AHBPD)] and poly[V<sup>IV</sup>O(sal-AHBPD)].

The TG thermograms for poly[allylSB-co-EGDMA] and poly[V<sup>IV</sup>O(allylSB-co-EGDMA)] showed similar decomposition patterns with unstable intermediates (**Figure 4.14**). The thermogram of poly[allylSB-co-EGDMA] showed that the evaporation of residual solvents (6.8%) occurred up to 280°C, followed by rapid decomposition with a weight loss of 93.2% in a temperature range of 280–650°C. However, for poly[V<sup>IV</sup>O(allylSB-co-EGDMA)] the removal of trapped inter/intra molecular solvents (8.5%) occurred up to 270°C, while the gradual collapse of the poly[V<sup>IV</sup>O(allylSB-co-EGDMA)] microspheres occurred at a temperature range of 290–660°C with a weight loss of 87.5% to give a vanadium oxide residue.

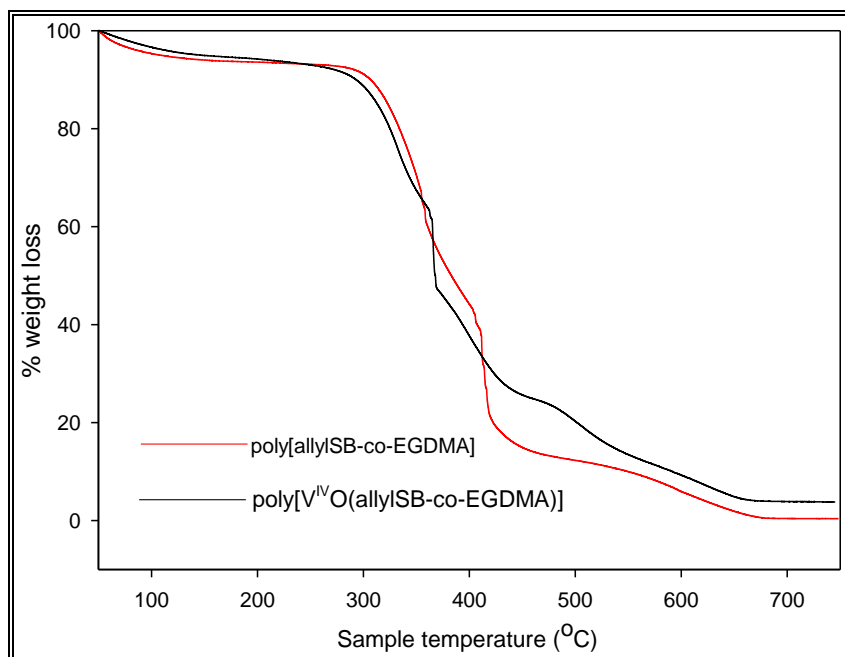


**Figure 4.14** TG profile curve for poly[allylSB-co-EGDMA] and poly[V<sup>IV</sup>O(allylSB-co-EGDMA)].

#### 4.3.7 UV-Vis electronic studies of [V<sup>IV</sup>O(sal-HBPD)], poly[V<sup>IV</sup>O(sal-AHBPD)] and poly[V<sup>IV</sup>O(allylSB-co-EGDMA)]

The diffuse reflectance spectra of [V<sup>IV</sup>O(sal-HBPD)] and the polymer anchored vanadium catalyst poly[V<sup>IV</sup>O(sal-AHBPD)] and poly[V<sup>IV</sup>O(allylSB-co-EGDMA)] exhibited relatively well-matched electronic transitions which are characteristic of a square pyramidal oxido vanadium(IV) complex (**Figures 4.15** and **4.16**). In both cases, the electronic transitions for heterogeneous catalysts were compared with the homogeneous catalyst and it seems that the tetradentate co-ordination was maintained within the polymers.

The electronic spectrum of the neat complex, [V<sup>IV</sup>O(sal-HBPD)], clearly showed three bands at 405 nm ( $a_1^* \leftarrow b_2$ ), 558 nm ( $b_1^* \leftarrow b_2$ ) and 635 nm ( $e_\pi^* \leftarrow b_2$ ) typical of the five-coordinate square pyramidal geometry (**Figure 4.15**).<sup>314</sup> The catalyst poly[V<sup>IV</sup>O(sal-AHBPD)] gave weak adsorption bands and slight shifts were also observed [365 nm ( $a_1^* \leftarrow b_2$ ) and 680 nm ( $e_\pi^* \leftarrow b_2$ )]. However, the  $b_1^* \leftarrow b_2$  transition was not easily detected, and this can be attributed to the presence of weak bands from the polymer material (**Figure 4.15**). Weak bands were also observed in the spectrum of the reused



catalyst, and this confirmed that the five-coordinate square pyramidal geometry was preserved after use.

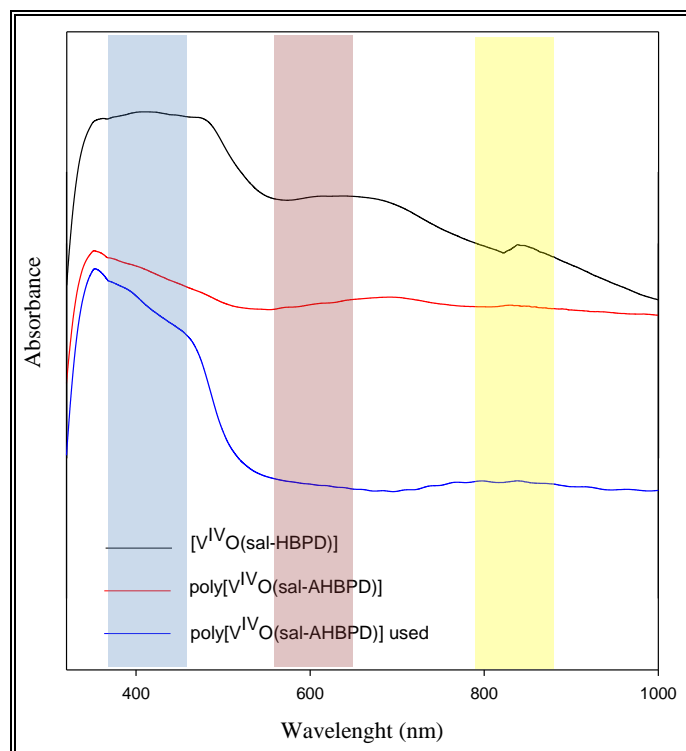


**Figure 4.15** Diffuse reflectance electronic spectra of  $[V^{IV}O(sal-HBPD)]$ ,  $poly[V^{IV}O(sal-AHBPD)]$  and used  $poly[V^{IV}O(sal-AHBPD)]$ .

$Poly[V^{IV}O(allylSB-co-EGDMA)]$  also gave weak adsorption bands with slight shifts observed around 373 nm ( $a_1^* \leftarrow b_2$ ) and 628 nm ( $e_\pi^* \leftarrow b_2$ ) and the  $b_1^* \leftarrow b_2$  transition was not easily noticed due to weak bands of the polymer material. Weak bands were also observed in the spectrum of the catalyst after use, and this confirmed that the five-coordinate square pyramidal geometry of  $[V^{IV}O(sal-HBPD)]$  within  $poly[V^{IV}O(allylSB-co-EGDMA)]$  was preserved after use (**Figure 4.16**).

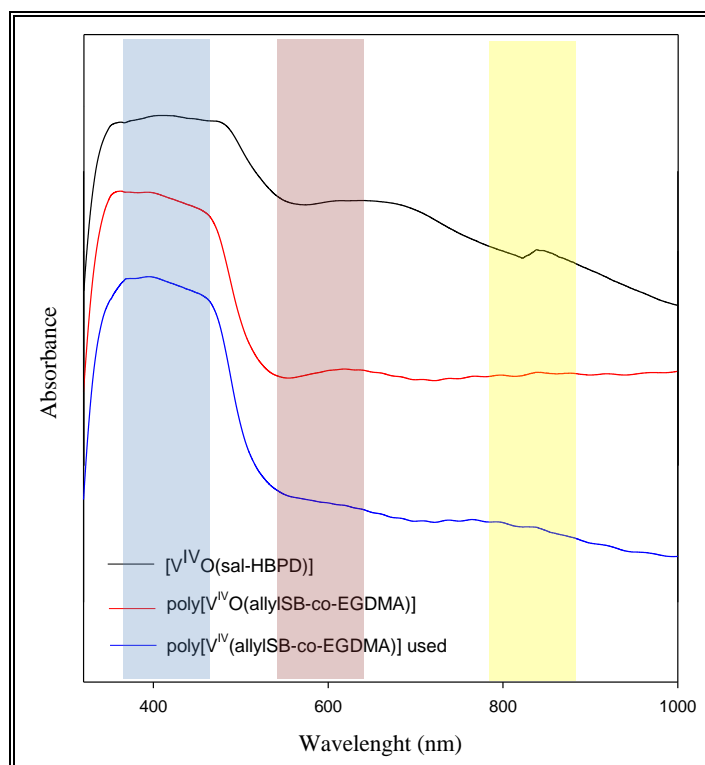


**Figure 4.16** Diffuse reflectance electronic spectra of  $[V^{IV}O(\text{sal-HBPD})]$ ,  $\text{poly}[V^{IV}O(\text{allylSB-co-EGDMA})]$  and used  $\text{poly}[V^{IV}O(\text{allylSB-co-EGDMA})]$ .

#### 4.3.8 FT-IR spectral studies of $\text{poly}[(\text{sal-AHBPD})]$ , $\text{poly}[V^{IV}O(\text{sal-AHBPD})]$ , $\text{poly}[\text{allylSB-co-EGDMA}]$ and $\text{poly}[V^{IV}O(\text{allylSB-co-EGDMA})]$

The IR spectra of  $\text{poly}[(\text{sal-AHBPD})]$  and  $\text{poly}[V^{IV}O(\text{sal-AHBPD})]$  exhibit similar bands for the  $\nu(\text{C}=\text{N})$  and  $\nu(\text{C}-\text{O})$ , except for the appearance of three new bands for  $\nu(\text{V}=\text{O})$ ,  $\nu(\text{V}-\text{N})$  and  $\nu(\text{V}-\text{O})$  in the spectrum of  $\text{poly}[V^{IV}O(\text{sal-AHBPD})]$ . Upon functionalizing the Merrified microspheres, the disappearance of the  $\text{CH}_2\text{-Cl}$  (bending) peak at  $1260\text{ cm}^{-1}$  was observed (**Figure 4.17**). The IR spectra of  $[\text{sal-HBPD}]$  and  $\text{poly}[\text{sal-AHBPD}]$  exhibited two sharp bands at  $1606\text{ cm}^{-1}$  and  $1636\text{ cm}^{-1}$  due to  $\nu(\text{C}=\text{N})$  (azomethine stretch). These bands undergo a bathochromic shift in the spectra of the complexes, indicating coordination of the azomethine nitrogen to the vanadium ion. The  $\text{V}=\text{O}$  stretching frequency of the complex,  $[V^{IV}O(\text{sal-HBPD})]$ , occurred at  $976\text{ cm}^{-1}$ , while  $\nu(\text{V}=\text{O})$  for  $\text{poly}[V^{IV}O(\text{sal-AHBPD})]$  appeared at  $982\text{ cm}^{-1}$  (**Figure 4.17**) which suggested the absence of  $-\text{V}=\text{O}-\text{V}=\text{O}-$  chain structure within the polymeric material.<sup>364</sup>

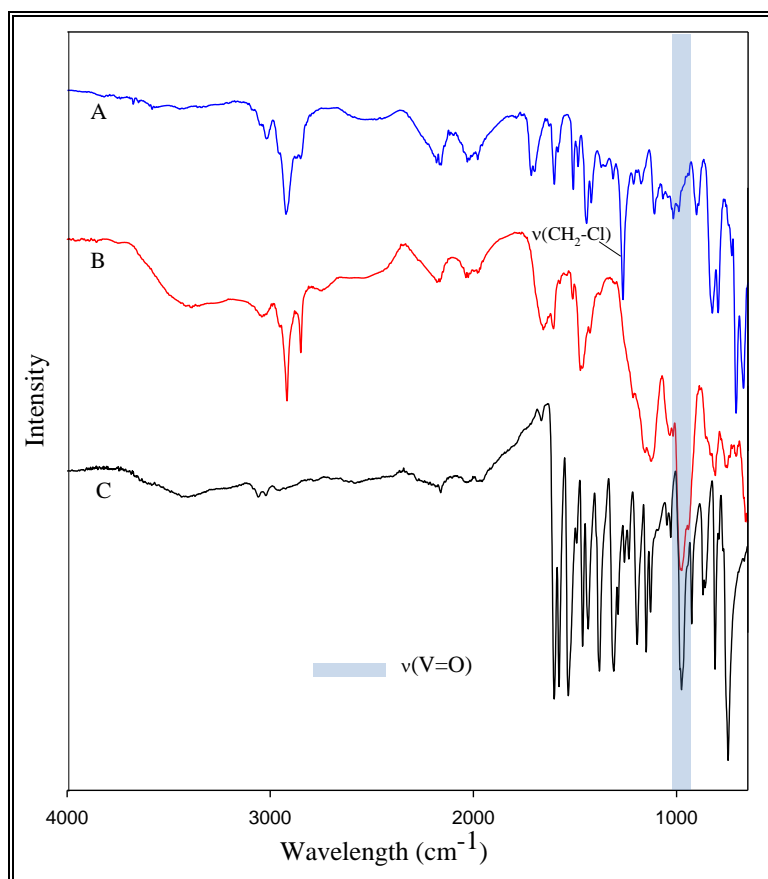


**Figure 4.17** FT-IR spectra of (A) Merrified microspheres, (B) poly[V<sup>IV</sup>O(sal-AHBPD)] and (C) [V<sup>IV</sup>O(sal-HBPD)].

The two non-ligand bands in the region 525-538 cm<sup>-1</sup> and 423-436 cm<sup>-1</sup> could be assigned to the  $\nu(\text{V}-\text{O})$  and  $\nu(\text{V}-\text{N})$  bands respectively, and used in distinguishing between poly[(sal-AHBPD)] and poly[V<sup>IV</sup>O(sal-AHBPD)] (**Figure 4.18**).<sup>364</sup>

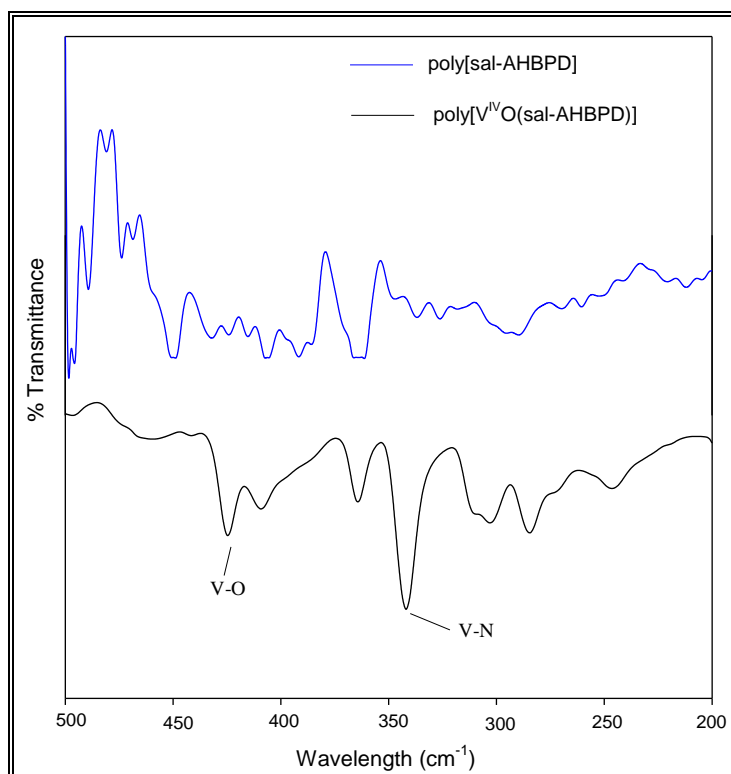


**Figure 4.18** FT-IR spectra of poly[(sal-AHBPD)] and poly[V<sup>IV</sup>O(sal-AHBPD)] showing  $\nu(\text{V-N})$  and  $\nu(\text{V-O})$  bands.

FT-IR spectra of poly[allylSB-co-EGDMA] and poly[V<sup>IV</sup>O(allylSB-co-EGDMA)] revealed similar characteristic bands for the  $\nu(\text{C=N})$  and  $\nu(\text{C-O})$  frequencies except for the appearance of three new bands  $\nu(\text{V=O})$ ,  $\nu(\text{V-N})$ , and  $\nu(\text{V-O})$  for poly[V<sup>IV</sup>O(allylSB-co-EGDMA)] (**Figure 4.19**). The broad band appearing in the region 3200-3350  $\text{cm}^{-1}$  in the spectrum of poly[V<sup>IV</sup>O(allylSB-co-EGDMA)] can be assigned to  $\nu(\text{OH})$  for the trapped solvent. Comparison of the spectra of the microspheres with free ligand poly[allylSB-co-EGDMA] to that of the vanadium-anchored microspheres, poly[V<sup>IV</sup>O(allylSB-co-EGDMA)], indicated that coordination of vanadium through N and O atoms took place as evidenced by peaks at 351  $\text{cm}^{-1}$  and 419  $\text{cm}^{-1}$  respectively (**Figure 4.19**). The  $\nu(\text{C=N})$  of poly[allylSB-co-EGDMA] appeared at 1445  $\text{cm}^{-1}$ , and this vibration frequency shifted to 1453  $\text{cm}^{-1}$  upon oxido vanadium(IV) coordination with the ligand to form poly[V<sup>IV</sup>O(allylSB-co-EGDMA)]. The V=O stretching frequency of the complex within the polymer occurred at 957  $\text{cm}^{-1}$ .<sup>364</sup>

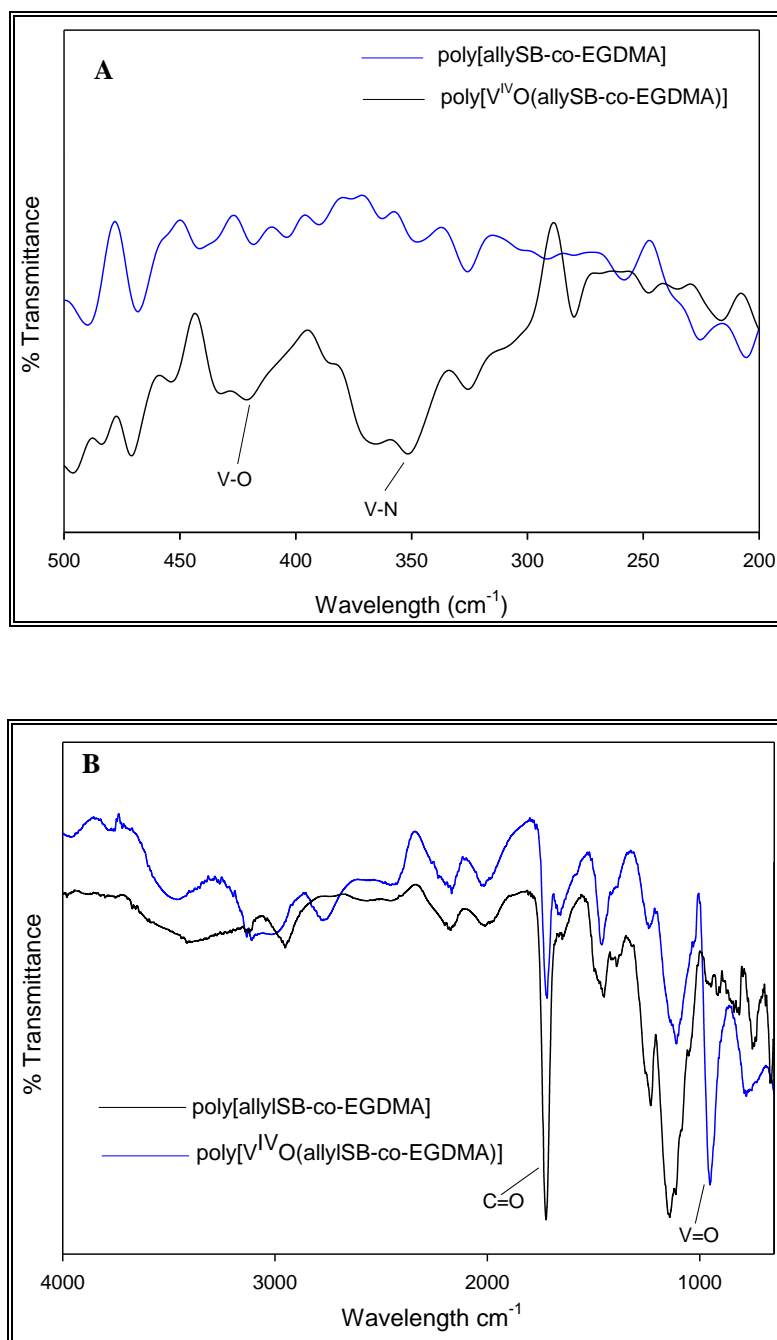


**Figure 4.19** The near-IR and mid-IR spectra of poly[allylSB-co-EGDMA] and poly[V<sup>IV</sup>O(allylSB-co-EGDMA)]. (A) showing the V-N and V-O range and (B) showing the C=O and V-O range.

#### 4.3.9 Electron paramagnetic resonance (EPR) studies of $V^{IV}O(\text{sal-HBPD})$ , $\text{poly}[V^{IV}O(\text{sal-AHBPD})]$ and $\text{poly}[V^{IV}O(\text{allylSB-co-EGDMA})]$

The isolated vanadium(IV) species exhibited a hyperfine structure derived from the interaction of the free electron ( $3d^1$ ) with the nuclear magnetic moment of  $^{51}\text{V}$  ( $I = 7/2$ ;  $n = 2I+1$ ).<sup>365</sup> The slight broadening observed for the EPR signals in the spectrum of the microspheres was probably due to vanadium(IV) collections around the ligand, as a result of dipolar interactions,<sup>366</sup> while the additional splitting was due to the restriction on isotropic tumbling (anisotropic signal) on the microspheres.

The EPR spectrum of  $[V^{IV}O(\text{sal-HBPD})]$  in  $10^{-5}$  M of *N,N*-dimethylformamide (DMF) is presented in **Figure 4.20** which gave 8 line splitting patterns compared to the polymer-supported catalysts  $\text{poly}[V^{IV}O(\text{sal-AHBPD})]$  and  $\text{poly}[V^{IV}O(\text{allylSB-co-EGDMA})]$  which have their isotropic tumbling restricted or annealed giving rise to additional splitting.<sup>367-369</sup> The isotropic spectrum of  $[V^{IV}O(\text{sal-HBPD})]$  showed  $g_{\perp} = 1.9572$ ,  $A_{\perp} = 56.5 \times 10^{-4} \text{ cm}^{-1}$ ,  $g_{\parallel} = 1.9482$  and  $A_{\parallel} = 161.2 \times 10^{-4} \text{ cm}^{-1}$ . The anisotropic spectrum of  $\text{poly}[V^{IV}O(\text{sal-AHBPD})]$  showed  $g_{\perp} = 1.9911$ ,  $A_{\perp} = 62.4 \times 10^{-4} \text{ cm}^{-1}$ ,  $g_{\parallel} = 1.9465$  and  $A_{\parallel} = 162.5 \times 10^{-4} \text{ cm}^{-1}$ , and the used  $\text{poly}[V^{IV}O(\text{sal-AHBPD})]$  signal parameters were  $g_{\perp} = 1.9952$ ,  $A_{\perp} = 56.1 \times 10^{-4} \text{ cm}^{-1}$ ,  $g_{\parallel} = 1.9369$  and  $A_{\parallel} = 160.4 \times 10^{-4} \text{ cm}^{-1}$ . The spectrum of  $\text{poly}[V^{IV}O(\text{sal-AHBPD})]$  and  $\text{poly}[V^{IV}O(\text{sal-AHBPD})]$  after use are presented in **Figure 4.21**.

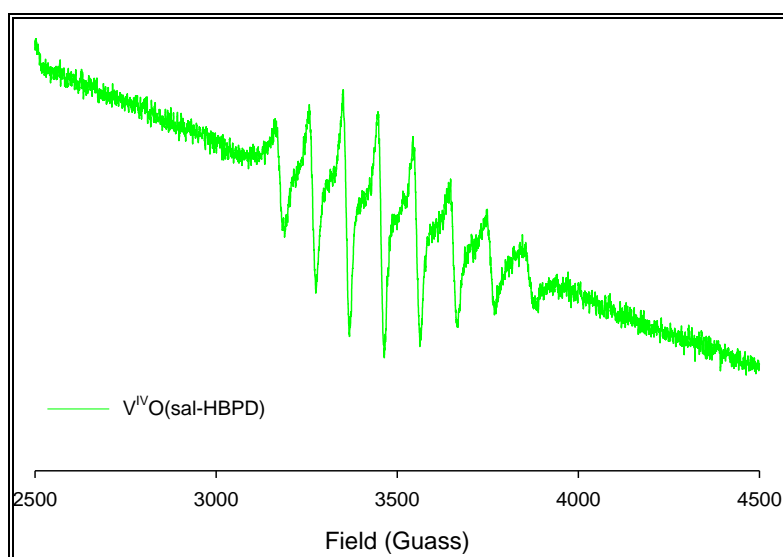


**Figure 4.20** First derivative EPR spectra of  $[V^{IV}O(\text{sal-HBPD})]$  in *N,N*-dimethylformamide (DMF).

The less intense EPR signals of the used solid poly[V<sup>IV</sup>O(sal-AHBPD)] indicated that some of the V(V) was not recycled to V(IV) when compared to its initial (**Figure 4.21**). These similarities in the signals indicate that the same vanadium(IV) species was retained on the microspheres after oxidation cycles.

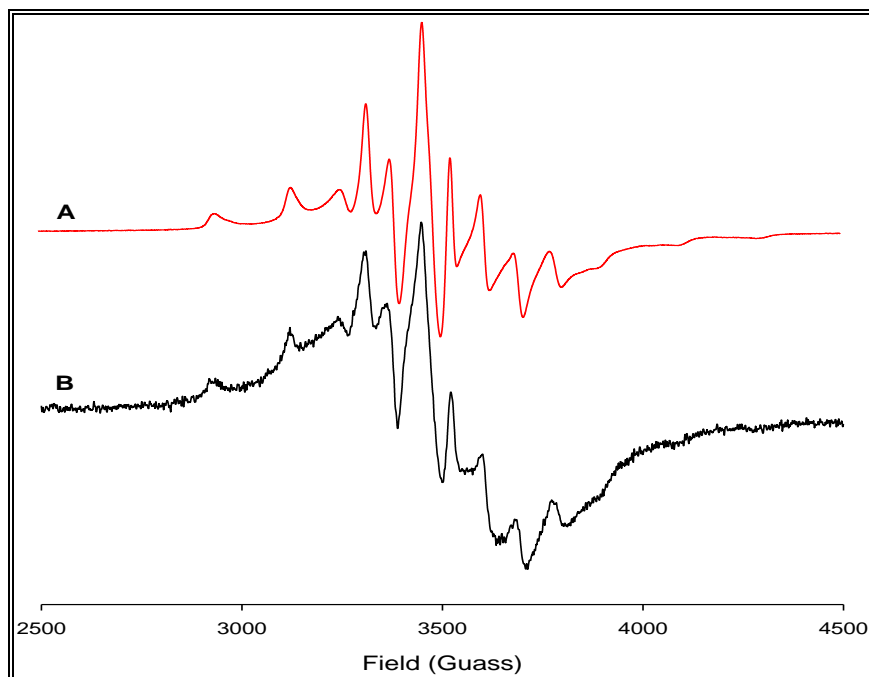


**Figure 4.21** First derivative EPR spectrum of (A) poly[V<sup>IV</sup>O(sal-AHBPD)] before, and (B) poly[V<sup>IV</sup>O(sal-AHBPD)] after use.

The anisotropic spectrum of poly[V<sup>IV</sup>O(allylSB-co-EGDMA)] showed  $g_{\perp} = 1.9567$ ,  $A_{\perp} = 55.3 \times 10^{-4} \text{ cm}^{-1}$ ,  $g_{\parallel} = 1.9218$  and  $A_{\parallel} = 161.2 \times 10^{-4} \text{ cm}^{-1}$ , and the used poly[V<sup>IV</sup>O(allylSB-co-EGDMA)] signal parameters were  $g_{\perp} = 1.9653$ ,  $A_{\perp} = 52.2 \times 10^{-4} \text{ cm}^{-1}$ ,  $g_{\parallel} = 1.9291$  and  $A_{\parallel} = 158.4 \times 10^{-4} \text{ cm}^{-1}$ . These confirmed vanadium(IV) within the polymer microspheres.<sup>370-371</sup> The spectrum of poly[V<sup>IV</sup>O(allylSB-co-EGDMA)] and poly[V<sup>IV</sup>O(allylSB-co-EGDMA)] before and after use are presented in **figure 4.22**. From the EPR signal of poly[V<sup>IV</sup>O(sal-AHBPD)] and poly[V<sup>IV</sup>O(allylSB-co-EGDMA)] the line signals are similar confirming that both catalyst are similar in functionalities.

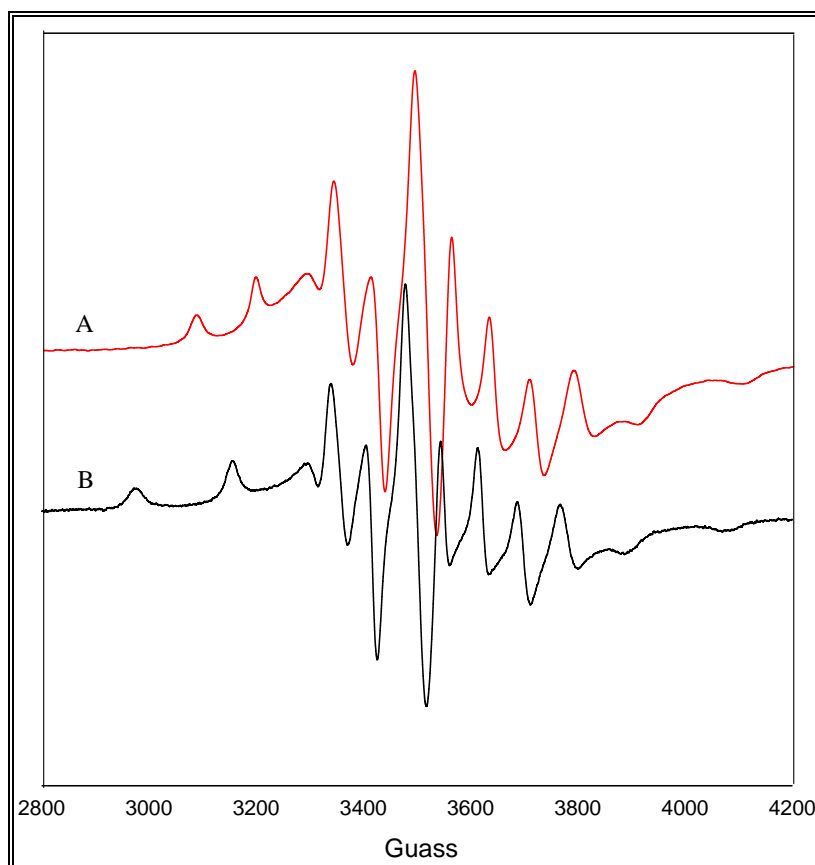


**Figure 4.22** First derivative EPR signals of (A) poly[V<sup>IV</sup>O(allylSB-co-EGDMA)] before, and (B) poly[V<sup>IV</sup>O(allylSB-co-EGDMA)] after use.

#### 4.3.10 Reactivity of [V<sup>IV</sup>O(sal-HBPD)] with *t*-BuOOH

[V<sup>IV</sup>O(sal-HBPD)] reacts with peroxides such as *tert*-butylhydroperoxide (*t*-BuOOH) to give the corresponding V<sup>IV</sup>O(O<sub>2</sub>)-complexes. Speciation studies of the complex [V<sup>IV</sup>O(sal-HBPD)] were monitored by employing a UV-vis spectrometer and <sup>51</sup>V-NMR.

On employing UV-vis spectrometer, addition of *t*-BuOOH to a solution of [V<sup>IV</sup>O(sal-HBPD)] in DMF (10<sup>-3</sup> M) yielded the oxidoperoxido-species according to the spectral changes observed. The gradual disappearance of the d-d bands around 405 nm, 568 nm and 635 nm was observed (**Figure 4.23**), while an increase in the intensity of the band at 324 nm also occurred which may be assigned the oxido-vanadium charge transfer band ( $\pi^*_{\text{v}} \rightarrow d\sigma^*$ ).<sup>372</sup> It is normally assumed that the corresponding oxidoperoxido-complex formed is the active catalyst which performs the oxidation, such as the oxidation of sulfur compounds to their corresponding sulfoxides and sulfones.



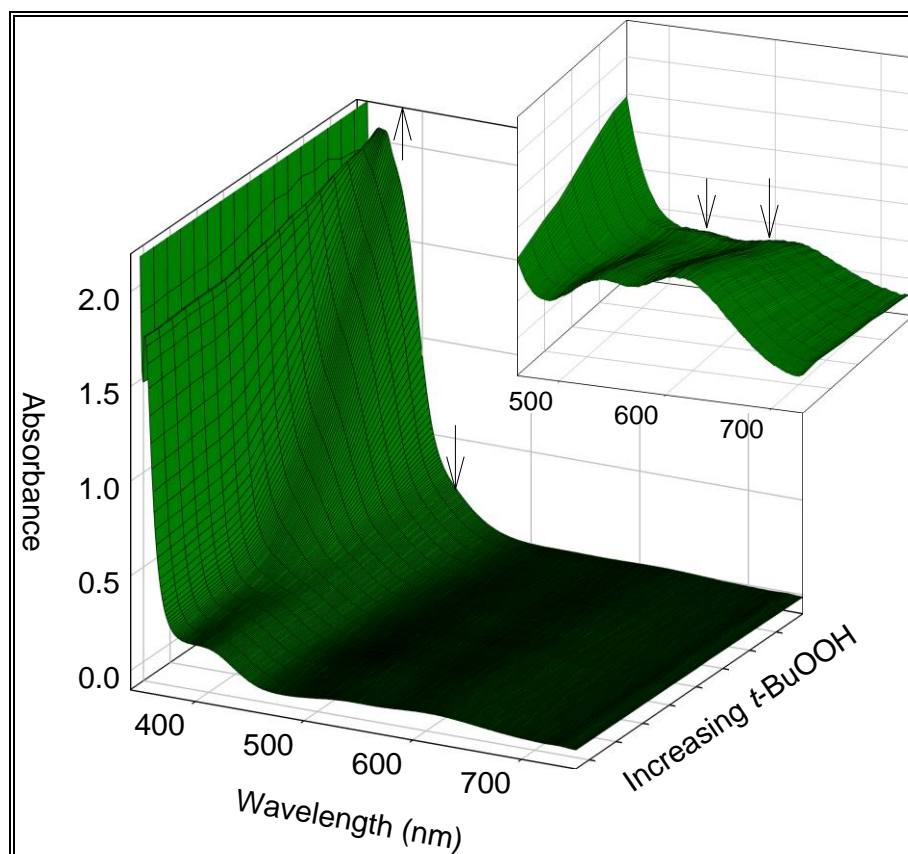


**Figure 4.23** Spectrophotometric titration of  $[V^{IV}O(\text{sal-HBPD})]$  with one drop portions of  $t\text{-BuOOH}$  ( $5 \times 10^{-2}$  M) in DMF. Inset shows the d-d transition which disappears upon addition of oxidant.

$^{51}\text{V}$ -NMR spectroscopic measurements were also carried-out to investigate the speciation of  $[V^{IV}O(\text{sal-HBPD})]$  upon interaction with peroxide by using a Bruker 400 MHz spectrometer and  $\text{VOCl}_3$  was used as a reference in MeOH as solvent (**Figure 4.24**). A  $^{51}\text{V}$  NMR spectrum of the oxidized  $[V^{IV}O(\text{sal-HBPD})]$ , (ca. 4 mM) dissolved in MeOH showed a strong resonance at  $\delta = -568$  ppm. Stepwise addition of an aqueous peroxide solution to a solution of  $[V^{IV}O(\text{sal-HBPD})]$  generated the peroxido-vanadium(V) complex species. The addition of 3.0 equivalent solution of  $t\text{-BuOOH}$  to vanadium did not lead to much change except for the broadening of signals around -568 ppm with a smaller resonance peak appearing around -598 ppm. At 7 mole equivalent of  $t\text{-BuOOH}$ , a new resonance peak appeared at -642 ppm and was assigned to  $V^V\text{O}(\text{O}_2)$ -species.<sup>135</sup> Leaving the NMR tube open for 24 h at room temperature, the resonance at -642 ppm disappeared and a resonance around -570 gains intensity, indicating the reversibility of the process.

The general mechanism for V(IV) oxidation is presented in **Chapter 1, Section 1.3.2.2**. UV-vis titration studies and  $^{51}\text{V}$  NMR confirmed the evidence of formation of dioxido and oxidoperoxido species.

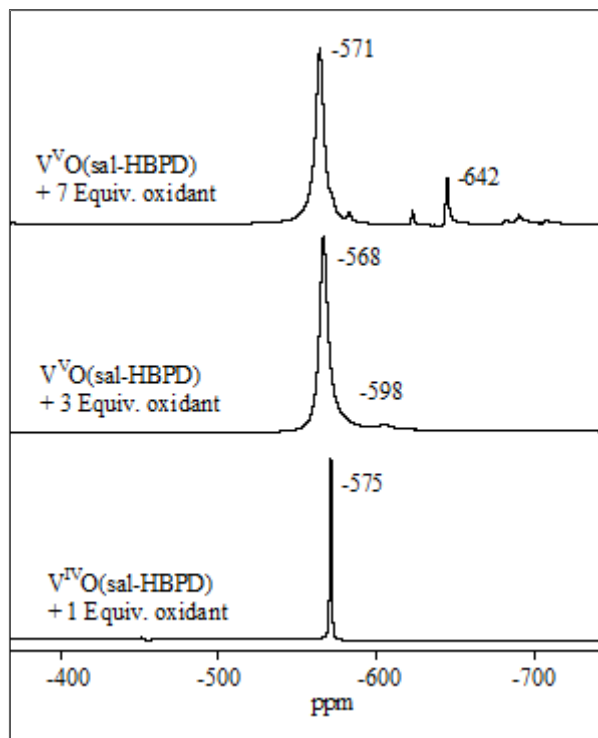


**Figure 4.24**  $^{51}\text{V}$  NMR spectrum of (a) solution of 4 mM  $[\text{V}^{\text{IV}}\text{O}(\text{sal-HBPD})]$  in 1 equivalent *t*-BuOOH in MeOH; (b) suspension of  $[\text{V}^{\text{V}}\text{O}(\text{sal-HBPD})]$  after addition of 3 equivalent *t*-BuOOH in MeOH; and (c) suspension of  $[\text{V}^{\text{V}}\text{O}(\text{sal-HBPD})]$  after addition of 7 equivalent *t*-BuOOH.

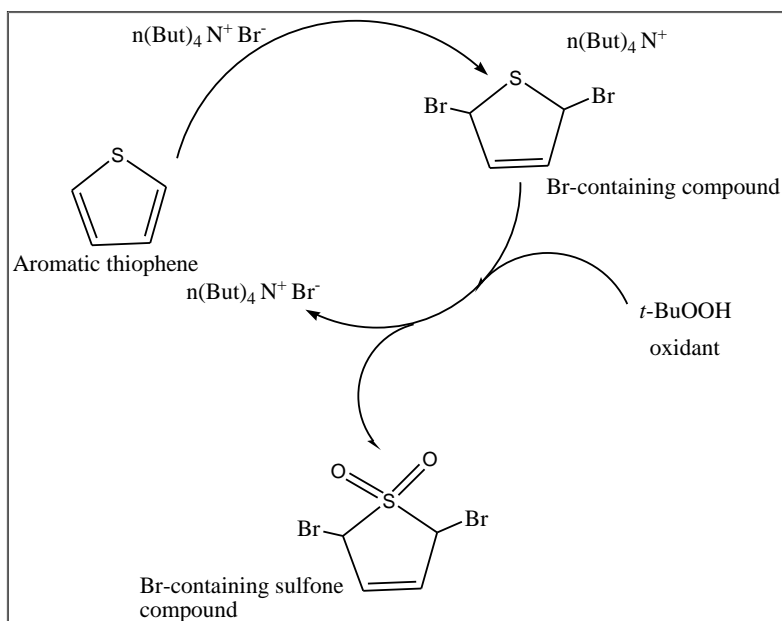
#### 4.4 Catalytic oxidation of organosulfur compounds

The catalytic oxidation of thiophene (TH), benzothiophene (BT), dibenzothiophene (DBT) and 4,6-dimethyldibenzothiophene (4,6-DMDBT) were carried out using the polymer-anchored oxidovanadium(IV) complexes poly[V<sup>IV</sup>O(sal-AHBPD)] and poly[V<sup>IV</sup>O(allylSB-co-EGDMA)], and the unsupported complex [V<sup>IV</sup>O(sal-HBPD)] respectively (as described in **Section 2.5**).

##### 4.4.1 Catalytic oxidation of thiophene, benzothiophene, dibenzothiophene and 4,6-dimethyldibenzothiophene using poly[V<sup>IV</sup>O(sal-AHBPD)] and poly[V<sup>IV</sup>O(allylSB-co-EGDMA)] as catalysts under batch condition

###### 4.4.1.1 Thiophene

Thiophene is considered an aromatic compound due to the aromaticity properties it exhibits. The electron pairs on the sulfur atom are significantly delocalized in the  $\pi$ -electron system rendering the sulfur atom unreactive thus enhancing thiophene stability and making the carbon center of the 2- and 5- positions susceptible to electrophilic attack.<sup>54,373</sup> Thiophene is also reported to have a lower electron density, therefore making it not easily oxidizable as compared to thiophene derivatives that have a much higher electron density on the sulfur atoms.<sup>131,374-375</sup> From the above classification of the properties of thiophene it is obvious that a possible way to effectively oxidize thiophene is to increase its electron density by interrupting conjugation (**Scheme 4.3**), and tetrabutylammonium bromide (TBAB) (0.01 g, 0.031 mmol) was used to achieve this.



**Scheme 4.3** Proposed mechanism showing the effect of tetrabutylammonium bromide (TBAB) during conjugation.

The catalysed oxidation of thiophene was carried out under four different conditions: (1) oxidation in the presence of catalyst and absence of TBAB, (2) oxidation in the absence of the catalyst and presence of TBAB, (3) oxidation in the presence of the catalyst and TBAB (oxidant eq. 2), and (4) oxidation in the presence of the catalyst and TBAB (oxidant eq. 6.8). Oxidation of thiophene gave a low overall conversion of 12% after 3 h in the absence of TBAB and presence of catalyst at 40°C with 8% sulfoxide and 4% sulfone yield when poly[V<sup>IV</sup>O(sal-AHBPD)] was employed as catalyst. In the absence of catalyst and presence of TBAB, an overall conversion of 10% was observed with a yield of 7% towards sulfoxide and 3% for sulfone (**Figure 4.25**). An overall conversion of 30% was observed with 17% yield for sulfoxides and 13% yield towards sulfone in the presence of catalyst and TBAB when a *t*-BuOOH-to-thiophene ratio of 2:1 was employed (**Figure 4.26, Table 4.5**). At a higher oxidant (*t*-BuOOH) ratio (6.8) in the presence of TBAB an overall conversion of 44% was observed (**Figure 4.25**), with 20% yield for sulfoxides and 24% yield towards sulfone in the presence of catalyst and TBAB.

In a similar manner, when poly[V<sup>IV</sup>O(allylSB-co-EGDMA)] was employed as catalyst at a low *t*-BuOOH-to-thiophene ratio of 2:1, in the presence of tetrabutylammonium bromide and catalyst at

40°C, an overall conversion of 45% (**Figure 4.27**) was obtained with a yield of 5% for sulfoxide and 40% for sulfone. An overall conversion yield of 60% after 3 h at 40°C with a yield of 1% for sulfoxides and 59% towards sulfone, when a *t*-BuOOH-to-thiophene ratio of 6.8:1 was employed (**Figure 4.28, Table 4.5**).

#### 4.4.1.2 Benzothiophene

Benzothiophene has a much higher electron density as compared to thiophene, and the catalysed oxidation studies were carried-out in the absence of tetrabutylammonium bromide (TBAB). When poly[V<sup>IV</sup>O(sal-AHBPD)] was employed as catalyst, a low overall conversion of 15% for benzothiophene was observed in the absence of a catalyst, and the yield for sulfoxides was 13% while it was 2% for sulfone (**Figure 4.25, Table 4.5**). At an oxidant (*t*-BuOOH) ratio (2.3:1) an overall conversion of 41% was observed after 3 h at 40°C (**Figure 4.26**) with high yield for sulfone (25%) and low sulfoxide yield (16%). The low conversion was due to insufficient oxidant in the oxidation system. On increasing the oxidant (*t*-BuOOH) ratio to (6.8) at 40°C, an increase in the overall conversion (73%) was observed (**Figure 4.25, Table 4.5**), with 54% yield towards sulfone and 8% yield towards sulfoxides. All oxidation reactions were conducted at 40°C. At a low oxidant-to-benzothiophene ratio (2.3:1) in the presence of poly[V<sup>IV</sup>O(allylSB-co-EGDMA)], an overall conversion of 62% was observed after 3 h at 40°C (**Figure 4.27**) with a yield of 24% for sulfoxide and 38% for sulfone. The higher yield towards sulfoxide was also attributed to insufficient oxidant to convert the sulfoxide to sulfone. On increasing the ratio of *t*-BuOOH-to-benzothiophene ratio to 6.8, an increase in the overall conversion to 81% was observed (**Figure 4.28**), with a high yield of 70% for sulfone and 11% for sulfoxide (**Table 4.5**). The reaction produced an overall conversion of 15% in the absence of catalyst with a yield of 13% sulfoxide and 2% sulfone.

#### 4.4.1.3 Dibenzothiophene

The catalysed oxidation of dibenzothiophene was carried out under similar conditions as the previous model organosulfur compounds, benzothiophene, in the absence of TBAB. The oxidation of dibenzothiophene in the absence of catalyst produced an overall conversion of 23% (20% of dibenzothiophene sulfone and 3% of dibenzothiophene sulfoxide) (**Figure 4.29**). When

poly[V<sup>IV</sup>O(sal-AHBPD)] was employed at an oxidant (*t*-BuOOH)-to-dibenzothiophene ratio of 2.3, an overall conversion of 62% was observed with high yield towards sulfone (54%) and low sulfoxide yield (8%) (**Figure 4.26, Table 4.5**). The oxidant ratio was increased to 6.8 so as to avoid deficiency of oxygen in the oxidation system. The reaction gave an overall yield of 88%, 86% towards dibenzothiophene sulfone and 2% towards dibenzothiophene sulfoxide within 3 h (**Figure 4.29**) of oxidation. Oxidation reaction time in the presence of poly[V<sup>IV</sup>O(sal-AHBPD)] were short, as no further conversions/oxidations were observed beyond 3 h. However, when poly[V<sup>IV</sup>O(allylSB-co-EGDMA)] was employed, oxidation reaction took a longer time to reach completion as compared to poly[V<sup>IV</sup>O(sal-AHBPD)]. A *t*-BuOOH-to-dibenzothiophene ratio of 2.3:1 was used in the presence of the catalyst to give an overall conversion of 65% with yield towards sulfone (**Figure 4.27, Table 4.5**). Increasing the ratio of *t*-BuOOH-to-dibenzothiophene to 6.8 (**Figure 4.30**) resulted in higher conversion of DBT (98%) after 4 h. The high electron density of dibenzothiophene is the key factor favoring the oxidation reaction. The yield for dibenzothiophene sulfone (DBTO<sub>2</sub>) in the oxidation experiments was above 99% of the overall oxidized product and no sulfoxide was detected (**Table 4.5**).

#### 4.4.1.4 4,6-Dimethyldibenzothiophene

The oxidation of 4,6-dimethyldibenzothiophene in the absence of catalyst at a *t*-BuOOH-to-4,6-dimethyldibenzothiophene ratio of 7.6 produced an overall conversion of less than 17% (**Figure 4.29**). However, when an oxidant (*t*-BuOOH) equivalent of 2.3 was employed in the presence of catalyst poly[V<sup>IV</sup>O(sal-AHBPD)], an overall conversion of 50% was observed after 3 h with 39% yield for sulfone and 11% towards sulfoxide, and this low conversion was also due to the limited oxidant within the system (**Figure 4.26**). At a higher mole ratio of 7.6:1 (*t*-BuOOH-to-4,6-dimethyldibenzothiophene) the catalysed oxidation progressed steadily to give an overall conversion of 73% (72% of 4,6-dimethyldibenzothiophene sulfone and 1% of 4,6-dimethyldibenzothiophene sulfoxide) (**Figure 4.29, Table 4.5**). When poly[V<sup>IV</sup>O(allylSB-co-EGDMA)] was employed as catalyst, a mole ratio of 1:2.3, (4,6-dimethyldibenzothiophene-to-*t*-BuOOH) gave an overall conversion of 52% with a yield of 12% for sulfoxide and 40% for sulfone (**Figure 4.27**). In 2 h of

addition of 7.6 mole equivalent of *t*-BuOOH-to-4,6-dimethyldibenzothiophene, the reaction yield reached a maximum of 87% (Figure 4.30) conversion after 6 h with a yield of 1% for sulfoxide and 86% for sulfone. The results revealed that increasing the moles of *t*-BuOOH in the reaction mixture not only increased the overall conversion of sulfur containing compound but also increased the product yield towards sulfone. The yield for 4,6-dimethyldibenzothiophene sulfone (4,6-DMDBTO<sub>2</sub>) in oxidation studies was above 95% of the overall oxidized product.

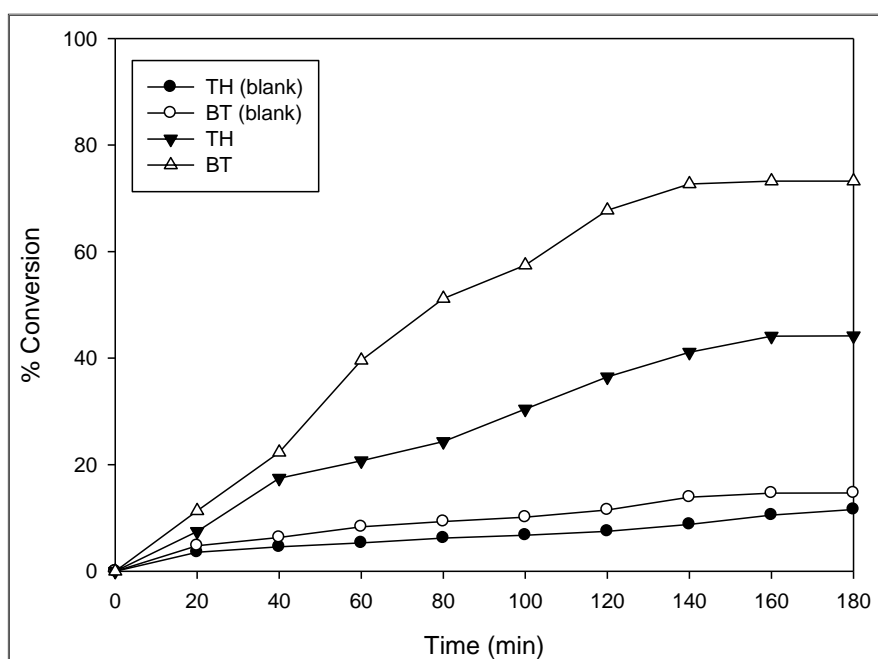


**Figure 4.25** Percentage conversion for the oxidation of thiophene (TH) and benzothiophene (BT) with time. [*t*-BuOOH]<sub>eq.</sub> = 6.8, thiophene = 0.54 g (0.0064 mol), benzothiophene = 0.15 g (0.0011 mol), poly[V<sup>IV</sup>O(sal-AHBPD)] = 0.015 g (0.0135 mmol). *Tert*-butylammonium bromide (TBAB) = 0.01 g (0.000031 mol), Temp. = 40°C. Toluene/Hexane (1:4) = 10 mL. Blank means in the absence poly[V<sup>IV</sup>O(sal-AHBPD)] (catalyst).

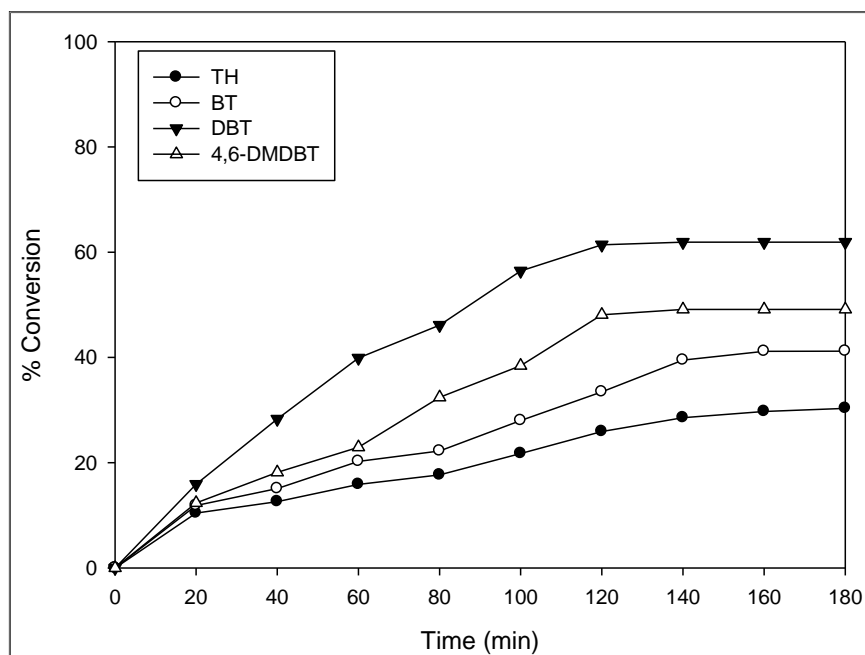


**Figure 4.26** Percentage conversion for the oxidation of thiophene (TH), benzothiophene (BT) dibenzothiophene (DBT) and 4,6-dimethyldibenzothiophene (4,6-DMDBT) with time. Thiophene = 0.54 g (0.0064 mol), benzothiophene = 0.15 g (0.0011 mol), dibenzothiophene = 0.15 g, (0.00081 mol), 4,6-dimethyldibenzothiophene = 0.15 g (0.00071 mol), poly[V<sup>IV</sup>O(sal-AHBPD)] = 0.015 g (0.0135 mmol), [*t*-BuOOH eq.] = 2.3. *Tert*-butylammonium bromide (TBAB) = 0.01 g (0.000031 mol), Temp. = 40°C. Toluene/Hexane (1:4) = 10 mL.



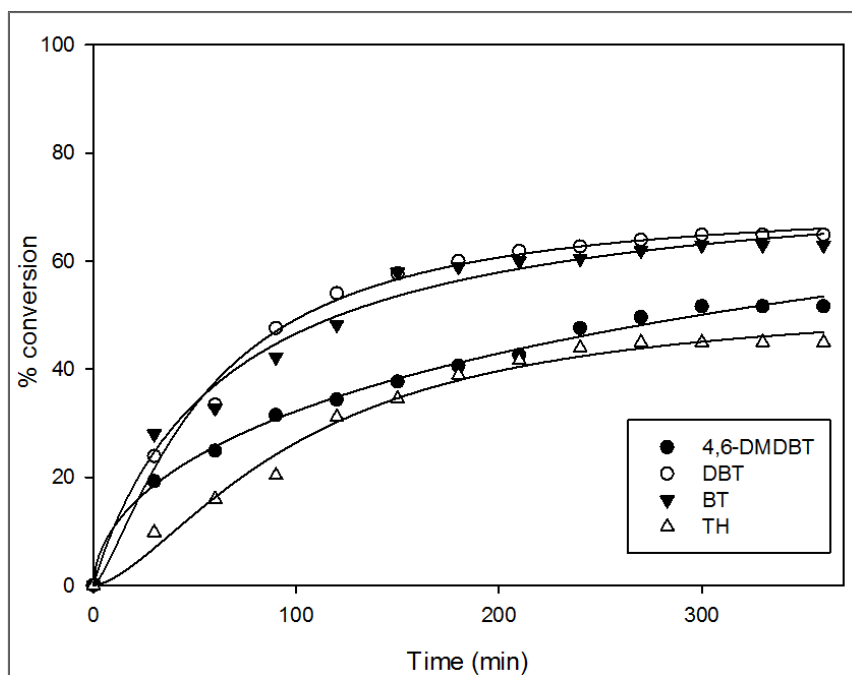


**Figure 4.27** Percentage conversion for the oxidation of thiophene (TH), benzothiophene (BT) dibenzothiophene (DBT) and 4,6-dimethyldibenzothiophene (4,6-DMDBT) with time. Thiophene = 0.54 g (0.0064 mol), benzothiophene = 0.15 g (0.0011 mol), dibenzothiophene = 0.15 g, (0.00081 mol), 4,6-dimethyldibenzothiophene = 0.15 g (0.00071 mol), poly[V<sup>IV</sup>O(allylSB-co-EGDMA)] = 0.024 g (0.0135 mmol), [*t*-BuOOH eq.] = 2.3, *tert*-butylammonium bromide (TBAB) = 0.01 g (0.000031 mol), Temp. = 40°C, toluene/hexane (1:4) = 10 mL.

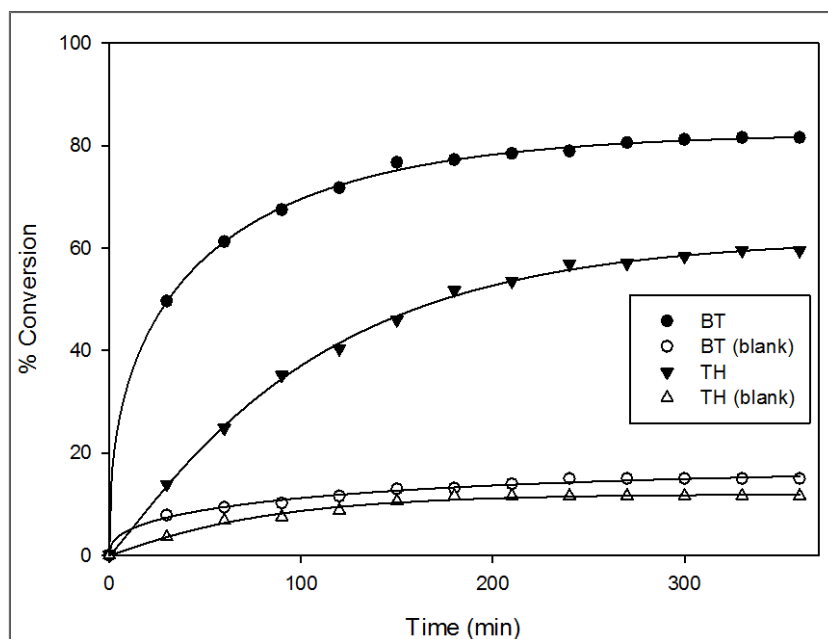


**Figure 4.28** Percentage conversion for the oxidation of thiophene (TH) and benzothiophene (BT) with time. Thiophene = 0.54 g (0.0064 mol), benzothiophene = 0.15 g (0.0011 mol), poly[V<sup>IV</sup>O(allylSB-co-EGDMA)] = 0.024 g (0.0135 mmol), *tert*-butylammonium bromide (TBAB) = 0.01 g (0.000031 mol), [*t*-BuOOH]<sub>eq.</sub> = 6.8, Temp. = 40°C. Toluene/Hexane (1:4) = 10 mL. Blank means in the absence poly[V<sup>IV</sup>O(allylSB-co-EGDMA)] (catalyst).

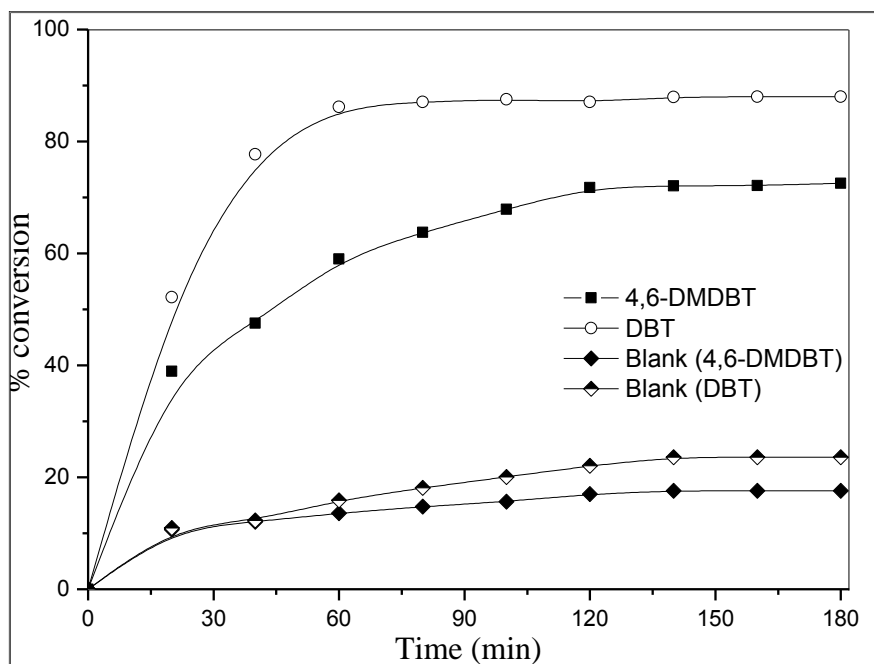


**Figure 4.29** Graph of % conversion for the oxidation of dibenzothiophene (DBT) and 4,6-dimethyldibenzothiophene (4,6-DMDBT) with time. Dibenzothiophene = 0.15 g (0.00081 mol), 4,6-dimethyldibenzothiophene = 0.15 g (0.00071 mol), poly[V<sup>IV</sup>O(sal-AHBPD)] = 0.015 g (0.0135 mmol), [*t*-BuOOH eq.] = 6.8 and 7.6, Temp. = 40°C. Toluene/Hexane (1:4) = 10 mL. Blank means in the absence of poly[V<sup>IV</sup>O(sal-AHBPD)].

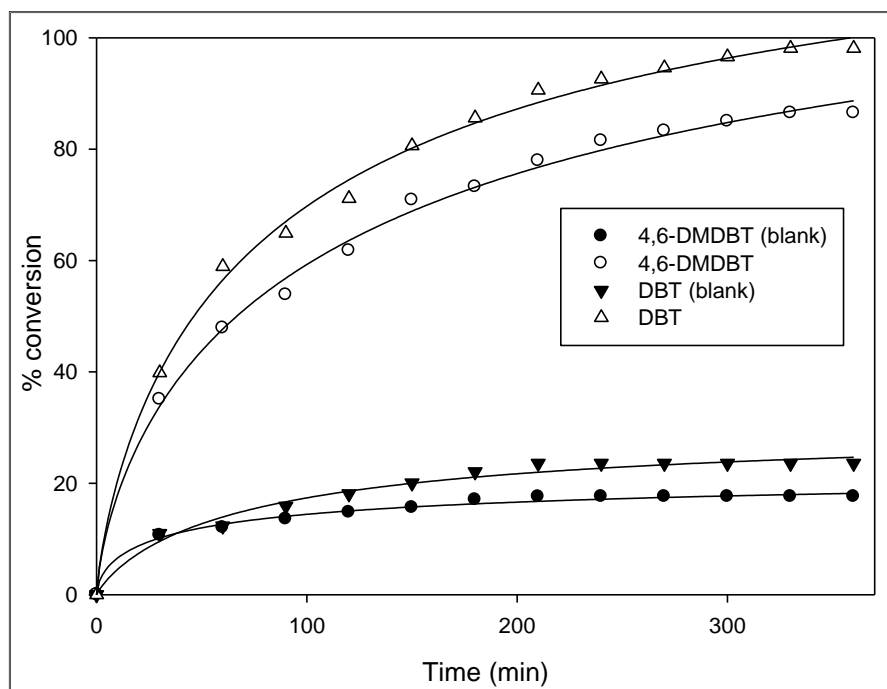


**Figure 4.30** Percentage conversion for the oxidation of dibenzothiophene (DBT) and 4,6-dimethyldibenzothiophene (4,6-DMDBT) with time.  $[t\text{-BuOOH eq.}] = 6.8$  for dibenzothiophene = 0.15 g (0.00081 mol),  $[t\text{-BuOOH eq.}] = 7.6$  for 4,6-dimethyldibenzothiophene = 0.15 g (0.00071 mol), poly[V<sup>IV</sup>O(allylSB-co-EGDMA)] = 0.024 g (0.0135 mmol), Temp. = 40°C, Toluene/Hexane (1:4) = 10 mL. Blank means in the absence poly[V<sup>IV</sup>O(allylSB-co-EGDMA)].

#### 4.4.2. Catalytic oxidation of organosulfur compounds using [V<sup>IV</sup>O(sal-HBPD)] as catalysts under batch condition

Oxidation of organosulfur compounds using the homogeneous catalyst, [V<sup>IV</sup>O(sal-HBPD)], was carried-out by using the highest oxidant ratio reported for the various organosulfur compounds when poly[V<sup>IV</sup>O(sal-AHBPD)] and poly[V<sup>IV</sup>O(allylSB-co-EGDMA)] were employed as oxidation catalysts. The oxidation of thiophene using homogeneous catalyst [V<sup>IV</sup>O(sal-HBPD)] produced an overall yield of 53% with 41% yield for sulfone and 12% for sulfoxide after 6 h (**Figure 4.31**, **Table 4.5**) when an oxidant ratio of 6.8 was employed in the presence of tetrabutylammonium bromide.<sup>376</sup> The oxidation of benzothiophene using [V<sup>IV</sup>O(sal-HBPD)] produced an overall yield of 71% with 56% yield for benzothiophene sulfones and 15% for benzothiophene sulfoxide after 5 h (**Figure 4.31**). The catalytic

turnover frequencies of the oxidation reactions were observed to increase as the oxidant ratio increased.

The oxidation of DBT using homogeneous catalyst [ $V^{IV}O(\text{sal-HBPD})$ ] produced an overall yield of 87% with 85% yield for dibenzothiophene sulfone and 2% for dibenzothiophene sulfoxide only after 5 h (**Figure 4.31**). **Table 4.5** showed that a higher yield for dibenzothiophene sulfone was obtained on polymer-anchored vanadium catalyst as compared to [ $V^{IV}O(\text{sal-HBPD})$ ], and this can be attributed to the active sites isolation on the supported catalyst which can also contribute to better yield during oxidation reaction.

A similar oxidation study was performed using the homogeneous catalyst [ $V^{IV}O(\text{sal-HBPD})$ ] at *t*-BuOOH-to-4,6-dimethyldibenzothiophene ratio of 7.6 under the same conditions applied when using a heterogeneous catalyst system. The study was aimed at comparing the catalytic activity of the homogeneous catalyst to its heterogeneous counterpart. A maximum overall yield of 64% (53% of 4,6-dimethyldibenzothiophene sulfone and 11% of 4,6-dimethyldibenzothiophene sulfoxide) was observed after 6 h (**Figure 4.31**).

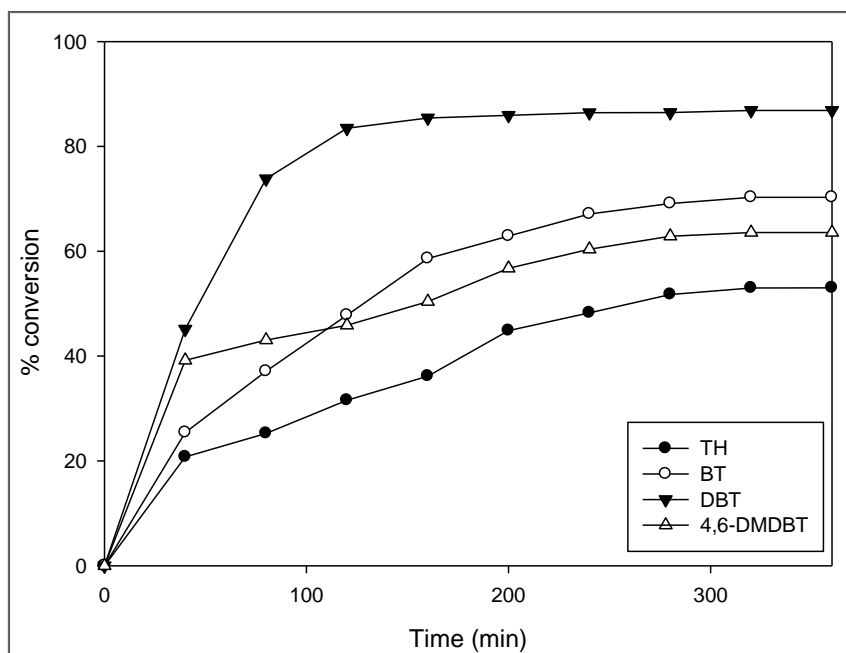


**Figure 4.31** Graph of % conversion for the oxidation of thiophene, benzothiophene, dibenzothiophene and 4,6-dimethyldibenzothiophene with time using homogenous catalyst  $[V^{IV}O(\text{sal-HBPD})]$ . Thiophene (TH) = 0.54 g (0.0064 mol), benzothiophene (BT) = 0.15 g (0.0011 mol), dibenzothiophene (DBT) = 0.15 g (0.00081 mol), 4,6-dimethyldibenzothiophene (4,6-DMDBT) = 0.15 g (0.00071 mol),  $[V^{IV}O(\text{sal-HBPD})]$  = 0.0047 g (0.0135 mmol) and Temp. = 40°C, [*t*-BuOOH eq.] for TH, BT and DBT = 6.8 and [*t*-BuOOH eq.] for 4,6-DMDBT is 7.6.

#### 4.4.3 Summary of the oxidation results

From the batch oxidation studies, poly $[V^{IV}O(\text{sal-AHBPD})]$  and poly $[V^{IV}O(\text{allylSB-co-EGDMA})]$  gave high conversions and better selectivity as compared to  $[V^{IV}O(\text{sal-HBPD})]$  (Table 4.5). Justification for the high conversion of dibenzothiophene to dibenzothiophene sulfone as compared to 4,6-dimethyldibenzothiophene conversion could be attributed to the less sterically hindered nature of dibenzothiophene. The oxidation results obtained were in close agreement with the work of Iglesia, *et al.*<sup>80</sup> on the oxidation of organosulfur compounds in which *tert*-butyl hydroperoxide (*t*-BuOOH) was employed. The oxidation reactivity decreased in the order of DBT > 4,6-DMDBT > BT > TH. From the overall catalysed batch oxidation process, sulfone-to-sulfoxide ratio and turnover frequencies (TOFs) increased as *t*-BuOOH-to-substrate ratio increased.

**Table 4.5** Oxidation of organosulfur compounds using *t*-BuOOH in the presence of [V<sup>IV</sup>O(sal-HBPD)], poly[V<sup>IV</sup>O(sal-AHBPD)] and using poly[V<sup>IV</sup>O(allylSB-co-EGDMA)]

SUBSTRATE	OXIDANT MOLE eq.	% SULFOXIDES			% SULFONES			% CONVERSION			SOO-to-SO ratio			TOF (h <sup>-1</sup> )		
		Cat 1	Cat 2	Cat 3	Cat 1	Cat 2	Cat 3	Cat 1	Cat 2	Cat 3	Cat 1	Cat 2	Cat 3	Cat 1	Cat 2	Cat 3
TH <sup>a</sup>	6.8	8	-	-	2	-	-	10	-	-	0.3	-	-	-	-	-
TH	6.8	7	6	-	3	4	-	10	10	-	0.4	0.7	-	19	17	-
TH*	2.0	17	5	-	13	40	-	30	45	-	0.8	8.0	-	47	106	-
TH*	6.8	20	1	12	24	59	41	44	60	53	1.2	59.0	3	69	141	58
BT <sup>a</sup>	6.8	13	-	-	2	-	-	15	-	-	0.2	-	-	-	-	-
BT	2.0	16	24	-	25	38	-	41	62	-	1.6	1.6	-	17	17	-
BT	6.8	15	11	15	58	70	56	73	81	71	3.9	6.4	4	30	22	12
DBT <sup>a</sup>	6.8	3	ND	-	20	-	-	23	-	-	6.7	-	-	-	-	-
DBT	2.3	8	ND	-	54	65	-	62	65	-	6.8	65.0	-	14	19	-
DBT	6.8	2	ND	2	86	98	85	88	98	87	43.0	98.0	43	18	29	5
4,6-DMDBT <sup>a</sup>	7.6	10	-	-	7	-	-	17	-	-	0.7	-	-	-	-	-
4,6-DMDBT	2.3	11	12	-	39	40	-	50	52	-	3.5	3.3	-	9	9	-
4,6-DMDBT	7.6	1	1	11	72	86	53	73	87	64	72.0	86.0	4.8	15	18	3

**Cat 1:** poly[V<sup>IV</sup>O(sal-AHBPD)], **Cat 2:** poly[V<sup>IV</sup>O(allylSB-co-EGDMA)] and **Cat 3:** [V<sup>IV</sup>O(sal-HBPD)].

TOF, h<sup>-1</sup>: (turnover frequency) moles of substrate converted per mole of metal ion (in the solid state catalyst) per hour. TOF (h<sup>-1</sup>) = (% conv.) × (substrate moles) / catalyst (vanadium) moles × h (time).

(\*) contains *tert*-butylammonium bromide (TBAB) = 0.01 g (0.000031 mol).

Substrates marked with (<sup>a</sup>) were oxidized in the absence of a catalyst.

TH: thiophene, BT: benzothiophene, DBT: dibenzothiophene, 4,6-DMDBT: 4,6-dimethyldibenzothiophene.

SO: sulfoxides, and SOO: Sulfones.

## 4.5 Recyclability studies

### 4.5.1 Reusability of heterogeneous catalysts poly[V<sup>IV</sup>O(sal-AHBPD)] and poly[V<sup>IV</sup>O(allylSB-co-EGDMA)] under batch process

The recyclability of poly[V<sup>IV</sup>O(sal-AHBPD)] and poly[V<sup>IV</sup>O(allylSB-co-EGDMA)] was investigated by regenerating and re-using the catalyst under the same conditions as illustrated in the oxidation study. Both catalysts showed signs of retaining activity after three catalytic cycles. Poly[V<sup>IV</sup>O(sal-AHBPD)] presented a low overall conversion after 3 cycles (**Figure 4.32**) as compared to poly[V<sup>IV</sup>O(allylSB-co-EGDMA)] which presented a higher activity after the same cycle under the same reaction conditions (**Figure 4.33**).

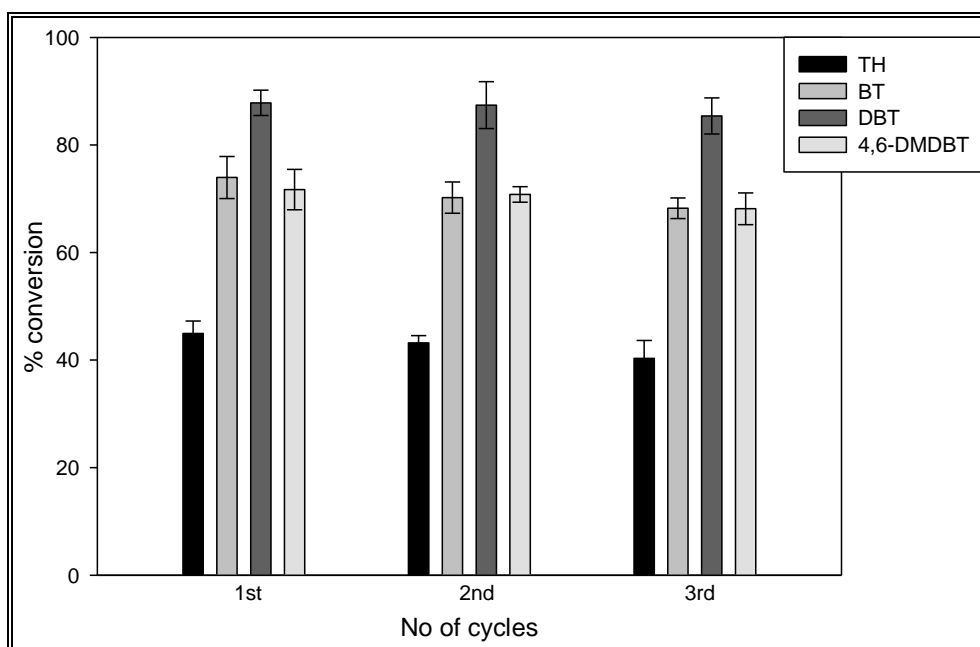


**Figure 4.32** Recyclability studies in the oxidation of thiophene (TH), benzothiophene (BT), dibenzothiophene (DBT) and 4,6-dimethyldibenzothiophene (4,6-DMDBT) using poly[V<sup>IV</sup>O(sal-AHBPD)] as catalyst. Time of reaction = 3 h.

The high activity of poly[V<sup>IV</sup>O(allylSB-co-EGDMA)], over poly[V<sup>IV</sup>O(sal-AHBPD)] confirmed that the former catalyst is resistant to sulfur poisoning as compared to the latter.



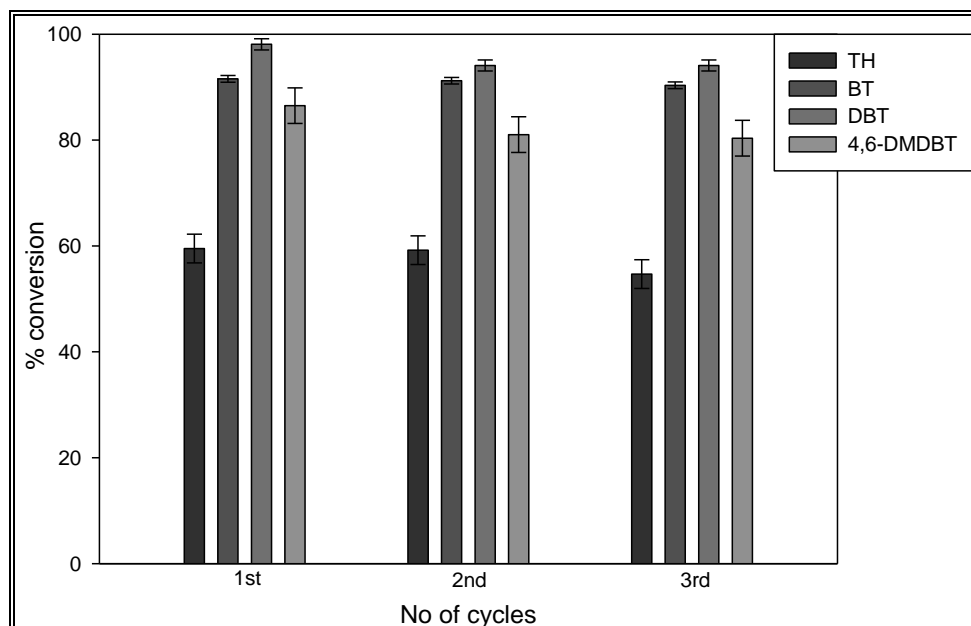


**Figure 4.33** Recyclability studies in the oxidation of thiophene (TH), benzothiophene (BT), dibenzothiophene (DBT) and 4,6-dimethyldibenzothiophene (4,6-DMDBT) using poly[V<sup>IV</sup>O(allylsB-co-EGDMA)] as catalyst. Time of reaction = 6 h.

## 4.6 Leaching studies

### 4.6.1 Determination of the amount of vanadium ion leached from poly[V<sup>IV</sup>O(sal-AHBPD)] and poly[V<sup>IV</sup>O(allylsB-co-EGDMA)] under batch process

To determine the quantity of vanadium leached, the product fractions were combined, concentrated and digested in nitric acid as described in the experimental section.<sup>314</sup> The vanadium leaching of poly[V<sup>IV</sup>O(sal-AHBPD)] gave no pattern. Vanadium leaching for thiophene catalysed oxidation was discovered to be the highest with a maximum of 3.7% vanadium leached after the 3<sup>rd</sup> oxidation. High amount of leaching were also recorded in benzothiophene oxidations (2<sup>nd</sup> cycle) (**Figure 4.34**). This could be attributed to the excess oxidant present in the system thereby causing leaching of the vanadium metal from the microspheres. Furthermore, this corresponded well to the slight drop in activity observed during the re-usability studies.

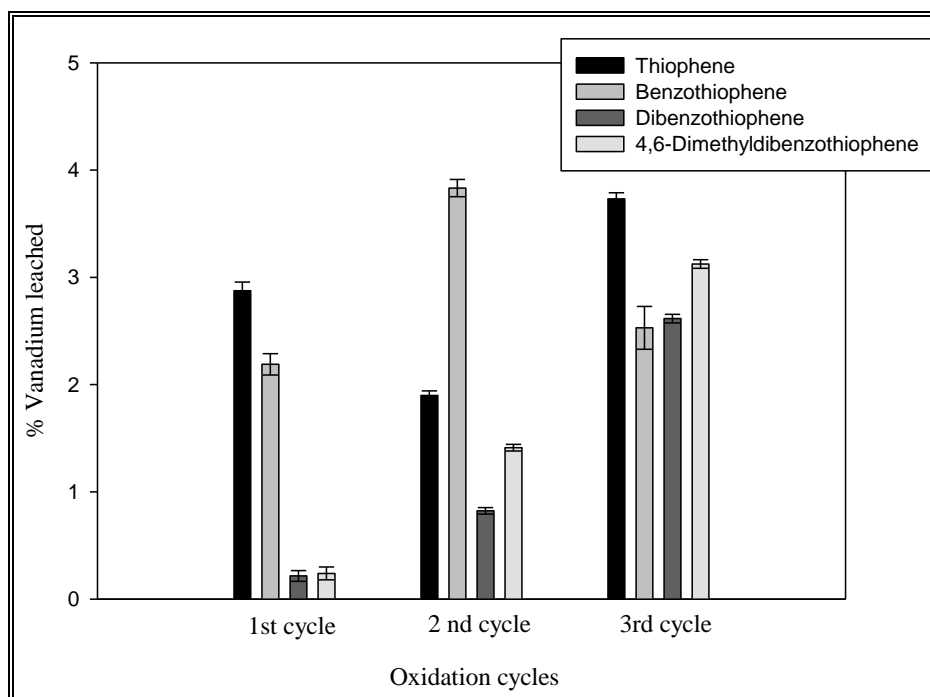


**Figure 4.34** Percentage vanadium leached from the polymer matrix, poly[V<sup>IV</sup>O(sal-AHBPD)] for the various oxidation reactions of organosulfur compounds. The amount of vanadium leached is presented for the 1<sup>st</sup>, 2<sup>nd</sup> and 3<sup>rd</sup> cycles. Time of reaction = 3 h.

For poly[V<sup>IV</sup>O(allylSB-co-EGDMA)], it was observed that the concentration of vanadium leached out increased as the oxidation cycle on the use of the catalyst increases. Total vanadium leached out after the 3<sup>rd</sup> cycle of thiophene oxidation was 1.6%, while it was lower for other substrates (**Figure 4.35**). From the results obtained, we see that poly[V<sup>IV</sup>O(allylSB-co-EGDMA)] is very stable as compared to poly[V<sup>IV</sup>O(sal-AHBPD)]. The functionalization of ligand and vanadyl on the surface of Merrified microspheres for poly[V<sup>IV</sup>O(sal-AHBPD)] synthesis is susceptible to the high vanadium leaching as compared to poly[V<sup>IV</sup>O(allylSB-co-EGDMA)] where functionalization takes place within polymer matrix. Leaching of vanadium from polymer support is attributed to the excess amount of oxidant in the oxidation system and collision between catalyst particles.

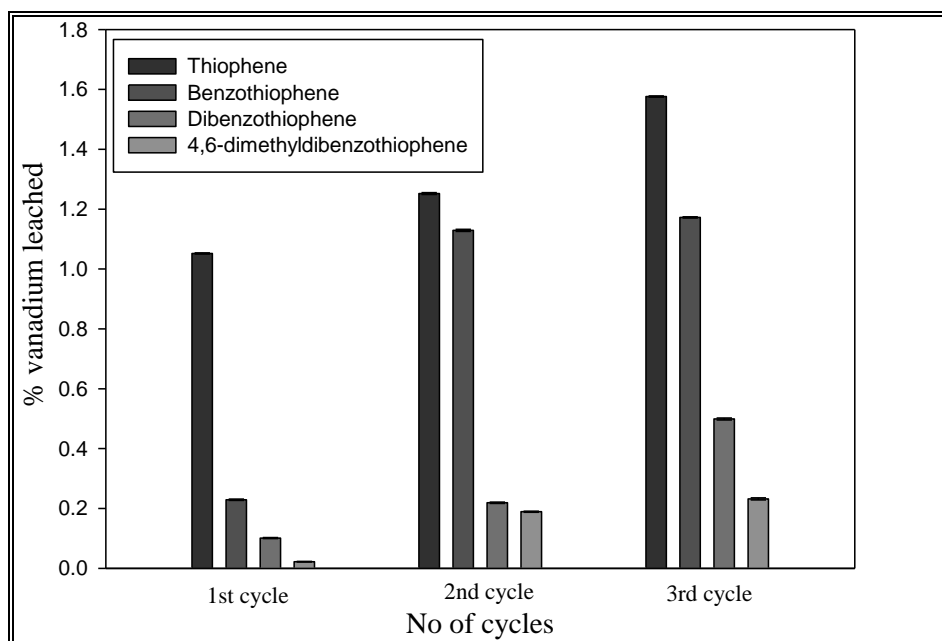


**Figure 4.35** Percentage vanadium leached from the polymer matrix, poly[V<sup>IV</sup>O(allylSB-co-EGDMA)] for the various oxidation reactions of organosulfur compounds. The amount of vanadium leached is presented for the 1<sup>st</sup>, 2<sup>nd</sup> and 3<sup>rd</sup> cycles. Time of reaction = 6 h.

#### 4.7 Catalysed oxidation of organosulfur compounds using poly[V<sup>IV</sup>O(sal-AHBPD)] and poly[V<sup>IV</sup>O(allylSB-co-EGDMA)] under continuous flow process

Most catalysed reaction processes are carried out under batch reactor conditions (Section 4.4).<sup>54, 341, 373, 377-378</sup> This process involves mechanical stirring of catalysts along side reactants and tends to damage catalyst support surface, thus leading to loss in catalyst activity.<sup>379</sup> Continuous flow process is seen as an emerging alternative in developing reaction methodology due to its importance in reducing the loss of catalyst activity for organic synthesis.<sup>381-382</sup> The process has been applied generally in biocatalysed processes<sup>383</sup> as well as in catalysed oxidation processes,<sup>187, 220</sup> as it preserves the surface of catalyst and catalyst support, and minimizes loss in catalyst activity. The process can be controlled, since reactants flow in an organized direction within the reactor, unlike the batch technique, in which reactants are not easily controlled. This section compared the catalytic oxidative activity of the two polymer-anchored oxidovanadium(IV) catalysts, poly[V<sup>IV</sup>O(sal-AHBPD)] and poly[V<sup>IV</sup>O(allylSB-

co-EGDMA)], on the organosulfur compounds under continuous flow oxidation process using the oxidation method described in **Chapter 2, Section 2.6**.

#### 4.7.1 Oxidation of thiophene under a continuous flow process

Tetrabutylammonium bromide (TBAB) 0.01 g (0.031 mmol) was added to the thiophene solution during its catalytic oxidation in order to increase the electron density of sulfur in the compound by interrupting conjugation, hence making the sulfur atom within the ring reactive.<sup>373, 374</sup> Oxidation in the presence of poly[V<sup>IV</sup>O(sal-AHBPD)] at a flow-rate of 1 mL/h gave an overall conversion of 79.1% with a sulfone-to-sulfoxide ratio of 1.3 (**Table 4.6, Figure 4.36a**), while at a higher flow-rate of 10 mL/h, the overall conversion dropped to 61% with a decrease in sulfone-to-sulfoxide ratio to 0.9. The catalyst poly[V<sup>IV</sup>O(allylSB-co-EGDMA)], under the same oxidation conditions as poly[V<sup>IV</sup>O(sal-AHBPD)] , presented an overall conversion of 71% with a sulfone-to-sulfoxide ratio of 1.7 at a flow-rate of 1 mL/h (**Table 4.6, Figure 4.36b**). At a flow-rate of 10 mL/h an overall conversion of 51% was recorded with a sulfone-to-sulfoxide ratio of 0.59. In both catalytic oxidation reactions of thiophene, it was observed that the overall conversions decreased as flow-rate increased, thus leading to higher sulfoxide yields. A mole ratio of (6.8:1) *t*-BuOOH-to-thiophene was employed throughout the study.

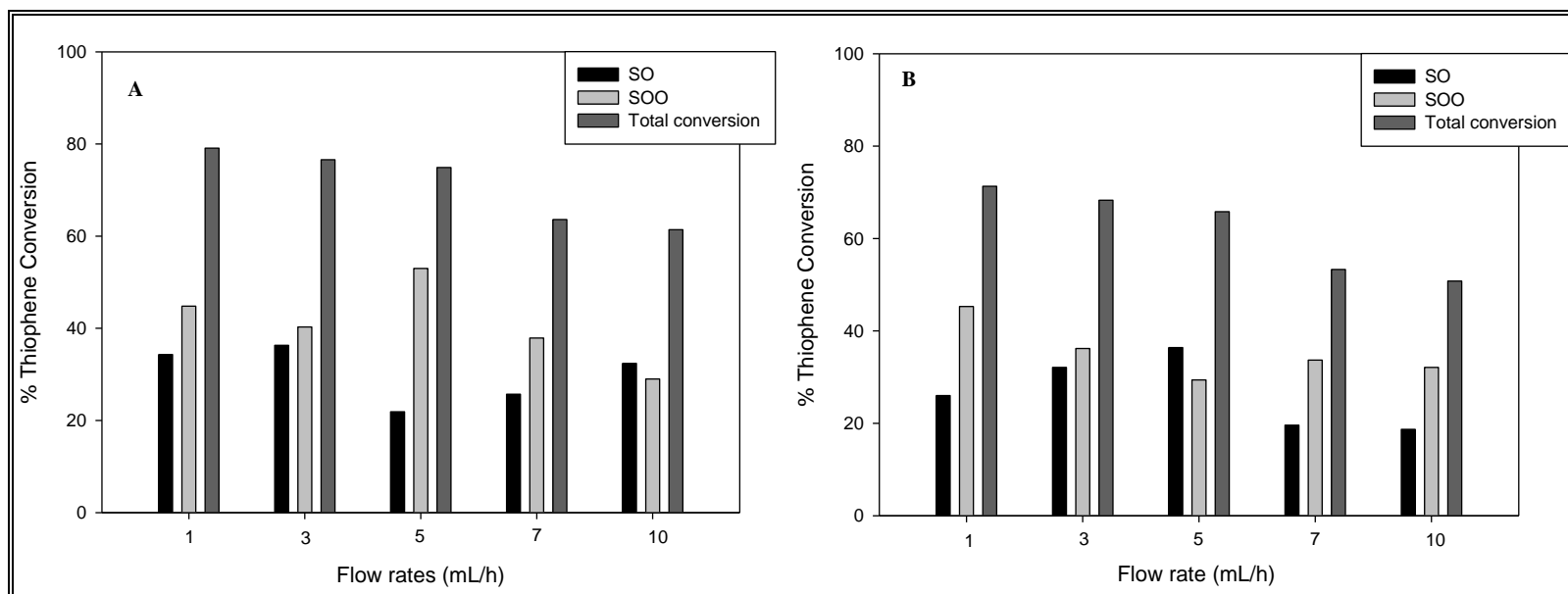


**Figure 4.36** Graph of % conversion for the oxidation of thiophene (TH). [*t*-BuOOH eq.] = 6.8, Temp.: 40°C, Toluene/Hexane (1:4) = 10 mL. Using (A) poly[V<sup>IV</sup>O(sal-AHBPD)] = 0.015 g (0.0135 mmol) and (B) poly[V<sup>IV</sup>O(allylsB-co-EGDMA)] = 0.024 g (0.0135 mmol).

#### 4.7.2 Oxidation of benzothiophene under a continuous flow process

The catalysed oxidation of benzothiophene gave a higher conversion when compared to the oxidation of thiophene owing to the higher electron density of the sulfur atom as displayed by benzothiophene (see **Figure 1.7**). For poly[V<sup>IV</sup>O(sal-AHBPD)] catalysed oxidation, the flow-rate of 1 mL/h gave the highest overall conversion of 90% (**Table 4.6, Figure 4.37a**) with an observed sulfone-to-sulfoxide ratio of 14.0, while at a higher flow-rate of 10 mL/h an overall conversion of 83% was observed with a decrease in sulfone-to-sulfoxide ratio to 1.8. An overall conversion of 89% was obtained when poly[V<sup>IV</sup>O(allylSB-co-EGDMA)] was employed at a flow-rate of 1 mL/h (**Table 4.6**), in which a sulfone-to-sulfoxide ratio of 16.8 was obtained (**Table 4.6, Figure 4.37b**), but on increasing the flow-rate to 10 mL/h, the sulfone-to-sulfoxide ratio decreased to 4.9 with a reduction in the overall conversion to 75%. As observed in thiophene oxidation, as the flow-rate increased, the contact time between the reactant mixture and catalyst tends to reduce thereby limiting catalysed oxidation conversions. A mole equivalent of 6.8 for *t*-BuOOH-to-benzothiophene was employed in the catalysed oxidation reaction.

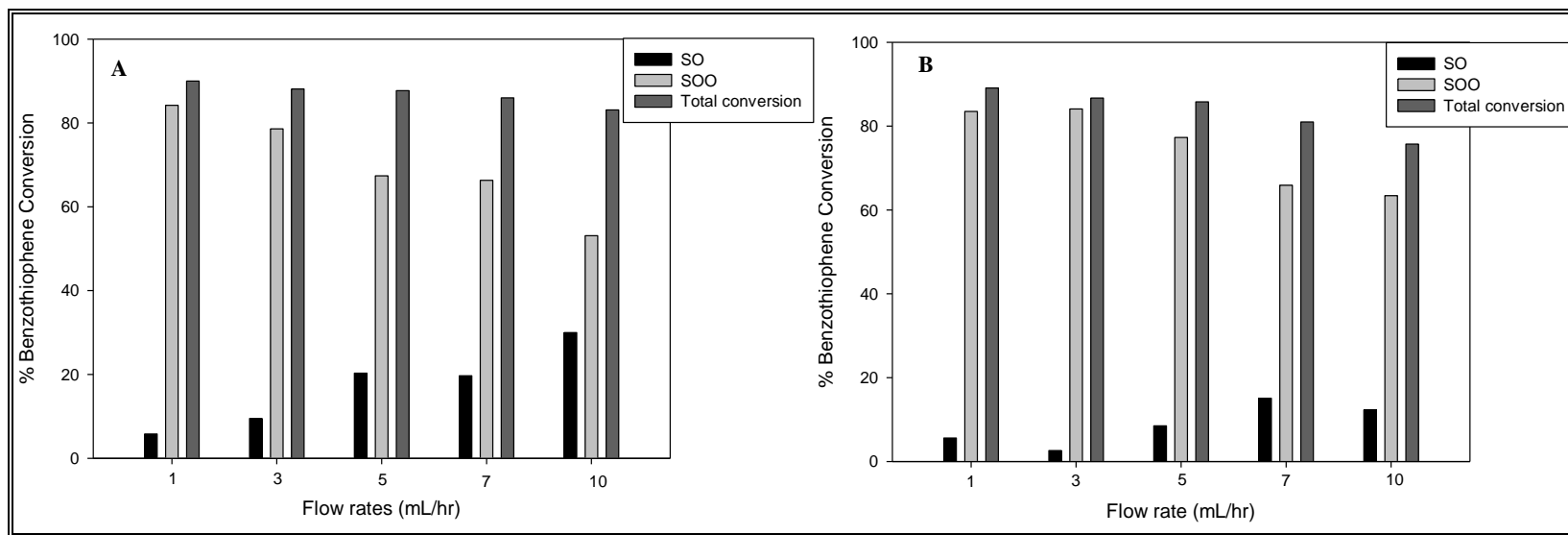


**Figure 4.37** Graph of % conversion for the oxidation of benzothiophene (BT). [*t*-BuOOH eq.] = 6.8, Temp. = 40°C, Toluene/Hexane (1:4) = 10 mL. Using (A) poly[V<sup>IV</sup>O(sal-AHBPD)] = 0.015 g (0.0135 mmol) and (B) poly[V<sup>IV</sup>O(allylSB-co-EGDMA)] = 0.024 g (0.0135 mmol).

### 4.7.3 Oxidation of dibenzothiophene under a continuous flow process

The catalysed oxidation of dibenzothiophene by poly[V<sup>IV</sup>O(sal-AHBPD)] at a flow-rate of 1 mL/h, gave an overall conversion of 98% (Table 4.6, Figure 4.38a), and the conversion, however, decreased to 96% when a flow-rate of 10 mL/h was employed. When poly[V<sup>IV</sup>O(allylSB-co-EGDMA)] was employed as catalyst, an overall conversion of 99% occurred at a flow-rate of 1 mL/h (Table 4.6, Figure 4.38b), but upon increasing the flow-rate to 10 mL/h the overall oxidation reduced to 93%. The high conversion of dibenzothiophene was ascribed to the high electron density of sulfur atom in dibenzothiophene which makes it more reactive as compared to thiophene and benzothiophene. No sulfoxides were detected in the oxidation reaction.



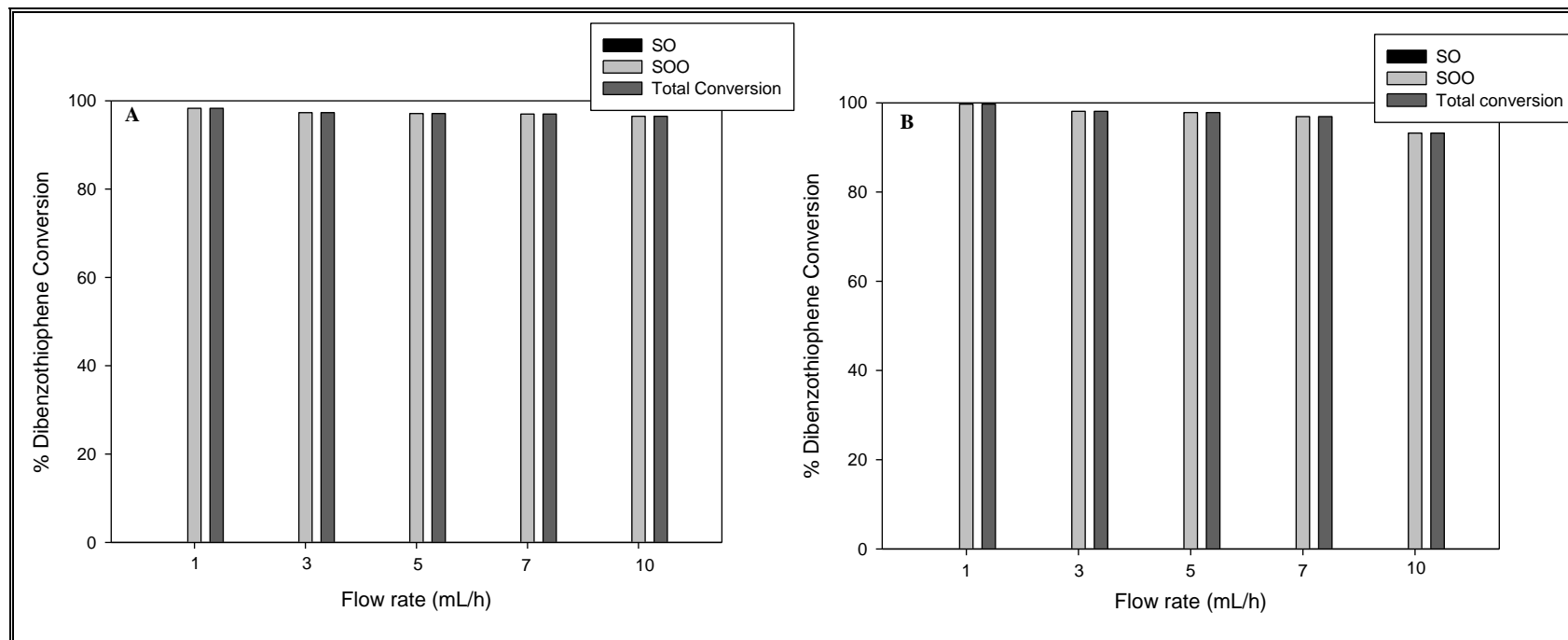


**Figure 4.38** Graph of % conversion for the oxidation of dibenzothiophene (DBT). [*t*-BuOOH eq.] = 6.8, Temp.: 40°C, Toluene/Hexane (1:4) = 10 mL. Using (A) poly[V<sup>IV</sup>O(sal-AHBPD)] = 0.015 g (0.0135 mmol) and (B) poly[V<sup>IV</sup>O(allylSB-co-EGDMA)] = 0.024 g (0.0135 mmol).

#### 4.7.4 Oxidation of 4,6-dimethyldibenzothiophene under a continuous flow process

The catalysed oxidation of 4,6-dimethyldibenzothiophene presented a reduction in its overall conversion when compared to dibenzothiophene. This is attributed to its bulkiness, sterically hindering the electron-rich sulfur atoms from being oxidized. With poly[V<sup>IV</sup>O(sal-AHBPD)] as the oxidation catalyst, an overall conversion of 91% at a flow-rate of 1 mL/h was recorded with a sulfone-to-sulfoxide ratio of 90.0 (**Figure 4.39a**, **Table 4.6**), while at a higher flow-rate of 10 mL/h the overall conversion decreased to 57% and the sulfone-to-sulfoxide ratio decreased to 2.6. However, when poly[V<sup>IV</sup>O(allylSB-co-EGDMA)] was employed for oxidation at a flow-rate of 1 mL/h an overall conversion of 88% was achieved (**Figure 4.39b**, **Table 4.6**), while at a flow-rate of 10 mL/h the overall conversion decreased to 60%. The sulfone-to-sulfoxide ratio decreased from 5.3 to 3.6 when changing the flow-rate from 1 mL/h to 10 mL/h.

The high conversion of dibenzothiophene and 4,6-dimethyldibenzothiophene was ascribed to the high electron density of sulfur atoms in the compound as compared to thiophene and benzothiophene (see **Section 1.2.2**, **Figure 1.7**). The higher the electron density of sulfur atom in an organosulfur compound the more reactive the sulfur atom in accepting electron from a donating group. The sulfone-to-sulfoxide ratio also increased as the flow-rate decreased indicating that more sulfones were formed at lower flow-rates as a result of the longer contact time between the reactant mixture and catalyst. From the catalysed oxidation of the organosulfur compounds, the overall conversions and turnover frequencies (TOFs) decreased steadily as flow-rate increased. The relative role that liquid mass transfer and transport mechanisms play in the catalysed oxidation reaction system is important, as chemical species movement from an area of high chemical potential to an area low chemical potential are encouraged *via* diffusion.<sup>384</sup> It is to be noted that the main factors governing mass transfer are diffusion, capillary flow, surface diffusion and hydrodynamic mechanisms.<sup>384</sup>

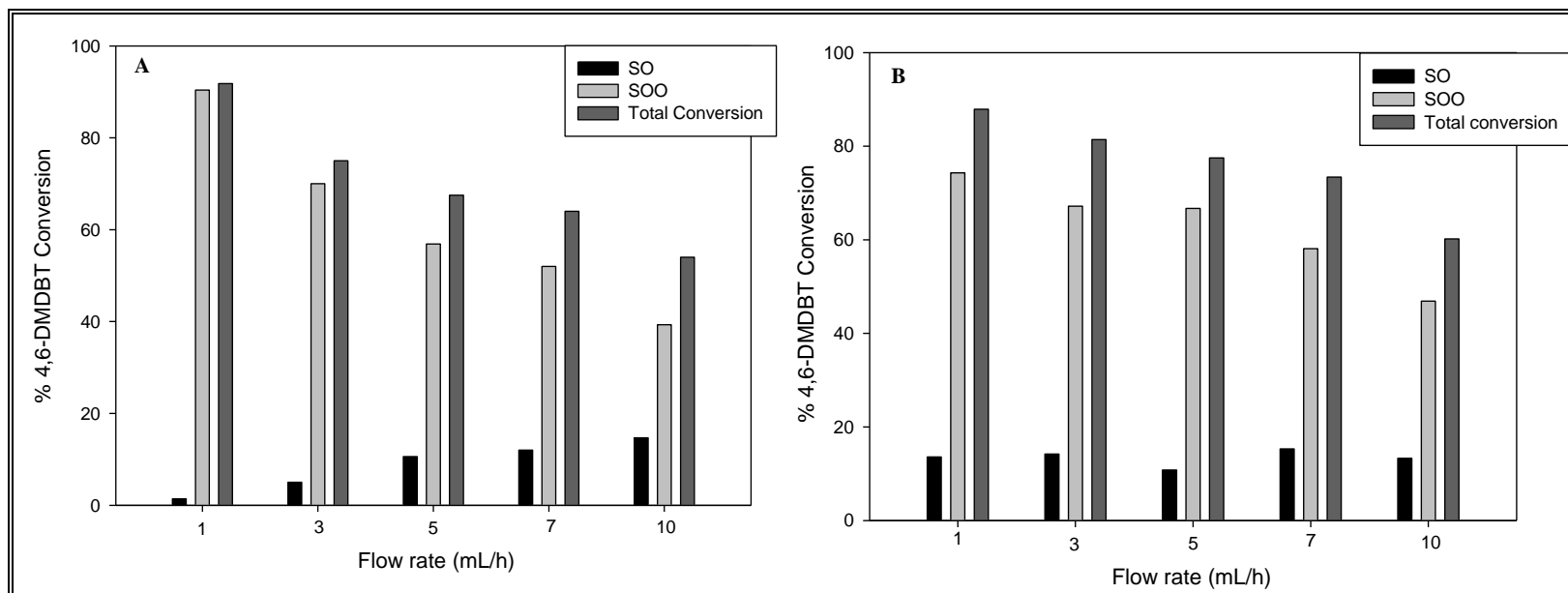


**Figure 4.39** Graph of % conversion for the oxidation of 4,6-dimethyldibenzothiophene (4,6-DMDBT). [*t*-BuOOH eq.] = 7.6, Temp.: 40°C, Toluene/Hexane (1:4) = 10 mL. Using (A) poly[V<sup>IV</sup>O(sal-AHBPD)] = 0.015 g (0.0135 mmol) and (B) poly[V<sup>IV</sup>O(allylSB-co-EGDMA)] = 0.024 g (0.0135 mmol).

**Table 4.6** Catalysed oxidation of organo-sulfur compounds using *t*-BuOOH in the presence of p[V<sup>IV</sup>O(sal-AHBPD)] (Cat 1) and poly[V<sup>IV</sup>O(allylSB-co-EGDMA)] (Cat 2).

SUBSTRATE	Flow-rate (mL/h)	% SULFOXIDES		% SULFONES		% CONVERSION		SOO-to-SO ratio		TOF (h <sup>-1</sup> )	
		Cat 1	Cat 2	Cat 1	Cat 2	Cat 1	Cat 2	Cat 1	Cat 2	Cat 1	Cat 2
TH*	1	34	26	45	45	79	71	1.3	1.7	1498	1346
TH*	3	36	32	40	36	76	68	1.1	1.1	1441	1290
TH*	5	22	36	53	29	75	65	2.4	0.8	1422	1233
TH*	7	26	20	38	33	64	53	1.5	1.7	1214	1005
TH*	10	32	19	29	32	61	51	0.9	1.7	1157	967
BT	1	6	5	84	84	90	89	14.0	16.8	293	290
BT	3	10	2	78	84	88	86	7.8	42.0	287	280
BT	5	20	8	67	77	87	85	3.8	9.6	284	277
BT	7	20	15	66	66	86	81	3.3	4.4	280	264
BT	10	30	12	53	63	83	75	1.8	4.9	271	244
DBT	1	ND	ND	98	99	98	99	98.0	99.0	235	238
DBT	3	ND	ND	97	98	97	98	97.0	98.0	233	235
DBT	5	ND	ND	97	98	97	98	97.0	98.0	233	235
DBT	7	ND	ND	97	97	97	97	97.0	97.0	232	233
DBT	10	ND	ND	96	93	96	93	96.0	93.0	230	223
4,6-DMDBT	1	1	14	90	74	91	88	90.0	5.3	191	185
4,6-DMDBT	3	5	14	70	67	75	81	14.0	4.8	158	170
4,6-DMDBT	5	10	11	57	66	67	77	5.7	6.0	141	162
4,6-DMDBT	7	12	15	52	58	64	73	4.3	3.9	135	154
4,6-DMDBT	10	15	13	39	47	54	60	2.6	3.6	114	126

**Cat 1:** poly[V<sup>IV</sup>O(sal-AHBPD)] and **Cat 2:** poly[V<sup>IV</sup>O(allylSB-co-EGDMA)].

\*Tetrabutylammonium bromide (TBAB) (0.01 g, 0.031 mmol) added to Thiophene (TH).

Moles of catalyst (vanadium content) employed =  $1.35 \times 10^{-5}$  moles. Thiophene (TH) = 0.54 g (0.0064 mol); Benzothiophene (BT) = 0.15 g (0.0011 mol); Dibenzothiophene (DBT) = 0.15 g, (0.00081 mol); 4,6-dimethyldibenzothiophene (4,6-DMDBT) = 0.15 g (0.00071 mol).

TOF (h<sup>-1</sup>) = (% conv.) × (substrate moles) / catalyst (vanadium) moles × h (time). Maximum conversion time of 1 h was employed.

SO: sulfoxides, and SOO: sulfones.

#### 4.8 Leaching studies of poly[V<sup>IV</sup>O(sal-AHBPD)] and poly[V<sup>IV</sup>O(allylsB-co-EGDMA)] under continuous flow oxidation process

Vanadium(IV) incorporated on polymer microspheres, poly[V<sup>IV</sup>O(sal-AHBPD)] and poly[V<sup>IV</sup>O(allylsB-co-EGDMA)], significantly influences the oxidation of organosulfur compounds under flow conditions. However, it was important to evaluate the leaching of vanadium from the polymer support. The quantity of vanadium leached from oxidation reactions was determined as described in **Chapter 2, Section 2.4**. The degree of vanadium leaching was in the order of TH > BT > DBT > 4,6-DMDBT, which corresponds to the order of bulkiness of the organosulfur compounds. The level of leaching is also dependent on (1) the amount of oxidant, (2) the amount of substrate, and (3) the oxidation reaction flow-rate. The amount of oxidant was regarded as the main reason for leaching in this study, and this is always a challenge as the desirable theoretical peroxide facilitated oxidation stoichiometry {substrate-to-oxidant (1:2)} is not sufficient to carry-out complete oxidation. Hence, a higher amount of oxidant is needed to overcome the oxidation limitations. The flow-rate influences leaching as it determines the contact time between oxidant and catalyst, hence at high flow-rates low leaching was observed. Generally, low vanadium quantities were leached from both catalysts (**Tables 4.7**), and this indicated that vanadium within the functionalized polymer supports was stable.

**Table 4.7** The leaching studies on the poly[V<sup>IV</sup>O(sal-AHBPD)] (Cat 1) and poly[V<sup>IV</sup>O(allylSB-co-EGDMA)] (Cat 2) microspheres

FLOW-RATE (mL/h)	10		7		5		3		1	
	Cat 1	Cat 2	Cat 1	Cat 2	Cat 1	Cat 2	Cat 1	Cat 2	Cat 1	Cat 2
<b>TH (%)</b>	1.152 (0.002)	1.041 (0.004)	1.232 (0.002)	1.124 (0.005)	1.393 (0.002)	1.233 (0.006)	1.637 (0.002)	1.467 (0.002)	2.333 (0.002)	2.113 (0.003)
<b>BT (%)</b>	0.529 (0.002)	0.432 (0.003)	0.699 (0.003)	0.453 (0.002)	0.849 (0.003)	0.672 (0.004)	1.089 (0.003)	0.832 (0.003)	1.239 (0.003)	1.019 (0.003)
<b>DBT (%)</b>	0.129 (0.002)	0.129 (0.001)	0.232 (0.004)	0.232 (0.005)	0.412 (0.001)	0.412 (0.002)	0.721 (0.004)	0.721 (0.003)	1.029 (0.003)	1.029 (0.002)
<b>4,6-DMDBT (%)</b>	0.122 (0.001)	0.110 (0.004)	0.221 (0.001)	0.132 (0.003)	0.241 (0.004)	0.203 (0.004)	0.332 (0.003)	0.301 (0.001)	0.529 (0.005)	0.411 (0.004)

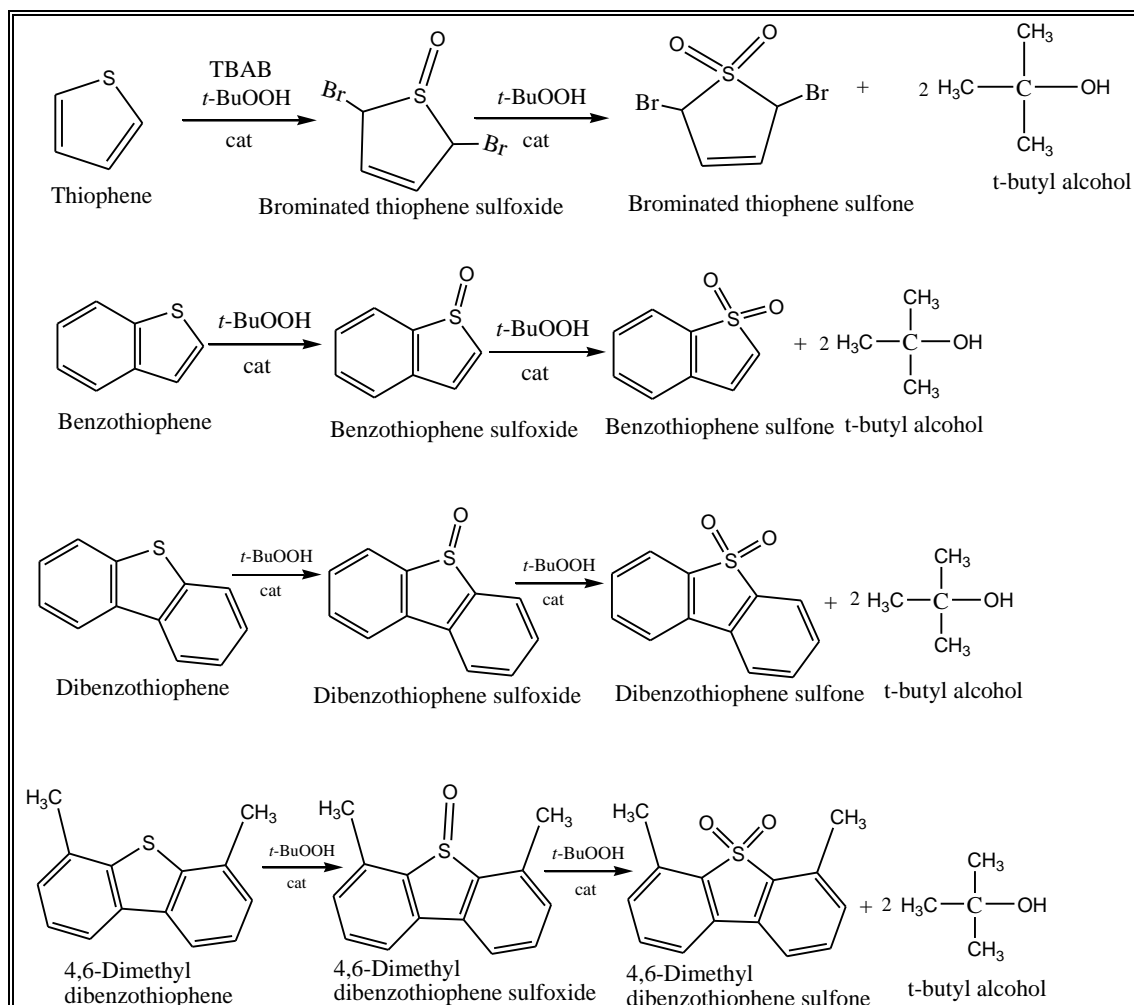
TH (thiophene), BT (benzothiophene), DBT (dibenzothiophene) and 4,6-DMDBT (4,6-dimethyldibenzothiophene).

NB: Standard deviations (SD) are given in parenthesis.

#### 4.9 General discussion on the catalysed oxidation of organosulfur compounds using [V<sup>IV</sup>O(sal-HBPD)], poly[V<sup>IV</sup>O(sal-AHBPD)] and poly[V<sup>IV</sup>O(allylsB-co-EGDMA)]

The oxidation pattern for the various organosulfur compounds and their expected products (sulfoxide and sulfone derivatives) are presented in **Scheme 4.4**. The oxidation reactivity decreased in the order of DBT > 4,6-DMDBT > BT > TH. The order of reactivity was governed by the electron density of sulfur and order of bulkiness (steric hinderance) of the organosulfur compounds. Thiophene and benzothiophene exhibited the lowest reactivity that was attributed to the significantly lower electron density of 5.696 and 5.716 on the sulfur atom of thiophene and benzothiophene, respectively.<sup>131</sup> However, for DBT and 4,6-DMDBT the electron density on the sulfur is relatively close with a very small difference (5.756 and 5.760 respectively). Therefore, the reactivity in terms of oxidation of the sulfur compounds, DBT and 4,6-DMDBT, was governed by the steric hindrance of the methyl groups which became an obstacle for the approach of the sulfur atom by the catalytically active species. The relative reactivity of the above organosulfur compounds was relatively comparable to the observations of Otsuki *et al.*,<sup>54</sup> which was based on the electron density at the sulfur atom in each of the compounds.

Poly[V<sup>IV</sup>O(allylsB-co-EGDMA)] gave higher overall oxidation (98%) for dibenzothiophene (DBT) which accounts for up to 70% of total organic sulfur in diesel,<sup>69</sup> as compared to the homogeneous catalyst [V<sup>IV</sup>O(sal-HBPD)] and polymer-anchored catalyst poly[V<sup>IV</sup>O(sal-AHBPD)] which gave 87% and 97%, respectively. This indicated the potential use of oxidovanadium(IV) catalyst, poly[V<sup>IV</sup>O(allylsB-co-EGDMA)], for the oxidation of hydro-treated diesel.



**Scheme 4.4** Oxidation studies on the different organosulfur compounds ( $t\text{-BuOOH}$ ) = *tert*-butylhydroperoxide; TBAB = *tert*-butylammonium bromide.

#### 4.10 Characterization of oxidized organosulfur compounds

Precipitates (sulfones) were formed after the completion of the oxidation process under batch conditions. These precipitates were collected by filtration and then dried for further analysis. The products were found to be soluble in DMSO, and the  $^1\text{H}$  NMR spectra of the products were recorded without purification. Thiophene-oxidation precipitates were formed on cooling the initial obtained liquid mixture to  $0^\circ\text{C}$  overnight.

##### 4.10.1 Microanalysis of oxidized products

Microanalysis of benzothiophene sulfone ( $\text{BTO}_2$ ): *Anal.* Calcd(found) for  $\text{C}_8\text{H}_6\text{O}_2\text{S}$  (%): C, 57.81(57.49); H, 3.64(3.89); S 19.29(19.02). For dibenzothiophene sulfone ( $\text{DBTO}_2$ ): *Anal.*



Calcd(found) for  $C_{12}H_{10}O_2S$  (%): C, 66.65(66.02); H, 3.73(4.04); S 14.83(14.83). For 4,6-dimethyldibenzothiophene sulfone (4,6-DMDBTO<sub>2</sub>): *Anal.* Calcd(found) for  $C_{14}H_{12}O_2S$  (%): C 68.38(68.38); H, 4.95(5.25); S, 13.12(12.83). Microanalysis results for thiophene sulfone were inconclusive.

#### 4.10.2 Nuclear magnetic resonance (NMR) characterization of oxidation products

<sup>1</sup>H NMR spectra of organosulfur compounds and corresponding sulfones in DMSO-*d*<sub>6</sub> present signal shifts. These spectral data are reported below:

Thiophenes (TH): <sup>1</sup>H NMR ( $\delta$ , ppm in DMSO)  $\delta$  7.52 (d,  $J = 5.6$ , 1H), 7.19 (s, 1H). Thiophenes sulfone (THO<sub>2</sub>) <sup>1</sup>H NMR ( $\delta$ , ppm in DMSO)  $\delta$  7.83 (s, 1H), 7.66 (d,  $J = 23.3$ , 2H), 7.34 (s, 1H).

Benzothiophenes (BT): <sup>1</sup>H NMR ( $\delta$ , ppm in DMSO)  $\delta$  8.00 (s,  $J = 4.2$ , 1H), 7.90 (d,  $J = 4.2$ , 1H), 7.75 (s, 1H), 7.46 (s, 1H) 7.38 (d,  $J = 2.3$ , 2H). Benzothiophenes sulfone (BTO<sub>2</sub>): <sup>1</sup>H NMR ( $\delta$ , ppm in DMSO)  $\delta$  7.83 (d,  $J = 7.2$ , 1H), 7.69 (t,  $J = 7.4$ , 1H), 7.62 (t,  $J = 9.1$ , 3H), 7.34 (d,  $J = 6.8$ , 1H).

Dibenzothiophene (DBT): <sup>1</sup>H NMR ( $\delta$ , ppm in DMSO) ( $\delta$ , ppm); 8.39 (m,  $J = 3.0$ , 2 H), 8.05 (m, 2 H), 7.53 (m, 2 H). Dibenzothiophene sulfone (DBTO<sub>2</sub>): <sup>1</sup>H NMR ( $\delta$ , ppm in DMSO): 8.22 (d,  $J = 7.7$ , 2 H), 8.00 (d,  $J = 7.6$ , 2 H), 7.82 (t,  $J = 7.6$ , 2 H), 7.67 (t,  $J = 7.6$ , 2 H).

4,6-Dimethyldibenzothiophene sulfone (4,6-DMDBTO<sub>2</sub>): <sup>1</sup>H NMR ( $\delta$ , ppm in DMSO): 7.98 (d,  $J = 7.6$ , 2 H), 7.66 (t, 2 H), 7.44 (d,  $J = 7.5$ , 2 H), 2.48 (s, 6 H).

4,6-Dimethyldibenzothiophene (4,6-DMDBT) was insoluble in DMSO-*d*<sub>6</sub>. From the GC-MS data, a mass/charge (*m/e*) of 166, 216 and 246 for BTO<sub>2</sub>, DBTO<sub>2</sub> and 4,6-DMDBTO<sub>2</sub> respectively was identified.

#### 4.10.3 FT-IR spectroscopic characterization of oxidation products

FT-IR spectroscopy was employed for further characterization of the oxidation products. The  $\nu(S=O)$  in sulfones which appeared around 1365-1340  $cm^{-1}$  and 1200-1100  $cm^{-1}$  were identified for the various products and shifts in  $\nu(C-S)$  between 730-800  $cm^{-1}$  were also observed after oxidation (**Table 4.8**). The band shift has previously been used by Castillo *et al.*,<sup>377</sup> to ascertain whether products were formed. **Figure 4.40** compared the infrared spectra of the individual organosulfur compounds and

their respective sulfone derivatives. From the thiophene oxidized product, a bromide containing sulfone compound was formed (**Scheme 4.4**) with the C-Br and C-S stretching bands observed to occur around the same region ( $700$  to  $730\text{ cm}^{-1}$ ), it was therefore not possible to use the FT-IR to conclude on the formation of the brominated product. A further test to confirm the presence of bromine (Br) in the thiophene oxidation product was conducted. To  $0.05\text{ g}$  of the oxidation product, excess dilute  $\text{HNO}_3$  ( $0.005\text{ M}$ ) followed by dilute aqueous silver nitrate ( $\text{AgNO}_3$ ) solution was added. The formation of creamy silver bromide precipitate confirmed the existence of bromides on the sulfone compounds.

**Table 4.8** The  $\nu(\text{C-S})$  band shifts observed for the various individual oxidation products with respect to their initial starting materials.

Organosulfur compounds	Thiophene (TH)	Benzothiophene (BT)	Dibenzothiophene (DBT)	4,6-Dimethyldibenzothiophene (4,6-DMDBT)
Before oxidation ( $\text{cm}^{-1}$ )	703	735	731	764
After oxidation ( $\text{cm}^{-1}$ )	712	750	755	778

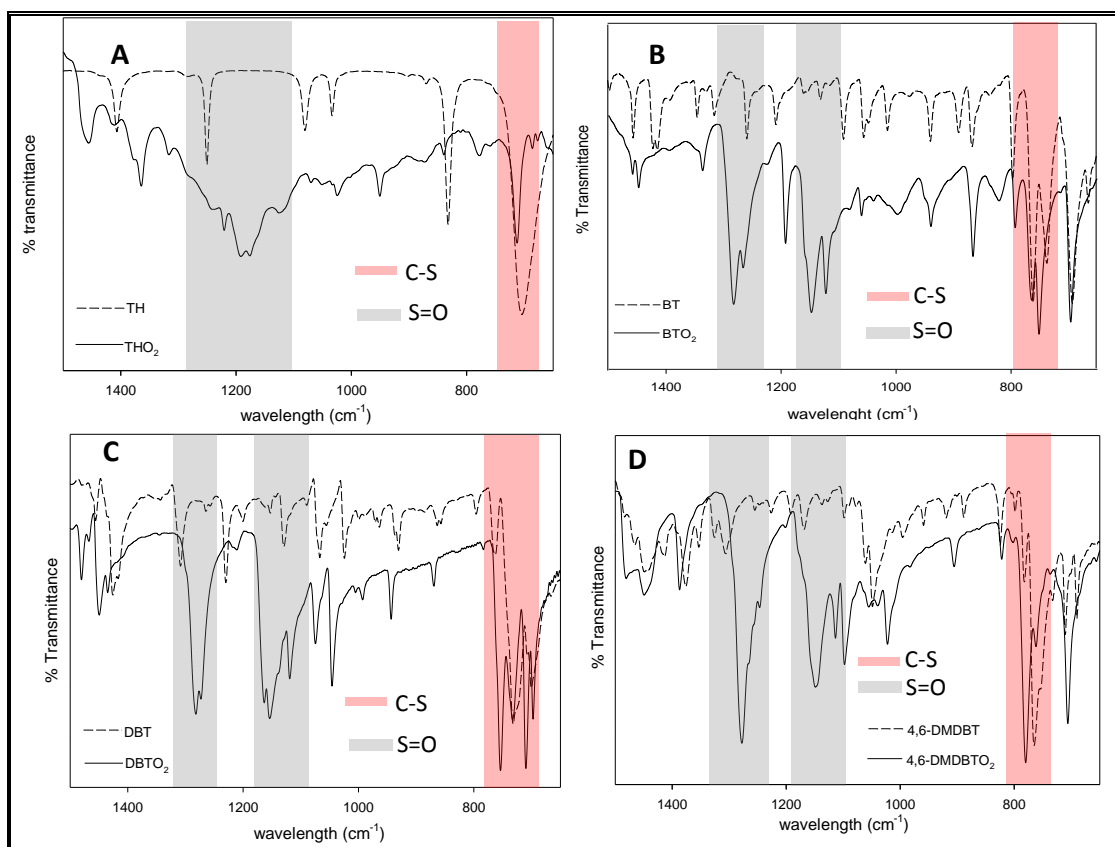


**Figure 4.40** FT-IR of (A) Thiophene (TH) and bromine-containing thiophene sulfone (THO<sub>2</sub>), (B) Benzothiophene (BT) and benzothiophene sulfone (BTO<sub>2</sub>), (C) Dibenzothiophene (DBT) and dibenzothiophene sulfone (DBTO<sub>2</sub>), (D) 4,6-Dimethyldibenzothiophene (4,6-DMDBT) and 4,6-dimethyldibenzothiophene sulfone (4,6-DMDBTO<sub>2</sub>).

## 4.11 Catalysed oxidation of model fuel oil

### 4.11.1 Catalysed oxidation of model fuel oil using poly[V<sup>IV</sup>O(sal-AHBPD)] and poly[V<sup>IV</sup>O(allylsB-co-EGDMA)] under batch process

Equivalent mass (0.15 g) of refractory sulfur containing compounds {benzothiophene (BT), dibenzothiophene (DBT) and 4,6-methyldibenzothiophene (4,6-DMDBT)} was dissolved in 10 mL of toluene/hexane (1:4) in the presence of a catalyst, poly[V<sup>IV</sup>O(sal-AHBPD)] (0.015 g, 0.0405 mmol) and poly[V<sup>IV</sup>O(allylsB-co-EGDMA)] (0.072 g, 0.0405 mmol). The reaction was assumed to begin on addition of an aqueous solution of *tert*-butylhydroperoxide (*t*-BuOOH) at 40°C for an oxidation time of required oxidation time of 3 h and 6 h for poly[V<sup>IV</sup>O(sal-AHBPD)] and poly[V<sup>IV</sup>O(allylsB-co-EGDMA)] respectively. A detailed batch oxidation process is described in **Section 2.5**. The 0.072 g of poly[V<sup>IV</sup>O(allylsB-co-EGDMA)] and 0.044 g of poly[V<sup>IV</sup>O(sal-AHBPD)] contained the same amount of vanadium.

The chromatograms for the catalysed oxidation reaction using poly[V<sup>IV</sup>O(sal-AHBPD)] showed that 70%, 86% and 73% of benzothiophene, dibenzothiophene and 4,6-dimethyldibenzothiophene respectively were oxidized to sulfoxides and sulfones (**Figure 4.41**). From the chromatograms (**Figure 4.42**), most of the sulfur compounds were oxidized to sulfones (i.e. 98% benzothiophene, 87% dibenzothiophene and 94% 4,6-methyldibenzothiophene). From the model fuel oxidation study, we see that poly[V<sup>IV</sup>O(allylsB-co-EGDMA)] presented the highest overall oxidation. Therefore, the best catalyst, poly[V<sup>IV</sup>O(allylsB-co-EGDMA)], was applied for the oxidation of hydrotreated fuel.

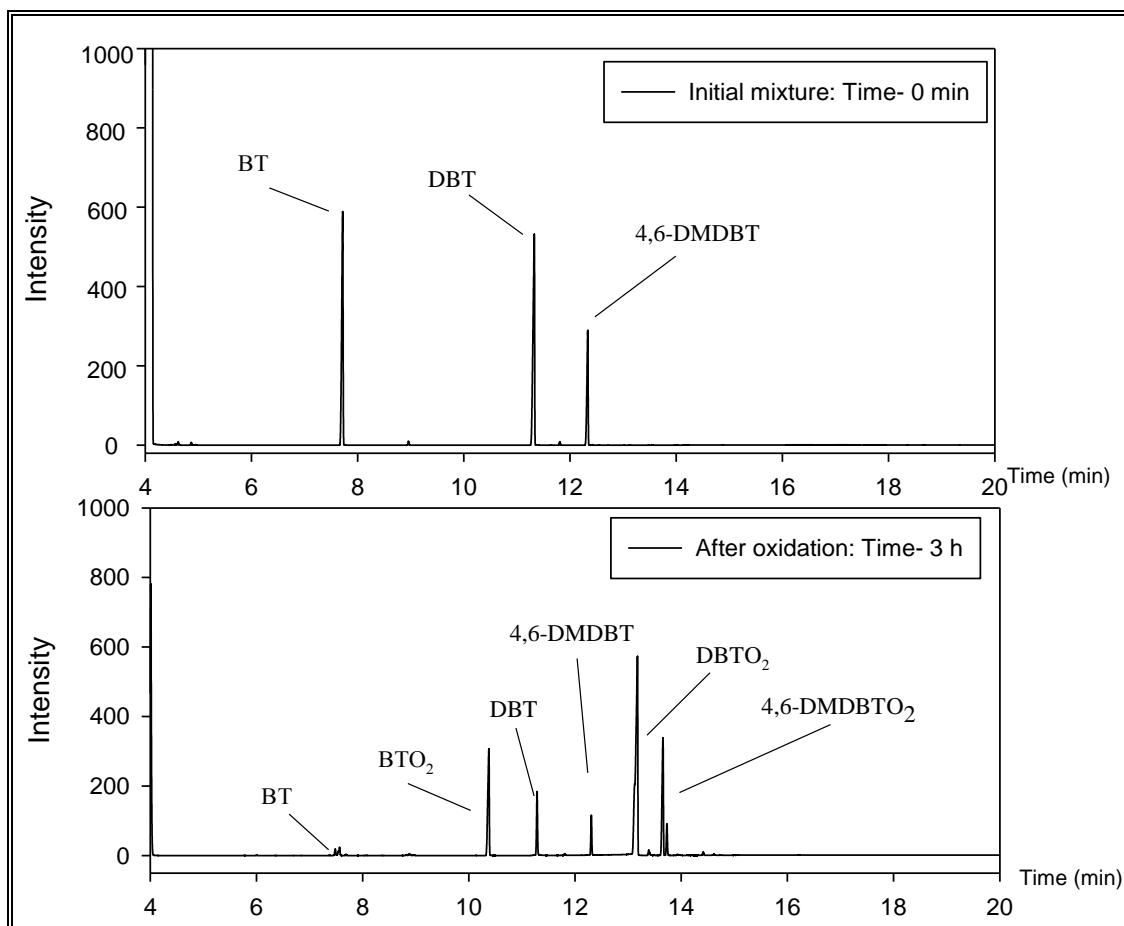


**Figure 4.41** GC-FID chromatograms of organosulfur mixture {benzothiophene (BT), dibenzothiophene (DBT) and 4,6-dimethyldibenzothiophene (4,6-DMDBT)} before and after oxidation using poly[V<sup>IV</sup>O(sal-AHBPD)] as catalyst. poly[V<sup>IV</sup>O(sal-AHBPD)] = 0.045 g (0.0405 mmol), Temp.= 40°C. Toluene/Hexane (1:4) = 10 mL. Benzothiophene sulfone (BTO<sub>2</sub>), dibenzothiophene sulfone (DBTO<sub>2</sub>) and 4,6-dimethyldibenzothiophene sulfone (4,6-DMDBTO<sub>2</sub>).

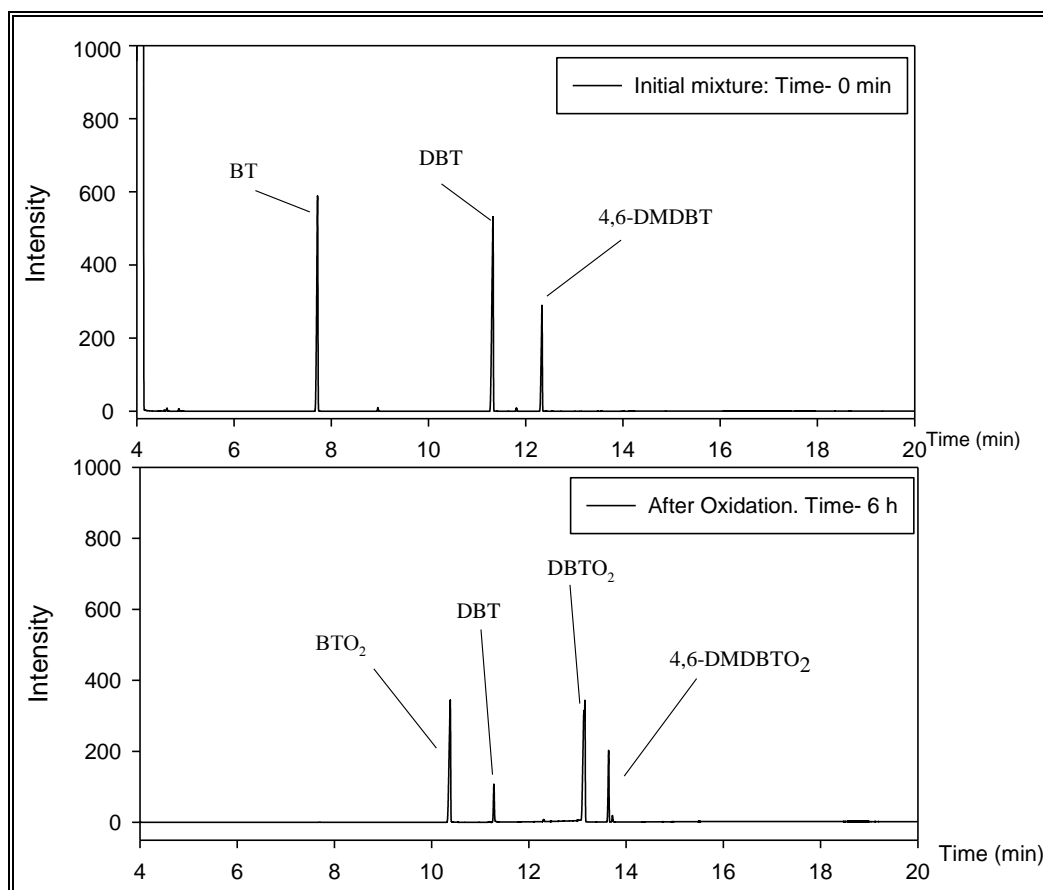


**Figure 4.42** GC-FID chromatograms of organosulfur mixture {benzothiophene (BT), dibenzothiophene (DBT) and 4,6-dimethyldibenzothiophene (4,6-DMDBT)} before and after oxidation using poly[V<sup>IV</sup>O(allylSB-co-EGDMA)] as catalyst. poly[V<sup>IV</sup>O(allylSB-co-EGDMA)] = 0.072 g (0.0405 mmol), Temp. = 40°C, Toluene/Hexane (1:4) = 10 mL. Benzothiophene sulfone (BTO<sub>2</sub>), dibenzothiophene sulfone (DBTO<sub>2</sub>) and 4,6-dimethyldibenzothiophene sulfone (4,6-DMDBTO<sub>2</sub>).

The low electron density of the sulfur atom on benzothiophene was attributed to the low oxidation value as compared to dibenzothiophene which has a high electron density, while 4,6-dimethyldibenzothiophene is known to present a high electron density.

#### 4.11.2 Catalysed oxidation of model fuel oil using poly[V<sup>IV</sup>O(sal-AHBPD)] and poly[V<sup>IV</sup>O(allylSB-co-EGDMA)] under continuous flow process

Equivalent mass (0.15 g) of refractory sulfur containing compounds {benzothiophene (3807 ppm S), dibenzothiophene (2606 ppm S) and 4,6-dimethyldibenzothiophene (2239 ppm S)} was dissolved in 10 mL solution of toluene/hexane (1:4), after which an aqueous solution of *tert*-butylhydroperoxide (*t*-BuOOH) (maximum equivalent oxidant moles to each compound) was added. The mixture was transferred into a 25 mL syringe, and pumped at 1 mL/h through the catalyst as described in **Chapter 2, Section 2.6** to achieve the desired products. Poly[V<sup>IV</sup>O(allylSB-co-EGDMA)] (0.072 g, 0.0405 mmol) and p[V<sup>IV</sup>O(sal-AHBPD)] (0.044 g, 0.0405 mmol) were employed as catalysts and a flow-rate of 1 mL/h was maintained for the catalyzed oxidation studies. The mass of poly[V<sup>IV</sup>O(allylSB-co-EGDMA)] and poly[V<sup>IV</sup>O(sal-AHBPD)] employed contains the same amount of vanadium.

From the results obtained (**Figure 4.43**), most of the dibenzothiophene and 4,6-dimethyldibenzothiophene were converted to their respective sulfone compounds after passing through the catalyst. The chromatogram showed that 60% of benzothiophene was oxidized to sulfone when poly[V<sup>IV</sup>O(allylSB-co-EGDMA)] was employed and 45% of benzothiophene was oxidized when poly[V<sup>IV</sup>O(sal-AHBPD)] was employed as catalyst. A total of 98% and 96% oxidation of dibenzothiophene and 4,6-dimethyldibenzothiophene respectively was observed for poly[V<sup>IV</sup>O(allylSB-co-EGDMA)] catalyst, while a total of 86% and 73% oxidation was observed for dibenzothiophene and 4,6-dimethyldibenzothiophene respectively when poly[V<sup>IV</sup>O(sal-AHBPD)] was employed as catalyst. The low electron density of benzothiophene sulfur atom was attributed to the low oxidation observed, while the higher high electron sulfur density compounds, dibenzothiophene and 4,6-dimethyldibenzothiophene gave higher oxidation yield. Confirmation of the respective sulfone compounds formed was followed *via* the use of a gas chromatography-mass spectrometry (**Figure 4.44**). The catalytic oxidation reactivity of the sulfur-containing compounds followed the order: BT < 4,6-DMDBT < DBT. The oxidation activity order of the sulfur-containing compounds agrees with the oxidation results obtained under batch studies.

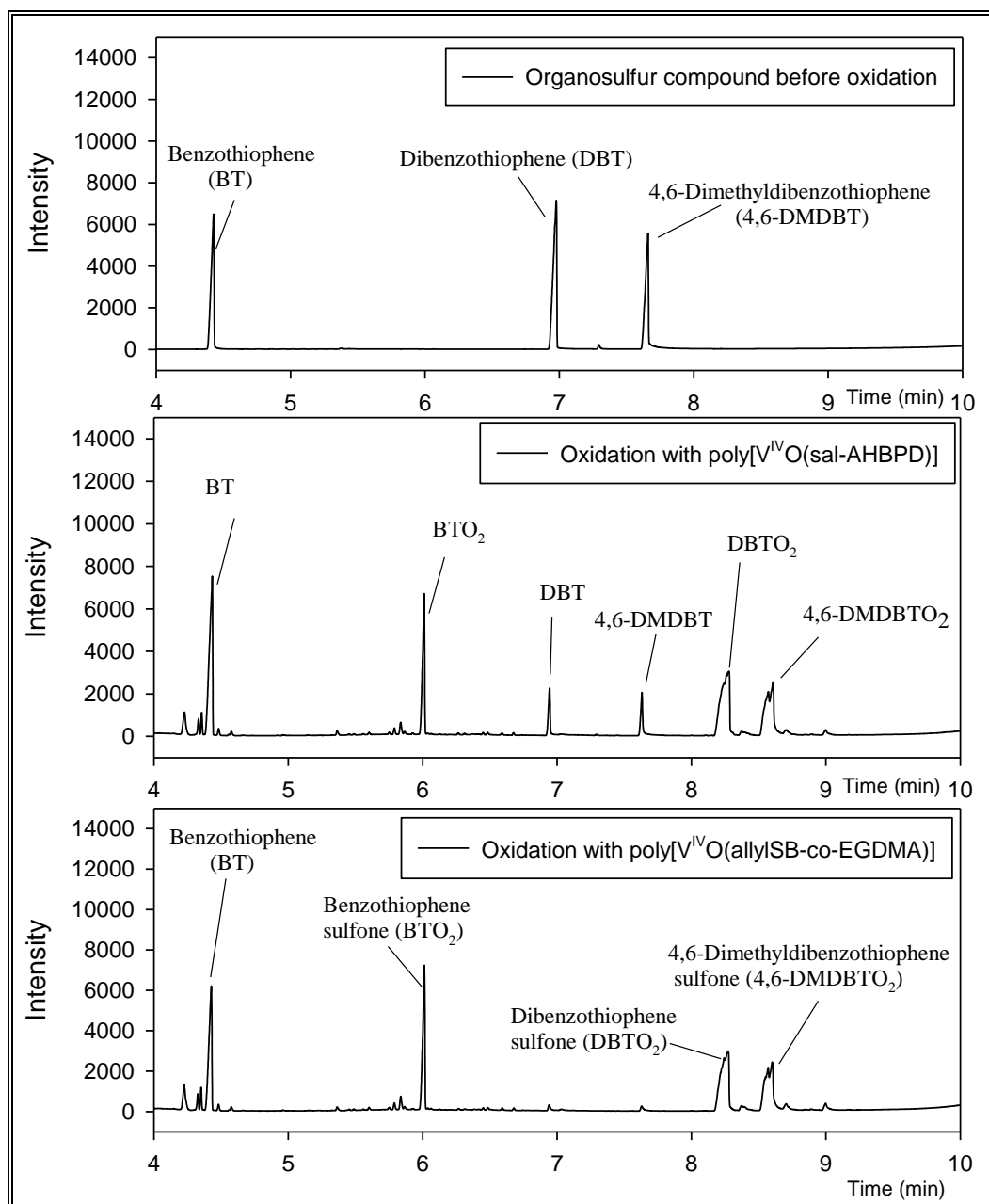


**Figure 4.43** GC-FID chromatograms of organosulfur mixture {benzothiophene (BT), dibenzothiophene (DBT) and 4,6-dimethyldibenzothiophene (4,6-DMDBT)} before and after oxidation using poly[V<sup>IV</sup>O(sal-AHBPD)] and poly[V<sup>IV</sup>O(allylSB-co-EGDMA)] (0.0405 mmol). Temp. = 40°C, toluene/hexane (1:4) = 10 mL, time of reaction = 10 h.



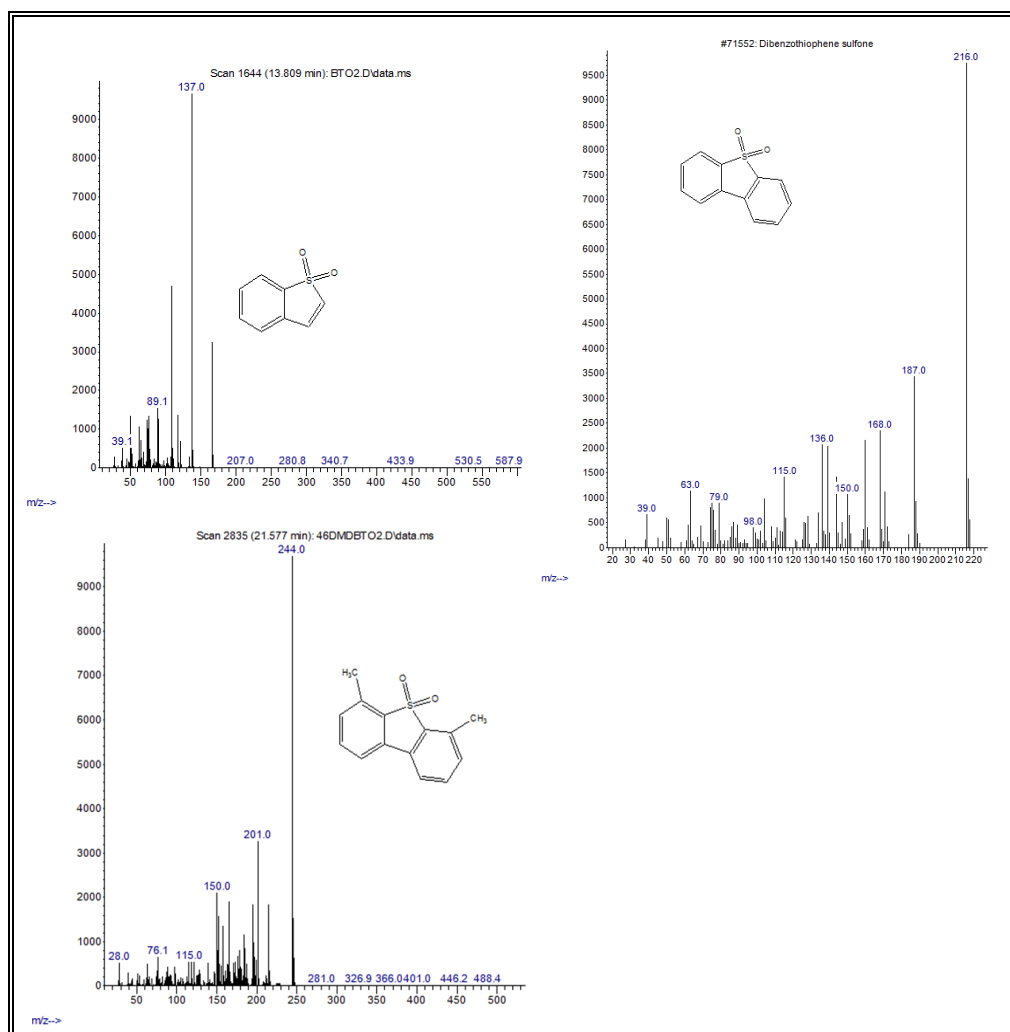


**Figure 4.44** GC-MS chromatograms for benzothiophene sulfone (BTO<sub>2</sub>), dibenzothiophene sulfone (DBTO<sub>2</sub>) and 4,6-dimethyldibenzothiophene sulfone (4,6-DMDBTO<sub>2</sub>).

From the model fuel catalysed oxidation under the batch and continuous process, it can be seen that poly[V<sup>IV</sup>O(allylsB-co-EGDMA)] gave higher oxidation. The catalyst, poly[V<sup>IV</sup>O(allylsB-co-EGDMA)], was therefore found suitable for the oxidation of hydro-treated diesel.

#### 4.12 Oxidovanadium(IV) catalysed oxidation of hydro-treated diesel (continuous flow and batch process)

Hydro-treated diesel fuel containing  $385 \pm 4.6$  ppm of sulfur (mainly dibenzothiophene and dibenzothiophene derivatives) was employed for oxidation. A similar set-up (batch and continuous flow study) as described for model sulfur compounds was also employed for the oxidation of hydro-treated diesel using a relative ratio (S/O ratio 7). Prior to oxidation, the sulfur in fuel was re-quantified

by employing sulfur standards in diesel produced by Matheson Tri-Gas and have direct traceability to NIST-SRM 2723a/SRM 2770. Sulfur 181 nm of the various sulfur standards in diesel concentrations are displayed in **Figure 4.45** and a linear plot showing peak area against concentration also presented in **Figure 4.46**.

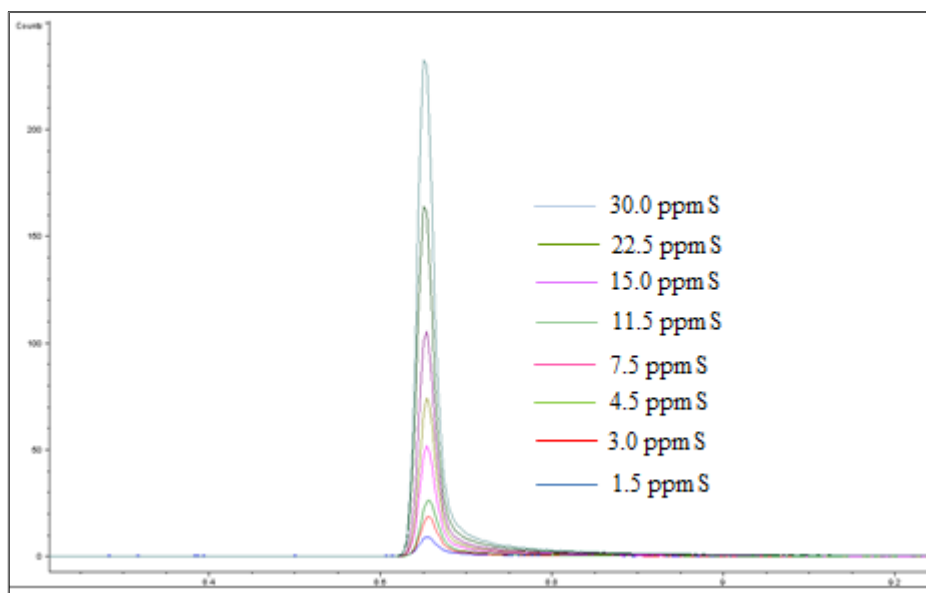


**Figure 4.45** GC-AED chromatogram of sulfur standards in diesel using a wavelength of 181 nm (1.5-30.0 ppm S)

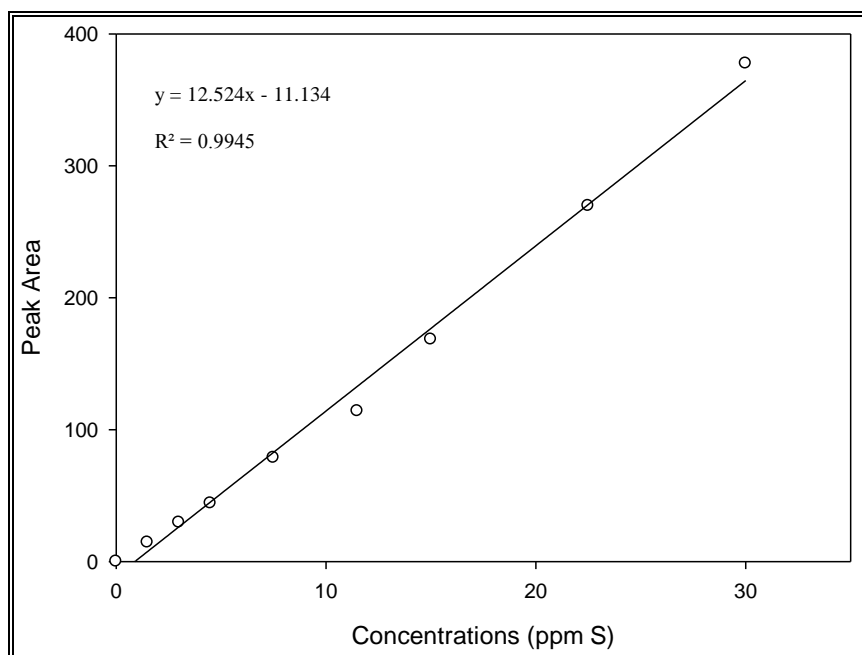


**Figure 4.46** Calibration plot for instrument response to sulfur concentration (ppm S).

Hydro-treated diesel and *t*-BuOOH in hexane was pre-heated to 40°C and then channelled into the catalyst-containing compartment with the aid of a syringe pump at 1 mL/h for continuous flow process, while the batch oxidation reaction was also conducted at 40°C. It is to be noted that the catalyst poly[V<sup>IV</sup>O(allylSB-co-EGDMA)] (0.072 g, 0.0405 mmol) was employed for the oxidation due to the higher overall oxidation yield it provided on the oxidation of model compounds. Progress in oxidation was monitored by a gas chromatograph equipped with an Atomic Emission Detector (AED), and this assists in the selective detection and tracking of elements of interest within a complex organic matrix.<sup>20,385</sup> From the 181 nm sulfur chromatograms obtained for the continuous flow oxidation, a shift in retention times was noticed from the initial organosulfur compounds to sulfur as sulfones compounds in the oxidized hydro-treated diesel. The absence of unaltered peaks indicated that all the sulfur compounds were oxidized completely (**Figure 4.47**). While under batch oxidation process, shift in retention time confirming oxidation was also noticed, however, some of the initial sulfur remains unaltered (**Figure 4.48**). It can be concluded that continuous flow process present better oxidation conversions as compared to the batch process.

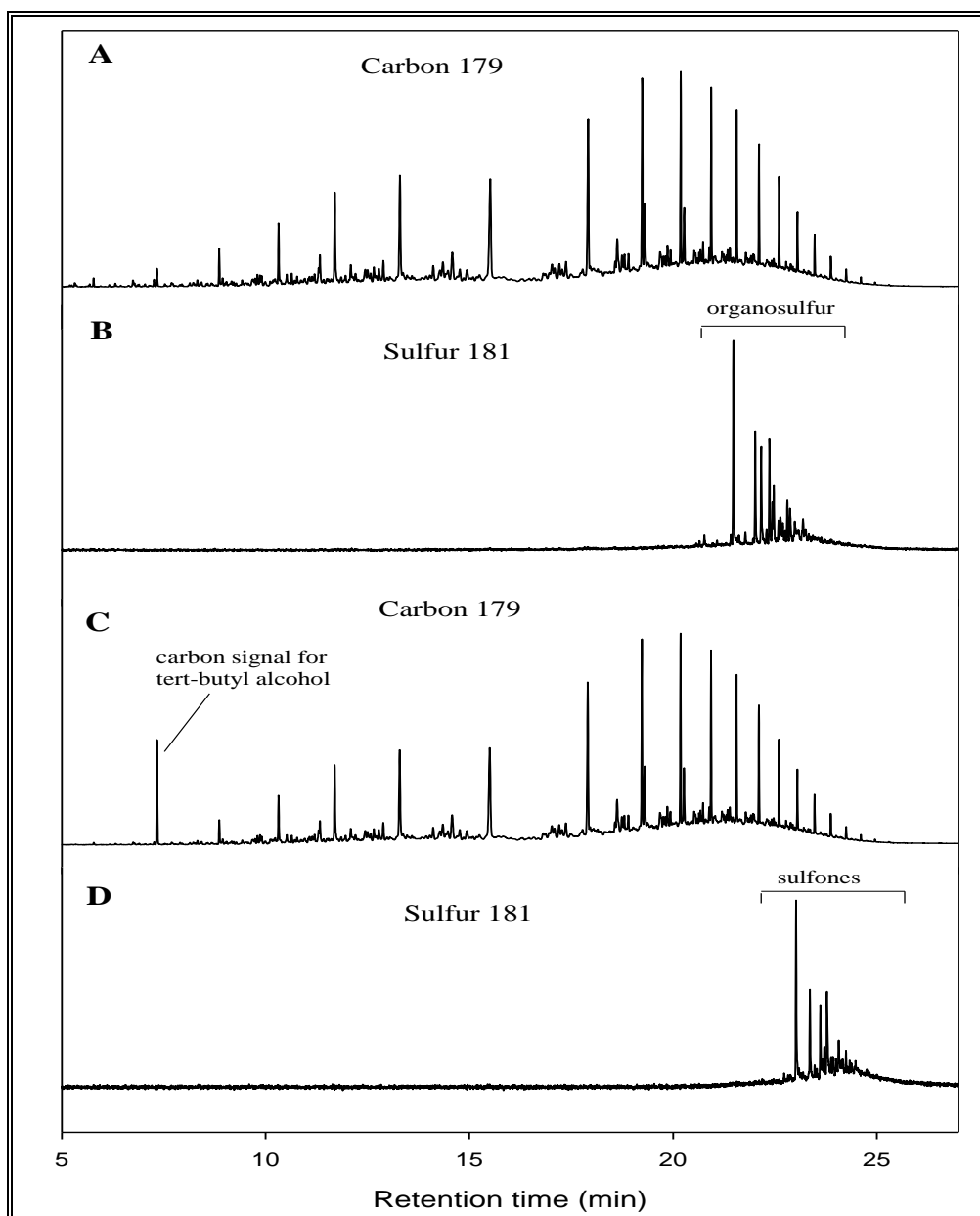


**Figure 4.47** GC-AED chromatograms of carbon (A) and sulfur (B) chromatograms of the hydro-treated diesel before oxidation and carbon (C) and sulfur (D) chromatograms of the hydro-treated diesel after oxidation while using poly[V<sup>IV</sup>O(allylSB-co-EGDMA)] as catalyst (continuous flow process). The chromatogram shows the loss of sulfides and the formation of sulfones.

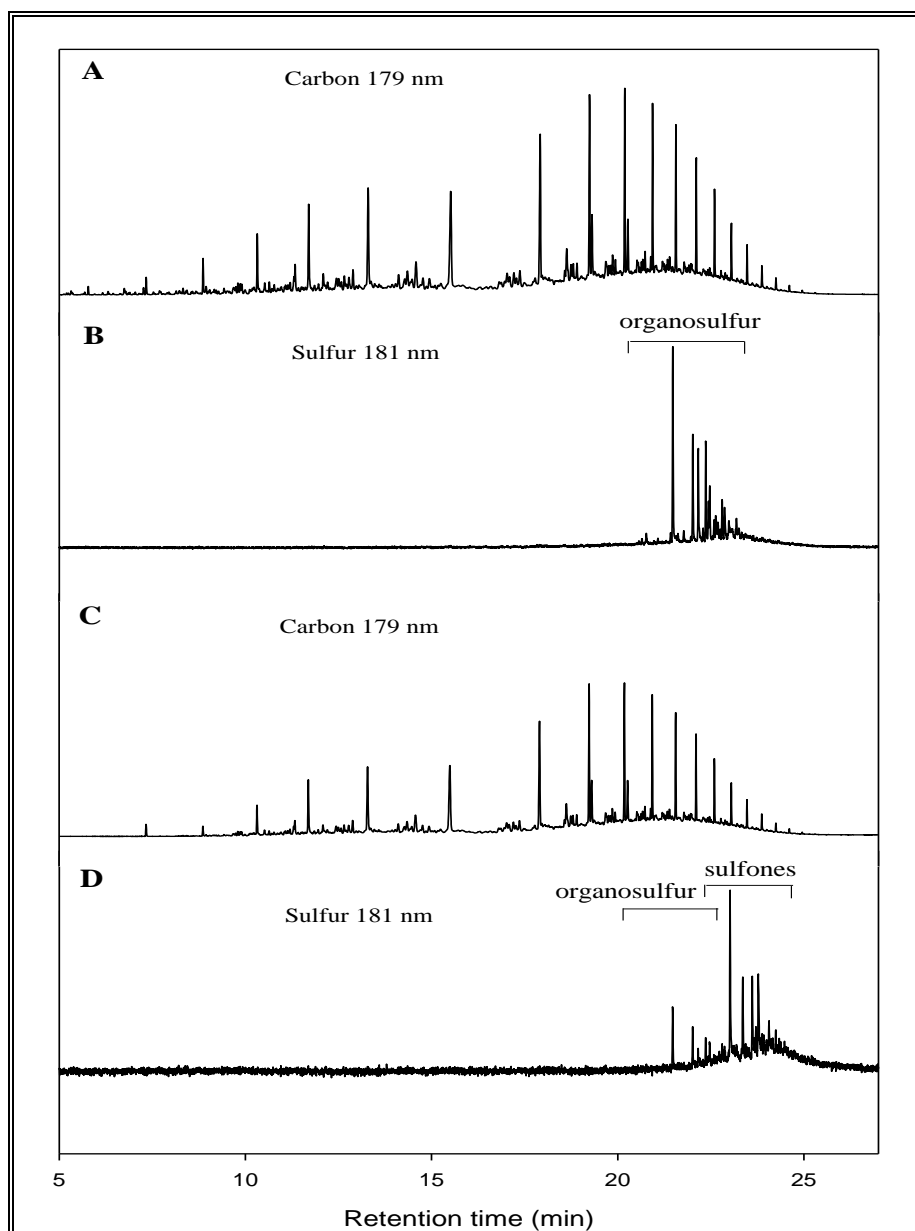


**Figure 4.48** GC-AED chromatograms of carbon at 179 nm (A) and sulfur at 181 nm (B) of the hydro-treated diesel before oxidation and carbon at 179 nm (C) and sulfur at 181 nm (D) chromatograms of the hydro-treated diesel fuel after oxidation while using poly[V<sup>IV</sup>O(allylSB-co-EGDMA)] as catalyst (batch process).

Oxidized hydro-treated diesel was characterized by FT-IR spectroscopy with sulfone (S=O) band frequencies visible around 1400-1300 cm<sup>-1</sup> and 1200-1100 cm<sup>-1</sup> on the oxidized diesel as compared to the non-oxidized diesel (Figure 4.49).<sup>377</sup> C-S stretching bands of the hydro-treated diesel was visible

around  $715\text{ cm}^{-1}$ , and upon oxidizing the diesel the C-S stretching band shifted to around  $761\text{ cm}^{-1}$  (Figure 4.50).

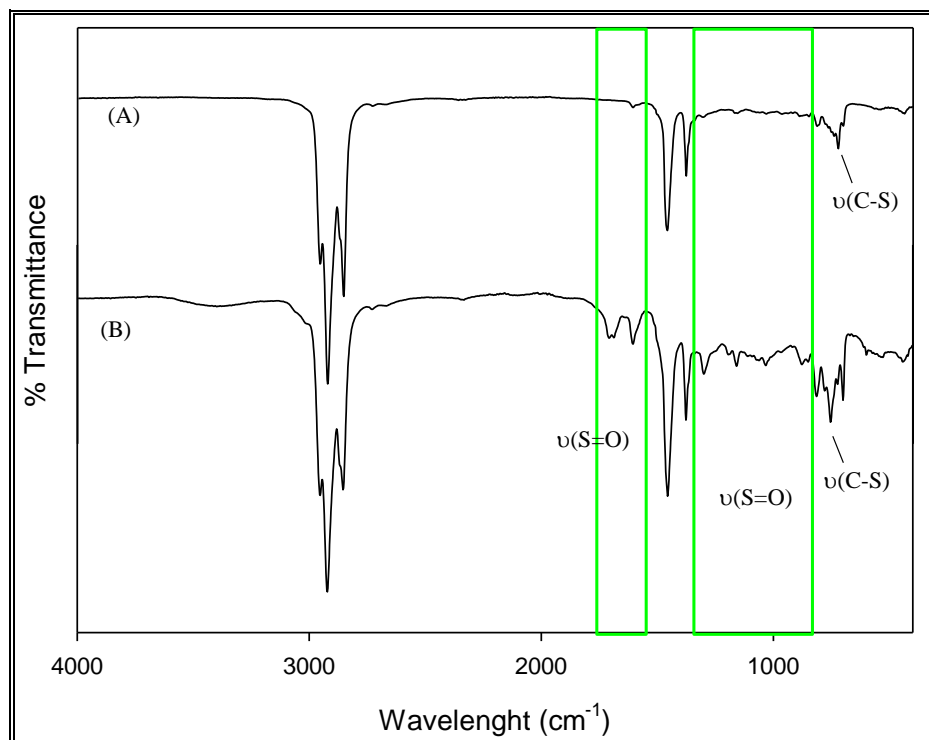


**Figure 4.49** FT-IR of (A) hydro-treated diesel fuel ( $385 \pm 4.6$  ppm S) and (B) oxidized hydro-treated diesel.

#### 4.13 Oxidovanadium(IV) catalysed oxidation of crude oil

Sulfur in crude oils is known to poison hydrotreatment catalysts during the hydro-desulfurization process, hence catalyst re-activation and/or change are often required.<sup>38-41</sup> The procurement and use of new catalyst after every hydrotreatment process affects fuel production cost. Oxidovanadium(IV) oxidation catalysts on the other hand, show resistance to sulfur poisoning, due to this unique property, oxidation and adsorption of produced sulfones in crude oil was carried-out before the hydrotreatment process in order to reduce the poisoning of hydrotreatment catalyst.<sup>129,386</sup> Catalysed oxidation of heavy crude oil (17 920 ppm S) under continuous flow process using an oxidant-to-sulfur (O/S) ratio of 7. Non-aromatic sulfur compounds were almost completely oxidized (Figure 4.50), while a shift in retention time of some aromatic sulfur compounds further confirmed oxidation, however some sulfur compounds retention time remained unchanged, confirming the presence of some unreactive sulfur compounds such as thiophenes and its derivatives.

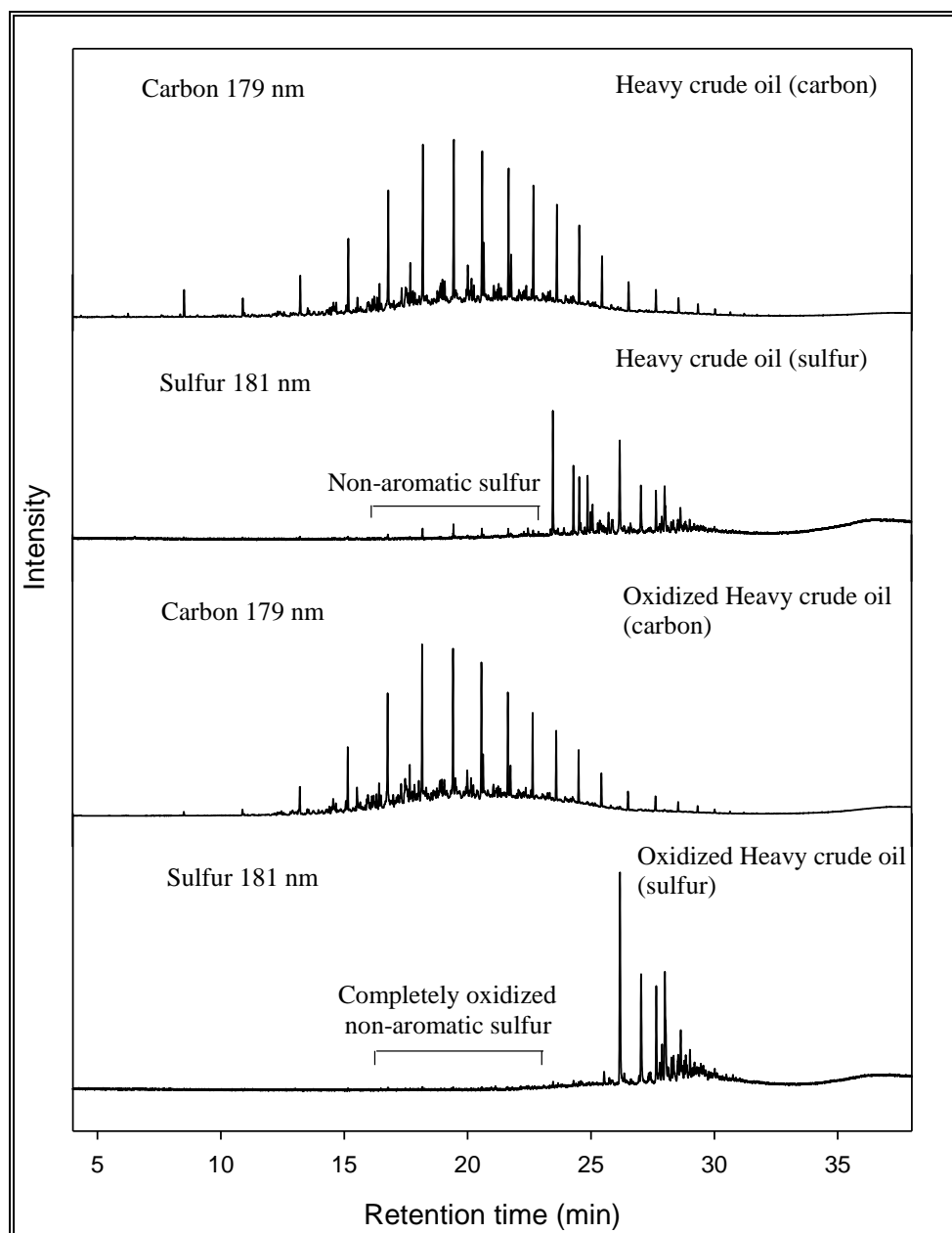


**Figure 4.50** GC-AED chromatograms of carbon at 179 nm and sulfur at 181 nm for heavy crude oil before oxidation, and carbon and sulfur chromatograms of oxidized heavy crude oil after oxidation while using poly[V<sup>IV</sup>O(allylSB-co-EGDMA)] as catalyst (continuous flow process).

#### 4.14 Conclusions

The oxidovanadium(IV) complex  $[V^{IV}O(\text{sal-HBPD})]$  containing a tetradentate Schiff base ligand and its polymer-anchored counterpart  $\text{poly}[V^{IV}O(\text{sal-AHBPD})]$  were synthesized. The tetradentate  $N_2O_2$ -donor ligand was obtained by the condensation of salicylaldehyde and *o*-phenylenediamine. Single-crystal X-ray diffraction of  $[V^{IV}O(\text{sal-HBPD})]$  showed a structure with a distorted square pyramidal geometry with the  $N_2O_2$  equatorial binding mode of the tetradentate ligand. The second polymer-anchored catalyst,  $\text{poly}[\text{allylSB-co-EGDMA}]$ , containing a tetradentate donor ligand, was synthesised by suspension polymerization of the monomer (allylSB) in the presence of a crosslinker EGDMA. Anchoring of oxidovanadium(IV) on the polymer microspheres to form  $\text{poly}[V^{IV}O(\text{allylSB-co-EGDMA})]$  was achieved by reacting  $VOSO_4$  with  $\text{poly}[\text{allylSB-co-EGDMA}]$ . XPS and EPR studies confirmed the presence of V(IV) within the polymer-anchored microspheres. The activity of the two heterogeneous catalyst was compared to the activity of oxidovanadium(IV) homogeneous catalyst counterpart,  $[V^{IV}O(\text{sal-HBPD})]$ , under batch process. The oxidation of organosulfur compounds using  $\text{poly}[V^{IV}O(\text{sal-AHBPD})]$  and  $\text{poly}[\text{allylSB-co-EGDMA}]$  as catalysts were also reported under continuous flow process.

The reaction between *t*-BuOOH and oxidovanadium(IV) complexes produced an oxidoperoxido-compound as the catalytically active species. It was also observed that oxidation of thiophene was possible in the presence of trace amount of tetrabutylammonium bromide (TBAB), which helped in the interruption of conjugation in thiophene thus making the sulfur atom reactive.

The higher activity and low level of vanadium leached from  $\text{poly}[V^{IV}O(\text{allylSB-co-EGDMA})]$  as compared to  $\text{poly}[V^{IV}O(\text{sal-AHBPD})]$  confirmed the stability of  $\text{poly}[V^{IV}O(\text{allylSB-co-EGDMA})]$  and resistance to sulfur poisoning during the oxidation of organosulfur compounds. Continuous flow oxidation process for hydro-treated diesel using  $\text{poly}[V^{IV}O(\text{allylSB-co-EGDMA})]$  gave better oxidation conversions > 99% as compared to the batch process, having an oxidation conversion of < 70%. Oxidation of crude oil under continuous flow process indicated that almost all the non-aromatic sulfur compounds and the reactive sulfur compounds (such as dibenzothiophenes and derivatives) were oxidized.



*This page is kept blank*

# Chapter 5

## Adsorption of oxidized organosulfur compounds in fuels by using molecularly imprinted polymers

### 5.1 Introduction

Molecular imprinting of polymers as described in **Chapter 1, Section 1.4.1** is a technique for the introduction of recognition sites into polymeric matrices, *via* the formation of a bond between the template (imprinting molecule) and functional groups within the polymer network.<sup>70,387,388</sup> Imprinted polymers have been reported for the selective adsorption of desired refractory organosulfur compounds in the production of clean fuels due to the recognisable functional groups present.<sup>389</sup> In this study, the organosulfur compounds were converted to polar sulfones which were then absorbed using sulfone-responsive molecularly imprinted polymers as absorbents (*viz.* chitosan and polybenzimidazole).

Chitosan, an amino polysaccharide (**Figure 5.1**) usually obtained by the deacetylation of chitin, is the most abundant natural structural polymer after cellulose. It has been investigated for the development of sorption systems due to the presence of free amine and hydroxyl groups in its structure which allow for chemical modifications through the formation of hydrogen bonding interactions.<sup>68,69,390</sup> Another favourable property of chitosan is the ability to swell when in contact with a thermodynamically compatible solvent.<sup>391,392</sup> Polybenzimidazole (PBI), a heterocyclic polymer with excellent chemical and thermal stability (**Figure 5.1**) was commercially developed by Celanese Corporation in 1983 for use as fire-retardant material and composite material reinforcement<sup>393</sup> due to their good molecular alignment.<sup>394</sup> Sherrington's group<sup>395-397</sup> as well as many others,<sup>398-401</sup> have exploited the PBI polymer as a support for a range of different metal-based catalysts with great success. The benzimidazole (-NH group) on the polymer, allows bonding interaction with compounds through the formation of hydrogen bonds. PBI also has a free amine which allows for the adsorption of sulfones in hydrocarbon mixtures through the formation of hydrogen bonds.<sup>68,386,402</sup>

The fabrication of molecularly imprinted polymers (MIPs) adsorbents (chitosan nanofibers, crosslinked chitosan microspheres and polybenzimidazole (PBI) nanofibers) is discussed in this

chapter. The use of these imprinted adsorbents for selective adsorption of sulfones, under batch and continuous flow adsorption process, obtained *via* the catalysed oxidation of sulfur compounds will be discussed. The development of a home-made pressurized hot water extraction system for desorption of the adsorbed sulfone compounds on the fibers was also carried-out.

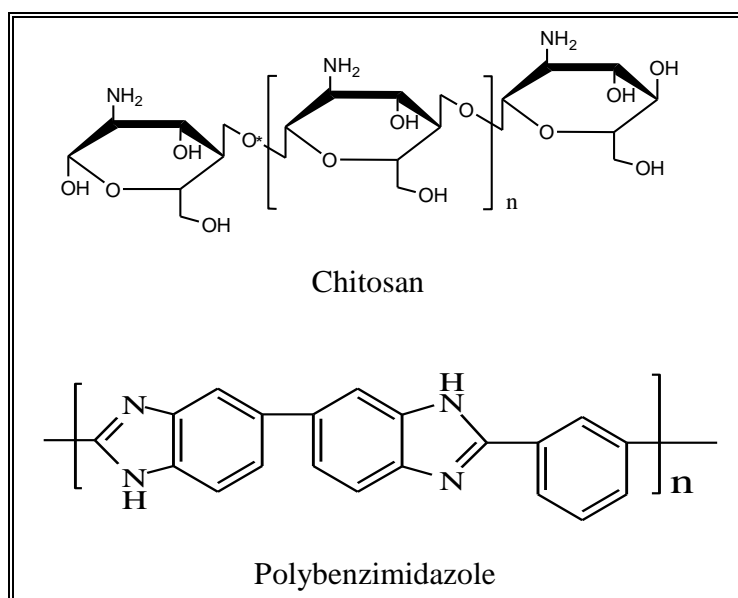


**Figure 5.1** Chemical structures of chitosan and polybenzimidazole.

## 5.2 General synthetic route for the fabrication of molecularly imprinted and non-imprinted polymer adsorbent

### 5.2.1 Preparation of molecularly imprinted and non-imprinted chitosan microspheres and nanofibers

#### 5.2.1.1 Preparation of molecularly imprinted and non-imprinted chitosan nanofibers

Template imprinting on chitosan gel polymers improves its adsorptive properties and also provides selectivity due to polymer flexibility which makes accessing of the recognition site and removal of absorbed template easier. An additional way of improving adsorption properties of polymers is through electrospinning, as it decreases adsorption time and mass transfer constraints.<sup>390,396,397</sup>

Electrospinning is a unique technology that produces non-woven fibers with diameters ranging between 10-1000 nm; and it provides polymer nanofibers with controlled pore size and also high surface area-to-volume ratio.<sup>405</sup> Trifluoroacetic acid (TFA) was employed as the main solvent of choice

for dissolution and electrospinning of chitosan due to the following reasons: Firstly, TFA forms salts with amino groups of chitosan, thus destroying the rigid interaction between chitosan molecules; and secondly, the high volatility of TFA is advantageous for the rapid solidification of the electrified jet of the chitosan-TFA solution.<sup>396,399</sup>

A polymer solution for electrospinning was prepared by dissolving 0.5 g of chitosan in 10 mL of TFA:DCM (7:3). The mixture was gently stirred overnight at room temperature to obtain a homogeneous solution which was electrospun and classified as non-imprinted nanofibers. For imprinted fibers, 1 mL of the respective sulfone compounds (10 mM in acetonitrile) containing 40  $\mu$ L of triton X-114 (surfactant agent) was added drop-wise to the dissolved chitosan solution. The mixture was then stirred for 2 h to achieve the desirable solution homogeneity for electrospinning.

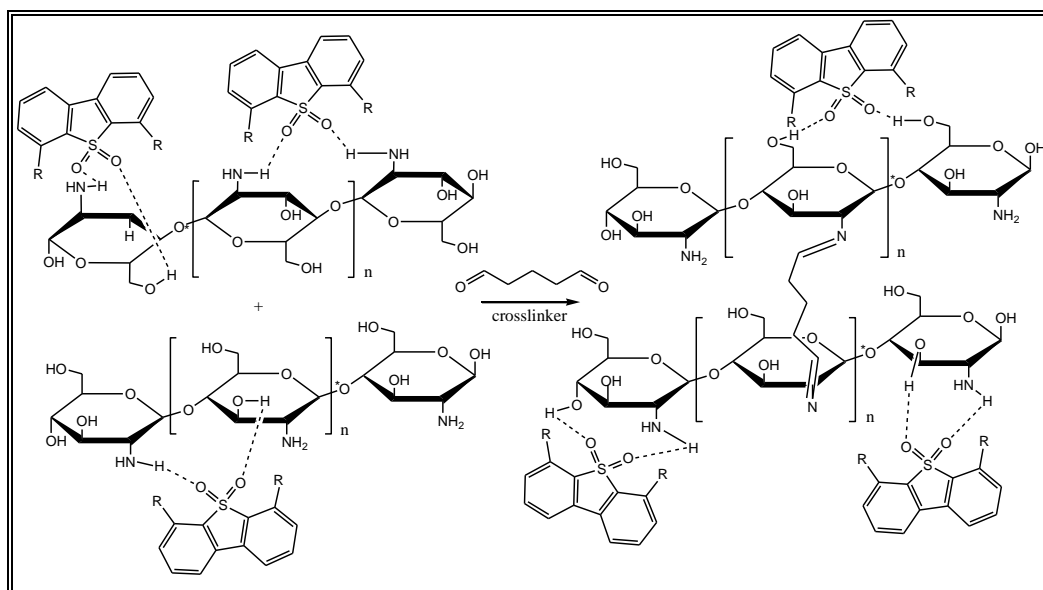
Polymer solutions were respectively poured into a 25 ml syringe attached to a needle connected to the positive electrode of a high voltage power supply. A syringe pump (Model NE-1010, New Era Pump Systems Inc. USA) was used to supply a constant flow of polymer solution from the syringe during the electrospinning process. A voltage of 30 kV was applied to the polymer solution which was pumped at a flow-rate of 1.2 mL/h, with a distance between the needle tip and aluminium collector plate placed at 17 cm. The repulsive electrical forces between charged nanofibers enable them to spread smoothly and the solvent evaporates resulting in solidification while traveling towards the grounded collector. The collected nanofibers were kept overnight in the fumehood to allow for complete residual solvent evaporation. Deprotonation of the nanofibers was carried out by soaking 0.5 g of the nanofibers overnight into 20 mL acetonitrile containing 1 mL of the 25% ammonia solution. The template molecules (sulfone compounds) imprinted within the nanofibers matrix was removed *via* Soxhlet extraction using a mixture of methanol and acetonitrile (1:1) until no templates was detected on the GC-FID. *Anal.* Found: C 32.33%, H 5.79%, N 5.64%. IR ( $\nu$ ,  $\text{cm}^{-1}$ ): 1606 (C=N), 1530 (C=C), 1090 (C-O-C).

### 5.2.1.2 Preparation of molecularly imprinted and non-imprinted chitosan microspheres

0.5 g of chitosan was dissolved in 20 mL of water containing 2% (v/v) acetic acid followed by the drop-wise addition of 1 mL of sulfone compounds (10 mM) containing 40  $\mu$ L of triton X-114

(surfactant agent). The mixture was stirred until a homogenous solution was obtained. Microspheres were then formed by making droplets of the chitosan solution into a beaker containing 2 M NaOH solution. The droplets were then allowed to stand for 24 h in order to allow for proper microspheres formation.<sup>407</sup> Cross-linking of the formed chitosan microspheres was necessary in order to preserve the desired spherical shape and also to strengthen the microspheres.<sup>408</sup> Glutaraldehyde was employed as a suitable cross-linker, and the mechanism of cross-linking is presented in **Scheme 5.1**.

To 5 g of the microspheres (wet imprinted and non-imprinted) in a 100 mL flask, 10 mL of 67 mM NaOH was added, and cross-linking of the microspheres effected by the addition of 0.5 mL glutaraldehyde. The reaction was allowed to proceed for 5 h at 45°C. The cross-linked microspheres were collected by filtration and were washed extensively with distilled-deionised water to remove any unreacted glutaraldehyde. Template removal from the glutaraldehyde-free microspheres was carried-out through Soxhlet extraction. The microspheres were then slowly dried at 40°C for 7 h. *Anal.* Found: C 33.72%, H, 4.74%, N 4.85%. IR ( $\nu$ ,  $\text{cm}^{-1}$ ): 1646 (C=N), 1570 (C-C), 1130 (C-O-C). The carbon-to-nitrogen (C:N) relationship, upon cross-linking, increased to 6.95 from its initial non-cross-linked ratio of 5.48. This indicated that more carbon element have been incorporated into the polymer microspheres matrix with a glutaraldehyde-to-chitosan ratio of 0.7 observed. The high level of cross-linking is said to enhance the binding and rebinding capacities of chitosan based MIPs to most target molecules.<sup>70</sup>



**Scheme 5.1** Proposed cross-linking of the imprinted chitosan microspheres using glutaraldehyde and possible hydrogen bonding interactions.

### 5.2.2 Preparation of molecularly imprinted and non-imprinted polybenzimidazole (PBI) nanofibers *via* electrospinning

A polybenzimidazole (PBI) polymer solution was prepared by dissolving 2.0 g of dry PBI polymer in 10 mL of *N,N*-dimethylacetamide containing 0.4 g (4% wt/vol) lithium bromide. The dissolution was carried-out under reflux condition in a nitrogen atmosphere for 4 h. The resulting viscous solution was cooled, and filtered to remove any particulates. LiBr (about 4% by weight) was employed for dissolution as it increases solution electrospinnability and also nanofibers shelf life.<sup>220</sup>

The imprinted PBI solution was obtained by adding 1 mL (0.01 M solution) of respective sulfone compounds containing 40  $\mu$ L Triton X-114 (surfactant agent) to dissolved PBI polymer solution, after which the mixture is stirred at room temperature for 5 h to form a homogeneous blend. The polymer solution was transferred into a 25 mL syringe and electrospun by using the following optimised electrospinning conditions; a high voltage of between 20 and 25 kV at a flow-rate of 0.4 mL/h and an applied distance of 15 to 20 cm between the needle tip and collector. The resulting nanofibers were subjected to an extensive washing process using a mixture of acetonitrile and methanol (1:1) *via* Soxhlet extraction to remove residual solvent (DMAc), LiBr and entrapped template (sulfone compounds). The washed nanofibers were later dried overnight at an oven temperature of 60°C.

### 5.3 Adsorbent characterization

#### 5.3.1 FT-IR spectra of adsorbents

The FT-IR spectra of the pristine chitosan, chitosan nanofibers and crosslinked chitosan microspheres are shown in **Figure 5.2**. In all spectra, a strong characteristic band attributed to C-O-C stretching in polysaccharides was observed between 1000 and 1200  $\text{cm}^{-1}$  confirming that the chitosan structure was preserved. Comparing pristine chitosan spectrum to cross-linked microspheres spectrum, two new bands were observed at 1646  $\text{cm}^{-1}$  and 1570  $\text{cm}^{-1}$ , and the bands were assigned to imine bond  $\nu(\text{C}=\text{N})$ .<sup>392,409</sup> The predominance of the  $\nu(\text{C}-\text{C})$  at 1370  $\text{cm}^{-1}$  in the spectrum of the microspheres when compared to the spectra of pristine chitosan and nanofibers, further confirmed cross-linking. No evidence of the characteristic band related to free glutaraldehyde (aldehydic group,  $-\text{CHO}$ ) around 1720  $\text{cm}^{-1}$  was observed, indicating that cross-linked imprinted chitosan microspheres were free of unreacted cross-linker.

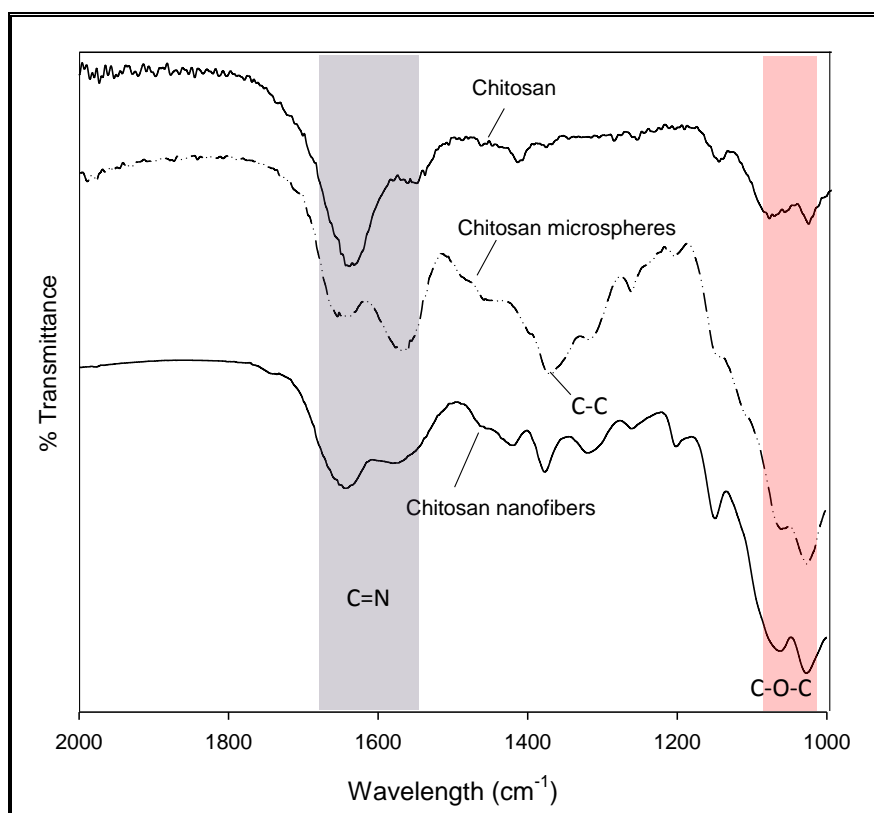


**Figure 5.2** FT-IR spectra of chitosan and its modified form (microspheres and electrospun chitosan nanofibers).

Brownish-yellow PBI nanofibers were obtained after electrospinning and washing. From elemental analysis of imprinted nanofibers, C:N ratio remained constant as compared to the initial C:N ratio for PBI, hence indicating that polymers properties were retained. The FT-IR spectra of non-imprinted and imprinted nanofibers are presented in **Figure 5.3**. *Anal.* Found for pristine PBI powder: C 71.28%, H 4.50%, N 16.55%, C:N ratio 4.31. IR ( $\nu$ ,  $\text{cm}^{-1}$ ): 3403 (N-H), 1630, 1531 (C=N), 1370 (C=C). *Anal.* Found for PBI-nanofibers: C 61.92%, H 4.91%, N 14.09%, C:N ratio 4.39. IR ( $\nu$ ,  $\text{cm}^{-1}$ ): 3411 (N-H), 1624, 1531 (C=N), 1439 (C=C). *Anal.* Found for PBI-BTO<sub>2</sub> nanofibers: C 58.06%, H 4.61%, N 13.00%, C:N ratio 4.47. IR ( $\nu$ ,  $\text{cm}^{-1}$ ): 3430 (N-H), 1623, 1538 (C=N), 1388 (C-C). *Anal.* Found for PBI-DBTO<sub>2</sub> nanofibers: C 57.30%, H 4.94%, N 12.67%, C:N ratio 4.52. IR ( $\nu$ ,  $\text{cm}^{-1}$ ): 3350 (N-H), 1630, 1530 (C=N), 1445 (C=C). *Anal.* Found for PBI-4,6-DMDBTO<sub>2</sub> nanofibers: C 59.54%, H 5.10%, N 13.75%, C:N ratio 4.33. IR ( $\nu$ ,  $\text{cm}^{-1}$ ): 3388 (N-H), 1625, 1530 (C=N), 1375 (C-C).

**NB:** PBI-BTO<sub>2</sub> nanofibers: Benzothiophene sulfone imprinted polybenzimidazole nanofibers; PBI-DBTO<sub>2</sub> nanofibers: Dibenzo thiophene sulfone imprinted polybenzimidazole nanofibers; and PBI-4,6-DMDBTO<sub>2</sub> nanofibers: 4,6-dimethyldibenzo thiophene sulfone imprinted polybenzimidazole nanofibers.



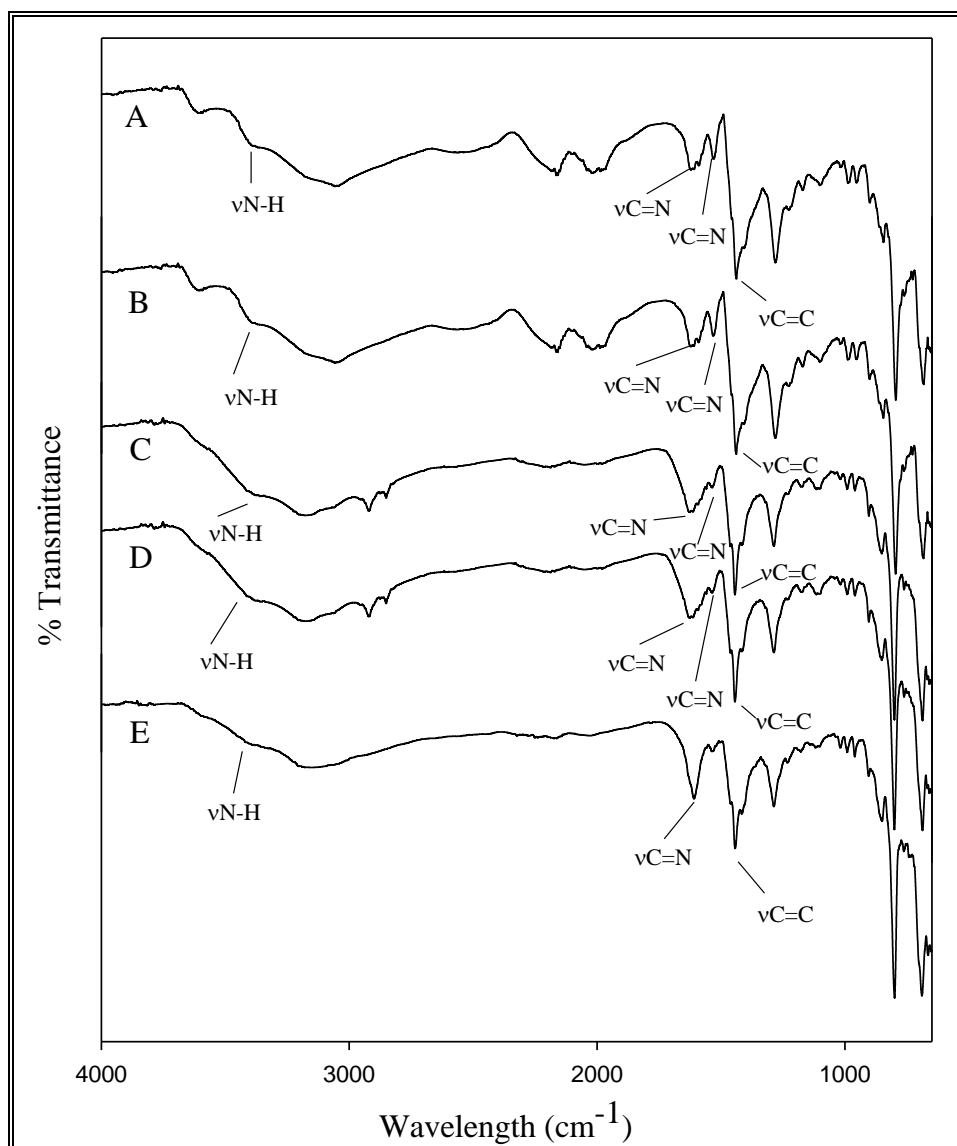


**Figure 5.3** FT-IR spectrum of (A) pristine PBI, (B) PBI-nanofibers, (C) PBI-BTO<sub>2</sub> nanofibers, (D) PBI-DBTO<sub>2</sub> nanofibers and (E) PBI-4,6-DMDBTO<sub>2</sub> nanofibers.

### 5.3.2 Energy Dispersive Spectroscopic analysis of adsorbents

Chemical characterization of adsorbents after deprotonation and template removal was evaluated. A reduction in fluorine (F) abundance confirming deprotonation was observed when non-deprotonated non-imprinted polymer (NIP) nanofibers were compared to the deprotonated counterpart (**Table 5.1**). Disappearance/reduction in sulfur (S) abundance after Soxhlet extraction of the templates was also confirmed by EDS. EDS spectra of non-imprinted and imprinted polymer nanofibers are presented in **Figure 5.4**. The use of EDS on imprinted and non-imprinted microspheres produced no meaningful results; however sulfur compounds on the microspheres were confirmed by using the GC.

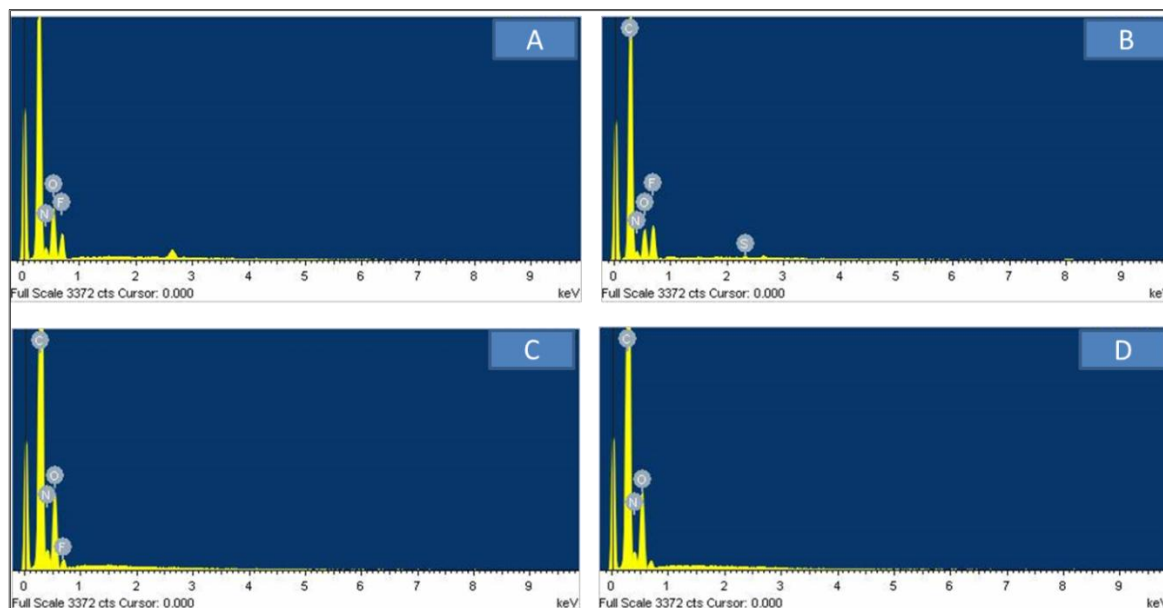


**Figure 5.4** EDS spectra of (A) non-imprinted nanofibers after washing, (B) BTO<sub>2</sub>-imprinted nanofibers after deprotonation and washing, (C) DBTO<sub>2</sub>-imprinted nanofibers after deprotonation and washing and (D) 4,6-DMDBTO<sub>2</sub>-imprinted nanofibers after deprotonation and washing.

For imprinted-PBI nanofibers, the presence of trace amount of sulfur (S) within the imprinted nanofibers confirmed that imprinting took place, and it also revealed that not all the sulfur containing molecules were removed after washing (**Figure 5.5**). The chemical compositions of imprinted and non-imprinted nanofibers are presented in **Table 5.1**.

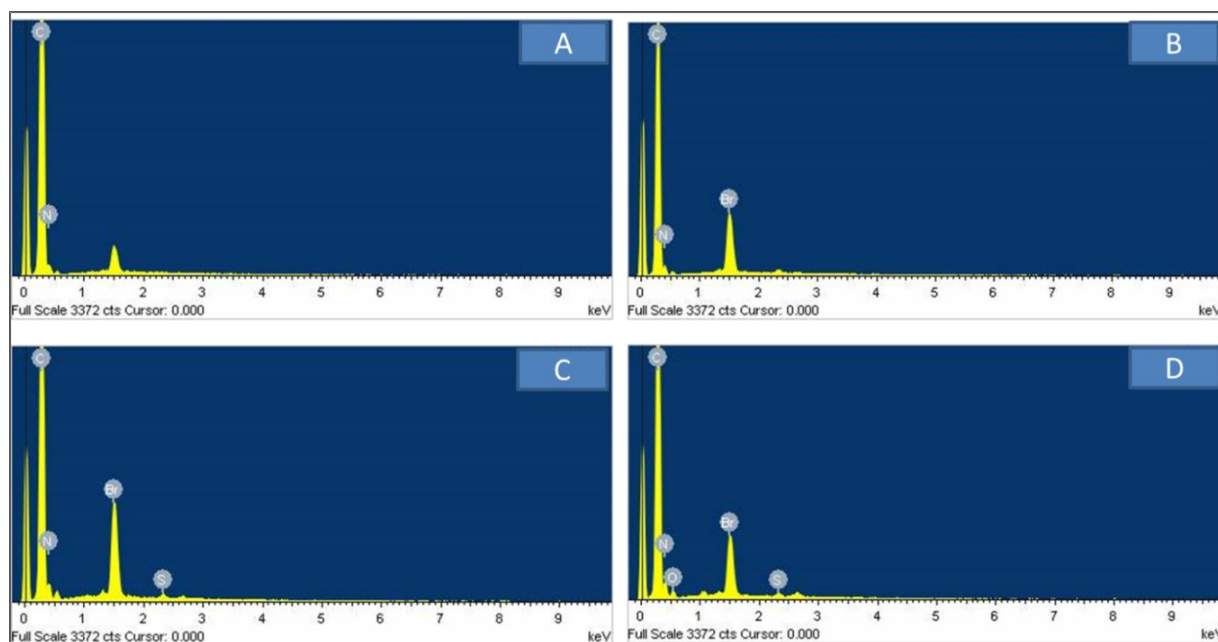


**Figure 5.5** EDS spectra of PBI nanofibers (A) non-imprinted PBI after washing, (B)  $\text{BTO}_2$  imprinted after washing, (C)  $\text{DBTO}_2$  imprinted after washing and (D)  $4,6\text{-DMDBTO}_2$  imprinted after washing.

**Table 5.1** EDS chemical composition of chitosan and polybenzimidazole (PBI)-imprinted and non-imprinted nanofibers.

Chitosan					
Elements	X-ray (keV)	Non-deprotonated nanofibers (non-imprinted nanofibers) (%)	Imprinted nanofibers (%)		
		ND-NIF	BTO <sub>2</sub>	DBTO <sub>2</sub>	4,6-DMDBTO <sub>2</sub>
Carbon (C)	0.277	56.39	64.15	61.64	67.68
Nitrogen (N)	0.392	8.69	8.48	9.60	9.04
Oxygen (O)	0.525	17.04	14.55	25.54	21.05
Flourine (F)	0.677	17.88	12.77	3.22	2.23
Sulfur (S)	2.307	-	0.05	-	-
Polybenzimidazole (PBI)					
Elements	X-ray (keV)	Non-imprinted nanofibers (%)	Imprinted nanofibers (%)		
		NIF	BTO <sub>2</sub>	DBTO <sub>2</sub>	4,6-DMDBTO <sub>2</sub>
Carbon (C)	0.277	73.39	74.65	72.62	73.73
Nitrogen (N)	0.392	17.92	16.02	18.13	15.91
Bromine (Br)	1.480	8.69	9.23	8.98	10.02
Sulfur (S)	2.307	-	0.10	0.27	0.34

### 5.3.3 Scanning electron micrographs of adsorbents

As discussed in **Section 5.2.1.1**, the mass of chitosan was optimized for electrospinning in order to obtain uniform nanofiber diameters. The SEM images obtained under electrospinning optimization conditions are presented in **Figure 5.6**. 0.5 g chitosan in 10 mL (TFA:DCM) gave uniform nanofibers and attempts to increase the chitosan mass resulted in electrospinning syringe needle tip blockage. Images of wet non-crosslinked chitosan microspheres, dried crosslinked chitosan microspheres (non-imprinted and imprinted) and nanofibers (non-imprinted and imprinted) are presented in **Figures 5.7, 5.8** and **5.9** respectively. A diameter range of 501-667  $\mu\text{m}$  was observed for the dried crosslinked microspheres. For the nanofibers a diameter range of 310-540 nm was observed.

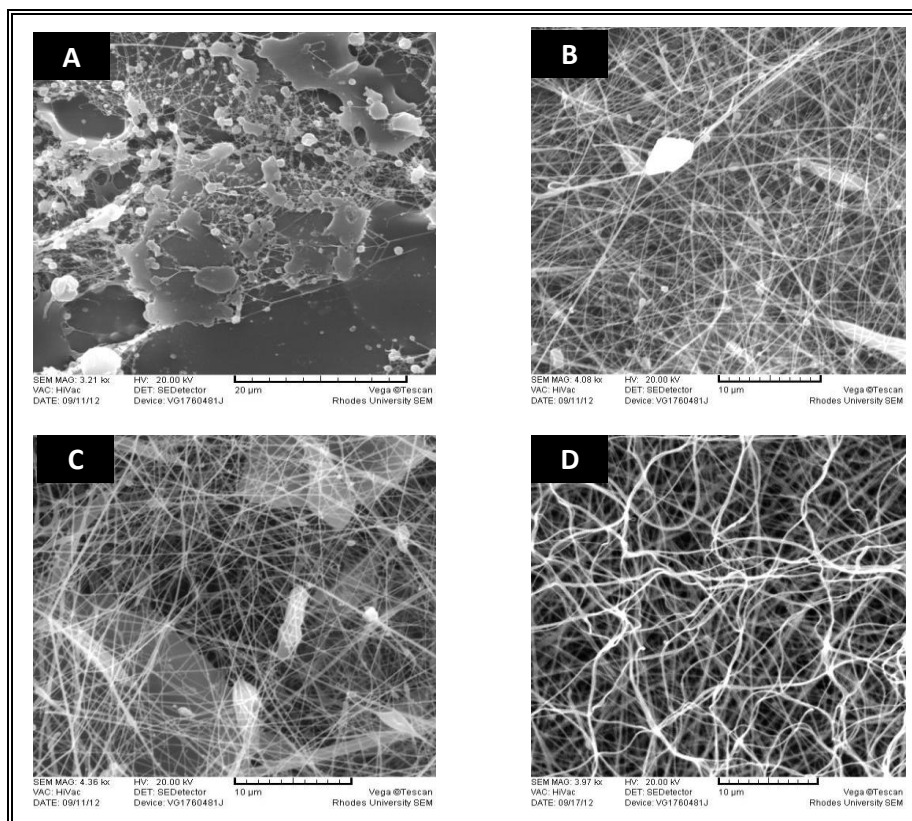


**Figure 5.6** Optimization of chitosan mass before electrospinning (A) 0.1 g in 10 mL (TFA:DCM); (B) 0.2 g in 10 mL (TFA:DCM); (C) 0.4 g in 10 mL (TFA:DCM); (D) 0.5 g in 10 mL (TFA:DCM). NB: TFA to DCM ratio is 7 to 3. Each containing 0.001M sulfone compounds.

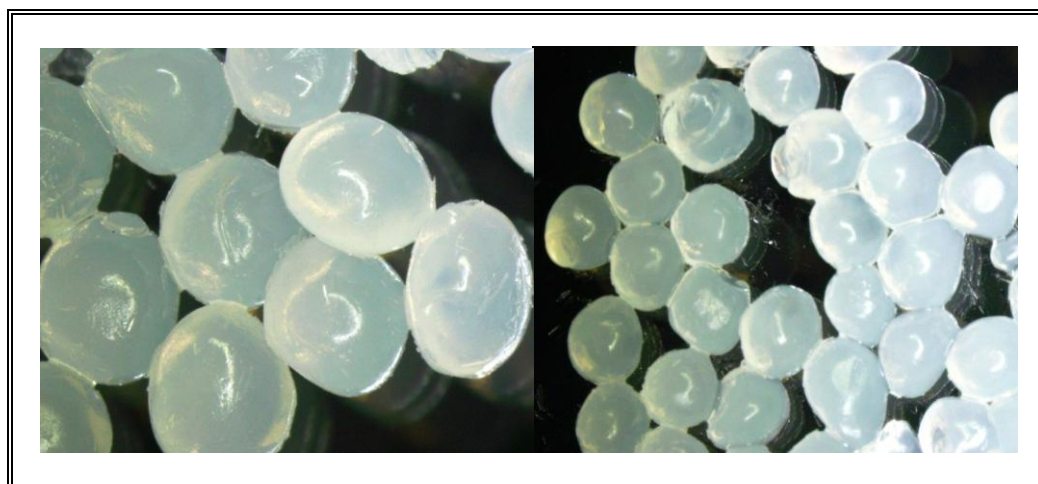


**Figure 5.7** Micrograph images of wet imprinted chitosan microspheres

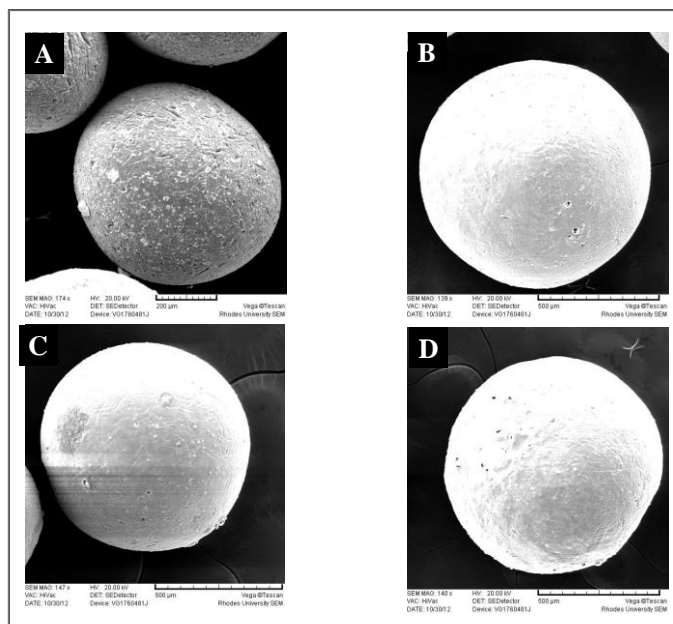


**Figure 5.8** Scanning electron microscopy (SEM) of (A) non-imprinted microspheres, (B) BTO<sub>2</sub>-imprinted microspheres, (C) DBTO<sub>2</sub>-imprinted microspheres, and (D) 4,6-DMDBTO<sub>2</sub>-imprinted microspheres. All images presented were taken after template removal.

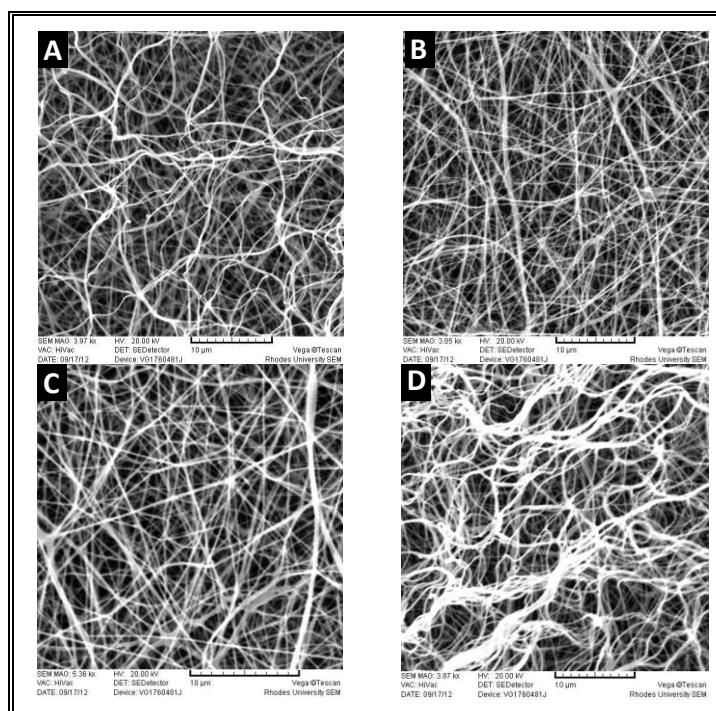


**Figure 5.9** Scanning electron micrograph (SEM) of (A) Non-imprinted nanofibers, (B) BTO<sub>2</sub>-imprinted nanofibers, (C) DBTO<sub>2</sub>-imprinted nanofibers, and (D) 4,6-DMDBTO<sub>2</sub>-imprinted nanofibers. All images presented were taken after template removal.

Electrospinning of PBI solution using the optimized electrospinning conditions (Section 5.2.2) in the absence of LiBr resulted in the production of particles (from electrospinning) rather than fibers (from electrospinning) as shown in Figure 5.10a,b. Optimization of PBI electrospinning conditions flow-rate conditions of 0.1 and 0.3 mL/h in the presence of LiBr gave beaded nanofibers (Figure 5.10c,d). SEM images of the optimized optimized molecularly imprinted and non-imprinted nanofibers are presented in Figure 5.11, slight changes in morphologies of the imprinted nanofibers was due to the presence of sulfone compounds imprinted within the nanofibers on electrospinning. The images presented for the optimised nanofibers were collected after employing Soxhlet extraction to remove template. The nanofibers were generally observed to be in the diameter range of 150-330 nm.

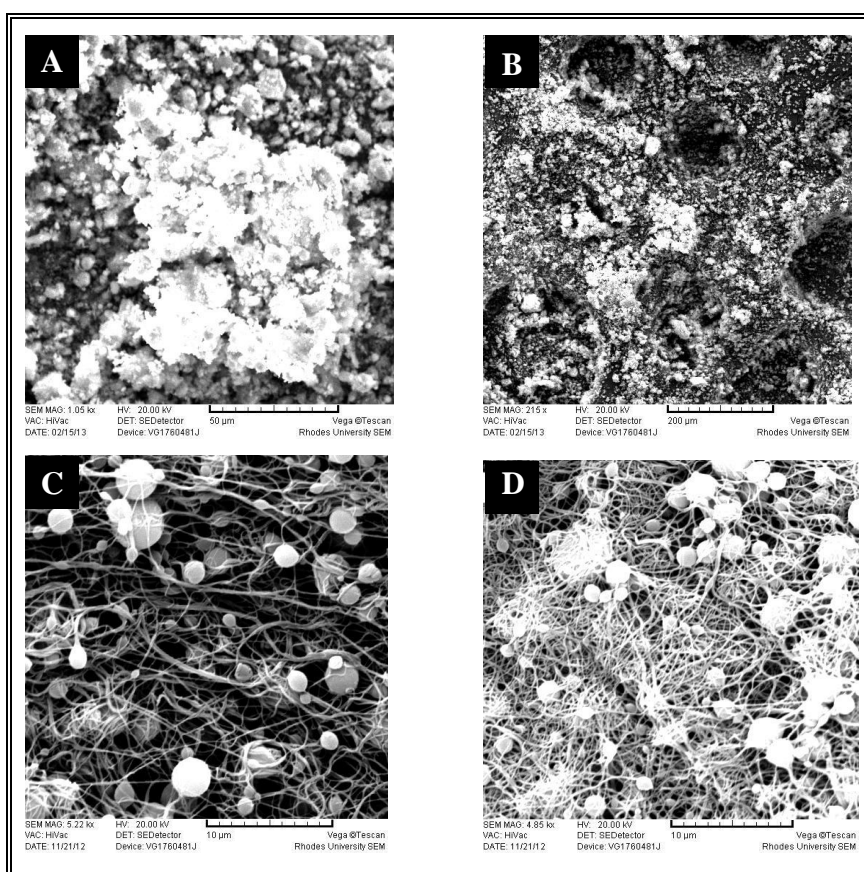


**Figure 5.10** Scanning electron microscopy (SEM) of PBI-nanofibers in the absence of LiBr (A and B) and electrospinning optimization images in the presence of LiBr (C and D).



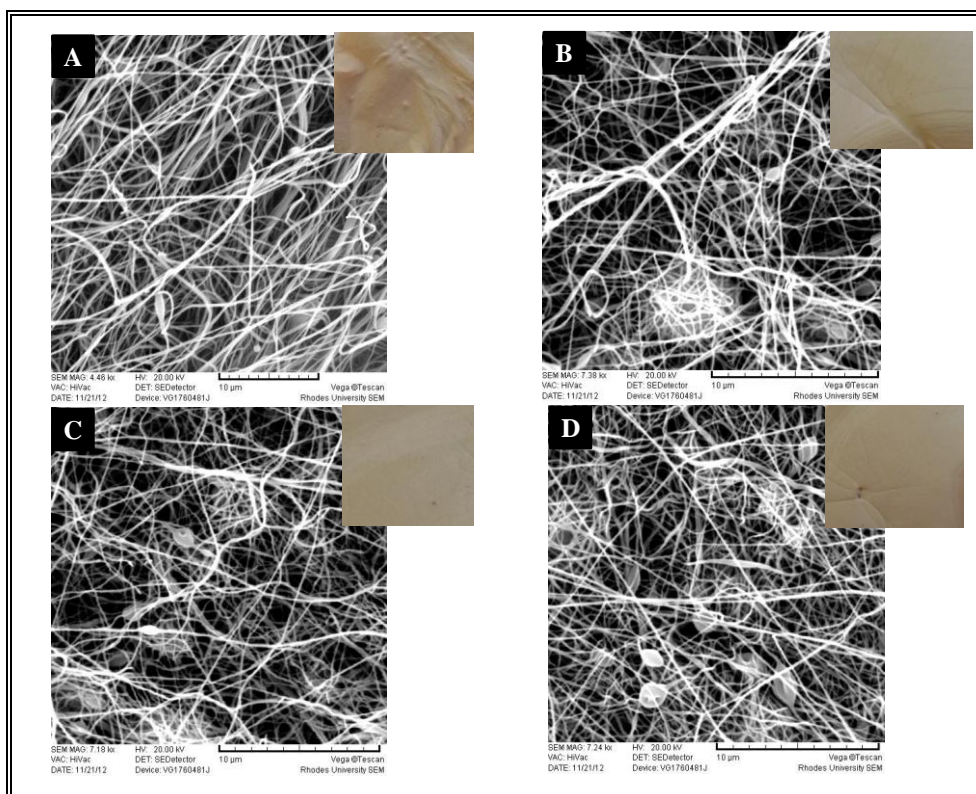


**Figure 5.11** Scanning electron microscopy (SEM) of (A) PBI-nanofibers, (B) PBI-BTO<sub>2</sub> nanofibers, (C) PBI-DBTO<sub>2</sub> nanofibers, and (D) PBI-4,6-DMDBTO<sub>2</sub> nanofibers showing surface morphology.

### 5.3.4 Surface area measurements of adsorbents

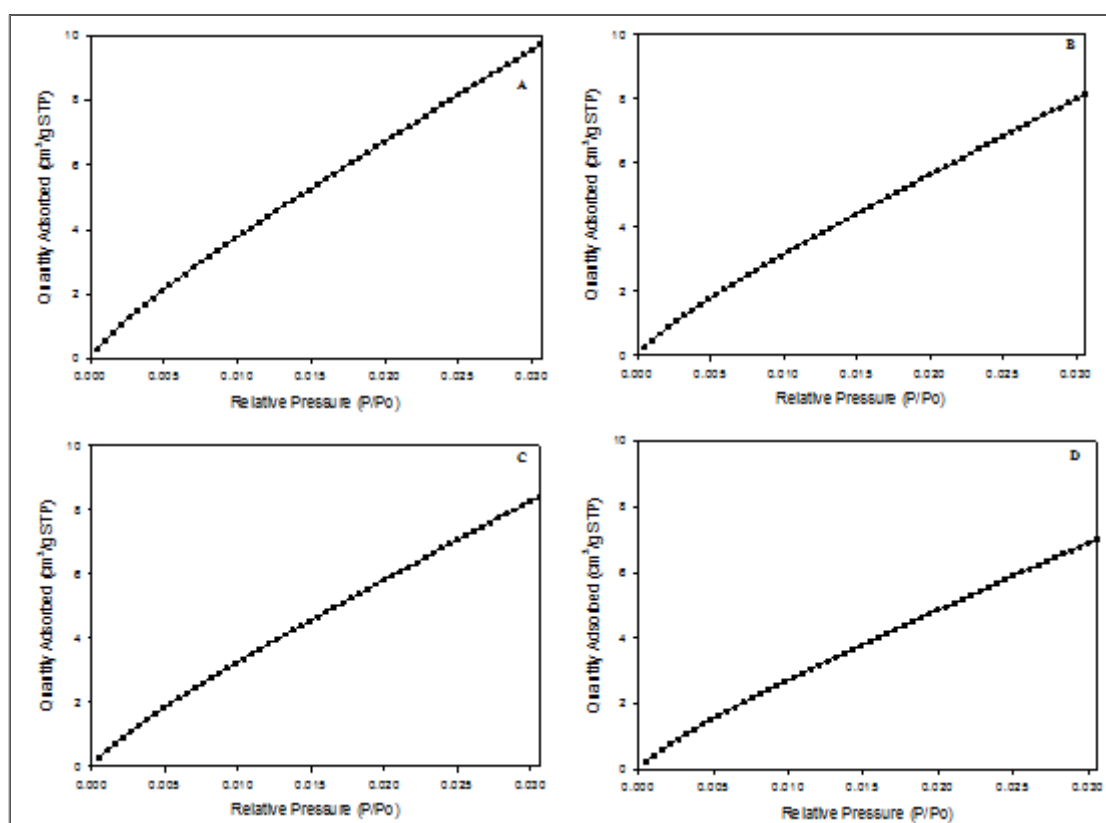
A BET surface area measurement for chitosan nanofibers and microspheres was recorded by using carbon dioxide (CO<sub>2</sub>) as the adsorbate gas. The nanofibers gave a higher surface area than the microspheres as shown in **Table 5.2**, and as also presented in CO<sub>2</sub>-adsorption isotherm (**Figures 5.12** and **5.13**).

For PBI nanofibers, nitrogen-adsorption gas was employed as adsorbate gas for surface area and porosity measurements. It was also noticed that the porosity of the nanofibers increased as the molecular size of the template increased (**Table 5.3**). The order of molecular size of these sulfone compounds increased in the order benzothiophene < dibenzothiophene < 4,6-dimethyldibenzothiophene. This is also evident in the pore size distribution of the various imprinted polymers. The BET nitrogen adsorption and desorption isotherm for PBI nanofibers are presented in **Figure 5.14**.



**Table 5.2** Surface area of imprinted and non-imprinted chitosan microspheres and nanofibers

Adsorbent types	Surface area (m <sup>2</sup> /g)	
	Microspheres	Nanofibers
Non- imprinted (control)	62	101
BTO <sub>2</sub> imprinted	57	85
DBTO <sub>2</sub> imprinted	59	87
4,6-DMDBTO <sub>2</sub> imprinted	56	73

**Figure 5.12** The BET isotherm linear plot of non-imprinted-chitosan nanofibers (A) BTO<sub>2</sub>-chitosan nanofibers (B) DBTO<sub>2</sub>- chitosan nanofibers (C) and 4,6-DMDBTO<sub>2</sub>-chitosan nanofibers (D).

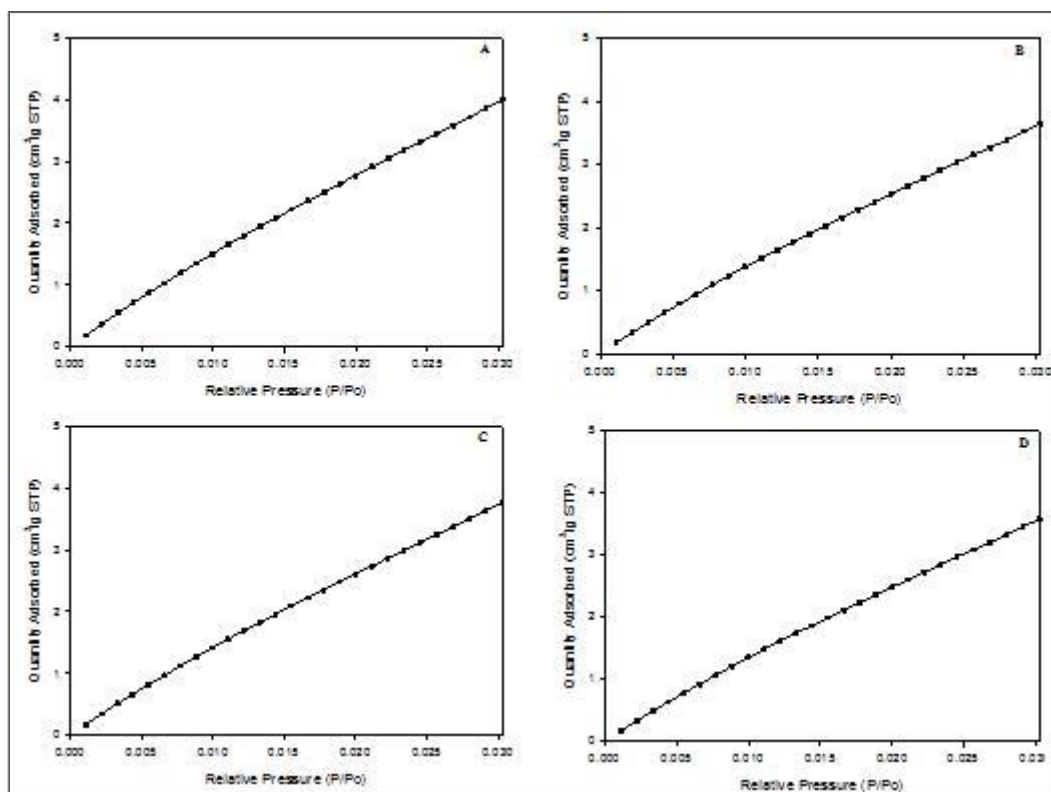


**Figure 5.13** The BET isotherm linear plot of non-imprinted-chitosan microspheres (A), BTO<sub>2</sub>-chitosan microspheres (B), DBTO<sub>2</sub>-chitosan microspheres (C), and 4,6-DMDBTO<sub>2</sub>-chitosan microspheres (D).

**Table 5.3** Surface area and porosity of imprinted- and non-imprinted-PBI nanofibers.

Adsorbent types	Surface measurements	
	Surface area (m <sup>2</sup> /g)	Pore size (Å)
Non- imprinted (control)	35	104
BTO <sub>2</sub> imprinted	33	140
DBTO <sub>2</sub> imprinted	29	154
4,6-DMDBTO <sub>2</sub> imprinted	25	193

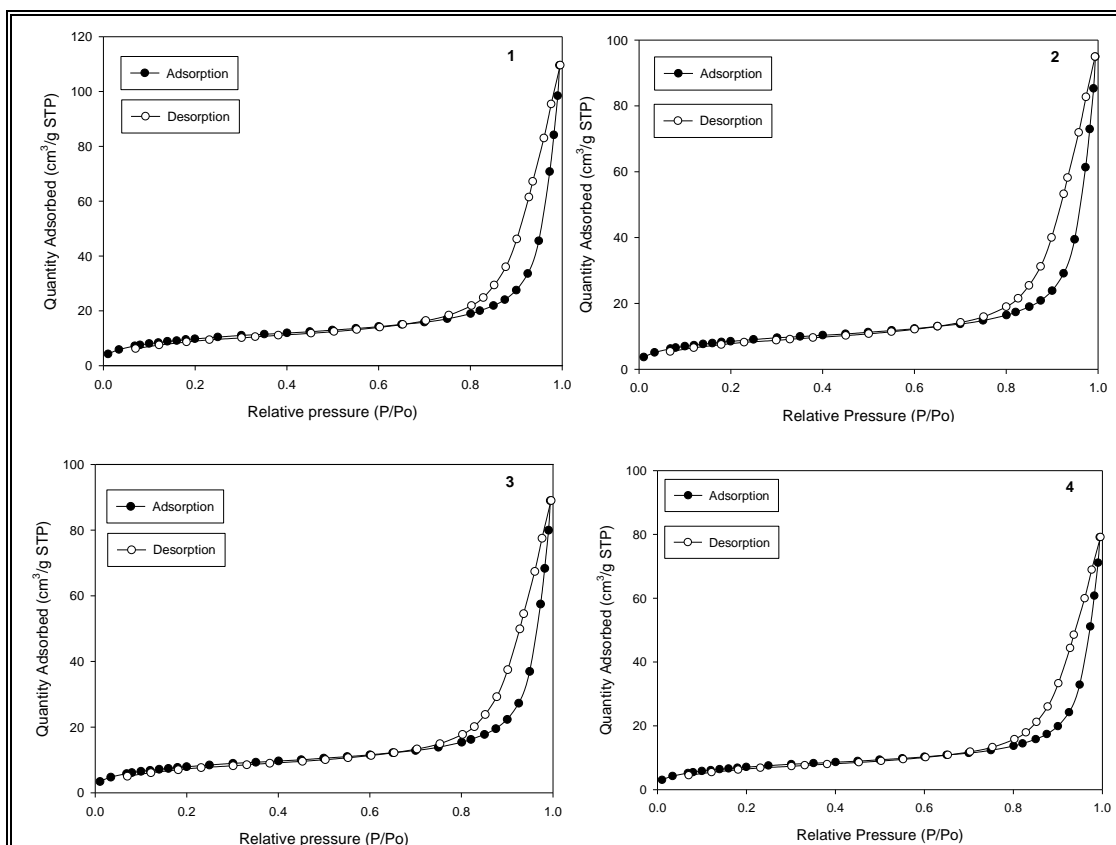


**Figure 5.14** The BET isotherm linear plot of NIP-PBI nanofibers (1), BTO<sub>2</sub>-PBI nanofibers (2), DBTO<sub>2</sub>-PBI nanofibers (3), and 4,6-DMDBTO<sub>2</sub>-PBI nanofibers (4).

### 5.3.5 Thermogravimetric analysis of adsorbents

The TG curves of the pristine chitosan, chitosan nanofibers and cross-linked microspheres can be seen in **Figure 5.15**. The nanofibers lose solvents present within its framework at a temperature of up to 150°C, thereafter stabilizes up to 200°C, after which structural collapse of the framework occurs. The higher stability observed on the chitosan nanofibers as compared to pristine chitosan was attributed to the partial salt formation with the amino-group of chitosan on dissolution with TFA. Cross-linked microspheres lose all the solvents within its framework at a temperature of 160°C, after which structural collapse began at 280°C. The greater stability of the microspheres at higher temperatures can be attributed to microspheres cross-linking which imparted stability on the chitosan. From the thermogravimetric curve, glutaraldehyde-cross-linked chitosan microspheres tend to be more stable when compared to pristine chitosan and chitosan nanofibers as a result of crosslinking. Similar

degradation pattern were observed for BTO<sub>2</sub>-, DBTO<sub>2</sub>- and 4,6-DMDBTO<sub>2</sub>-imprinted chitosan nanofibers (**Figure 5.15**).

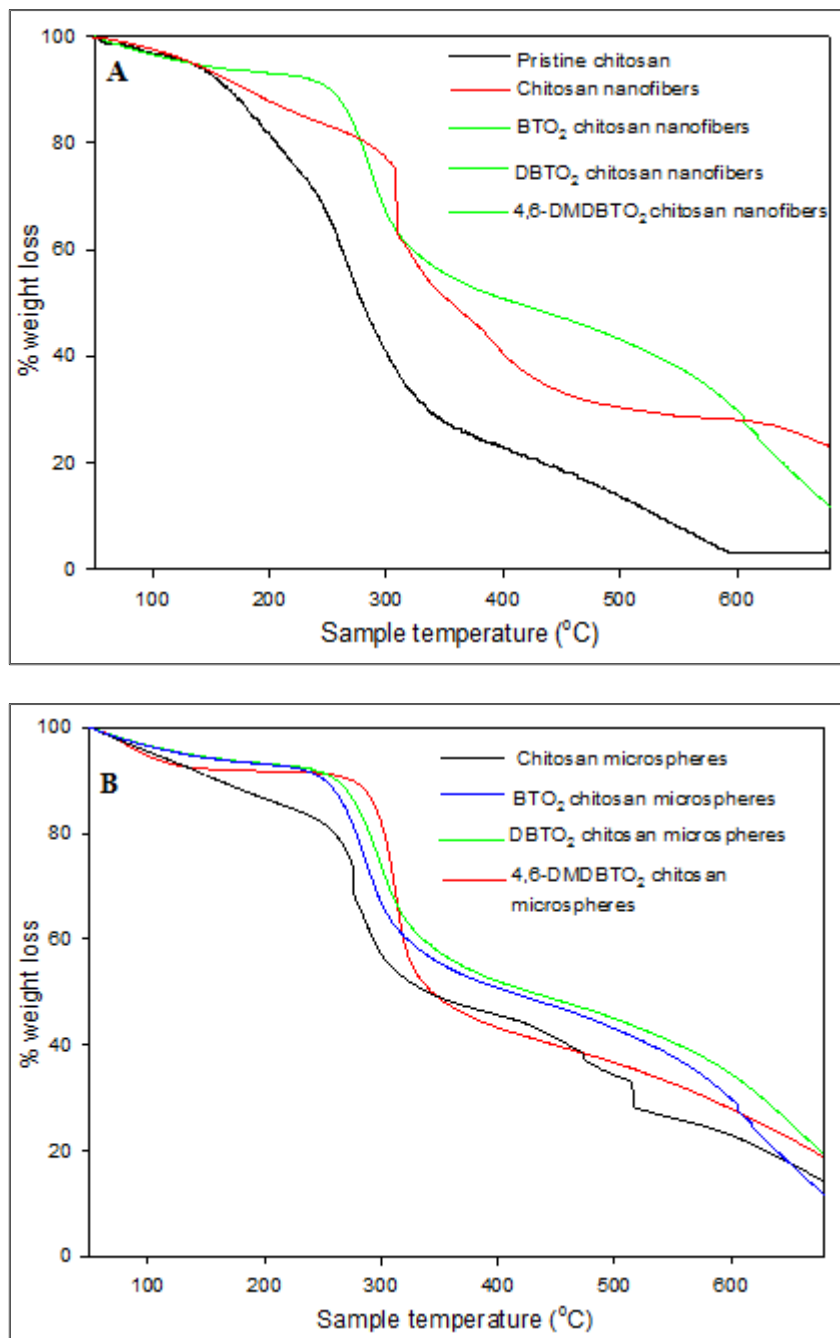


**Figure 5.15** TG profile curve for (A) pristine chitosan flakes and imprinted nanofibers, and (B) non-imprinted and imprinted chitosan microspheres.

Thermogravimetric analysis of PBI-nanofibers, PBI-BTO<sub>2</sub> nanofibers, PBI-DBTO<sub>2</sub> nanofibers and PBI-4,6-DMDBTO<sub>2</sub> nanofibers were conducted under a nitrogen atmosphere in a temperature range of 40-650°C (**Figure 5.16**). The nanofibers (imprinted and non-imprinted) gave similar

decomposition patterns with three distinct weight losses at 110°C, between 220 and 400°C and between 500 and 650°C. The first two weight losses can be assigned to loosely bound solvent/water molecules, which occurred as a result of moisture absorption on the nanofibers.<sup>410,411</sup> The decomposition of PBI nanofibers backbone only began to occur at a temperature of about 500°C, hence confirming its high thermal stability.<sup>411, 412</sup> For the PBI nanofibers, a total of 19.3% weight loss was attributed to moisture and solvent molecules, a further 20.7% weight loss occurred from 500 to 650°C as a result of the breakdown in PBI polymer backbone. For the BTO<sub>2</sub>-PBI nanofibers, a total of 10.0% weight loss was attributed to moisture and solvent molecule, while a further 25.7% weight loss was due to the breakdown in polymer backbone from 500 to 650°C. For the DBTO<sub>2</sub>-PBI nanofibers, a total of 8.1% weight loss was attributed to moisture and solvent molecule. A further 18.7% weight loss which occurred from 500 to 650°C was as a result of a breakdown in the polymer backbone. For the 4,6-DMDBTO<sub>2</sub>-PBI nanofibers, a total of 9.7% weight loss was attributed to moisture and adsorbed solvent, while a further 7.3% weight loss occurred between 500 to 650°C due to the partial collapse of the polymer backbone.

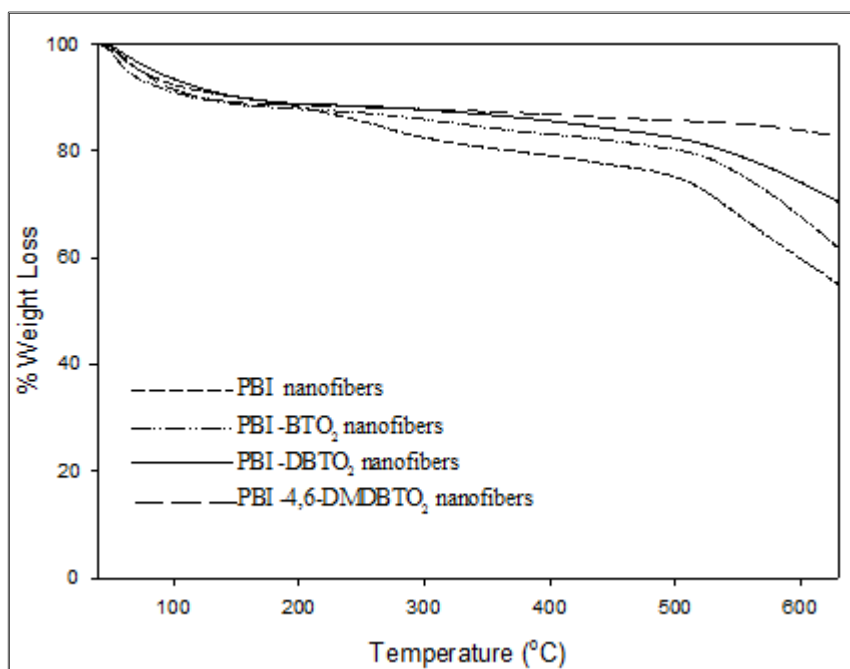


**Figure 5.16** TG profile curve for PBI-nanofibers, PBI-BTO<sub>2</sub> nanofibers, PBI-DBTO<sub>2</sub> nanofibers and PBI-4,6-DMDBTO<sub>2</sub> nanofibers.

#### 5.4 Equilibrium swelling ratio of adsorbents

Equilibrium swelling experiments of nanofibers and cross-linked microspheres in acetonitrile and hexane were carried out at room temperature to confirm the degree of cross-linking of adsorbents and also to understand their swelling patterns. The equilibrium swelling ratio (ESR) was calculated as follows:  $ESR = (W - W_0) / W_0$ , where  $W_0$  is the weight (mg) of sample before immersion into solvent and  $W$  is the final weight (mg) of adsorbents after immersion into solvent (acetonitrile and hexane) with time.<sup>413</sup>

To perform the swelling experiment, 30 mg of adsorbents (microspheres and nanofibers) was added to 5 mL of each selected solvent in 15 mL vials, the study was carried-out and monitored at room temperature. Adsorbents were removed by filtration through a Büchner funnel and weighed at specific time intervals. From the results obtained, the adsorbents (nanofibers and microspheres) swelled more in acetonitrile (**Figure 5.17**). Swelling in hexane was minimal due to its poor affinity for the hydrophilic adsorbent.

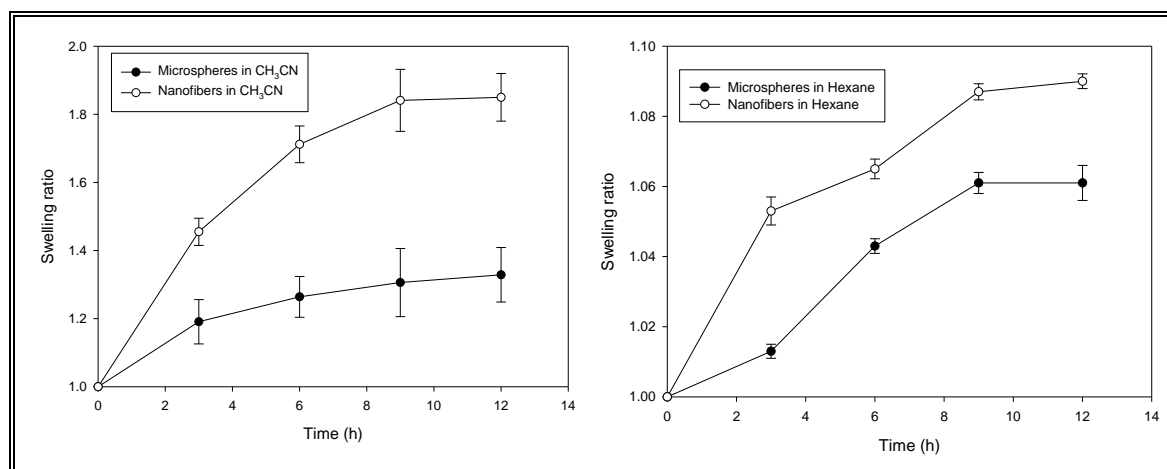


**Figure 5.17** Swelling ratio of adsorbents in CH<sub>3</sub>CN and hexane.

The low degree of swelling in the microspheres as compared to the nanofibers confirmed that the microspheres were cross-linked (**Figure 5.17**). On drying the swollen nanofiber strands, non-smooth nanofibers surface morphology was observed (**Figure 5.18**). However, this change in the nanofibers morphology did not affect the re-usability of the adsorbent, as the available functionalities, -OH and -NH<sub>2</sub>, determines its reusability.

Polybenzimidazole (PBI) nanofibers also presented a similar trend as observed for chitosan microspheres and nanofibers (**Figure 5.19**). Low level of swelling in hexane was attributed to the poor affinity between PBI and hexane. However, the polybenzimidazole nanofibers swell higher than the chitosan counterpart, with no change in nanofibers surface morphology.

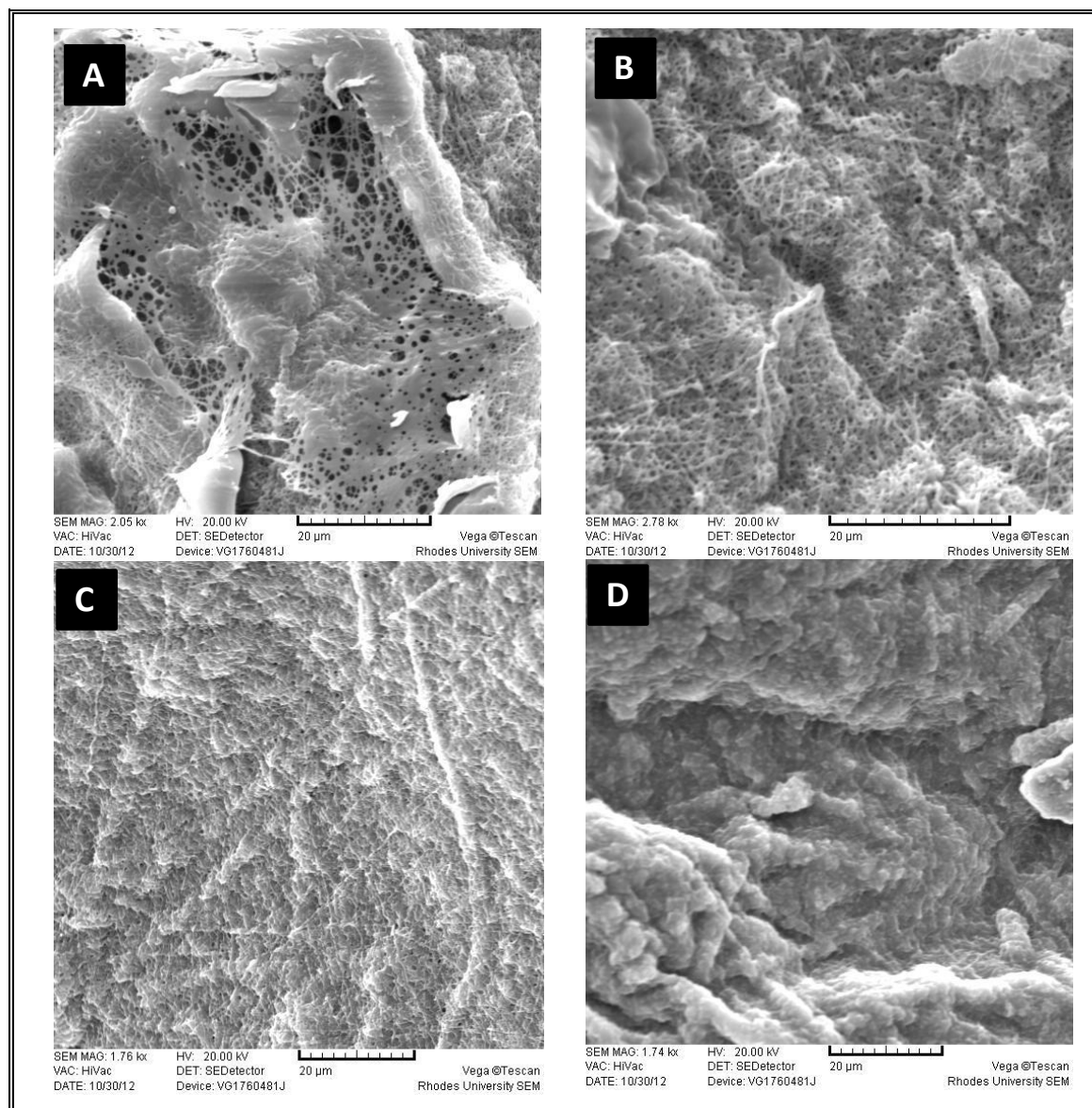


**Figure 5.18** Scanning electron microscopy (SEM) micrograph of chitosan nanofibers (A) Non-imprinted (B) BTO<sub>2</sub>-imprinted (C) DBTO<sub>2</sub>-imprinted and (D) 4,6-DMDBTO<sub>2</sub>-imprinted, showing surface morphology change after contact with CH<sub>3</sub>CN.

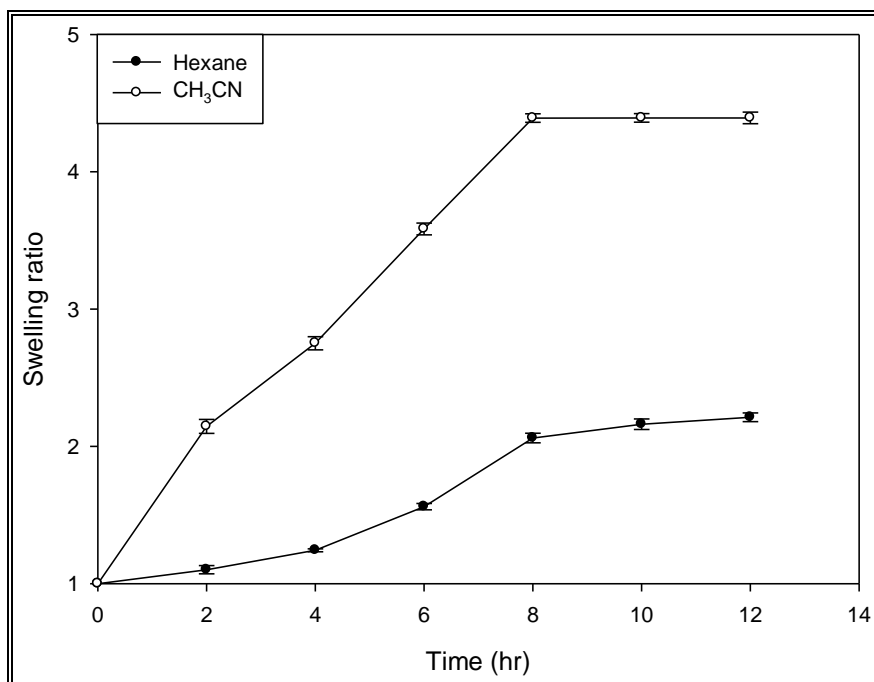


**Figure 5.19** Swelling ratio of polybenzimidazole nanofibers in CH<sub>3</sub>CN and hexane.

## 5.5 Sulfone compounds adsorption studies

Adsorption and desorption procedures are described in **Sections 2.7** and **2.8**.

### 5.5.1 Adsorption studies employing chitosan adsorbents

#### 5.5.1.1 Adsorbent mass optimization studies

In order to ascertain the mass of adsorbent to be used for the study, various mass of adsorbents (30 mg, 50 mg, 100 mg and 150 mg) were employed at constant volume and concentration of the sulfone compounds. For this study, the adsorption procedure described in **Section 2.7** was followed. From the results obtained, it can be seen that 100 mg gave a good adsorption for both the microspheres (**Figure 5.20**) and nanofibers (**Figure 5.21**). For the rest of the adsorption studies 100 mg of adsorbent was used.



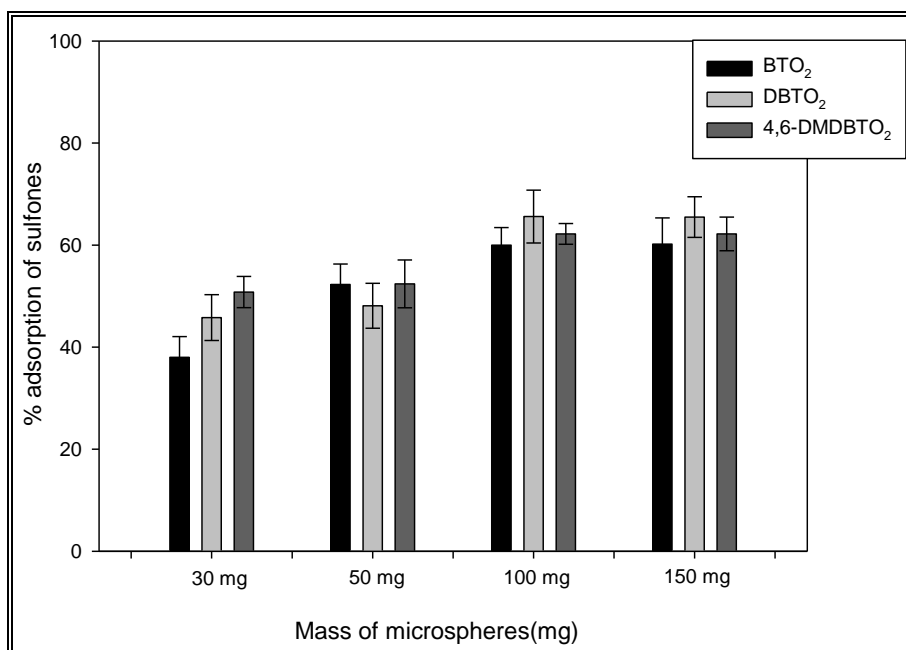


**Figure 5.20** Effect of microspheres mass variation on the adsorption of benzothiophene sulfone (BTO<sub>2</sub>), dibenzothiophene sulfone (DBTO<sub>2</sub>) and 4,6-dimethyldibenzothiophene sulfone (4,6-DMDBTO<sub>2</sub>).

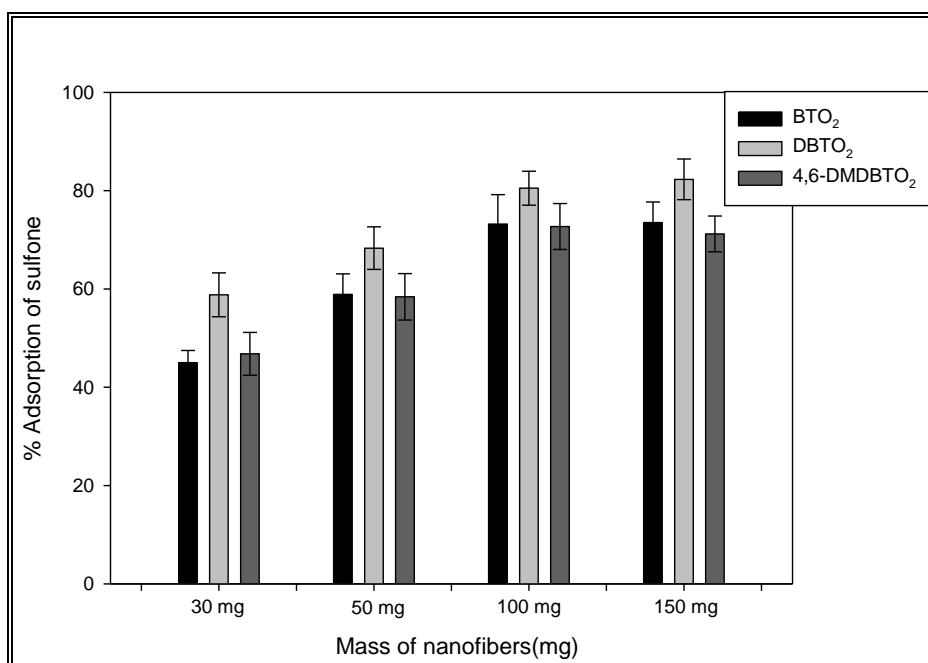


**Figure 5.21** Effect of nanofibers mass variation on the adsorption of benzothiophene sulfone (BTO<sub>2</sub>), dibenzothiophene sulfone (DBTO<sub>2</sub>) and 4,6-dimethyldibenzothiophene sulfone (4,6-DMDBTO<sub>2</sub>).

### 5.5.1.2 Adsorption selectivity on molecularly imprinted chitosan microspheres and nanofibers

Adsorption assays were carried out to evaluate the loading capacity and selectivity of imprinted chitosan adsorbents. 100 mg of the imprinted adsorbents were added to vials and mixed with a mixture of organosulfur compounds, BTO<sub>2</sub>, DBTO<sub>2</sub> and 4,6-DMDBTO<sub>2</sub> (2 mL, 5 mM each). The corresponding adsorption assays were also carried out using non-imprinted adsorbents. The suspension was left under mechanical agitation at 150 rpm for 24 h as described in the adsorption studies. Maximum adsorption observed for BTO<sub>2</sub>, DBTO<sub>2</sub> and 4,6-DMDBTO<sub>2</sub> respectively was  $8.5 \pm 0.6$  mg/g,  $7.0 \pm 0.5$  mg/g and  $6.6 \pm 0.7$  mg/g when imprinted chitosan nanofibers were employed, and  $4.9 \pm 0.5$  mg/g,  $4.2 \pm 0.7$  mg/g and  $3.9 \pm 0.6$  mg/g on molecularly imprinted chitosan microspheres (**Figure 5.22**). However, high adsorption capacities with no selectivity were observed for non-imprinted nanofibers and microspheres ( $11.2 \pm 1.1$  mg/g,  $10.4 \pm 0.9$  mg/g and  $8.9 \pm 1.2$  mg/g when non-imprinted chitosan nanofibers were employed, and  $5.7 \pm 0.7$  mg/g,  $5.6 \pm 0.4$  mg/g and  $5.1 \pm 0.6$  mg/g on non-imprinted chitosan microspheres for BTO<sub>2</sub>, DBTO<sub>2</sub> and 4,6-DMDBTO<sub>2</sub> respectively) (**Figure 5.22**). The non-specific binding nature on non-imprinted hydrogel adsorbents enhanced the high adsorption as compared to imprinted adsorbents which binding sites are restricted.<sup>389,414</sup> Desorption of sulfone compound was relatively high in both the imprinted and non-imprinted polymers.

Imprinted polymer adsorbents were reasonably selective for their target sulfone-containing compounds. BTO<sub>2</sub>-imprinted nanofibers showed a high adsorption capacity of  $8.5 \pm 0.6$  mg/g for BTO<sub>2</sub>, while adsorption capacities for DBTO<sub>2</sub> and 4,6-DMDBTO<sub>2</sub> were  $2.3 \pm 0.2$  mg/g and  $2.1 \pm 0.3$  mg/g respectively on this material. DBTO<sub>2</sub>-imprinted nanofibers' adsorption capacity for DBTO<sub>2</sub> was  $7.0 \pm 0.5$  mg/g, while BTO<sub>2</sub> and 4,6-DMDBTO<sub>2</sub> adsorption capacities were  $2.8 \pm 0.5$  mg/g and  $1.5 \pm 0.1$  mg/g respectively. 4,6-DMDBTO<sub>2</sub>-imprinted nanofibers gave an adsorption capacity of  $6.6 \pm 0.7$  mg/g for 4,6-DMDBTO<sub>2</sub>, while BTO<sub>2</sub> and DBTO<sub>2</sub> adsorption capacities were  $1.5 \pm 0.2$  mg/g and  $2.4 \pm 0.5$  mg/g respectively. A similar selectivity trend was also observed with imprinted microspheres as BTO<sub>2</sub>-imprinted microspheres adsorption capacity for BTO<sub>2</sub> was  $4.9 \pm 0.5$  mg/g, while adsorption for DBTO<sub>2</sub> and 4,6-DMDBTO<sub>2</sub> were  $1.3 \pm 0.5$  mg/g and  $1.1 \pm 0.3$  mg/g respectively. DBTO<sub>2</sub>-imprinted microspheres' adsorption capacity for DBTO<sub>2</sub> was  $4.2 \pm 0.7$  mg/g, while BTO<sub>2</sub> and 4,6-DMDBTO<sub>2</sub>

were  $1.5 \pm 0.3$  mg/g and  $1.2 \pm 0.2$  mg/g respectively. 4,6-DMDBTO<sub>2</sub>-imprinted microspheres adsorption capacity for 4,6-DMDBTO<sub>2</sub> was  $3.9 \pm 0.6$  mg/g, while BTO<sub>2</sub> and DBTO<sub>2</sub> adsorption capacities were  $1.3 \pm 0.7$  mg/g and  $1.8 \pm 0.4$  mg/g respectively.

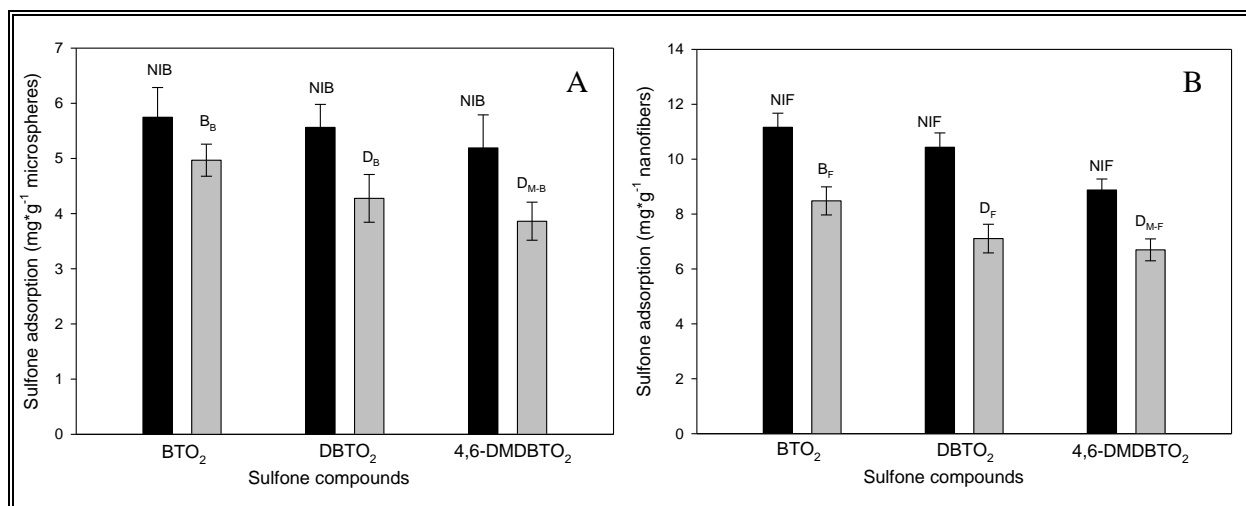


**Figure 5.22** Effect of selectivity on the adsorption of benzothiophene sulfone (BTO<sub>2</sub>), dibenzothiophene sulfone (DBTO<sub>2</sub>) and 4,6-dimethyldibenzothiophene sulfone (4,6-DMDBTO<sub>2</sub>). Using microspheres (A) employed are NIB: Non-imprinted microspheres; B<sub>B</sub>: benzothiophene sulfone imprinted microspheres; D<sub>B</sub>: dibenzothiophene sulfone imprinted microspheres; D<sub>M-B</sub>: 4,6-dimethyldibenzothiophene sulfone imprinted microspheres and nanofibers (B) are: NIF: Non-imprinted nanofibers; B<sub>F</sub>: benzothiophene sulfone imprinted nanofibers; D<sub>F</sub>: dibenzothiophene sulfone imprinted nanofibers; D<sub>M-F</sub>: 4,6-dimethyldibenzothiophene sulfone imprinted nanofibers.

### 5.5.1.3 Adsorption kinetics of molecularly imprinted chitosan microspheres and nanofibers

Adsorption kinetic studies showed that sulfone molecule adsorption was initially fast due to the availability of surface adsorption and thereafter adsorption rate slowed down as a result of surface saturation, thus, limiting further sulfone molecules penetration. **Figure 5.23** represents the adsorption kinetics curve for the various sulfone compounds using imprinted adsorbents with adsorption equilibrium achieved after 10 h. Nanofibers were reported to have a higher adsorption capacity before equilibrium as compared to the microspheres. The high adsorption capacity exhibited by nanofibers

was attributed to their larger surface area. The quantity adsorbed on both adsorbents increases in the order of  $\text{BTO}_2 > \text{DBTO}_2 > 4,6\text{-DMDBTO}_2$ , the observed adsorption trend was as a result of steric hindrance posed by the bulkiness of each sulfone compound.

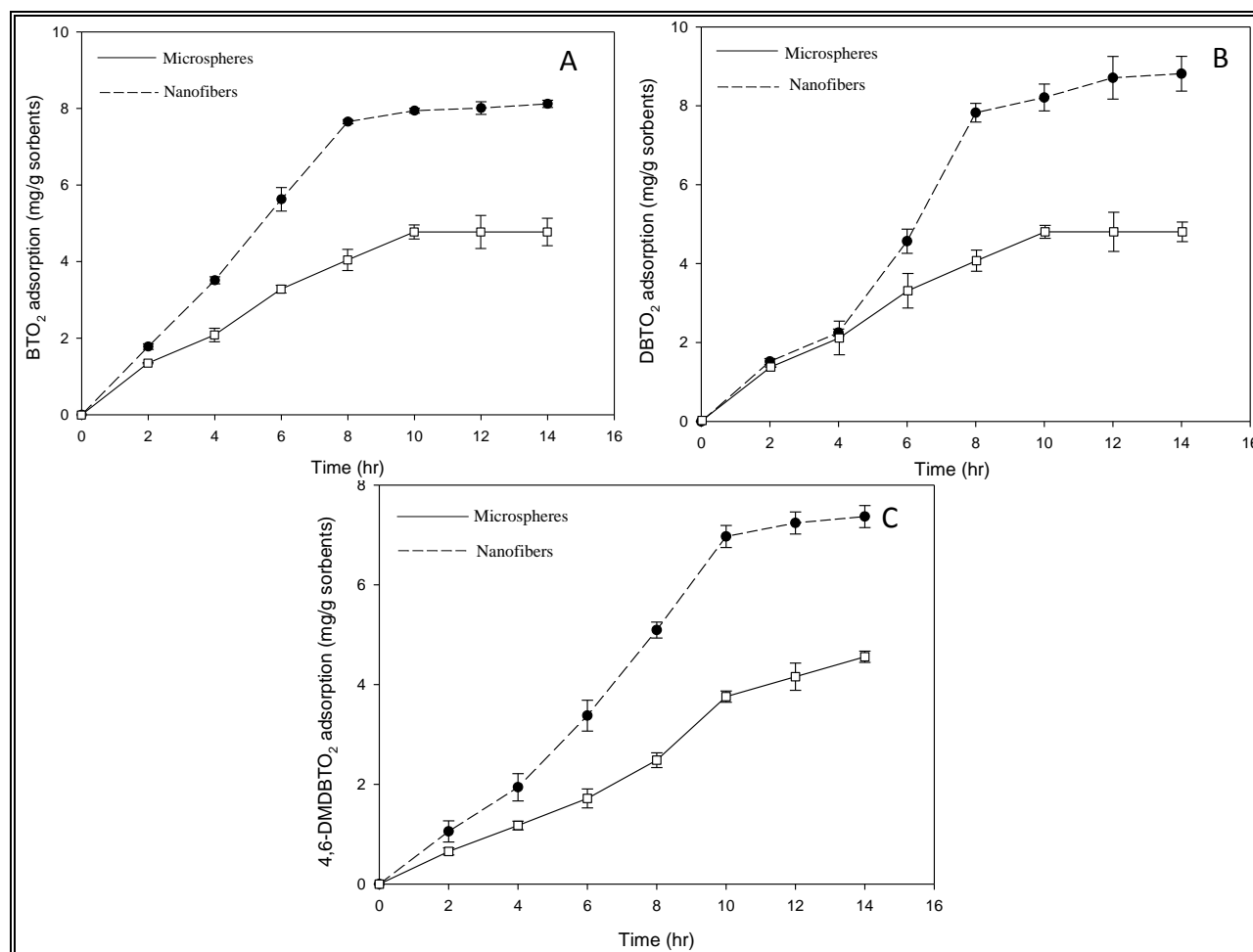


**Figure 5.23** Kinetic studies on the various sulfone compounds (A) benzothiophene sulfone (BTO<sub>2</sub>), (B) dibenzothiophene sulfone (DBTO<sub>2</sub>) and (C) 4,6-dimethyldibenzothiophene sulfone (4,6-DMDBTO<sub>2</sub>).

The kinetic mechanism that controls the adsorption process under batch study was monitored by using pseudo-first-order model (**Equation 5.1**) and pseudo-second-order model (**Equation 5.2**). Kinetic studies were carried out by using an adsorbent (nanofibers and microspheres) mass of 100 mg contained in 2 mL of 5 mM sulfone compounds solution. Batch study was employed to monitor adsorption capacity with time.

$$\log(q_e - q_t) = \log q_e - \frac{K_1}{2.303} t \quad 5.1$$

$$\frac{t}{q_e} = \frac{1}{q_e^2 K_2} + \frac{1}{q_e} t \quad 5.2$$

where  $q_e$  and  $q_t$  (mg/g) are the amounts of sulfone compounds adsorbed on the adsorbent at equilibrium and time  $t$ , respectively.  $K_1$  ( $h^{-1}$ ) is the pseudo-first-order adsorption rate constant and was calculated by plotting the  $\log(q_e - q_t)$  versus  $t$  (**Figure 5.24**).  $K_2$  (g/mg/h) is the adsorption rate constant of pseudo-second-order and was calculated from the slope and intercept of the plots  $t/q_t$  versus  $t$  (**Figure 5.25**). Based on the obtained correlation coefficients ( $R^2$ ) from both graphs, pseudo-first-order model showed a fitted plot for the adsorption studies. These results illustrated that the adsorption rate was controlled by mass transfer in solution. Pseudo-first and pseudo-second order parameters (coefficients) are presented in **Table 5.4**.

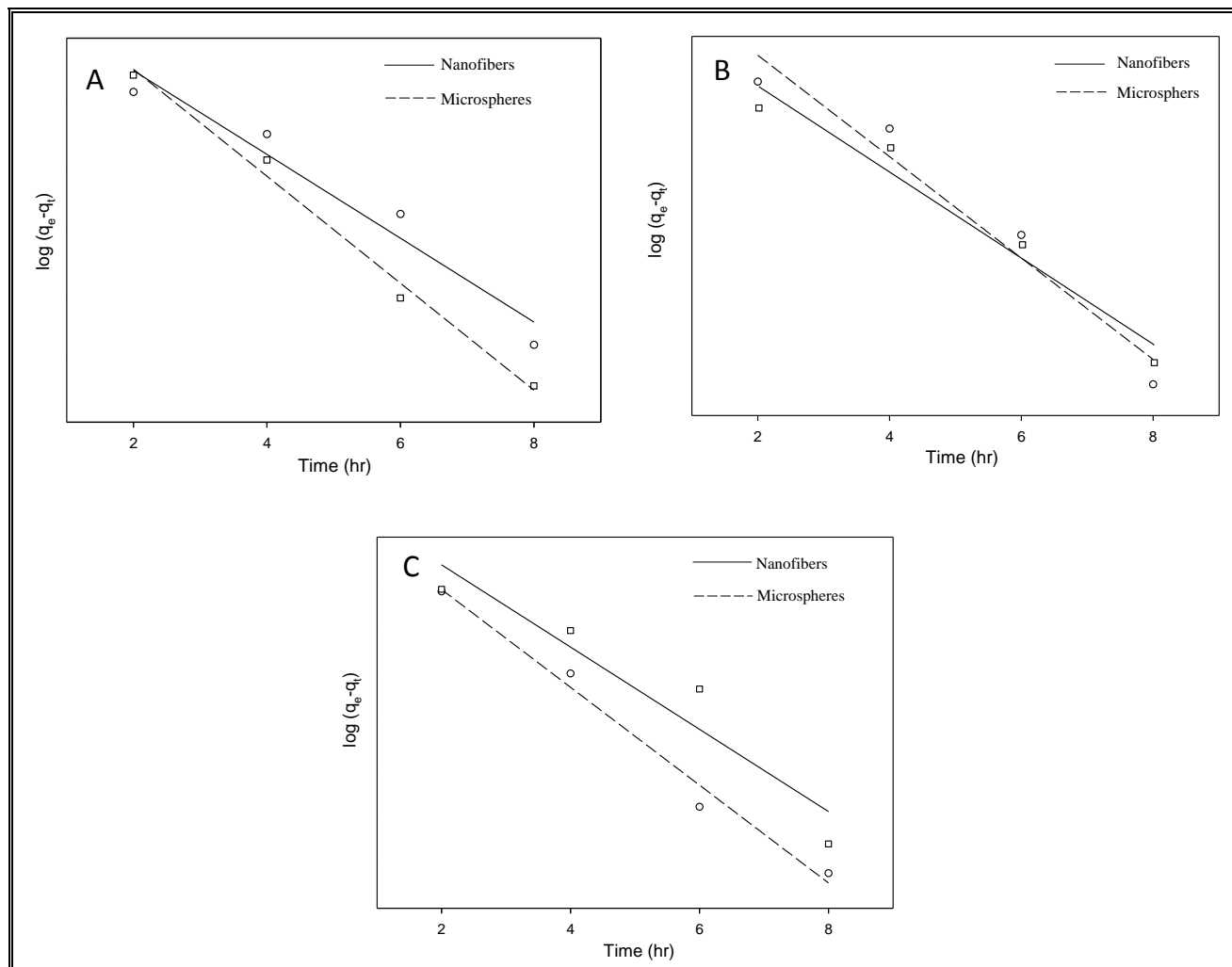


**Figure 5.24** Pseudo-first-order plot of the various sulfone compounds (A) benzothiophene sulfone (BTO<sub>2</sub>), (B) dibenzothiophene sulfone (DBTO<sub>2</sub>) and (C) 4,6-dimethyldibenzothiophene sulfone (4,6-DMDBTO<sub>2</sub>).

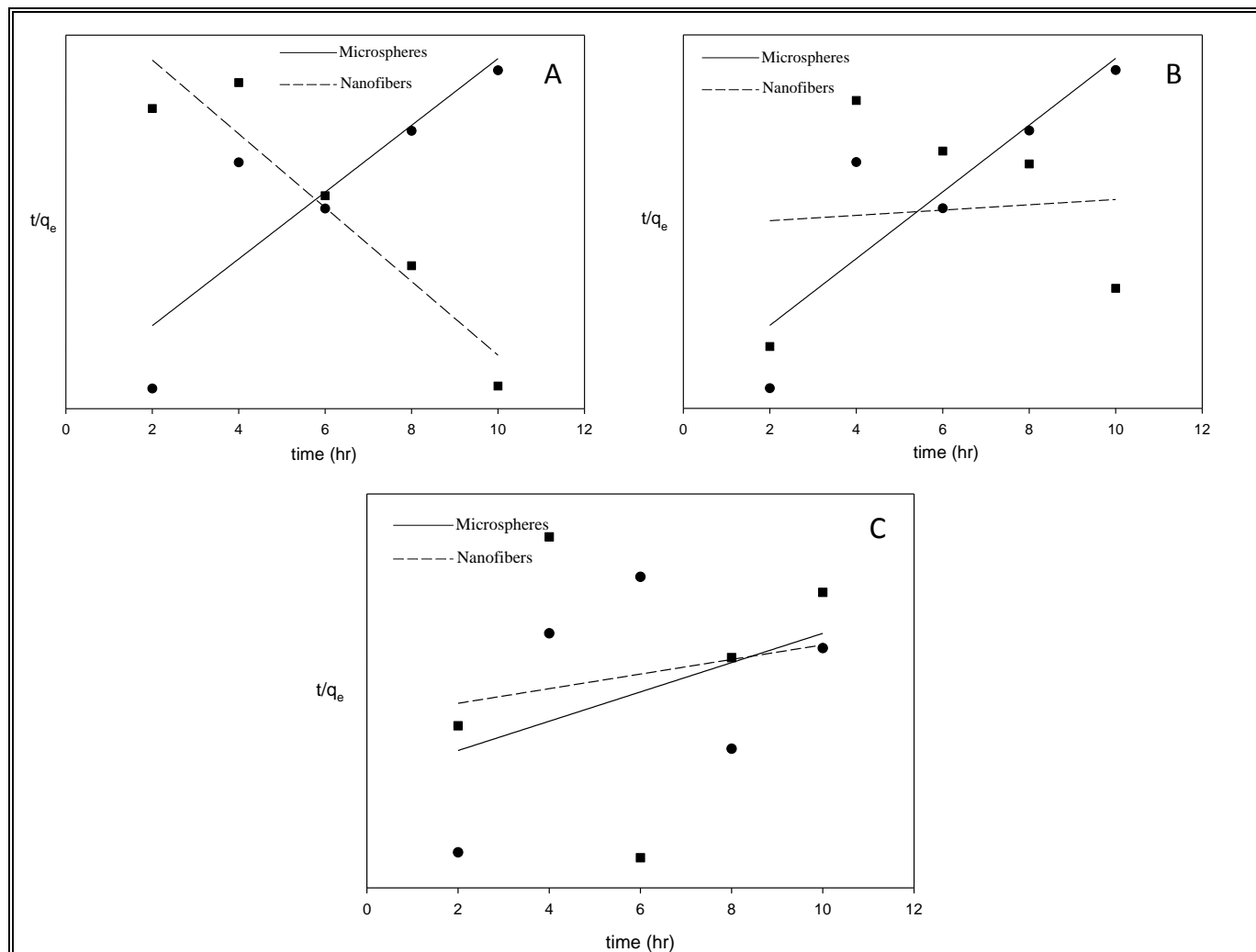


**Figure 5.25** Pseudo-second-order plot of the various sulfone compounds (A) benzothiophene sulfone (BTO<sub>2</sub>), (B) dibenzothiophene sulfone (DBTO<sub>2</sub>) and (C) 4,6-dimethyldibenzothiophene sulfone (4,6-DMDBTO<sub>2</sub>).



### 5.5.1.4 Adsorption isotherms of molecularly imprinted chitosan microspheres and nanofibers

The adsorption behaviour of sulfone compounds on imprinted chitosan adsorbents is an important factor to investigate. Langmuir and Freundlich isothermal equations (**Equations 5.3** and **5.4**) were employed to describe the equilibrium adsorption behaviour.<sup>415-417</sup>

$$\frac{C_e}{q_e} = \frac{C_e}{Q_m} + \frac{K_d}{Q_m} \quad \mathbf{5.3}$$

$$\log q_e = \frac{1}{n} \log C_e + \log K \quad \mathbf{5.4}$$

where  $q_e$  (mg/g) and  $C_e$  (mg/g) are the amount adsorbed at equilibrium and the equilibrium concentration  $Q_m$  is the theoretical maximum adsorption capacity at monolayer (mg/g), and  $K_d$  is the Langmuir constant (related to the affinity of adsorption sites).<sup>418</sup>

Freundlich constants  $k$  and  $n$  indicating adsorption capacity and intensity, respectively, were determined from the linear plot of  $\log q_e$  against  $\log C_e$ . Freundlich isotherm indicated multiple layered adsorption on adsorbents, which may possibly infer sulfone-sulfone interactions. While Langmuir equation obtained from a plot of  $C_e/q_e$  against  $C_e$  is probably proof of chemical adsorption, which may usually mean monolayer adsorption on the surface of adsorbents. From the plots, Freundlich adsorption equation fitted better {larger correlation coefficient ( $R^2$ ), (**Figure 5.26 a, b**)} as compared to the Langmuir parameters (**Figure 5.27 a, b**). Freundlich constant 'n' value lies within the range 1 to 10, thus indicating that adsorption on the adsorbent (microspheres and fibers) is favourable.<sup>419-421</sup> Freundlich and Langmuir equation parameters are presented in **Table 5.5**.

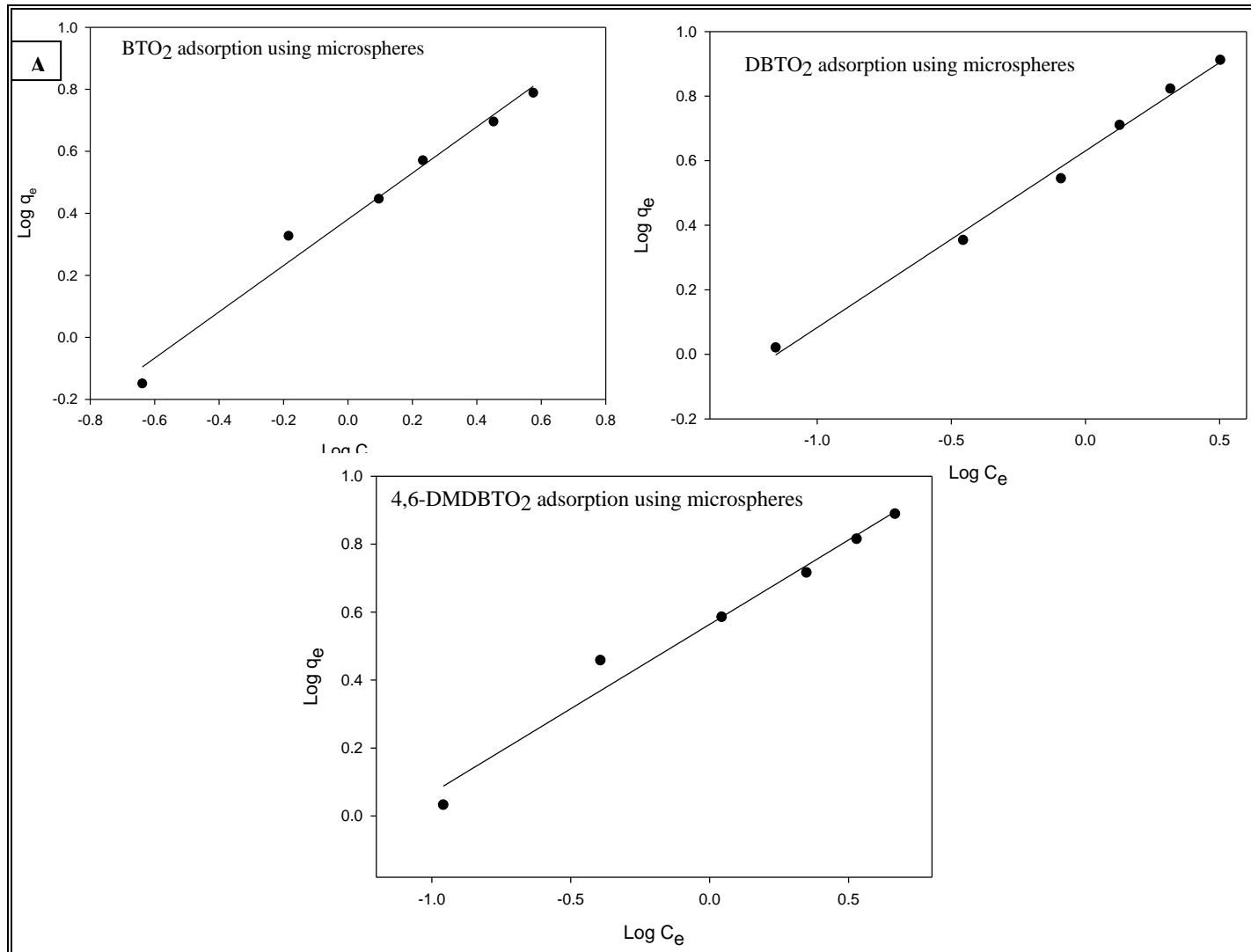


**Figure 5.26a** Freundlich plot the  $\log q_e$  versus  $\log C_e$  using chitosan microspheres.

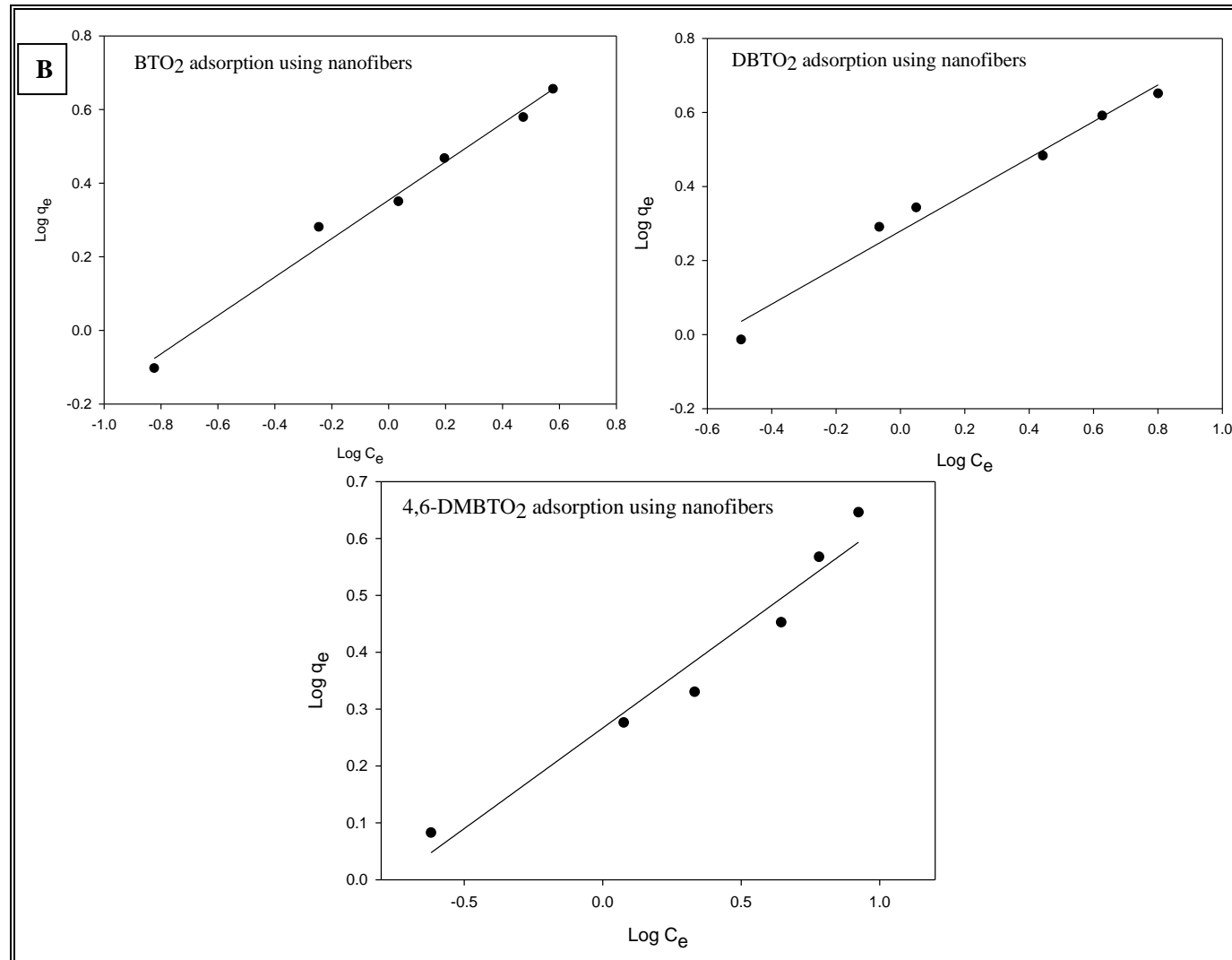


**Figure 5.26b** Freundlich plot the  $\log q_e$  versus  $\log C_e$  using chitosan nanofibers.

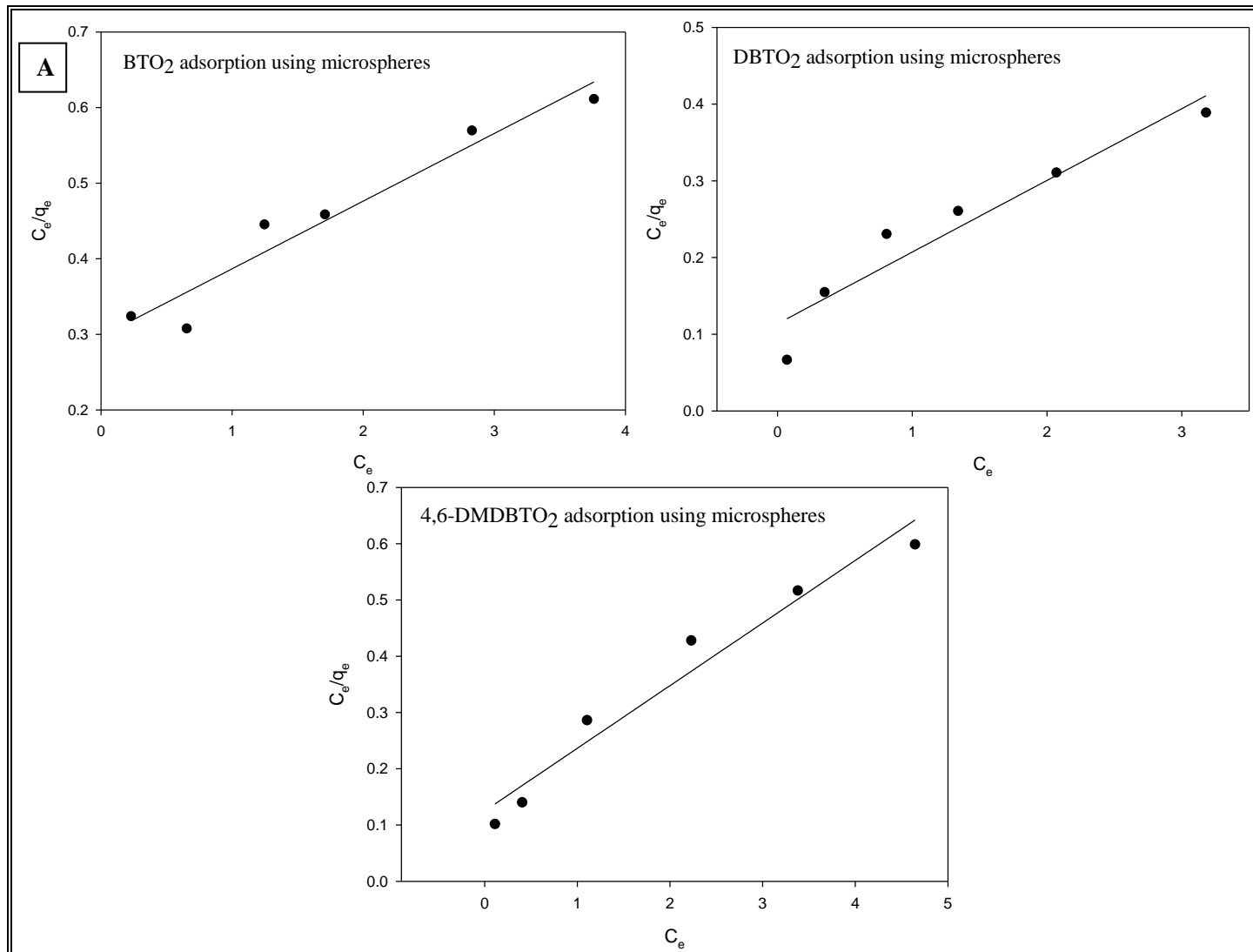


**Figure 5.27a** Langmuir plot of  $C_e/q_e$  versus  $C_e$  using chitosan microspheres.

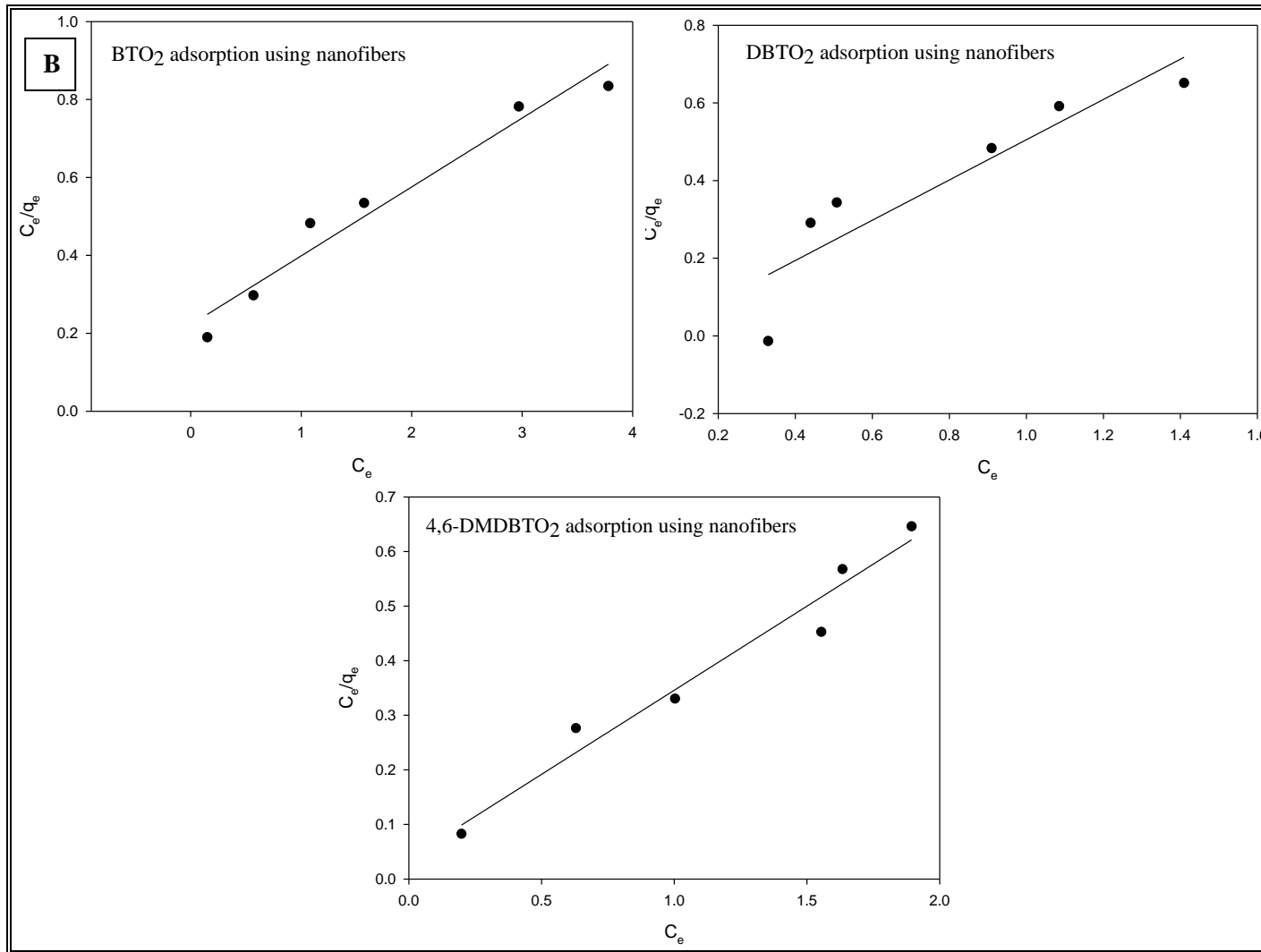


**Figure 5.27b** Langmuir plot of  $C_e/q_e$  versus  $C_e$  using chitosan nanofibers.

**Table 5.4** Kinetic data of pseudo-first-order and second order for the imprinted-chitosan nanofibers and microspheres.

Adsorbents	Pseudo-first-order kinetics						Pseudo-second-order kinetics					
	BTO <sub>2</sub>		DBTO <sub>2</sub>		4,6-DMDBTO <sub>2</sub>		BTO <sub>2</sub>		DBTO <sub>2</sub>		4,6-DMDBTO <sub>2</sub>	
	k (h <sup>-1</sup> )	R <sup>2</sup>	k (h <sup>-1</sup> )	R <sup>2</sup>	k (h <sup>-1</sup> )	R <sup>2</sup>	k <sub>2</sub> (g mg <sup>-1</sup> h <sup>-1</sup> )	R <sup>2</sup>	k <sub>2</sub> (g mg <sup>-1</sup> h <sup>-1</sup> )	R <sup>2</sup>	k <sub>2</sub> (g mg <sup>-1</sup> h <sup>-1</sup> )	R <sup>2</sup>
Microspheres	1.284	0.9908	0.261	0.9793	1.214	0.9844	0.054	0.7649	0.05	0.7649	0.019	0.1806
Nanofibers	0.151	0.9468	0.154	0.9754	0.255	0.9052	-0.11	0.8962	-0.12	0.8962	0.006	0.034

**Table 5.5** Parameters of Langmuir adsorption model and Freundlich adsorption model for the imprinted-chitosan nanofibers and microspheres.

Adsorbents	Langmuir parameters						Freundlich parameters					
	BTO <sub>2</sub>		DBTO <sub>2</sub>		4,6DMDBTO <sub>2</sub>		BTO <sub>2</sub>		DBTO <sub>2</sub>		4,6DMDBTO <sub>2</sub>	
	Q <sub>m</sub>	R <sup>2</sup>	Q <sub>m</sub>	R <sup>2</sup>	Q <sub>m</sub>	R <sup>2</sup>	n	R <sup>2</sup>	n	R <sup>2</sup>	n	R <sup>2</sup>
Microspheres	5.66	0.8560	5.52	0.8846	5.00	0.8065	1.92	0.9870	2.03	0.9774	1.95	0.9549
Nanofibers	11.17	0.8397	10.70	0.8114	8.98	0.7476	1.34	0.9802	1.83	0.9945	2.01	0.9758

### 5.5.1.5 Reusability studies of the molecularly imprinted chitosan microspheres and nanofibers

Reusability studies on the adsorbents were carried out using the similar adsorption procedure described under the batch adsorption process (**Chapter 2, Section 2.7**). The rebinding adsorption capacities of non-imprinted chitosan nanofibers decreased drastically for all sulfone compounds, from  $11.2 \pm 1.1$  mg/g,  $10.4 \pm 0.9$  mg/g and  $8.9 \pm 1.2$  mg/g to  $4.2 \pm 0.2$  mg/g,  $3.9 \pm 0.3$  mg/g and  $3.5 \pm 0.1$  mg/g for BTO<sub>2</sub>, DBTO<sub>2</sub> and 4,6-DMDBTO<sub>2</sub> respectively. A reduction from  $5.7 \pm 0.7$  mg/g,  $5.6 \pm 0.4$  mg/g and  $5.1 \pm 0.6$  mg/g to  $3.2 \pm 0.2$  mg/g,  $2.9 \pm 0.3$  mg/g and  $3.8 \pm 0.5$  mg/g for BTO<sub>2</sub>, DBTO<sub>2</sub> and 4,6-DMDBTO<sub>2</sub> respectively were observed when non-imprinted chitosan microspheres were employed. From the second adsorption cycle, adsorption capacities of  $7.5 \pm 0.5$  mg/g,  $6.2 \pm 0.3$  mg/g and  $5.8 \pm 0.6$  mg/g were observed for BTO<sub>2</sub>, DBTO<sub>2</sub> and 4,6-DMDBTO<sub>2</sub> respectively when imprinted nanofibers were employed, and the imprinted microspheres gave maximum adsorption capacity of  $4.5 \pm 0.4$  mg/g,  $3.9 \pm 0.6$  mg/g and  $3.4 \pm 0.2$  mg/g for BTO<sub>2</sub>, DBTO<sub>2</sub> and 4,6-DMDBTO<sub>2</sub> respectively. The imprinted adsorbents presented a slight decrease in adsorption capacity upon the second cycle of usage as can be seen in **Figure 5.22** (first cycle) and **Figure 5.28** (second cycle), and this confirms the integrity of the imprinting effect which was also reported by Chang *et al.*<sup>417</sup>

Soxhlet extraction using methanol/acetonitrile (1:1) was employed for desorbing the sulfone compounds from the adsorbents (nanofibers and microspheres). Desorption of sulfone compound was relatively high in both the imprinted and non-imprinted polymers (**Figure 5.28**) confirming effective removal of adsorbed sulfone compounds from the polymer matrix.

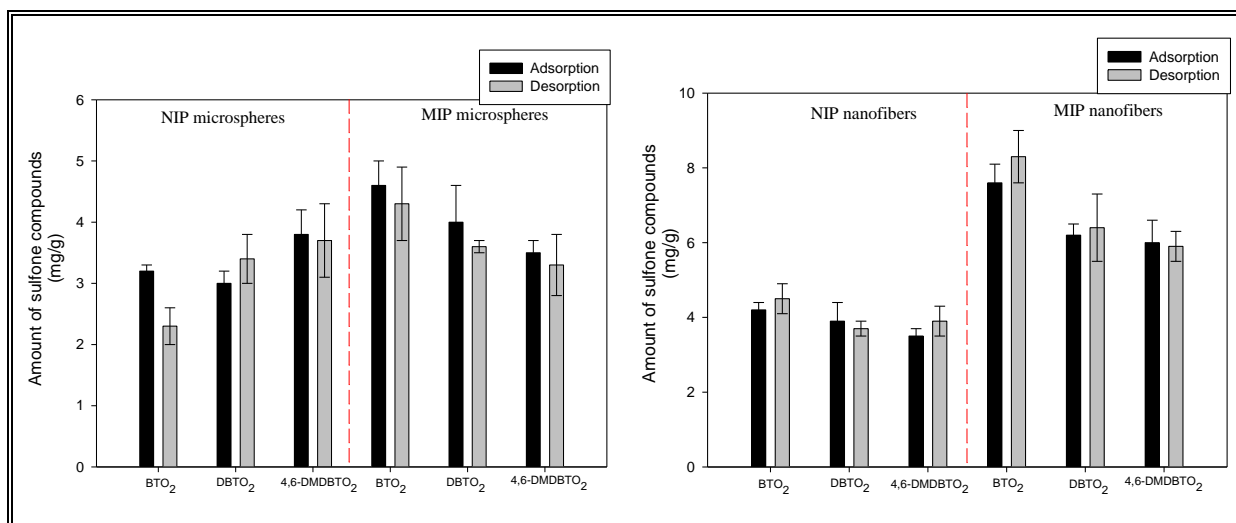


**Figure 5.28** Reusability adsorption and desorption capacities of the microspheres and nanofibers  
NIP: Non-imprinted polymer, MIP: Molecularly imprinted polymer.

## 5.5.2 Adsorption studies employing polybenzimidazole (PBI) nanofibers

### 5.5.2.1 Molecularly imprinted-PBI nanofibers mass adsorption optimization study

Different masses of imprinted-PBI nanofibers (30 mg, 50 mg and 100 mg) were employed for adsorption in constant volume and concentration of sulfone compounds (**Section 2.7**). From the results obtained, it can be seen that 50 mg gave a good adsorption for each of the sulfone compounds (**Figure 5.29**). 50 mg of imprinted fibers was employed throughout the adsorption studies.



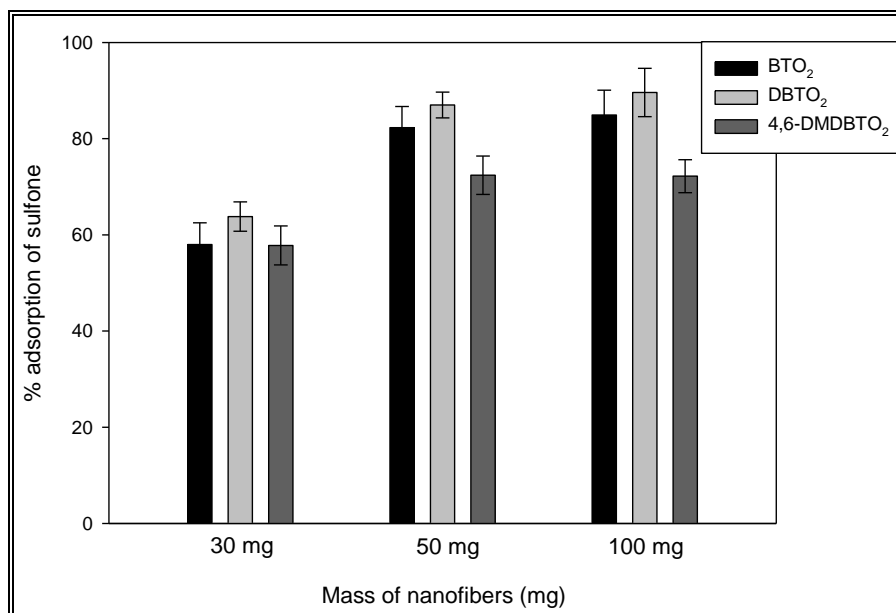


**Figure 5.29** Effect of imprinted-PBI nanofibers mass variation on the adsorption of benzothiophene sulfone (BTO<sub>2</sub>), dibenzothiophene sulfone (DBTO<sub>2</sub>) and 4,6-dimethyldibenzothiophene sulfone (4,6-DMDBTO<sub>2</sub>).

### 5.5.2.2 Adsorption selectivity on molecularly imprinted PBI nanofibers

Adsorption assays were carried out to evaluate the loading capacity and selectivity of imprinted PBI nanofibers. 50 mg of the imprinted adsorbents were added to vials and mixed with a mixture of organosulfur compounds, BTO<sub>2</sub>, DBTO<sub>2</sub> and 4,6-DMDBTO<sub>2</sub> (2 mL, 5 mM each). The corresponding adsorption assays were also carried out using non-imprinted adsorbents. The suspensions were left under mechanical agitation at 150 rpm for 24 h as described in the adsorption studies. Selectivity for sulfone compounds were noticed as high adsorption capacities were observed for sulfone compound solution which is in contact with its respective imprinted nanofibers, as compared to the non-imprinted and other imprinted nanofibers which displayed low adsorption capacities. The maximum adsorption capacities observed for BTO<sub>2</sub>, DBTO<sub>2</sub> and 4,6-DMDBTO<sub>2</sub> respectively were  $28.5 \pm 0.9$  mg/g,  $29.8 \pm 1.2$  mg/g and  $20.1 \pm 1.4$  mg/g when imprinted PBI nanofibers were employed (**Figure 5.30**). Desorption of sulfone compound was relatively high in both the imprinted and non-imprinted

polymers. Adsorption of sulfone compounds onto nanofibers is said to be largely controlled by imprinting properties, chemical interactions and physical factors (specific surface area and porosity, see **Table 5.3**).<sup>392</sup> The observed phenomenon could be attributed to specific binding sites recognizable to their respective sulfone compounds.<sup>392, 414</sup>

BTO<sub>2</sub>-imprinted PBI nanofibers showed a high adsorption capacity of  $28.5 \pm 0.9$  mg/g for BTO<sub>2</sub>, while adsorption capacities for DBTO<sub>2</sub> and 4,6-DMDBTO<sub>2</sub> were  $3.9 \pm 0.6$  mg/g and  $2.6 \pm 1.1$  mg/g respectively on this material. DBTO<sub>2</sub>-imprinted nanofibers' adsorption capacity for DBTO<sub>2</sub> was  $29.8 \pm 1.2$  mg/g, while BTO<sub>2</sub> and 4,6-DMDBTO<sub>2</sub> adsorption capacities were  $3.2 \pm 0.3$  mg/g and  $2.5 \pm 0.8$  mg/g respectively. 4,6-DMDBTO<sub>2</sub>-imprinted nanofibers gave an adsorption capacity of  $20.1 \pm 1.4$  mg/g for 4,6-DMDBTO<sub>2</sub>, while BTO<sub>2</sub> and DBTO<sub>2</sub> adsorption capacities were  $4.1 \pm 2.1$  mg/g and  $3.5 \pm 1.2$  mg/g respectively. Non-imprinted PBI nanofibers on the other hand, gave low loading capacity, a loading capacity of  $4.2 \pm 0.4$  mg/g,  $4.1 \pm 0.5$  mg/g and  $1.7 \pm 0.5$  mg/g were observed for BTO<sub>2</sub>, DBTO<sub>2</sub> and 4,6-DMDBTO<sub>2</sub> respectively. From the obtained data, imprinted nanofibers displayed higher selectivity than non-imprinted nanofibers.

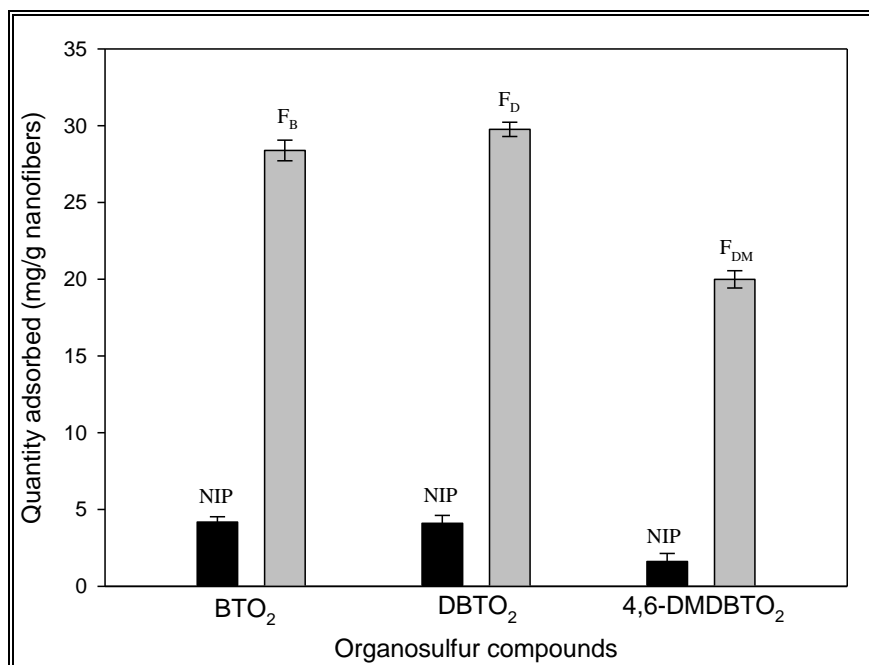


**Figure 5.30** Effect of selectivity on the adsorption of benzothiophene sulfone (BTO<sub>2</sub>), dibenzothiophene sulfone (DBTO<sub>2</sub>) and 4,6-dimethyldibenzothiophene sulfone (4,6-DMDBTO<sub>2</sub>). NIP: Non-imprinted nanofibers; F<sub>B</sub>: benzothiophene sulfone imprinted nanofibers; F<sub>D</sub>: dibenzothiophene sulfone imprinted nanofibers; F<sub>DM</sub>: 4,6-dimethyldibenzothiophene sulfone imprinted nanofibers.

### 5.5.2.3 Adsorption kinetics of molecularly imprinted PBI nanofibers

Adsorption kinetics of imprinted nanofibers on respective sulfone compounds is presented in **Figure 5.31**, with adsorption equilibrium being attained after 10 h. From the kinetic studies, sulfone compounds adsorption was initially fast due to the availability of surface sites, and thereafter adsorption rate slowed down as a result of surface saturation. From the adsorption curves, 4,6-DMDBTO<sub>2</sub> had the lowest adsorption capacity, due to the compound's steric bulk, making the sulfone reactive center inaccessible. However, BTO<sub>2</sub> and DBTO<sub>2</sub> showed high adsorption, the quantity adsorbed increased in the order of DBTO<sub>2</sub> > BTO<sub>2</sub> > 4,6-DMDBTO<sub>2</sub>.

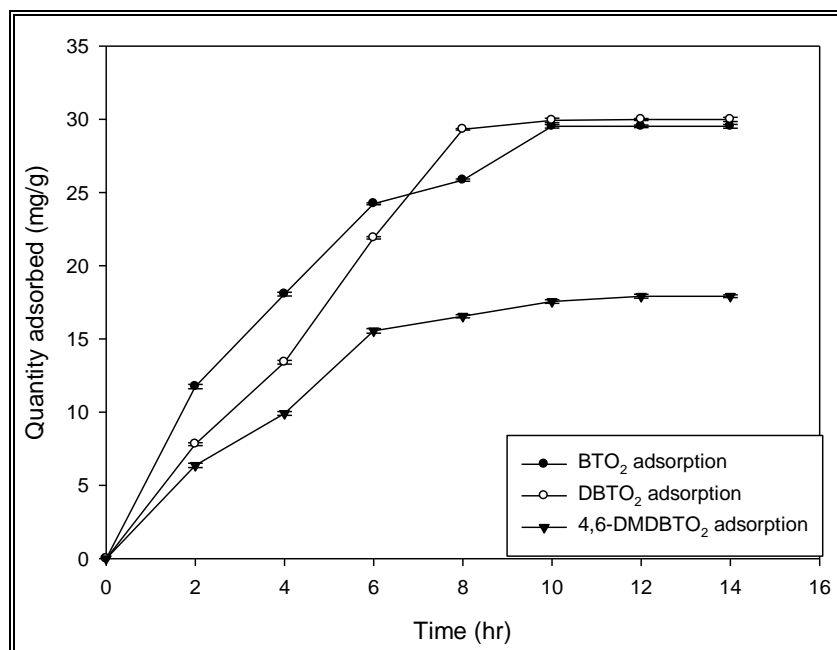


**Figure 5.31** Adsorption kinetics of imprinted nanofibers on their respective sulfone compounds.

The kinetic mechanism that controlled the adsorption process was evaluated by the pseudo-first-order model (**Equation 5.1**) and pseudo-second-order model (**Equation 5.2**). A batch adsorption process was employed to monitor the quantity of sulfone compound adsorbed over time. From the two plots (**Figures 5.32** and **5.33**), it can be seen that the pseudo-first-order adsorption rate was obeyed. BTO<sub>2</sub>, DBTO<sub>2</sub> and 4,6-DMDBTO<sub>2</sub> gave regression values of 0.9437, 0.9336 and 0.9047 respectively for the first-order plot, while second-order plot for BTO<sub>2</sub>, DBTO<sub>2</sub> and 4,6-DMDBTO<sub>2</sub> gave regression values of 0.1430, 0.3281 and 0.3655 respectively. Pseudo-first and pseudo-second order parameters (coefficients) are presented in **Table 5.6**.

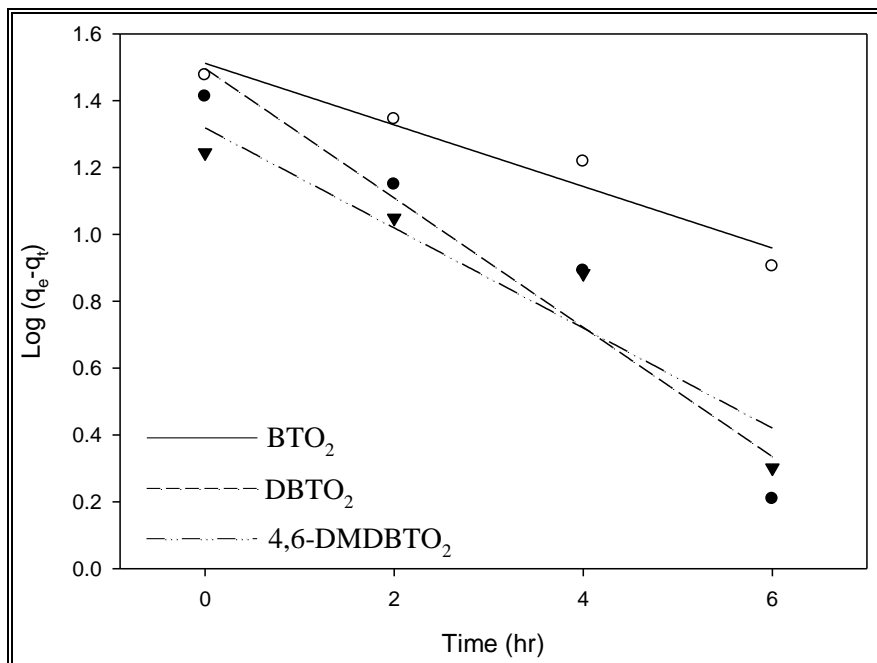


**Figure 5.32** Pseudo-first-order adsorption plot of  $\log (q_e - q_t)$  versus  $t$  (time).

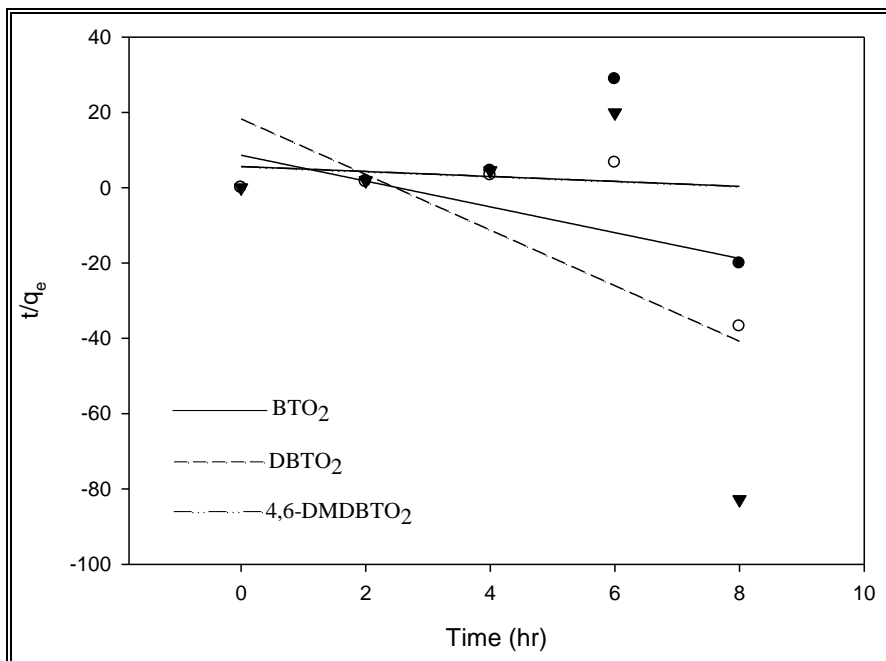


**Figure 5.33** Pseudo-second-order adsorption plot of  $t/q_e$  versus  $t$  (time).

**Table 5.6** Kinetic data of pseudo-first-order and second order for the imprinted-PBI nanofibers.

Adsorbents	Pseudo-first-order kinetics					
	BTO <sub>2</sub>		DBTO <sub>2</sub>		4,6-DMDBTO <sub>2</sub>	
	k (h <sup>-1</sup> )	R <sup>2</sup>	k (h <sup>-1</sup> )	R <sup>2</sup>	k (h <sup>-1</sup> )	R <sup>2</sup>
Nanofibers	1.512	0.9437	1.495	0.9336	1.312	0.9047
Adsorbents	Pseudo-second-order kinetics					
	BTO <sub>2</sub>		DBTO <sub>2</sub>		4,6-DMDBTO <sub>2</sub>	
	k (g mg <sup>-1</sup> h <sup>-1</sup> )	R <sup>2</sup>	k (g mg <sup>-1</sup> h <sup>-1</sup> )	R <sup>2</sup>	k (g mg <sup>-1</sup> h <sup>-1</sup> )	R <sup>2</sup>
Nanofibers	5.614	0.0143	8.221	0.3281	8.620	0.3655

#### 5.5.2.4 Adsorption isotherms of molecularly imprinted PBI nanofibers

Batch adsorption experiments was also conducted to describe the equilibrium adsorption behaviour. Langmuir and Freundlich isothermal equations (**Equations 5.3** and **5.4**) were employed to describe the adsorption behaviour.<sup>415-419</sup>

From the adsorption isotherms plots, Freundlich adsorption data plot (**Figure 5.34**) fitted better (larger correlation coefficient, R<sup>2</sup>) as compared to the Langmuir adsorption data plot (**Figure 5.35**). Freundlich constants, k and n indicating adsorption capacity and intensity respectively were determined from the linear plot of log q<sub>e</sub> against log C<sub>e</sub>. From the study, Freundlich constant, n, falls within the range 1 to 10, thus indicating that adsorption on imprinted nanofibers were favourable.<sup>419</sup> The adsorption parameters for the Freundlich isotherm models are presented in **Table 5.7**.

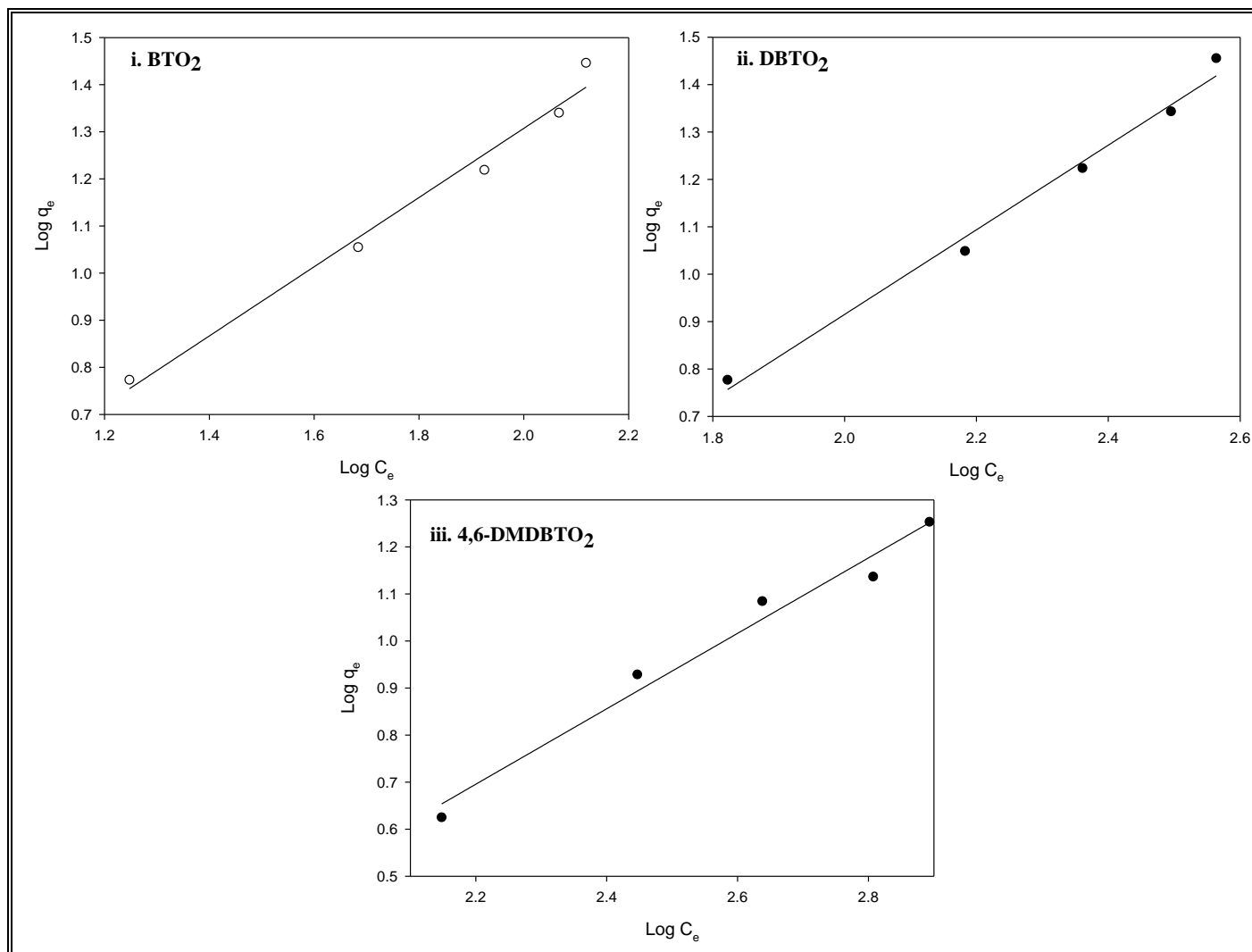


**Figure 5.34** Freundlich plot the  $\log q_e$  versus  $\log C_e$  for the imprinted-PBI nanofibers.

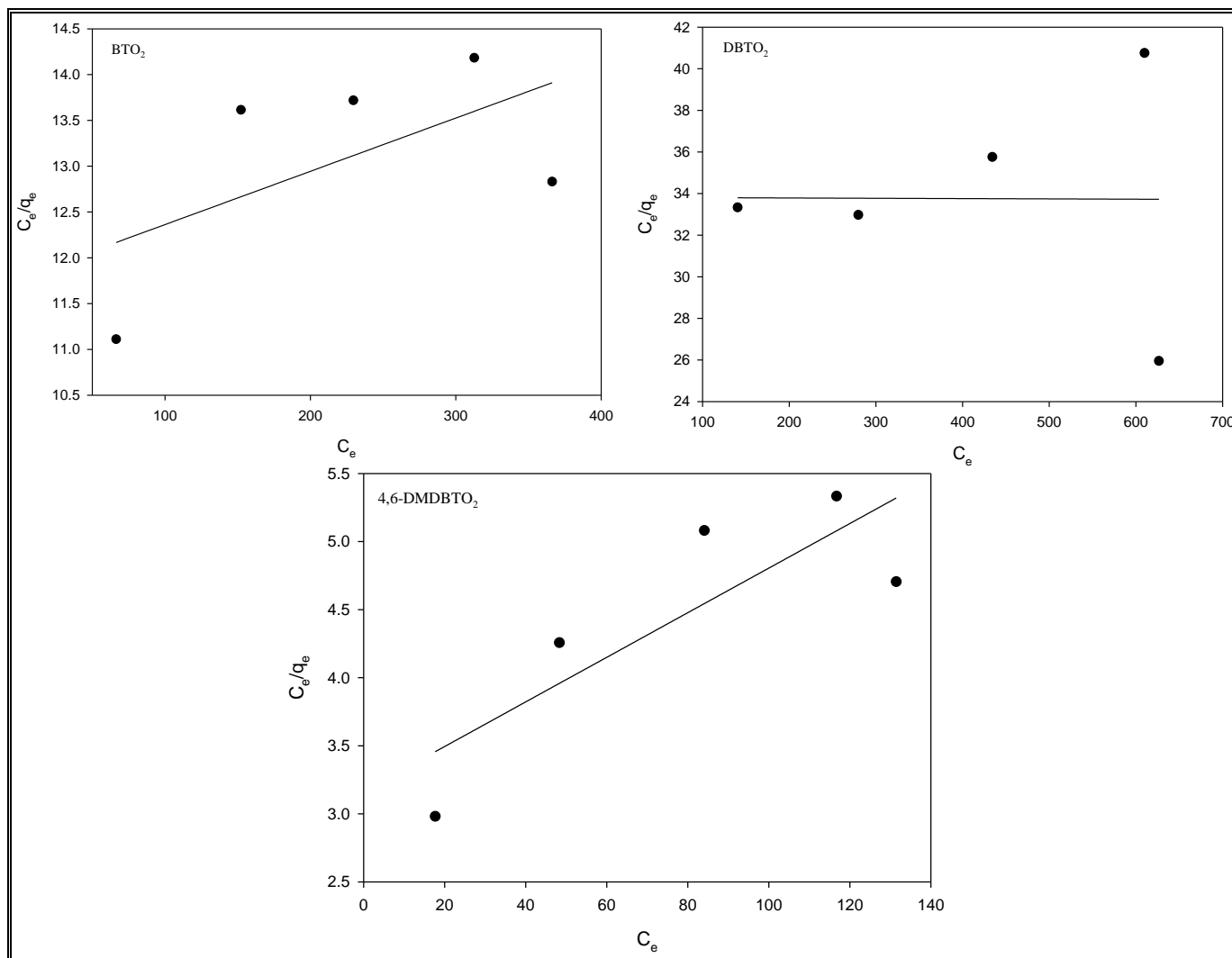


**Figure 5.35** Langmuir plot the  $C_e/q_e$  versus  $C_e$  for the imprinted PBI nanofibers.



**Table 5.7** Parameters of Freundlich adsorption model for the imprinted-PBI nanofibers.

Adsorbents	Freundlich parameters					
	BTO <sub>2</sub>		DBTO <sub>2</sub>		4,6-DMDBTO <sub>2</sub>	
	n	R <sup>2</sup>	n	R <sup>2</sup>	n	R <sup>2</sup>
Nanofibers	1.1197	0.9893	1.3613	0.9828	1.2470	0.9762

### 5.5.2.5 Reusability studies on the molecularly imprinted polybenzimidazole nanofibers

Reusability studies of imprinted nanofibers were carried out by using the same adsorption studies described in the batch adsorption procedure. The rebinding adsorption-desorption capacities of the imprinted nanofibers are presented in **Figure 5.36**. The imprinted PBI nanofibers presented a slight decrease in adsorption capacity upon the second cycle of usage as can be seen in **Figures 5.30** (first cycle) and **5.36** (second cycle), confirming the integrity of the imprinting effect as reported by Yonghui *et al.*<sup>417</sup> From the second adsorption cycle, adsorption capacities of  $24.2 \pm 1.5$  mg/g,  $27.4 \pm 1.2$  mg/g and  $17.8 \pm 2.6$  mg/g were observed for BTO<sub>2</sub>, DBTO<sub>2</sub> and 4,6-DMDBTO<sub>2</sub>, when the respective imprinted PBI nanofibers were employed. The second cycle presented lower adsorption capacities as compared to the first cycle which gave adsorption capacities  $28.5 \pm 0.9$  mg/g,  $29.8 \pm 1.2$  mg/g and  $20.1 \pm 1.4$  mg/g for BTO<sub>2</sub>, DBTO<sub>2</sub> and 4,6-DMDBTO<sub>2</sub> respectively. Soxhlet extraction using methanol/acetonitrile (1:1) was employed for desorbing the sulfone compounds from the nanofibers. Desorption was relatively high confirming effective removal of adsorbed sulfone compounds from the polymer matrix (**Figure 5.36**).

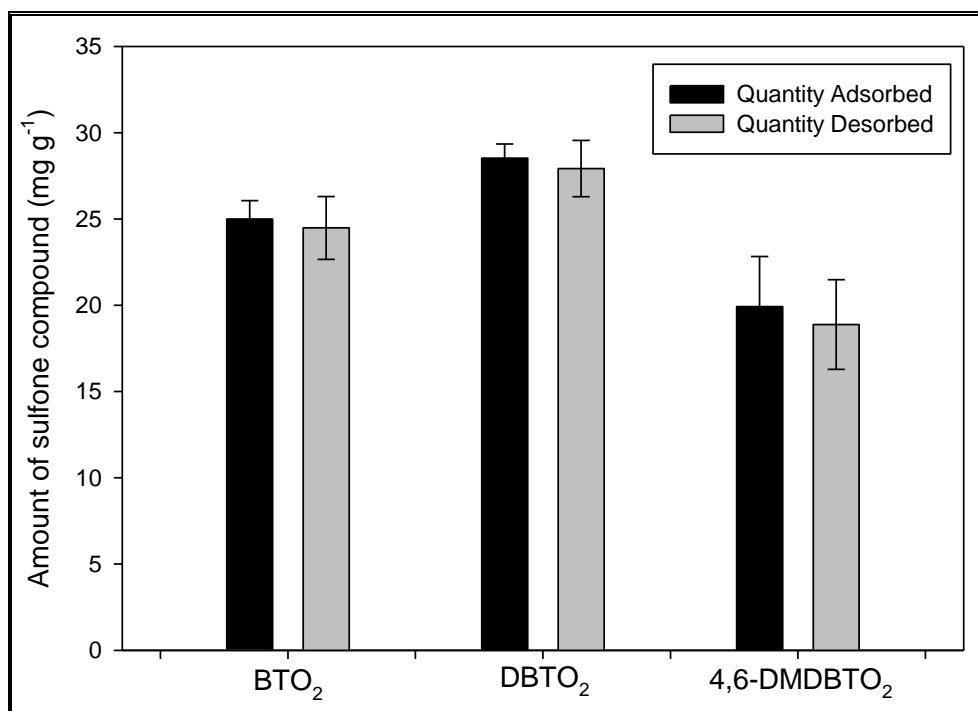


**Figure 5.36** Reusability of the imprinted nanofibers showing the adsorption/desorption capacities.

#### 5.5.2.6 Desorption process using pressurized hot water extraction (PHWE)

A schematic image of a home-made subcritical hot water extraction apparatus is presented in **Figure 5.37**. The system consists of an ion chromatography gradient pump (GS50, DIONEX), an oven (GC 5890A oven) and a stainless steel extraction vessel connected from the pump through the extraction sample holder to the collecting flask *via* metal tubing. The water temperature was set by means of a pre-heating coil inside the GC oven before entering the extraction vessel and also pressure build up was created through restrictions created on the metal tubing (**Figure 5.37**). A cooling water bath (or ice bath) was used to cool the extract recovered, thus avoiding loss of products which may be caused by hot water. Optimization of the extraction process was carried out by varying oven temperature (90, 120, 150, and 180 °C) at constant pressure (30 bars) and a flow rate 1 mL/min. After each extraction process, the extraction vessel and metal tubing were flushed to eliminate any precipitated organic compound. The parameter that has a significant effect on the extraction efficiencies of marker compounds is the applied temperature. This process of desorption could not be used for chitosan nanofibers as the polymer matrix collapsed and dissolved thereby blocking the metal tubing.

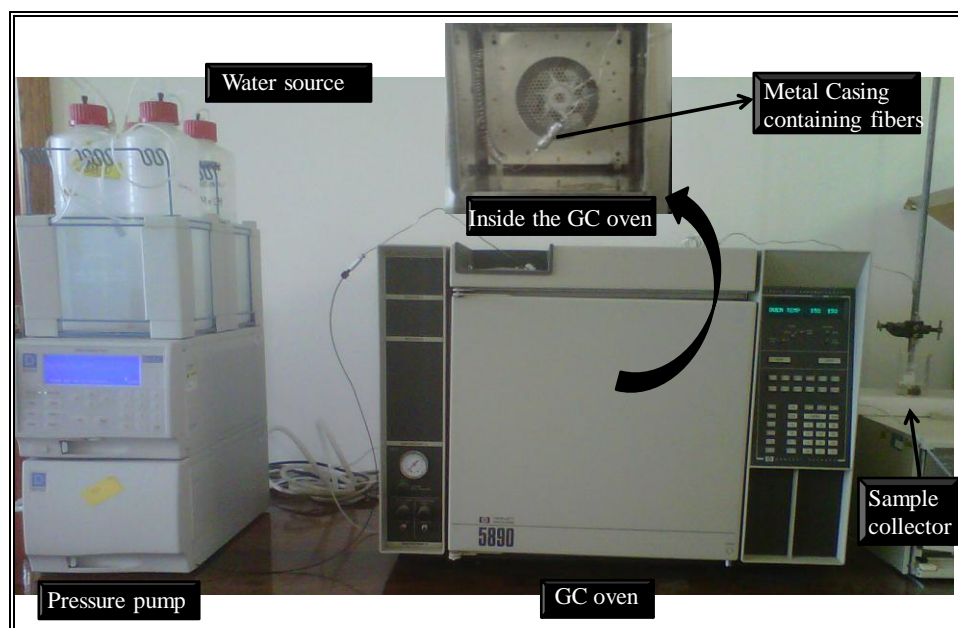


**Figure 5.37** A home-made pressurized hot water extraction (PHWE) system.

Water is termed “subcritical” when its temperature is between its boiling point ( $100^{\circ}\text{C}$ ) and critical temperature ( $374.15^{\circ}\text{C}$ ), in the presence of a pressure high enough to maintain it in the liquid state. In the subcritical region, water’s dielectric constant is greatly increased thereby decreasing its polarity,<sup>422</sup> thereby mimicking the properties of organic solvents. Under this condition, water can be employed as an alternative solvent for extraction/desorption of active compounds within a matrix.

Desorption/extraction yield increased as temperature increased up to  $150^{\circ}\text{C}$  and afterwards began to decrease (**Figure 5.38**). Sulfone compound desorption yield from the respective imprinted PBI nanofibers for the first adsorption cycle was 98%, 85% and 94% for  $\text{BTO}_2$ ,  $\text{DBTO}_2$  and 4,6- $\text{DMDBTO}_2$ , while the second cycle desorption yield were 95%, 89% and 97% for  $\text{BTO}_2$ ,  $\text{DBTO}_2$  and 4,6- $\text{DMDBTO}_2$ . An extraction/desorption cycle of 40-50 min was found to be optimal in desorbing the target compound (sulfones), thus making the process faster than Soxhlet extraction. PHWE did not have any negative effect on the reusability of the nanofibers as the cavity structural pores within the nanofibers were preserved. The pressure was reported to have no effect on the extraction efficiency as it was applied to establish the subcritical conditions of the solvent.<sup>423-425</sup> The major parameter that had a significant effect on extraction/desorption efficiency of sulfone compounds adsorbed with imprinted nanofibers was the applied temperature (**Figure 5.38**).

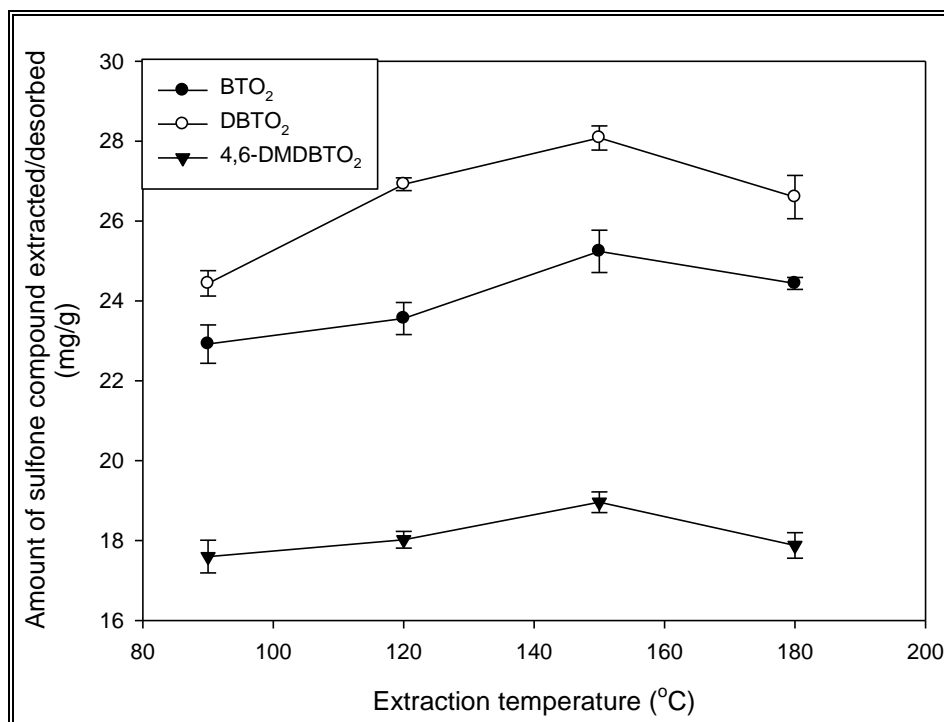


**Figure 5.38** Effects of temperature on the amount of sulfone compounds (analyte) extracted from imprinted nanofibers by PHWE method (first cycle). PHWE conditions: flow, 1 mL/min; time for extraction, 40-50 min; solvent, water ( $n = 3$ ).

## 5.6 Continuous flow adsorption studies

### 5.6.1 Adsorption studies on the sulfone compounds using imprinted chitosan and PBI nanofibers

For continuous flow adsorption process, nanofibers were employed because they gave better adsorption capacity in the batch process. The imprinted nanofibers were easily contained in the tube without leaving much space and the packing was compacted by conditioning the material with solvent at 1 mL/h. 100 mg of imprinted chitosan nanofibers was packed into a cylindrical tube attached to the tip of a syringe containing 5 mL of 5 mM solution of sulfone compound as shown in **Chapter 2, Figure 2.2**. Adsorption progressed as respective sulfone compounds were pumped through the conditioned adsorbent at a flow-rate of 1 mL/h. From the adsorption curve, the maximum amount of sulfone compounds was retained only after 1 mL (1000  $\mu$ L) of the solution have been dispensed (**Figure 5.39**), and at this volume the nanofibers is said to be saturated and it is called the breakthrough volume ( $V_B$ ).

However, with 50 mg of imprinted-PBI nanofibers, maximum amount of sulfone compound was retained only after 2 mL (2000  $\mu$ L) of the solution had been dispensed (**Figure 5.40**). The number of theoretical plates (N), linear capacity of the column ( $n_s$ ), capacity factor of the solute (k) and percentage recovery (r) calculated for chitosan and PBI nanofibers from **Equations 5.5-5.8**,<sup>426-427</sup> are presented in **Table 5.8**.

$$N = \frac{V_R}{\sigma_V^2} (V_R - \sigma_V) \quad 5.5$$

$$\text{where } 2\sigma_V = V_R - V_B$$

$$k = \frac{V_R}{V_M} - 1 \quad 5.6$$

$$n_s = V_M k C_o \quad 5.7$$

$$r = \frac{n_s}{C_o V_o} \times 100\% \quad 5.8$$

where  $V_o$  is the initial volume of the analyte, breakthrough volume ( $V_B$ ), retention volume ( $V_R$ ) and hold-up volume ( $V_M$ ) of the analyte (sulfone solution). **Table 5.8** presents the values of the percentage sulfone recovery of the nanofibers, which is the amount of substrate that can be recovered in the continuous flow process.

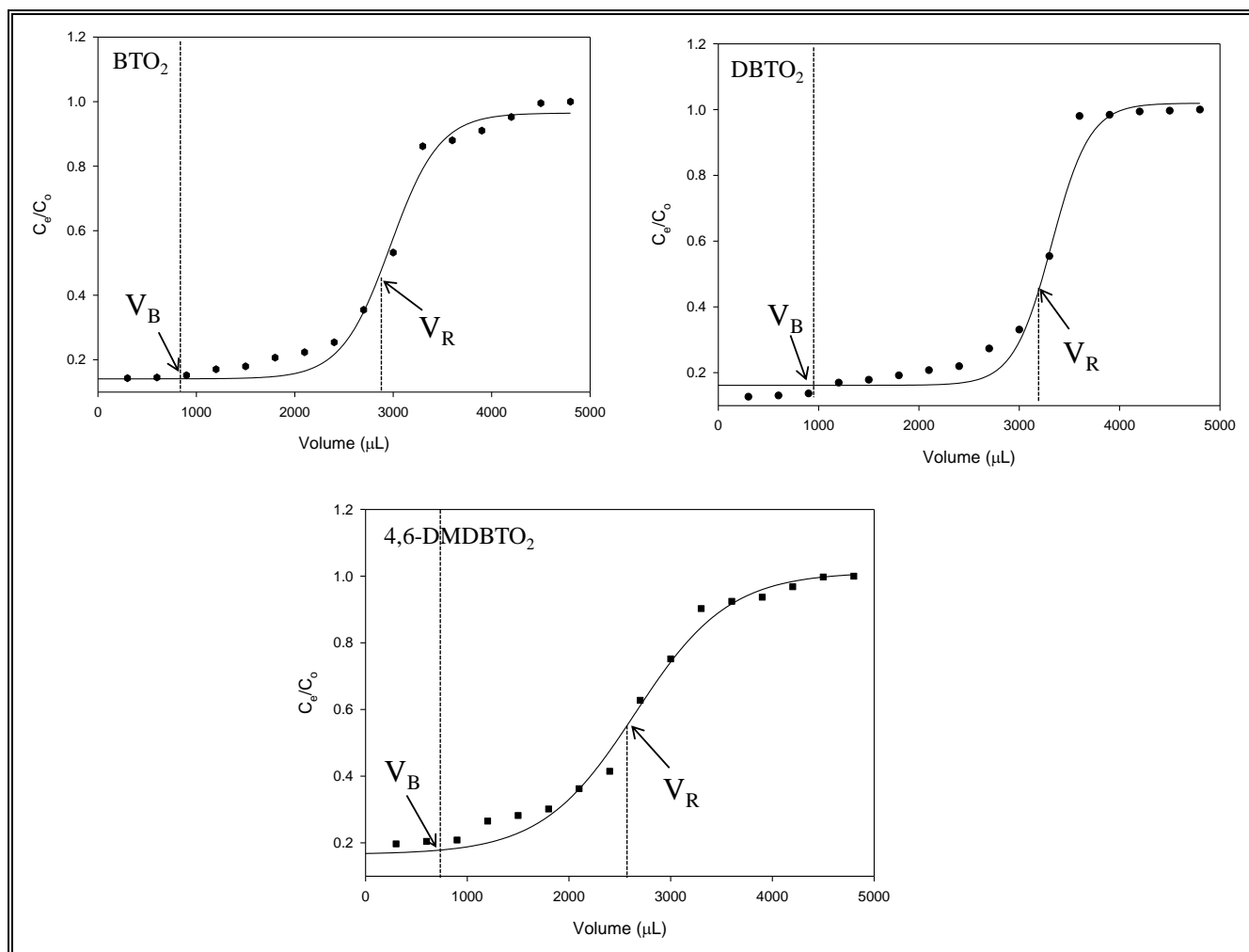


**Figure 5.39** Breakthrough curves for various sulfone compounds (A) benzothiophene sulfone (BTO<sub>2</sub>), (B) dibenzothiophene sulfone (DBTO<sub>2</sub>), and (C) 4,6-dimethyldibenzothiophene (4,6DMDBTO<sub>2</sub>), using imprinted chitosan nanofibers.

**Table 5.8** Influence of sulfone compounds upon adsorption on imprinted-chitosan and -PBI nanofibers.

<b>Imprinted-chitosan nanofibers</b>							
Sulfone compounds	V <sub>B</sub> (mL)	V <sub>R</sub> (mL)	V <sub>M</sub> (mL)	N	K	n (mmol/g) × 10 <sup>-2</sup>	r %
BTO <sub>2</sub>	0.9	2.9	0.2	5.6	12.8	1.3	53.7
DBTO <sub>2</sub>	0.9	3.2	0.2	4.9	13.1	1.5	60.2
4,6-DMDBTO <sub>2</sub>	0.9	2.5	0.2	6.8	11.3	1.1	45.2
<b>Imprinted-PBI nanofibers</b>							
Sulfone compounds	V <sub>B</sub> (mL)	V <sub>R</sub> (mL)	V <sub>M</sub> (mL)	N	k	n (mmol/g) × 10 <sup>-2</sup>	r %
BTO <sub>2</sub>	1.8	2.9	0.2	21.6	15.7	1.4	56.5
DBTO <sub>2</sub>	2.1	3.5	0.2	20.9	12.9	1.6	64.5
4,6-DMDBTO <sub>2</sub>	1.5	3.2	0.3	11.3	9.5	1.4	57.0

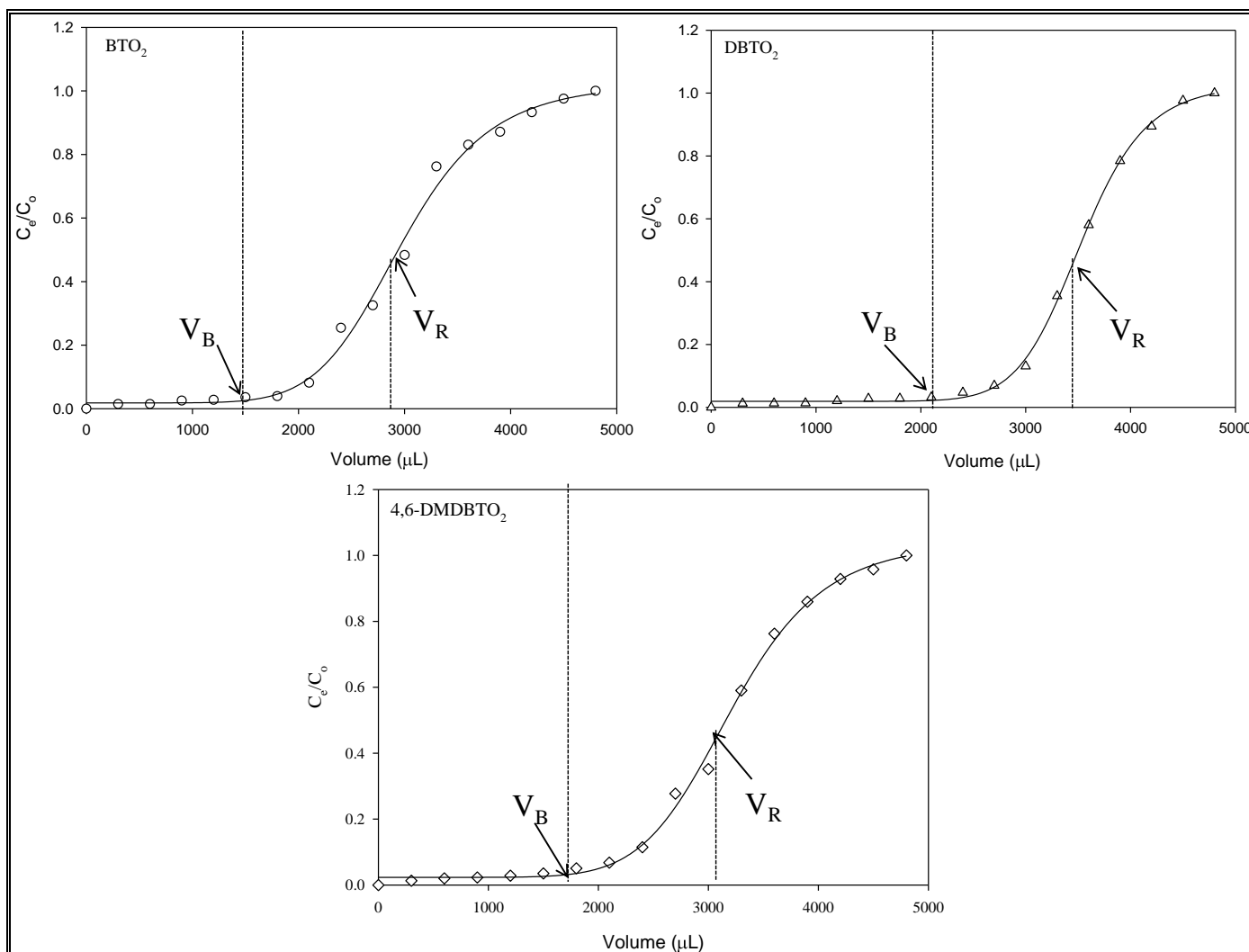


**Figure 5.40** Breakthrough curves for various sulfone compounds (A) benzothiophene sulfone ( $\text{BTO}_2$ ), (B) dibenzothiophene sulfone ( $\text{DBTO}_2$ ), and (C) 4,6-dimethyldibenzothiophene (4,6DMDBTO<sub>2</sub>), using the various imprinted-PBI nanofibers.



## 5.7 Adsorption studies of sulfone compounds on oxidized model fuel and oxidized diesel

### 5.7.1 Continuous flow and batch adsorption studies using imprinted chitosan and PBI imprinted nanofibers on oxidized model fuel

An adsorption study on a mixture of the model sulfone compounds were carried out under the continuous flow system and also the batch system. 300 mg of conditioned imprinted-chitosan nanofibers (comprising of 100 mg BTO<sub>2</sub>-imprinted, 100 mg DBTO<sub>2</sub>-imprinted and 100 mg 4,6-DMDBTO<sub>2</sub>-imprinted) was employed for the continuous flow adsorption process. The adsorbent was packed into a tube attached to a syringe containing 2 mL of a mixture of 830 ppm BTO<sub>2</sub> (160 ppm S), 1080 ppm DBTO<sub>2</sub> (163 ppm S) and 1230 ppm 4,6-DMDBTO<sub>2</sub> (167 ppm S). A similar mixture containing 300 mg of conditioned chitosan imprinted nanofibers was also contained in a screw-capped vial for batch adsorption process. A reduction in concentration of the sulfone compounds was observed after passing through the imprinted-chitosan nanofibers, BTO<sub>2</sub> concentration was reduced to 148 ppm ( $28.5 \pm 3.4$  ppm S), DBTO<sub>2</sub> concentration was reduced to 102 ppm ( $15.1 \pm 1.4$  ppm S) and 4,6-DMDBTO<sub>2</sub> concentration was reduced to 120 ppm ( $15.6 \pm 2.6$  ppm S) in the continuous flow adsorption process (**Figure 5.41**). In batch adsorption process, BTO<sub>2</sub> concentration was reduced to 393 ppm ( $75.7 \pm 4.5$  ppm S), DBTO<sub>2</sub> concentration was reduced to 365 ppm ( $54.1 \pm 7.1$  ppm S) and 4,6-DMDBTO<sub>2</sub> reduced to 232 ppm ( $30.2 \pm 3.1$  ppm S) (**Figure 5.41**).

150 mg of conditioned imprinted-PBI nanofibers (comprising of 50 mg BTO<sub>2</sub>-imprinted nanofibers, 50 mg DBTO<sub>2</sub>-imprinted nanofibers and 50 mg 4,6-DMDBTO<sub>2</sub>-imprinted nanofibers). The nanofibers were also packed into a tube attached to a syringe containing 2 mL of a mixture of 830 ppm BTO<sub>2</sub> (160 ppm S), 1080 ppm DBTO<sub>2</sub> (163 ppm S) and 1230 ppm 4,6-DMDBTO<sub>2</sub> (167 ppm S). A similar mixture containing 150 mg of imprinted nanofibers was also contained in a screw-capped vial for batch adsorption process. A reduction in concentration of the sulfone compounds was observed after passing through the imprinted nanofibers (**Figure 5.42**). For the continuous flow studies, BTO<sub>2</sub> was reduced to 37 ppm ( $7.1 \pm 1.4$  ppm S), DBTO<sub>2</sub> was reduced to 32 ppm ( $4.7 \pm 0.7$  ppm S) and 4,6-DMDBTO<sub>2</sub> was reduced to 22 ppm ( $2.9 \pm 0.2$  ppm S). In batch adsorption process, BTO<sub>2</sub> was reduced to 151 ppm ( $29.1 \pm 4.6$  ppm S), DBTO<sub>2</sub> was reduced to 130 ppm ( $19.3 \pm 2.4$  ppm S) and 4,6-DMDBTO<sub>2</sub> was reduced to 85 ppm ( $11.1 \pm 0.9$  ppm S) (**Figure 5.42**). From the results obtained,

imprinted-PBI nanofibers under continuous flow process gave better adsorption as compared to imprinted-chitosan nanofibers. The continuous flow adsorption process employing chitosan and imprinted-PBI nanofibers was taken further for the adsorption sulfonated compounds in oxidized hydro-treated diesel.

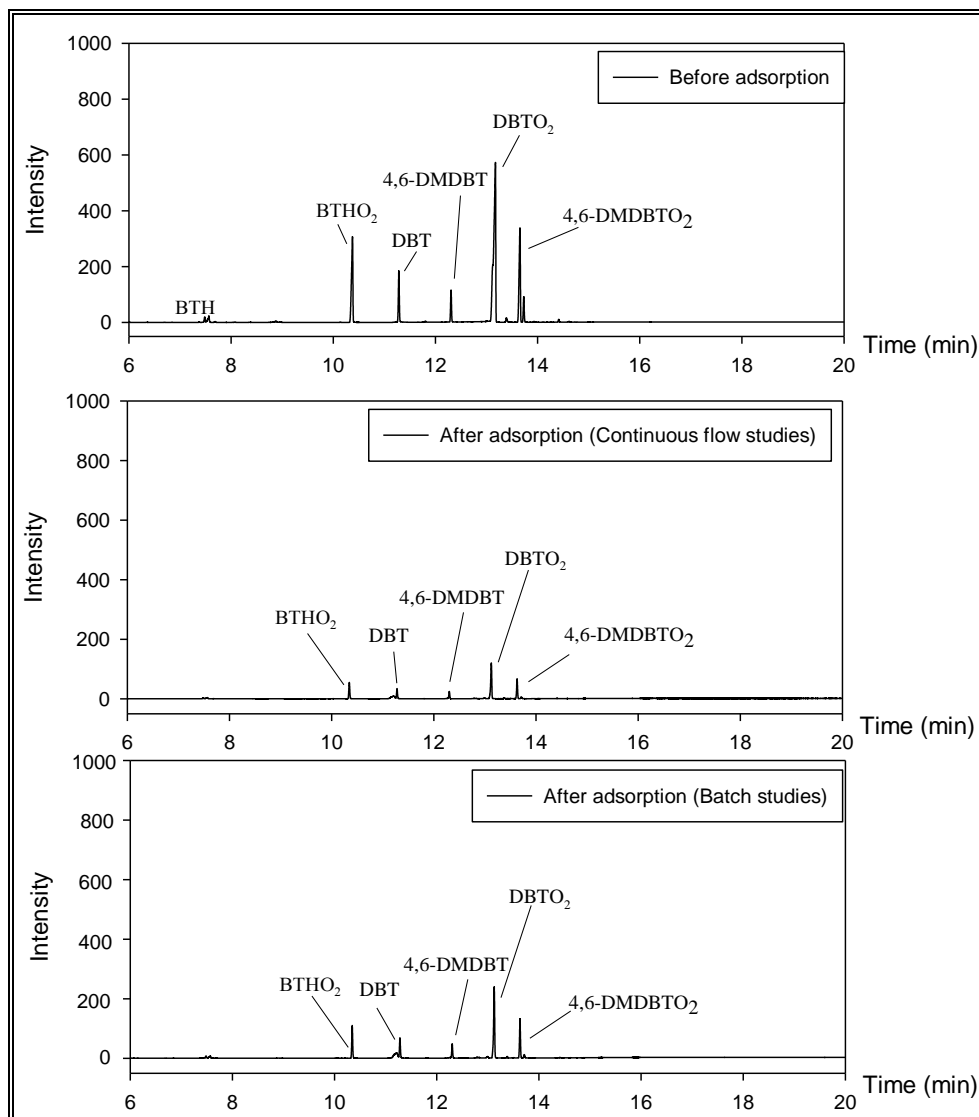


**Figure 5.41** GC-FID chromatograms of oxidized model fuel containing benzothiophene sulfone (BTO<sub>2</sub>), dibenzothiophene sulfone (DBTO<sub>2</sub>) and 4,6-dimethyldibenzothiophene (4,6-DMDBTO<sub>2</sub>) before and after adsorption with imprinted-chitosan nanofibers.

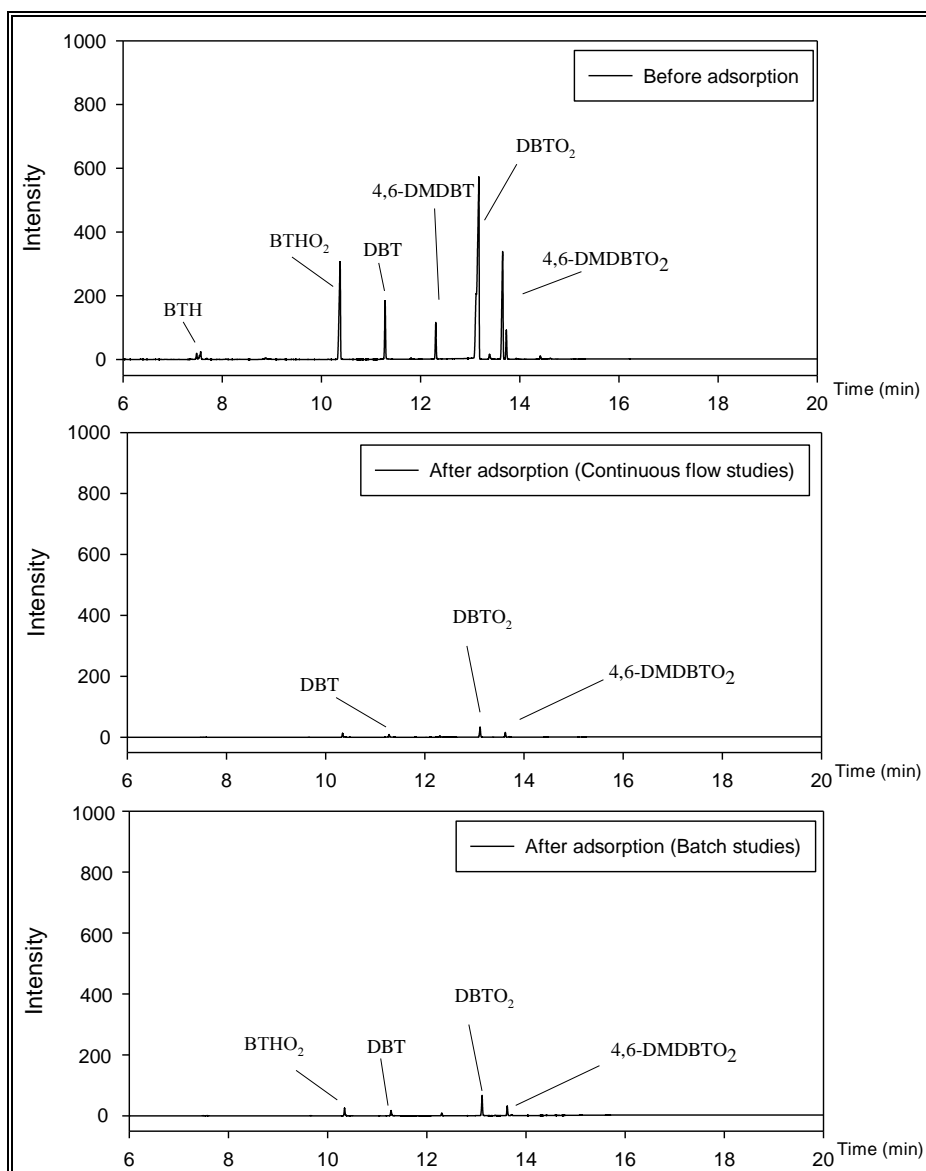


**Figure 5.42** GC-FID chromatograms of benzothiophene sulfone (BTO<sub>2</sub>), dibenzothiophene sulfone (DBTO<sub>2</sub>) and 4,6-dimethyldibenzothiophene (4,6-DMDBTO<sub>2</sub>) before and after adsorption with imprinted-PBI nanofibers.

### 5.7.2 Continuous flow adsorption studies using imprinted chitosan and PBI nanofibers on oxidized hydro-treated diesel

Oxidized hydro-treated diesel containing sulfur in the form of sulfonated compounds was desulfurized by using imprinted-chitosan nanofibers under continuous flow process as described in model fuel adsorption system (Section 5.7.1). Prior to the sulfonated compound removal, the concentration of sulfur in the form of sulfonated compound in oxidized fuel was quantified, and a total sulfur content

of  $394 \pm 4.2$  ppm S was observed. The limit of detection (LOD) and limit of quantification (LOQ) for the assay were calculated from **Equations 5.9** and **5.10** respectively.<sup>428</sup>

$$\text{LOD} = \frac{3 \text{ SD}}{S} \quad 5.9$$

$$\text{LOQ} = \frac{10 \text{ SD}}{S} \quad 5.10$$

where SD is standard deviation units, and S is the slope.

The linear plot of peak areas against standard sulfur concentrations presented in **Chapter 4, Figure 4.46** was employed to determine the sensitivity (LOD and LOQ) of the GC-AED detection method. The limit of detection (LOD) and limit of quantification (LOQ) of the GC-AED assays were found to be  $2.4 \mu\text{g S/mL}$  and  $7.6 \mu\text{g S/mL}$  respectively. The LOD represents the lowest concentration of sulfur in the sample which can be detected but not necessarily quantified as precise value while LOQ is the lowest concentration of sulfur in a sample which can be quantitatively determined with a high degree of confidence. The LOQ values obtained fall well below the 10 ppm mandated sulfur limit in fuel.<sup>428</sup>

300 mg of imprinted chitosan nanofibers (100 mg BTO<sub>2</sub>-imprinted, 100 mg DBTO<sub>2</sub>-imprinted and 100 mg 4,6-DMDBTO<sub>2</sub>-imprinted) was applied as adsorbent for adsorption. Adsorption was allowed to proceed by employing the conditioned imprinted nanofibers at a flow-rate of 1 mL/h. GC-AED sulfur analysis after the adsorption process indicated that a total of  $62 \pm 3.2$  ppm S was left in the diesel (**Figure 5.43**). The saturated sulfur adsorption capacity of the molecularly imprinted adsorbents was  $2.2 \pm 0.2$  mg/g. The adsorption of sulfur through the use of chitosan is in agreement with the work of Jorge *et al.*<sup>70, 392</sup> and Yonghui *et al.*<sup>417</sup> Desorption of adsorbed sulfone compounds on chitosan nanofibers were carried out by using a Soxhlet extraction process, and it was observed that 78% of the absorbed sulfones were desorbed from the nanofibers (**Figure 5.44**). However, when 150 mg of conditioned imprinted PBI nanofibers (consisting of 50 mg BTO<sub>2</sub>-imprinted nanofibers, 50 mg DBTO<sub>2</sub>-imprinted nanofibers and 50 mg 4,6-DMDBTO<sub>2</sub>-imprinted nanofibers) was applied for adsorption of sulfur in oxidized hydro-treated diesel under continuous flow at a flow-rate of 1 mL/h. The sulfur left within the diesel after adsorption process could not be quantified as it is below the limit of detection (**Figure 5.45**). The saturated sulfur adsorption capacity of the molecularly imprinted

adsorbents was  $5.3 \pm 0.4$  mg/g. Imprinted-PBI nanofibers displayed excellent adsorptive properties due to its imprinting effect, hydrogen bonding and  $\pi$ - $\pi$  aromatic interactions it possess.

Pressurized hot water extractions (PHWE) using the optimised extraction conditions (150°C, 30 bars) was applied to desorb the adsorbed sulfone compounds on imprinted PBI nanofibers, and the desorption efficiency was compared with that of the Soxhlet extraction process using acetonitrile:methanol (1:1). The pressurized hot water extraction gave a higher desorption yield of  $310 \pm 2.9$  ppm S as compared to Soxhlet extraction process which gave an overall desorption yield of  $216 \pm 3.2$  ppm S (**Figure 5.46**). Low recovery/desorption of sulfone compounds in Soxhlet extraction method was attributed to the complexity of extraction set-up which leads to loss of some volatile organics during extraction.

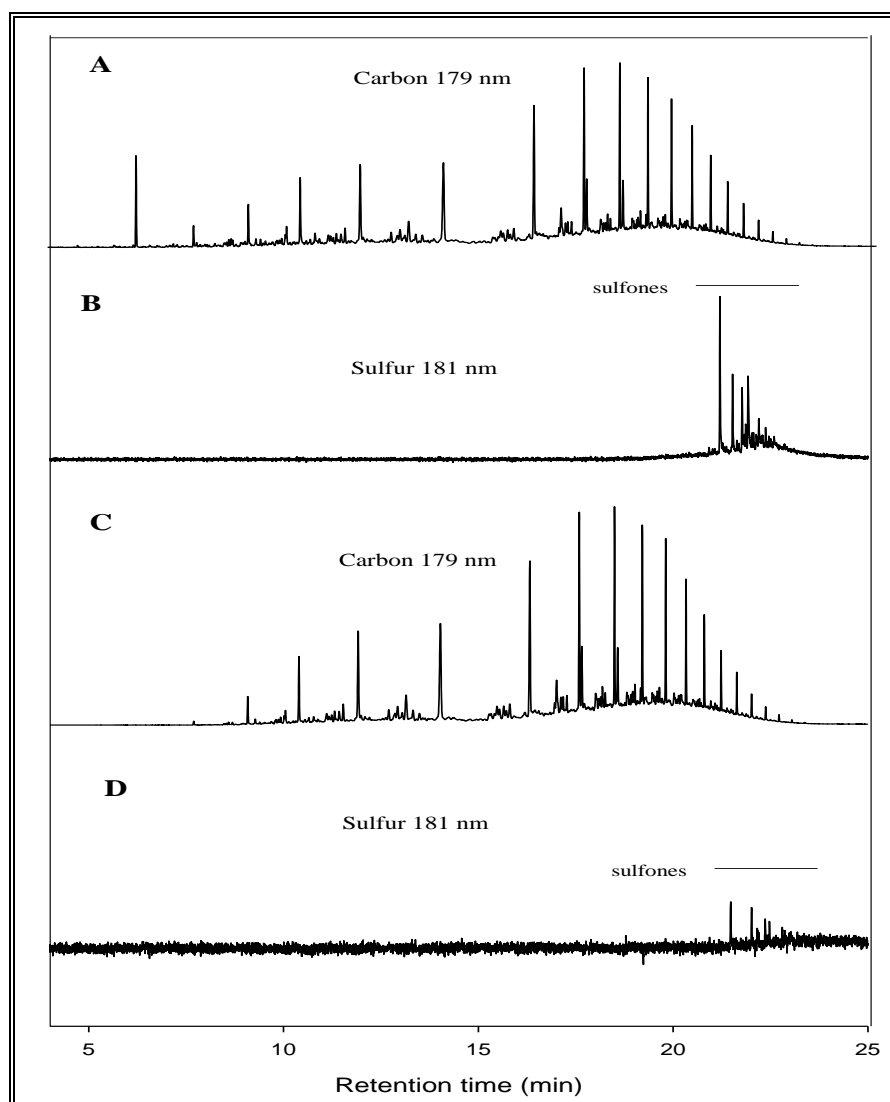


**Figure 5.43** GC-AED chromatograms of carbon (A) at 179 nm, and sulfur (B) at 181 nm in hydro-treated diesel after oxidation, and chromatograms of carbon (C) at 179 nm and sulfur (D) at 181 nm in oxidized hydro-treated diesel after using imprinted-chitosan nanofibers as adsorbent.

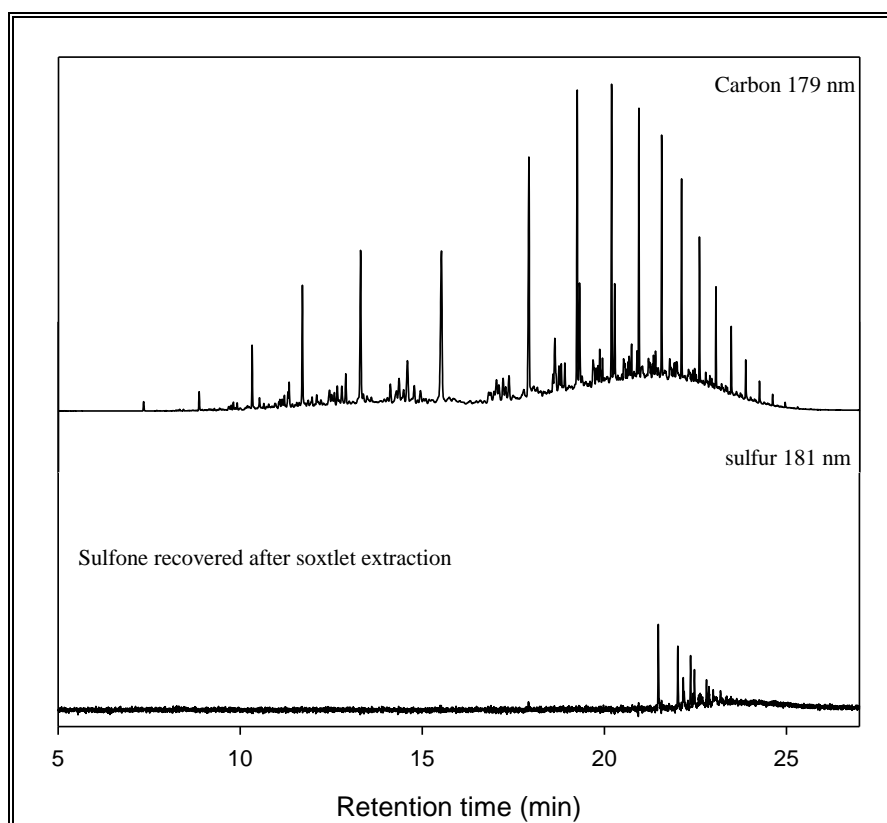


**Figure 5.44** GC-AED chromatograms showing desorbed sulfones from imprinted-chitosan nanofibers after Soxhlet extraction using a mixture of methanol and acetonitrile (1:1).

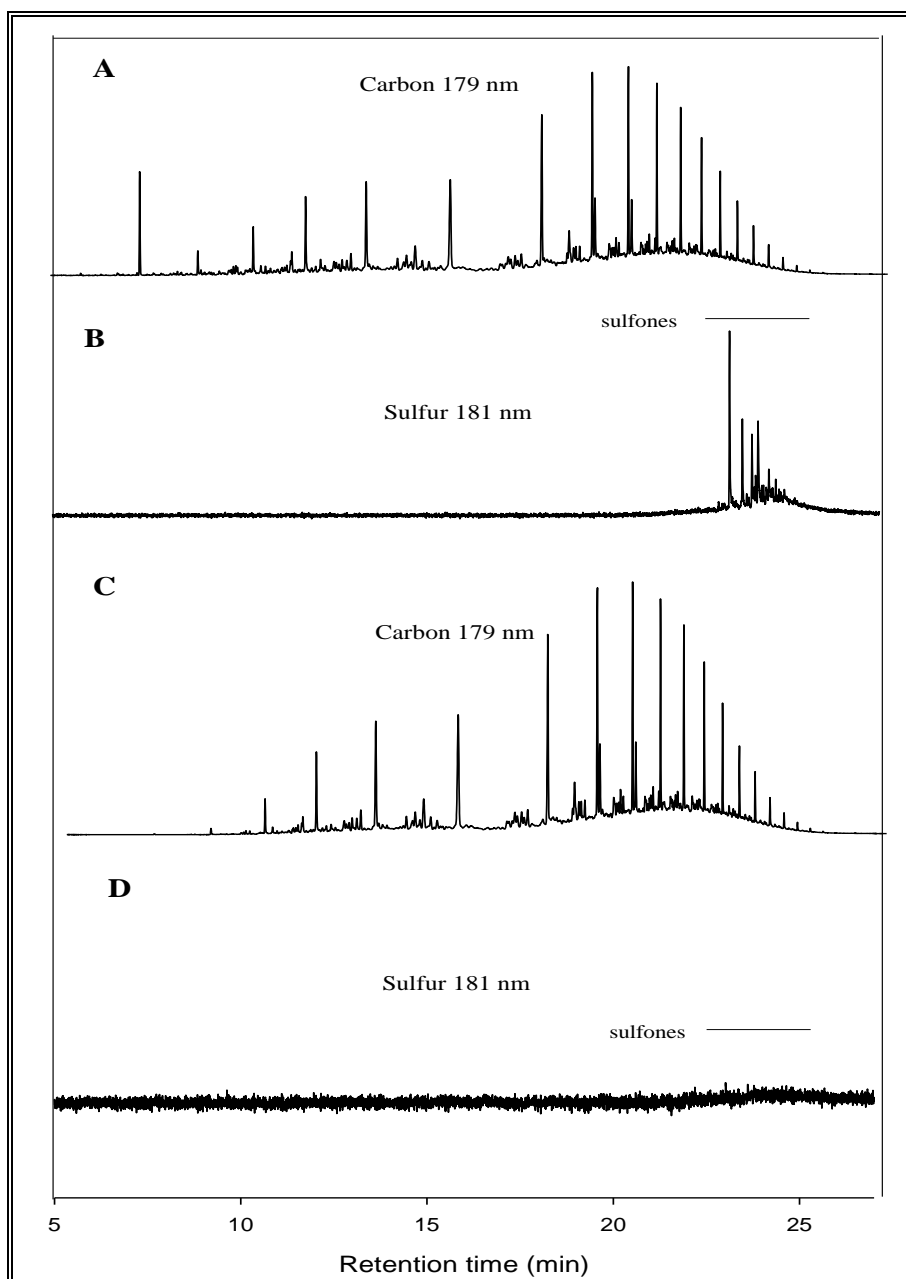


**Figure 5.45** GC-AED chromatograms of carbon (A) at 179 nm, and sulfur (B) at 181 nm in hydro-treated diesel after oxidation, and chromatograms of carbon (C) at 179 nm and sulfur (D) at 181 nm in oxidized hydro-treated diesel after using imprinted-PBI nanofibers as adsorbent.



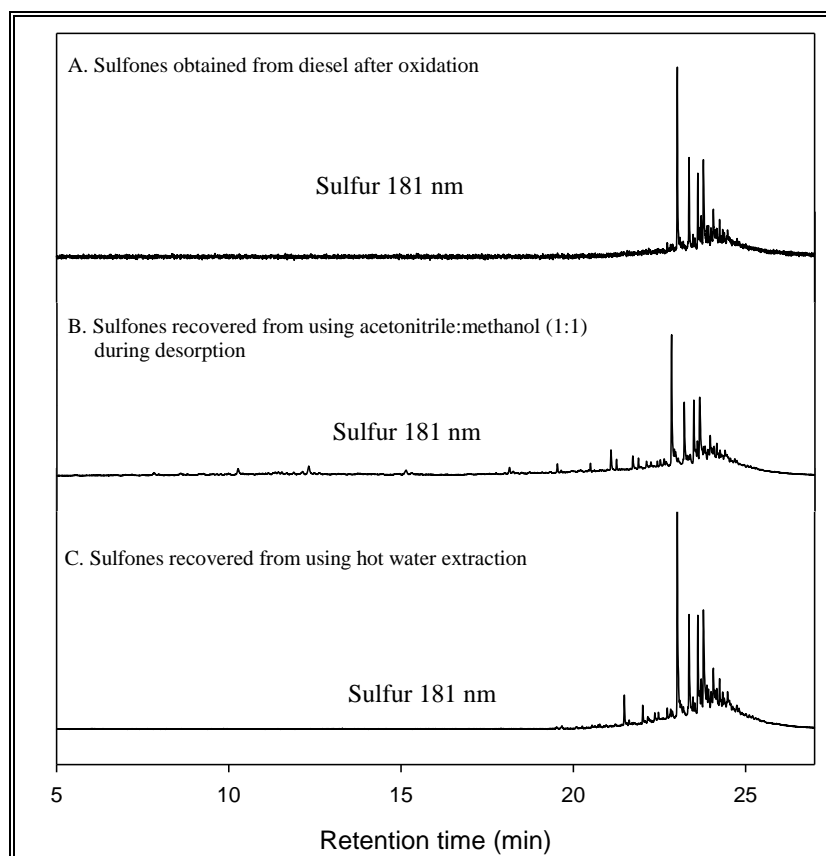


**Figure 5.46** GC-AED chromatograms of sulfur at 181 nm comparing (A) initial abundance of sulfonated compounds (oxidized sulfur) in hydro-treated diesel before adsorption on imprinted PBI nanofibers to the (B) abundance of desorbed sulfones from the imprinted nanofibers after using methanol and (C) pressurized hot water.

### 5.7.3 Continuous flow adsorption studies using imprinted PBI nanofibers on oxidized crude oil

Adsorption attempts on 1 mL oxidized heavy crude oil ( $17\,920 \pm 100.9$  ppm S) was carried out by using imprinted polybenzimidazole nanofibers (150 mg) under continuous adsorption process. GC-AED chromatograms after passing through polybenzimidazole-imprinted nanofibers showed that a total of  $8900 \pm 200.2$  ppm sulfur was left in the oxidized heavy crude oil (**Figure 5.47**). The saturated sulfur adsorption capacity of the molecularly imprinted PBI nanofibers was  $60.2 \pm 6.9$  mg/g. However, a crude aqueous extraction step would be ideal for the removal of excessive sulfur before hydrotreatment. The imprinted polymers would be desirable for removal of traces of sulfur before the fuel polishing step.

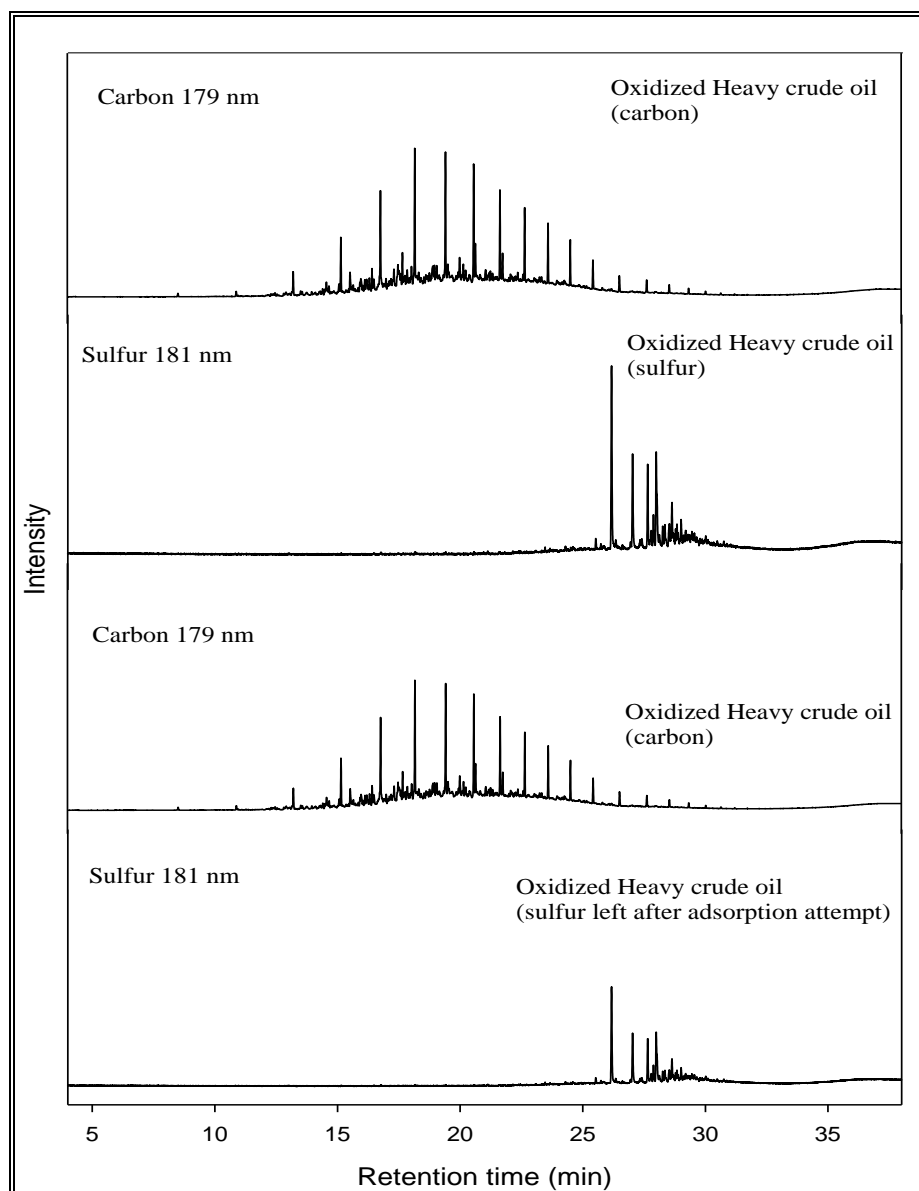


**Figure 5.47** GC-AED chromatograms of carbon (A) at 179 nm, and sulfur (B) at 181 nm in oxidized heavy crude oil, and chromatograms of carbon (C) at 179 nm and sulfur (D) at 181 nm in oxidized heavy crude oil after using imprinted-PBI nanofibers as adsorbent.

### 5.8 Intermolecular interaction studies between adsorbent (chitosan and PBI) and sulfone compounds using the density functional theory (DFT)

Absorbent (polybenzimidazole and chitosan) interaction with sulfone compounds through the formation of association adduct was evaluated by employing density functional theory (DFT) molecular modelling.<sup>429-431</sup> Geometry optimisations and vibrational analyses of absorbent-sulfone

adducts were performed using the Gaussian03 software. B3LYP functional was employed with a 6-31G(d) basis set.<sup>432</sup> The enthalpies of formation, Gibb's free energies and entropy of formation were calculated for each functional monomer and adduct, as well as the enthalpies of formation of the adduct ( $\Delta\Delta H_{\text{adduct}}$ ) according to the following **Equations 5.11** and **5.12**.<sup>433</sup>

$$\Delta\Delta H_{\text{adduct}} = \Delta H_{\text{adduct}} - (m\Delta H_{\text{chitosan/PBI}} + t\Delta H_{\text{sulfones}}) \quad \mathbf{5.11}$$

where  $m$  and  $t$  are the stoichiometric amounts of functional monomers and template molecules involved in adduct formation.

$$\Delta\Delta G_{\text{adduct}} = \Delta\Delta H_{\text{adduct}} - T\Delta\Delta S_{\text{adduct}} \quad \mathbf{5.12}$$

$\Delta\Delta G$ ,  $T$  and  $\Delta\Delta S$  are the Gibbs free energy for the adduct formation, temperature (273 K) and entropy for adduct formation at standard conditions (i.e. 1 molar concentration for solvents and 1 atm pressure for gases) respectively.

Three possible interaction sites for adduct formations with chitosan and polybenzimidazole (PBI) were modelled for each sulfonated compound. For chitosan adduct formation, the modelled thermodynamic parameters (preferably the negative enthalpy change) presented in **Table 5.9**, adduct formed between -OH, -NH<sub>2</sub> of the same unit of chitosan (site A) and adduct formed on -NH<sub>2</sub> only (site C) of chitosan with sulfone compounds gave promising interactions. The adduct formation occurred *via* hydrogen bond formation through the interactions between sulfone oxygen groups with -OH and -NH groups of the chitosan (**Figure 5.48**). From the thermodynamic parameters obtained (**Table 5.9**), the order of adduct formation is given as BTO<sub>2</sub> > DBTO<sub>2</sub> > 4,6-DMDBTO<sub>2</sub> due to steric effect.

With polybenzimidazole (PBI), adducts formed in (i) compounds perpendicular to ( $\perp$ ) PBI in cis position (site A) and (ii) compounds perpendicular to ( $\perp$ ) PBI in trans/twisted position (site B) gave better thermodynamic parameters (**Figure 5.49**). The adduct formation occurred *via*  $\pi$ - $\pi$  interaction and hydrogen bond formation through the interactions between sulfone oxygen groups with -NH groups of polybenzimidazole. Thermodynamic parameters for adduct formation are presented in **Table 5.10**. The order of adduct formation is given as DBTO<sub>2</sub> > BTO<sub>2</sub> > 4,6-DMDBTO<sub>2</sub>. The

observed adduct formation trend was also in confirmation with the observed experimental adsorption results.

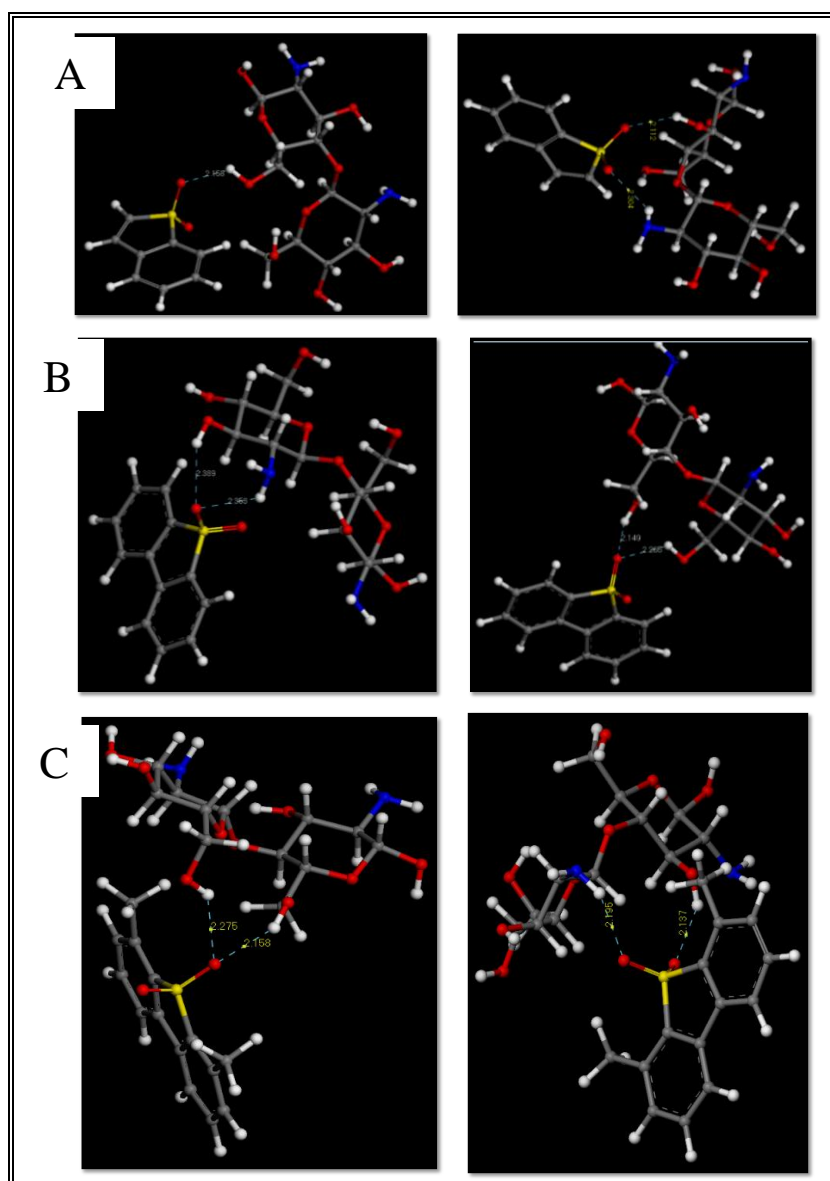


**Figure 5.48** Molecular modelled stable configurations for the 1:1 adduct of BTO<sub>2</sub> (A), DBTO<sub>2</sub> (B), and 4,6-DMDBTO<sub>2</sub> (C) with chitosan. The dashed lines represent hydrogen bonds.

**Table 5.9** DFT modelling studies on the adducts formed between benzothiophene sulfone (BTO<sub>2</sub>), dibenzothiophene sulfone (DBTO<sub>2</sub>) and 4,6-dimethyldibenzothiophene sulfone (4,6-DMDBTO<sub>2</sub>) and chitosan ( $\Delta\Delta H$ ,  $\Delta\Delta G$  and  $\Delta\Delta S$  complex)

BTO <sub>2</sub>	$\Delta H$ (kcal.mol <sup>-1</sup> )		$\Delta G$ (kcal.mol <sup>-1</sup> )		$\Delta S$ (cal.mol <sup>-1</sup> )	
		-537697		-537724		90
Chitosan “dimer”	-789235		-789283		162	
	$\Delta H$ (kcal.mol <sup>-1</sup> )*	$\Delta\Delta H$ (kcal.mol <sup>-1</sup> )	$\Delta G$ (kcal.mol <sup>-1</sup> )*	$\Delta\Delta G$ (kcal.mol <sup>-1</sup> )	$\Delta S$ (cal.mol <sup>-1</sup> )*	$\Delta\Delta S$ (cal.mol <sup>-1</sup> )
Adduct OH-NH <sub>2</sub> same unit (site A)	-1326945	-13	-1327009	-1	215	-38
Adduct OH-NH <sub>2</sub> dif unit (site B)	-1326939	-6	-1327004	4	219	-34
Adduct NH <sub>2</sub> only (site C)	-1326945	-13	-1327009	-1	214	-38
	$\Delta H$ (kcal.mol <sup>-1</sup> )		$\Delta G$ (kcal.mol <sup>-1</sup> )		$\Delta S$ (cal.mol <sup>-1</sup> )	
DBTO <sub>2</sub>	-634089		-634120		104	
	$\Delta H$ (kcal.mol <sup>-1</sup> )*	$\Delta\Delta H$ (kcal.mol <sup>-1</sup> )	$\Delta G$ (kcal.mol <sup>-1</sup> )*	$\Delta\Delta G$ (kcal.mol <sup>-1</sup> )	$\Delta S$ (cal.mol <sup>-1</sup> )*	$\Delta\Delta S$ (cal.mol <sup>-1</sup> )
Adduct OH-NH <sub>2</sub> same unit (site A)	-1423336	-11	-1423404	-1	229	-37
Adduct OH-NH <sub>2</sub> dif unit (site B)	-1423330	-6	-1423399	5	231	-35
Adduct NH <sub>2</sub> only (site C)	-1423337	-13	-1423405	-1	227	-39
	$\Delta H$ (kcal.mol <sup>-1</sup> )		$\Delta G$ (kcal.mol <sup>-1</sup> )		$\Delta S$ (cal.mol <sup>-1</sup> )	
4,6-DMDBTO <sub>2</sub>	-683400		-683436		120	
	$\Delta H$ (kcal.mol <sup>-1</sup> )*	$\Delta\Delta H$ (kcal.mol <sup>-1</sup> )	$\Delta G$ (kcal.mol <sup>-1</sup> )*	$\Delta\Delta G$ (kcal.mol <sup>-1</sup> )	$\Delta S$ (cal.mol <sup>-1</sup> )*	$\Delta\Delta S$ (cal.mol <sup>-1</sup> )
Adduct OH-NH <sub>2</sub> same unit (site A)	-1472646	-11	-1472719	-1	246	-37
Adduct OH-NH <sub>2</sub> dif unit (site B)	-1472640	-5	-1472713	6	247	-36
Adduct NH <sub>2</sub> only (site C)	-1472647	-12	-1472719	1	243	-39

\* Energy of the system

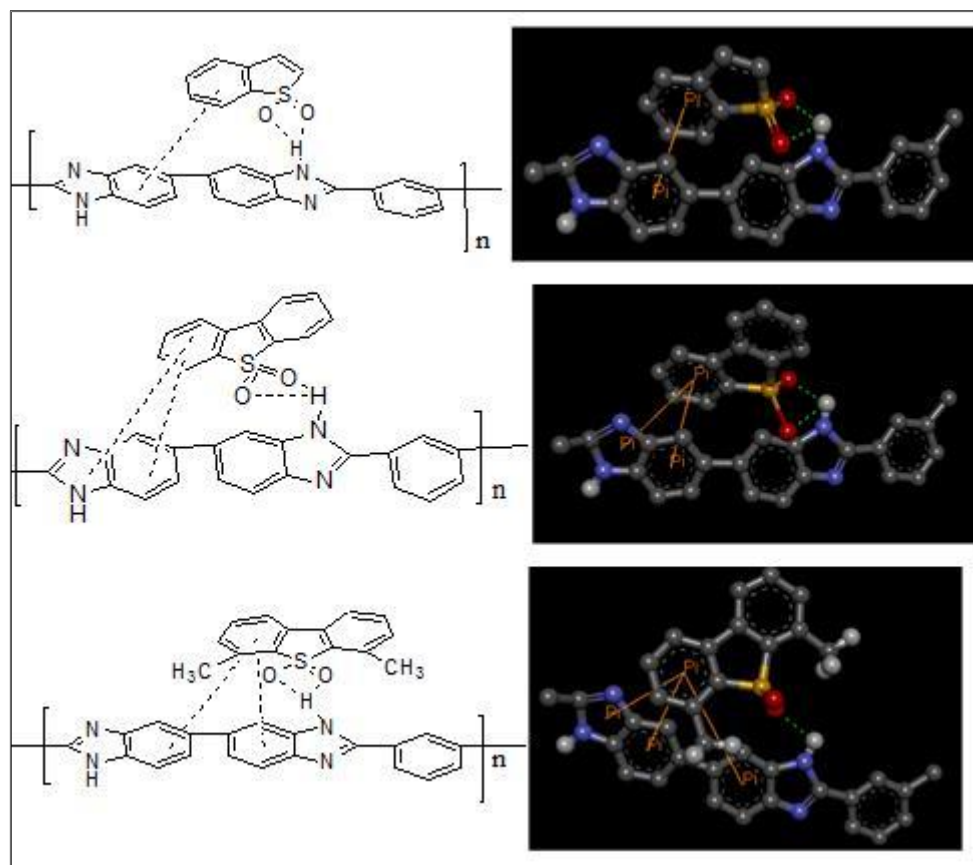


**Figure 5.49** Molecular modelled stable configurations for the 1:1 adduct of BTO<sub>2</sub> (A), DBTO<sub>2</sub> (B), and 4,6-DMDBTO<sub>2</sub> (C) with polybenzimidazole. The dashed lines represent hydrogen bonds.

**Table 5.10** DFT modelling studies on the adducts formed between benzothiophene sulfone (BTO<sub>2</sub>), dibenzothiophene sulfone (DBTO<sub>2</sub>) and 4,6-dimethyldibenzothiophene sulfone (4,6-DMDBTO<sub>2</sub>) and PBI ( $\Delta\Delta H$ ,  $\Delta\Delta G$  and  $\Delta\Delta S$  complex)

	$\Delta H$ (kcal.mol <sup>-1</sup> )		$\Delta G$ (kcal.mol <sup>-1</sup> )		$\Delta S$ (cal.mol <sup>-1</sup> )	
	<b>BTO<sub>2</sub></b>	-537697		-537724		91
<b>PBI “dimer”</b>	-620792		-620833		138	
	$\Delta H$ (kcal.mol <sup>-1</sup> )*	$\Delta\Delta H$ (kcal.mol <sup>-1</sup> )	$\Delta G$ (kcal.mol <sup>-1</sup> )*	$\Delta\Delta G$ (kcal.mol <sup>-1</sup> )	$\Delta S$ (cal.mol <sup>-1</sup> )*	$\Delta\Delta S$ (cal.mol <sup>-1</sup> )
<b>Adduct <math>\perp</math> PBI plane, cis (site A)</b>	-1158502	-13	-1158559	-2	194	-34
<b>Adduct <math>\perp</math> PBI plane, twisted (site B)</b>	-1158502	-13	-1158559	-2	194	-34
<b>Adduct <math>\parallel</math> PBI plane (site C)</b>	-1158498	-9	-1158557	1	193	-34
	$\Delta H$ (kcal.mol <sup>-1</sup> )		$\Delta G$ (kcal.mol <sup>-1</sup> )		$\Delta S$ (cal.mol <sup>-1</sup> )	
<b>DBTO<sub>2</sub></b>	-634089		-634120		104	
	$\Delta H$ (kcal.mol <sup>-1</sup> )*	$\Delta\Delta H$ (kcal.mol <sup>-1</sup> )	$\Delta G$ (kcal.mol <sup>-1</sup> )*	$\Delta\Delta G$ (kcal.mol <sup>-1</sup> )	$\Delta S$ (cal.mol <sup>-1</sup> )*	$\Delta\Delta S$ (cal.mol <sup>-1</sup> )
<b>Adduct <math>\perp</math> PBI plane, cis (site A)</b>	-1254894	-13	-1254955	-3	206	-35
<b>Adduct <math>\perp</math> PBI plane, twisted (site B)</b>	-1254894	-13	-1254956	-3	207	-34
<b>Adduct <math>\parallel</math> PBI plane (site C)</b>	-1254891	-10	-1254952	1	205	-37
	$\Delta H$ (kcal.mol <sup>-1</sup> )		$\Delta G$ (kcal.mol <sup>-1</sup> )		$\Delta S$ (cal.mol <sup>-1</sup> )	
<b>4,6DMDBTO<sub>2</sub></b>	-683399.884		-683435.655		119.975	
	$\Delta H$ (kcal.mol <sup>-1</sup> )*	$\Delta\Delta H$ (kcal.mol <sup>-1</sup> )	$\Delta G$ (kcal.mol <sup>-1</sup> )*	$\Delta\Delta G$ (kcal.mol <sup>-1</sup> )	$\Delta S$ (cal.mol <sup>-1</sup> )*	$\Delta\Delta S$ (cal.mol <sup>-1</sup> )
<b>Adduct <math>\perp</math> PBI plane, cis (site A)</b>	-1304205	-14	-1304271	-3	220	-38
<b>Adduct <math>\perp</math> PBI plane, twisted (site B)</b>	-1304205	-14	-1304271	-2	219	-39
<b>Adduct <math>\parallel</math> PBI plane (site C)</b>	-1304199	-7	-1304265	4	220	-37

\* Energy of the system

## 5.9 Conclusions

Molecularly imprinted adsorbents (chitosan nanofibers, microspheres and PBI nanofibers) were successfully applied to the adsorption of sulfone compounds found in oxidized hydro-treated diesel. The imprinted adsorbents exhibited conformational memory for recognizing sulfones. The Freundlich adsorption isotherm confirmed multilayer adsorption was attributed to the interactions between imprinted adsorbents and sulfone compounds, and possibly between sulfone molecules. From the adsorbent thermograms, polybenzimidazole is generally more stable as compared to chitosan due to the rigid aromatic compound structure it possesses.

The high adsorption capacities observed for non-imprinted chitosan adsorbents were due to the non-specific binding nature of the adsorbents compared to imprinted-chitosan adsorbents where binding environments are restricted through the formation of high specific sites. Hydrogen bond formation through the interactions between sulfone oxygen groups with -OH and/or -NH groups of the chitosan is responsible for adsorption. Surface area measurements showed that non-imprinted chitosan microspheres and nanofibers have higher surface area as compared to imprinted chitosan adsorbents (nanofibers and microspheres), this phenomenon is due to surface morphological modifications on imprinting with template of different molecular sizes. Continuous flow adsorption process showed that adsorbent saturation begins only after about 1 mL of the respective sulfone solutions have been passed through the imprinted chitosan nanofibers.

On the other hand, imprinted-PBI nanofibers, gave a much higher adsorption capacities as compared to imprinted-chitosan adsorbents. The high adsorption capacities was due to hydrogen bond formation through the interactions between sulfone oxygen groups with NH groups of the PBI and secondly aromatic stacking  $\pi$ - $\pi$  interactions between sulfone compounds and PBI. Desorption of adsorbed sulfonated compounds from imprinted-PBI nanofibers using pressurized hot water extraction system proved to be faster and gave better extraction yields as compared to the Soxhlet extraction process. High adsorption of sulfones (> 99%) in oxidized hydro-treated diesel when imprinted-PBI nanofibers



were employed under continuous flow process indicated its potential use for industrial adsorption purposes.

*This page is kept blank*

# Chapter 6

## Conclusions and future work

### 6.1 Conclusions

In this study, crude oils origin source were classified based on their nickel-to-vanadium and phenanthrene-to-dibenzothiophene ratios (**Chapter 3**). It was concluded that light crude oil originated from marine organic matter due to its low sulfur content, while the heavy crude oil originated from the terrestrial organic matter due to the high sulfur content it possess and the medium crude oil was formed due to the migration of the composition of petroleum hydrocarbon of the light and heavy crude oil. The metal content determination method validation using a fuel oil SRM 1634c ( $28.19 \pm 0.40$  ppm and  $17.54 \pm 0.21$  ppm for vanadium and nickel respectively) gave a value of  $28.82 \pm 0.36$  ppm and  $17.45 \pm 0.41$  ppm for vanadium and nickel respectively. The identification of some organosulfur compounds available in fuels was also reported.

In **Chapter 4**, polymer supported oxidovanadium(IV) catalysts, poly[V<sup>IV</sup>O(sal-AHBPD)] and poly[V<sup>IV</sup>O(allylsB-co-EGDMA)], were prepared, characterized and employed in the oxidation of organosulfur compounds. Poly[V<sup>IV</sup>O(allylsB-co-EGDMA)], synthesized *via* suspension polymerization, had a higher surface area of 23 m<sup>2</sup>/g compared to a Merrifield resin-based catalyst, poly[V<sup>IV</sup>O(sal-AHBPD)] which had a surface area of 7 m<sup>2</sup>/g. Both catalysts, poly[V<sup>IV</sup>O(sal-AHBPD)] and poly[V<sup>IV</sup>O(allylsB-co-EGDMA)], demonstrated promising catalytic activity for the *tert*-butylhydroperoxide-facilitated oxidation of thiophene, benzothiophene, dibenzothiophene and 4,6-dimethyldibenzothiophene, which is the first step in oxidative-desulfurization (ODS) of hydro-treated fuels. The polymer supported catalysts showed better activity than the homogeneous counterpart, [V<sup>IV</sup>O(sal-HBPD)]. Higher oxidation yields, towards the formation of sulfone compounds, were recorded in the continuous flow oxidation process while employing poly[V<sup>IV</sup>O(allylsB-co-EGDMA)] as catalyst. The catalysed oxidation of hydro-treated diesel using poly[V<sup>IV</sup>O(allylsB-co-EGDMA)] gave a high oxidation yield (> 99%) with all the sulfur compounds oxidized to sulfonated compounds. In both the batch and continuous flow oxidation process, the polymer-supported catalysts showed

good catalytic activity for the oxidation of organosulfur compounds with excellent recyclability, mechanical stability and relatively low vanadium leaching.

Adsorption of the sulfonated compounds in hydro-treated diesel oils was carried-out by employing molecularly imprinted polymers (MIPs) (**Chapter 5**). Prior to desulfurization of oxidized fuels, sulfonated compounds {benzothiophene sulfone (BTO<sub>2</sub>), dibenzothiophene sulfone (DBTO<sub>2</sub>) and 4,6-dimethyldibenzothiophene sulfone (4,6-DMDBTO<sub>2</sub>)} were imprinted on chitosan microspheres, chitosan nanofibers and polybenzimidazole (PBI) nanofibers. Polybenzimidazole (PBI) imprinted nanofibers presented higher adsorption capacities for the individual sulfone compounds as compared to imprinted chitosan nanofibers and microspheres. The excellent adsorption capacity displayed by imprinted-PBI nanofibers for the removal of sulfonated compounds in oxidized hydro-treated fuel oils was attributed to imprinting effect, hydrogen bonding and  $\pi$ - $\pi$  aromatic stacking interactions the PBI nanofibers possess. Desorption of adsorbed sulfone compounds using a home-made pressurized hot water extraction (PHWE) unit displayed excellent results as compared to a Soxhlet extraction process which required a longer desorption time and use of expensive organic solvents. Imprinted-PBI nanofibers unlike chitosan adsorbents maintained its mechanical, chemical and thermal stability, hence, encouraging material reusability. PHWE process could not be employed on chitosan nanofibers as the polymer matrix collapsed. A schematic representation of the catalysed oxidative-desulfurization (ODS) process demonstrated in this thesis is summarized in **Figure 6.1**.

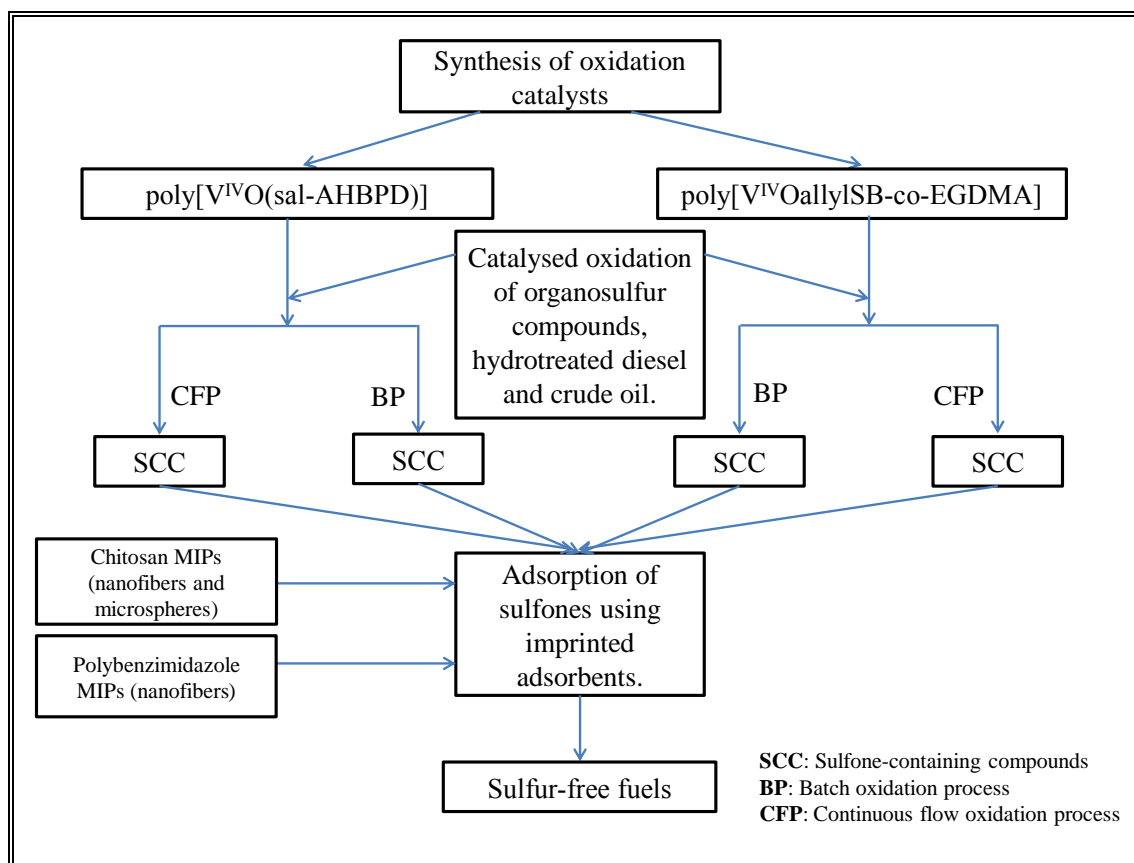


**Figure 6.1** Schematic representation of the catalysed oxidative-desulfurization (ODS) process.

## 6.2 Future work

*Tert*-butylhydroperoxide (*t*-BuOOH) employed as an oxidant for the catalysed oxidation of organosulfur compounds displayed excellent potential, but is expensive. The use of *t*-BuOOH for oxidation in the oxidative-desulfurization of fuels may lead to an expensive end product (ultra-clean fuels) due to the high cost of oxidant. To overcome this oxidant challenge, the use of oxygen is desirable. An experimental oxidative-desulfurization (ODS) process will be carried out by a two-step *in-situ* air oxidation procedure coupled with the adsorption step. In the first step, the hydro-treated fuel will be mixed with air in the presence of oxidovanadium(IV) catalyst to produce hydroperoxides *in-situ*. The hydroperoxide will then oxidise the sulfur compounds to their corresponding sulfones. The generated sulfones will then be removed by adsorption to produce ultralow sulfur fuels.

The use of imprinted polybenzimidazole presented excellent adsorption properties, however its use for sulfone adsorption on industrial scale may be costly considering that they can only be used for a few

cycles. Imprinted silica adsorbents can be employed as alternative for the adsorption of sulfones on industrial scale by mimicking the properties of imprinted PBI nanofibers. Silica is known to be mechanically robust and thermally stable, and in this way moieties such as aromatic rings with functionalities for hydrogen bonding interactions could be introduced on silica without compromising its chemical stability.

It would be desirable to study the effects of reactive nitrogen compounds (such as pyridines, phenantridines, quinoline) in the oxidation process as they can also be oxidized during the ODS process. Nitrogen compounds are known to enhance fuel properties such fuel stability, but nitrogen reduction in fuel is required to maintain NO<sub>x</sub> emissions below regulatory level (500 ppm).<sup>334</sup> The hydro-denitrogenation (HDN) process currently been employed for the removal of nitrogenated compounds suffer limitations in achieving the nitrogen content requirement. Catalyst deactivations as well as the lack of reactivity of N-compounds of some nitrogen-containing compounds such as indoles, carbazoles, benzcarbazoles, pyrrole, azapyridines, aniline and porphyrins are identified as important factors affecting the HDN process.<sup>434, 435</sup> The catalysed oxidation of nitrogenated molecules in fuels to nitrogen oxides using vanadia supported on silica or alumina, followed by the selective adsorption/removal of the nitrogen oxide compounds *via* molecularly imprinted polymers (MIPs) is encouraged. The supported vanadia can also be explored for their oxidation of sulfur-containing molecules so as to develop a catalyst for converting both nitrogen and sulfur compounds to their respective oxides using air as an oxidant. The catalysed oxidation of both nitrogen and sulfur compounds can be performed in micro-structured reactors to produce oxygenated compounds.

Micro-reactors provide higher heat and mass transfer rates, along with better product yield and selectivity as compared to conventional reactors.<sup>436-440</sup> Micro-reactors guarantee a higher heat and mass transfer rates for chemical reactions hence facilitating a fast and highly exothermic reaction performed under isothermal conditions.<sup>440,441</sup> Micro-reactors also enable a better process control and well distributed production.<sup>441</sup>

**References**

- [1] Sami, M.; Hatch, L. F. Chemistry of petrochemical processes, Gulf publishing company, Houston, Texas. **1994**, p11-17.
- [2] Hatch, L.F.; Matar, S., From hydrocarbons to petrochemicals, Gulf publishing company, **1981**, p 5.
- [3] Barbara, P.; Rufino, M.N.; Campos-Martin, J.M.; Fierro, J.L.G. Towards near zero-sulfur liquid fuels: a perspective review. *Catal. Sci. Technol.*, **2011**, 1, 23-42.
- [4] Kenney, J.F. Considerations about recent predictions of impending shortages of petroleum evaluated from the perspective of modern petroleum science. *Energy World*, **1996**, 240, 16-18.
- [5] Wellings, F.E. Geological aspects the origin of oil. *Inst. Petrol. J.*, **1966**, 52, 124-130.
- [6] Dott, R.H. Hypotheses for an organic origin: In sourcebook for petroleum geology, Part 1. Genesis of petroleum. Dott, R.H.; Reynolds, M.J. (Eds). AAPG Memoir 5, Tulsa, **1969**, p 1-244.
- [7] Musser, B. J.; Kilpatrick, P.K. Molecular characterization of wax isolated from a variety of crude oils. *Energy Fuels* **1998**, 12, 715-725.
- [8] Zaki, N.; Schorling, P.C.; Rahimian, I. The role of asphaltene solubility and chemical composition on asphaltene aggregation. *Pet. Sci. Technol.*, **2000**, 18, 945-963.
- [9] Lee, R.F. Agents which promote and stabilize water-in-oil emulsions. *Spill Sci. Technol. Bull.*, **1999**, 5, 117-126.
- [10] Speight, J.G. The chemistry and technology of petroleum, Marcel Dekker, New York, 1999.
- [11] Sheu, E.Y.; Mullins, O.C. Asphaltenes: Fundamentals and applications, Plenum Press: New York. **1995**.
- [12] Andersen, S.I.; Speight, J.G. Thermodynamic models for asphaltene solubility and precipitation. *Pet. Sci. Technol.*, **2001**, 19, 1-34.

- [13] Rall, H.C. The Characteristics of a low temperature in-situ shale. *Oil Proc. Am. Petrol. Inst.*, **1962**, 42, 19.
- [14] EPA sulfur distribution. Source: <http://www.eia.gov/todayinenergy/detail.cfm?id=7110>. Date assessed: **28/01/2013**
- [15] Hartung, G.K.; Jewell, D.M. Identification of nitriles in petroleum products: Complex formation as a method of isolation. *Anal. Chim. Acta.*, **1972**, 27, 219-232.
- [16] Odebunmi E.O.; Ogunsakin. E.A.; Ilukhor. P.E.P. Characterization of crude oil and petroleum products I. Elution liquid chromatographic separation and gas chromatographic analysis of crude oils and petroleum products. *Bull. Chem. Soc. Ethiop.*, **2002**, 16 (2), 115-132.
- [17] South African National Standard, *Automotive diesel fuel*, Edition 4, SANS 342: **2006**, ISBN 0-626-18752-4.
- [18] Yoshimura, Y.; Sato, T.; Shimada, H.; Matsubayashi, N.; Imamura, M.; Nishijima, A. Proc. 1st Japan-EC Joint workshop on the frontiers of catalytic science and technology (JECAT'91). Tokyo, **1991**, p P-06.
- [19] Maruyama, F.; Morinaga, K.; Suzuka, T. Proc. 1st Japan-EC Joint workshop on the frontiers of catalytic science and technology (JECAT'91), Tokyo, **1991**, p 8.
- [20] Amorelli, A.; Amos, Y.D.; Hälsig, C.P.; Kosman, J.J.; Jonker, R.J.; de Wind, M.; Vrieling, J. Estimate feedstock processability-characterize sulfur compounds in middle distillates and deeply hydrotreated products. *Hydrocarbon Proc.*, **1992**, 71, 93-100.
- [21] Ma, X.; Sakanishi, K.; Isoda, T.; Mochida, I. Comparison of sulfided CoMo/Al<sub>2</sub>O<sub>3</sub> catalysts in hydro-desulfurization of gas oil fractions. *Prepr. Div. Pet. Chem. Am. Chem. Soc.*, **1994**, 39, 622-626.
- [22] Topsøe, H.; Clausen, B.S.; Massoth, F.E. Hydrotreating catalysis, Vol 11, Ed. Anderson, J.R and Boudart, M.;Springer, Berlin, **1996**.



- [23] Reinhoudt, H.R.; Troost, R.; Van Schalkwijk, S.; Van Langeveld, A.D.; Sie, S.T.; Schulz, H.; Chadwick, D.; Cambra, J.; de Beer, V.H.J.; van Veen, J.A.R.; Fierro, J.L.G.; Moulijn, J.A. Application of ASA supported noble metal catalysts in the deep hydro-desulfurization of diesel fuel. *Stud. Surf. Sci. Catal.*, **1997**, 106, 237-244.
- [24] Wang, S.L.; Flamberg, A.; Kikabhai, T. Select the optimum pour point depressant. *Hydrocarbon Proc.*, **1999**, 78(2), 59-62.
- [25] Dara, S.S. A textbook on experiments and calculations in engineering chemistry, 9<sup>th</sup> Edition, Ram Nagar, New Delhi, India, 149, **2003**.
- [26] Booth, B.; Buglass, J.G.; Unsworth, J.F. Tailoring fuels for the new millennium. *Top. Catal.*, **2001**, 16-17, 39-46.
- [27] Boron, D.J.; Deever, W.R.; Atlas, R.M.; McFarland, B.L.; Meyer, J.A.; Johnson, A.R. NPRA meeting, San Antonio, **1999**, AM-99-54.
- [28] Monticello, D.J. Biodesulfurization and the upgrading of petroleum distillates. *Curr. Opin. Biotechnol.*, **2000**, 11, 540-546.
- [29] Soleimani, M.; Bassi, A.; Margaritis, A. Biodesulfurization of refractory organic sulfur compounds in fossil fuels. *Biotechnol. Adv.*, **2007**, 25, 570-596.
- [30] Kodama, K.; Umehara, K.; Shimizu, K.; Nakatani, S.; Minoda, Y.; Yamada, K. Identification of microbial products from dibenzothiophene and its proposed oxidation pathway. *Agric. Biol. Chem.*, **1973**, 37, 45-50.
- [31] Song, C.S. An overview of new approaches to deep desulfurization for ultra-clean gasoline, diesel fuel and jet fuel. *Catal. Today*, **2003**, 86, 211-263.
- [32] Babich, V.I.; Moulijn, J.A. Science and technology of novel processes for deep desulfurization of oil refinery streams: A review. *Fuel*, **2003**, 82, 607-631.
- [33] Song, C.; Ma, X.L. New design approaches to ultra-clean diesel fuels by deep desulfurization and deep dearomatization. *Appl. Catal. B.*, **2003**, 41, 207-238.

- [34] Song, C.S.; Ma, X.L. Ultra-deep desulfurization of liquid hydrocarbon fuels: Chemistry and process. *Int. J. Green Energy*, **2004**, 1, 167-191.
- [35] Schulz, H.; Böhringer, W.; Ousmanov, F.; Waller, P. Refractory sulfur compounds in gas oils. *Fuel Process. Technol.*, **1999**, 61, 5-41.
- [36] Schulz, H.; Böhringer, W.; Waller, P.; Ousmanov, F. Gas oil deep hydrodesulfurization: refractory compounds and retarded kinetics. *Catal. Today*, **1999**, 49, 87-97.
- [37] Ma, X.; Lu, S.; Yin, Z.; Song, C. New Approaches to deep desulfurization of diesel fuel, jet fuel, and gasoline by adsorption for ultra-clean fuels and for fuel cell applications. *Am. Chem. Soc. Div. Fuel. Chem. Prepr.*, **2001**, 46 (2), 648-649.
- [38] Song, C. Designing sulfur-resistant, noble-metal hydrotreating catalysts. *Chemtech.*, **1999**, 29 (3), 26-30.
- [39] Song, C. Sulfur-resistant noble metal catalysts based on shape-selective exclusion and hydrogen spillover, in: Song, C.; Garces, J.M.; Sugi, Y. (Eds.), shape-selective catalysis, chemicals synthesis and hydrocarbon processing (ACS Symposium Series 738), American Chemical Society, Washington, DC, **1999**, p. 381-390 (Chapter 27).
- [40] Song, C.; Reddy, K.M. Mesoporous molecular sieve MCM-41 supported Co-Mo catalyst for hydrodesulfurization of dibenzothiophene in distillate fuels. *Appl. Catal. A.*, **1999**, 176, 1-10.
- [41] Song, C.; Reddy, K.M. in: Murugesan, V.; Arabindoo, B.; Palanichamy, M. Recent trends in catalysis, Narosa Publishing House, (Eds.), New Delhi, India, **1999**, p. 1-13 (Chapter 1).
- [42] Tam, P.S.; Kittrell, J.R.; Eldridge, J.W. Desulfurization of fuel oil by oxidation and extraction. 1. Enhancement of extraction oil yield. *Ind. Eng. Chem. Res.*, **1990**, 29, 321-324.
- [43] Tam, P.S.; Kittrell, J.R.; Eldridge, J.W. Desulfurization of fuel oil by oxidation and extraction. 2. Kinetic modeling of oxidation reaction. *Ind. Eng. Chem. Res.*, **1990**, 29, 324-329.

- [44] Baxendale, J.H.; Evans, M.G.; Park, G.S. The mechanism and kinetics of the initiation of polymerisation by systems containing hydrogen peroxide. *Trans. Faraday Soc.*, **1946**, 42, 155-169.
- [45] Venturiello, C.; Alneri, E.; Ricci, M. A new effective catalytic system for epoxidation of olefins by hydrogen peroxide under phase-transfer conditions. *J. Org. Chem.*, **1983**, 48, 3831-3833.
- [46] Tam, P.S.; Kittrell, J.R. Process for purifying hydrocarbonaceous oils. U.S. Patent 4, 485, 007, **1984**.
- [47] Chica, A.; Corma, A.; Dómine, M.E. Catalytic oxidative desulfurization (ODS) of diesel fuel on a continuous fixed-bed reactor. *J. Catal.*, **2006**, 242, 299-308.
- [48] Karas, L.J.; Grey, R.A.; Lynch, M.W. Desulfurization process. US Patent 2008047875, **2008**.
- [49] Kocal, J.A. process for the desulfurization of a hydro-carbonaceous oil. US Patent 6277271, **2001**.
- [50] Kocal, J.A.; Branvold, T.A. Removal of sulfur-containing compounds from liquid hydrocarbon streams. US Patent 6368495, **2002**.
- [51] Karas, L.J.; Han, Y.Z.; Leyshon, D.W. Organosulfur oxidation process. US Patent 2004178122, **2004**.
- [52] Zannikos, F.; Lois, E.; Stournas, S. Desulfurization of petroleum fractions by oxidation and solvent extraction. *Fuel Process. Technol.*, **1995**, 42, 35-45.
- [53] Aida, T.; Yamamoto, D. *Prepr. Pap. Am. Chem. Soc., Div. Fuel Chem.*, **1994**, 39, 623. Annual book of ASTM standards, 2005. Standard test method for determination of sulfur compounds in natural gas and gaseous fuels by gas chromatography and chemiluminescence, vol 05.05.

- [54] Otsuki, S.; Nonaka, T.; Takashima, N.; Qian, W.; Ishihara, A.; Imai, T.; Kabe, T. Oxidative desulfurization of light gas oil and vacuum gas oil by oxidation and solvent extraction. *Energy Fuels*, **2000**, 14, 1232-1239.
- [55] Collins, F.M.; Lucy, A. R.; Sharp, C. Oxidative desulfurization of oils *via* hydrogen peroxide and heteropolyanion catalysis. *J. Mol. Catal. A: Chem.*, **1997**, 117, 397-403.
- [56] Otsuki, S.; Nonaka, T.; Qian, W.; Ishihara, A.; Kabe, T. Oxidative desulfurization of middle distillate using ozone. *J. Jpn. Pet. Inst.*, **1999**, 42 (5), 315-320.
- [57] Yazu, K.; Furuya, T.; Miki, K.; Ukegawa, K. Tungstophosphoric acid-catalysed oxidative desulfurization of light oil with hydrogen peroxide in a light oil/acetic acid biphasic system. *Chem. Lett.*, **2003**, 32, 920-921.
- [58] Paybarah, A.; Bone, R.L.; Corcoran, W.H. Selective oxidation of dibenzothiophene by peroxybenzoic acid formed in situ. *Ind. Eng. Chem. Prod. Res. Dev.*, **1982**, 21, 426-431.
- [59] Hulea, V.; Fajula, F.; Bousquet, J. Mild oxidation with H<sub>2</sub>O<sub>2</sub> over Ti-containing molecular sieves-a very efficient method for removing aromatic sulfur compounds from fuels. *J. Catal.*, **2001**, 198, 179-186.
- [60] Anisimov, A.V.; Fedorova, E.V.; Lesnugin, A.Z.; Senyavin, V.m.; Aslanov, L.A.; Rybakov, V.B.; Tarakanova, A.V. Vanadium peroxocomplexes as oxidation catalysts of sulfur organic compounds by hydrogen peroxide in bi-phase systems. *Catal. Today*, **2003**, 78, 319-325.
- [61] Palomeque, J.; Clacens, J.M.; Figueras, F. Oxidation of dibenzothiophene by hydrogen peroxide catalysed by solid bases. *J. Catal.*, **2002**, 211, 103-108.
- [62] Yazu, K.; Yamamoto, Y.; Furuya, T.; Miki, K.; Ukegawa, K. Oxidation of dibenzothiophenes in an organic biphasic system and its application to oxidative desulfurization of light oil. *Energy Fuels*, **2001**, 15, 1535-1536.

- [63] Djangkung, S.; Murti, S.; Yang, H.; Choi, K.; Kora, Y.; Mochida, I. Influences of nitrogen species on the hydrodesulfurization reactivity of a gas oil over sulfide catalysts of variable activity. *Appl. Catal., A*, **2003**, 252, 331-346.
- [64] Shiraishi, Y.; Naito, T.; Hirai, T. Vanadosilicate molecular sieve as a catalyst for oxidative desulfurization of light oil. *Ind. Eng. Chem. Res.*, **2003**, 42, 6034-6039.
- [65] Campos-Martin, J.M.; Capel-Sanchez, M.C.; Perez-Presas, P.; Fierro, J.L.G. Oxidative processes of desulfurization of liquid fuels. *J. Chem. Technol. Biotechnol.*, **2010**, 85, 879-890.
- [66] Sughrue, E.L.; Khare, G.P.; Bertus, B.J.; Johnson, M.M. US Patent 6.254.766, **2001**.
- [67] Velu, S.; Ma, X.; Song, C. Selective adsorption for removing sulfur from jet fuel over zeolite-based adsorbents. *Ind. Eng. Chem. Res.*, **2003**, 42, 5293-5304.
- [68] Ryu, K.; Heo, J.; Yoo, I. K. Removal of dibenzothiophene and its oxidized product in anhydrous water-immiscible organic solvent by immobilized cytochrome c. *Biotechnol. Lett.*, **2002**, 24, 143-146.
- [69] Castro, B.; Whitcombe, M.J.; Vulfson, E.N.; Vazquez-Duhalt, R.; Barzana, E. Molecular imprinting for the selective adsorption of organosulfur compounds present in fuels. *Anal. Chim. Acta.*, **2001**, 435, 83-90.
- [70] Jorge, A.; Le Borgne, S. Selective adsorption of dibenzothiophene sulfone by an imprinted and stimuli-responsive chitosan hydrogel. *Macromolecules*, **2004**, 37, 2938-2943.
- [71] Blanco-Brieva, G.; Campos-Martin, J.M.; Al-Zahrani, S.M.; Fierro, J.L.G. Thermal regeneration of the metal organic frameworks used in the adsorption of refractory organosulfur compounds from liquid fuels. *Fuel*, **2013**, 105, 459-465.
- [72] Zhao, B.; Moore, J.S. Fast pH- and ionic strength-responsive hydrogels in microchannels. *Langmuir*, **2001**, 17, 4758-4763.
- [73] Thomson, S.J.; Webb, G. Heterogeneous catalysis. Oliver and Boyd Ltd, **1968**.

- [74] Marek, L.F.; Dorothy A.H. The catalytic oxidation of organic compounds in the vapor phase the chemical” Catalog company Inc, New York, U.S.A., **1932**.
- [75] Hagen, J. Industrial Catalysis: A practical approach. 2<sup>nd</sup> ed.; Wiley-VCH Verlag, Weinheim, **2006**.
- [76] Benaglia, M. Recoverable and recyclable catalysts; John Wiley & Sons, Ltd: West Sussex, **2009**.
- [77] Walmsley, R. An investigation into the antidiabetic and catalytic properties of oxovanadium(IV) Complexes, PhD thesis, Rhodes University, **2011**.
- [78] Wang, D.H.; Qian, E.W.H.; Amano, H.; Okata, K.; Ishihara, A.; Kabe, T. Oxidative desulfurization of fuel oil - Part I. Oxidation of dibenzothiophenes using *tert*-butylhydroperoxide. *Appl. Catal., A*, **2003**, 253, 91-99.
- [79] Ishihara, A.; Wang, D.H.; Dumeignil, F.; Amano, H.; Qian, E.W.H.; Kabe, T. Oxidative desulfurization and denitrogenation of a light gas oil using an oxidation/adsorption continuous flow process. *Appl. Catal., A*, **2005**, 279, 279-287.
- [80] Chica, A.; Gatti, G.; Moden, B.; Marchese, L.; Iglesia, E. Selective catalytic oxidation of organosulfur compounds with *tert*-butylhydroperoxide. *Chem. Eur. J.*, **2006**, 12, 1960-1967.
- [81] Zhou, X.R.; Zhao, C.X.; Yang, J.Z.; Zhang, S.F. Catalytic oxidation of dibenzothiophene using cyclohexanone peroxide. *Energy Fuels*, **2007**, 21, 7-10.
- [82] Kuznetsova, L.; Detusheva, L.; Kuznetsov, N.; Duplyakin, V.; Likholobov, V. Liquid-phase oxidation of benzothiophene and dibenzothiophene by cumyl-hydroperoxide in the presence of catalysts based on supported metal oxides. *Kinet. Catal.*, **2008**, 49, 644-652.
- [83] Prasad, V.V.D.N.; Jeong, K-E.; Chae, H-J.; Kim, C-U.; Jeong, S-Y. Oxidative desulfurization of 4,6-dimethyl dibenzothiophene and light cycle oil over supported molybdenum oxide catalysts. *Catal. Commun.*, **2008**, 9, 1966-1969.

- [84] Sharipov, A.; Nigmatullin, V. Finishing of diesel fuel to remove sulfur compounds after hydrotreating. *Chem. Tech. Fuels Oils*, **2005**, 41, 309-312.
- [85] Cheng, S.F.; Liu, Y.M.; Gao, J.B.; Wang, L.L.; Liu, X.L.; Gao, G.H.; Wu, P.; He, M.Y. Catalytic oxidation of benzothiophene and dibenzothiophene in model light oil over Ti-MWW. *Chin. J. Catal.*, **2006**, 27, 547-549.
- [86] Cui, S.H.; Ma, F.; Wang, Y.Q. Oxidative desulfurization of model diesel oil over Ti-containing molecular sieves using hydrogen peroxide. *React. Kinet. Catal. Lett.*, **2007**, 92, 155-163.
- [87] Si, X.; Cheng, S.; Lu, Y.; Gao, G.; He, M.Y. Oxidative desulfurization of model oil over Au/Ti-MWW. *Catal. Lett.*, **2008**, 122, 321-324.
- [88] Di-Giuseppe, A.; Crucianelli, M.; De Angelis, F.; Crestini, C.; Saladino, R. Efficient oxidation of thiophene derivatives with homogeneous and heterogeneous MTO/H<sub>2</sub>O<sub>2</sub> systems: A novel approach for oxidative desulfurization (ODS) of diesel fuel. *Appl. Catal., B*, **2009**, 89, 239-245.
- [89] Clark, R.J.H. The chemistry of titanium and vanadium, Elsevier, Amsterdam, **1968**.
- [90] Cotton, F.A.; Wilkinson, G. Advanced Inorganic Chemistry, A Comprehensive Text, 4th ed., Wiley, New York, **1980**.
- [91] Greenwood, N.N.; Earnshaw, A. Chemistry of the elements, Pergamon Press, Oxford, **1984**.
- [92] Magee, J.S.; Mitchell Jr, M.M. Studies in surface science and catalysis; John, S. M., Maurice, M.M., Eds.; Elsevier, London **1993**.
- [93] Weckhuysen, B.M.; Keller, D.E. Chemistry, spectroscopy and the role of supported vanadium oxides in heterogeneous catalysis. *Catal. Today*, **2003**, 78, 25-46.
- [94] Nielsen, F.H.; Uthus, E.O. In vanadium in biological systems; Chasteen, N.D., Ed.; Kluwer Academic Publishers: Boston, **1990**.

- [95] Weckhuysen, B.M.; Keller, D.E. Chemistry, spectroscopy and the role of supported vanadium oxides in heterogeneous catalysis, *Catal. Today*, **2003**, 78, 25-46.
- [96] Lopez Nieto, J.M.; Concepcion, P.; Dejoz, A.; Knozinger, H.; Melo, F.; Vazquez, M.I. Selective oxidation of *n*-butane and butenes over vanadium-containing catalysts *J. Catal.*, **2000**, 189, 147-157.
- [97] Wada, K.; Yamada, H.; Watanabe, E.; Mitsudo, T. Selective photo-assisted catalytic oxidation of methane and ethane to oxygenates using supported vanadium oxide catalysts. *J. Chem. Soc. Faraday Trans.*, **1998**, 94, 1771-1778.
- [98] Zhu, Z.P.; Liu, Z.Y.; Liu, S.J.; Niu, H.X. A novel carbon-supported vanadium oxide catalyst for NO reduction with NH<sub>3</sub> at low temperatures. *Appl. Catal., B.*, **1999**, 23, 229-233.
- [99] Bosch, H.; Janssen, F.J.J.G.; Van den Kerkhof, F.M.G.; Oldenziel, J.; Van Ommen, J.G.; Ross, J.R.H. The activity of supported vanadium oxide catalysts for the selective reduction of NO with ammonia. *Appl. Catal., A.*, **1986**, 25, 239-248.
- [100] Amiridis, M.D.; Wachs, I.E.; Deo, G.; Jehng, J.M.; Kim, D.S. Reactivity of V<sub>2</sub>O<sub>5</sub> catalysts for the selective catalytic reduction of NO by NH<sub>3</sub>: influence of vanadia loading, H<sub>2</sub>O, and SO<sub>2</sub>. *J. Catal.*, **1996**, 161, 247-253.
- [101] Dias, C.R.; Portgela, M.F.; Galan-Fereres, M.; Banares, M.A.; Granados, M.L.; Pena, M.A.; Fierro, J.L.G. Selective oxidation of *o*-xylene to phthalic anhydride on V<sub>2</sub>O<sub>5</sub> supported on TiO<sub>2</sub>-coated SiO<sub>2</sub>. *Catal. Lett.*, **1997**, 43, 117-121.
- [102] Nobbenhuis, M.G.; Baiker, A.; Barnickel, P.; Wokaun, A. Titania-supported vanadium oxide catalysts for the selective oxidation of *o*-xylene to phthalic anhydride: Influence of vanadia content on activity and surface species *Appl. Catal. A.*, **1992**, 85, 157-172.
- [103] Sanati, M.; Andersson, A.; Wallenberg, L.R.; Rebenstorf, B. Zirconia-supported vanadium oxide catalysts for ammoxidation and oxidation of toluene: A characterization and activity study. *Appl. Catal., A*, **1993**, 106, 51-72.



- [104] Narayana, K.V.; Venugopal, A.; Rama-Rao, K.S.; Masthan, S.K.; Rao, V.V.; Kanta-Rao, P. Ammoxidation of 3-picoline over  $V_2O_5/TiO_2$  (anatase) system. II. Characterization of the catalysts by DTA, SEM, FTIR, ESR and oxygen and ammonia chemisorption. *Appl. Catal., A*, **1998**, 167, 11-22.
- [105] Cavani, F.; Trifiro, F.; Jiru, P.; Habersberger, K.; Tvaruzkova, W. Vanadium-zeolite catalysts for the ammoxidation of xylenes. *Zeolites*, **1988**, 8, 12-18.
- [106] Burcham, L.J.; Gao, G.T.; Gao, X.T.; Wachs, I.E. In situ IR, Raman, and UV-Vis DRS spectroscopy of supported vanadium oxide catalysts during methanol oxidation. *Top. Catal.*, **2000**, 11, 85-100.
- [107] Dunn, J.P.; Koppula, P.R.; Stenger, H.G.; Wachs, I.E. Oxidation of sulfur dioxide to sulfur trioxide over supported vanadia catalysts. *Appl. Catal., B*, **1998**, 19, 103-117.
- [108] Dunn, J.P.; Stenger, H.G.; Wachs, I.E. Oxidation of sulfur dioxide over supported vanadia catalysts: molecular structure – reactivity relationships and reaction kinetics. *Catal. Today*, **1999**, 51, 301-318.
- [109] Dunn, J.P.; Stenger, H.G.; Wachs, I.E. Oxidation of  $SO_2$  over supported metal oxide catalysts. *J. Catal.*, **1999**, 181, 233-243.
- [110] Huuhtanen, J.; Andersson, S.L.T. Oxidation of toluene over  $V_2O_5/Nb_2O_5$  catalysts. *Appl. Catal., A*, **1993**, 98, 159-171.
- [111] Whittington, B.I.; Anderson, J.R. Nature and activity of some vanadium catalysts. *J. Phys. Chem.*, **1993**, 97, 1032-1041.
- [112] Li, K.T.; Chien, T.Y. Effect of supports in hydrogen sulfide oxidation on vanadium-based catalysts. *Catal. Lett.*, **1999**, 57, 77-80.
- [113] Bagajewicz, M.J.; Tamhankar, S.S.; Stephanopoulos, M.F.; Gavalas, G.R. Hydrogen sulfide removal by supported vanadium oxide. *Environ. Sci. Technol.*, **1998**, 22, 467-470.

- [114] Khodakov, A.; Olthof, B.; Bell, A.T.; Iglesia, E. Structure and catalytic properties of supported vanadium oxides: Support effects on oxidative dehydrogenation reactions. *J. Catal.*, **1999**, 181, 205-216.
- [115] Chen, K.; Khodakov, A.; Yang, J.; Bell, A.T.; Iglesia, E. Isotopic tracer and kinetic studies of oxidative dehydrogenation pathways on vanadium oxide catalysts. *J. Catal.*, **1999**, 186, 325-333.
- [116] Concepcion, P.; Lopez Nieto, J.M.; Perez-Pariente, J. Oxidative dehydrogenation of propane on VAPO-5, V<sub>2</sub>O<sub>5</sub>/ALPO<sub>4</sub>-5 and V<sub>2</sub>O<sub>5</sub>/MgO catalysts: Nature of selective sites. *J. Mol. Catal. A: Chem.*, **1995**, 99, 173-182.
- [117] Bond, G.C.; Flamerz, S.; Shukri, R. Structure and reactivity of transition-metal oxide monolayers. *Faraday Discuss. Chem. Soc.*, **1989**, 87, 65-77.
- [118] Vassileva, M.; Andreev, A.; Dancheva, S. Complete catalytic oxidation of benzene over supported vanadium oxides modified by silver. *Appl. Catal., A*, **1991**, 69, 221-234.
- [119] Reddy, B.M.; Ganesh, I.; Chowdhury, B. Vapour-phase selective oxidation of 4-methylanisole to anisaldehyde over V<sub>2</sub>O<sub>5</sub>/Ga<sub>2</sub>O<sub>3</sub>-TiO<sub>2</sub> catalyst. *Chem. Lett.*, **1997**, 1145-1146.
- [120] Patterson, H.H.; Cheng, J.; Despres, S.; Sunamoto, M.; Anpo, M. Relationship between the geometry of the excited state of vanadium oxides anchored onto silica and their photoreactivity toward carbon monoxide molecules. *J. Phys. Chem.*, **1991**, 95, 8813-8818.
- [121] Dang, Z.Y.; Gu, J.F.; Lin, J.Z.; Yang, D.X. BaCO<sub>3</sub>-supported vanadium oxide catalysts for the oxidative coupling of methane. *Chem. Commun.*, **1996**, 1901-1902.
- [122] Banares, M.A.; Alemany, L.J.; Granados, M.L.; Faraldos, M.; Fierro, J.L.G. Partial oxidation of methane to formaldehyde on silica-supported transition metal oxide catalysts. *Catal. Today*, **1997**, 33, 73-83.

- [123] Parmaliana, A.; Fursteri, F.; Mezzapica, A.; Scurrall, M.S.; Giordano, N. Novel high activity catalysts for partial oxidation of methane to formaldehyde. *J. Chem. Soc., Chem. Commun.*, **1993**, 751-753.
- [124] Herman, R.G.; Sun, Q.; Shi, C.; Klier, K.; Wang, C.B.; Hu, H.; Wachs, I.E.; Bhasin, M.M. Development of active oxide catalysts for the direct oxidation of methane to formaldehyde. *Catal. Today*, **1997**, 37, 1-14.
- [125] Ishida, S.; Imamura, S.; Ren, F.; Tatematsu, Y.; Fujimara, Y. Ethylene polymerization on lewis acid sites of a reduced  $V_2O_5/Al_2O_3$  catalyst. *React. Kinet. Catal. Lett.*, **1992**, 46, 199-207.
- [126] Weckhuysen, B.M.; Wang, D.; Rosynek, M.P.; Lunsford, J.H. Conversion of methane to benzene over transition metal ion ZSM-5 zeolites: I. Catalytic characterization. *J. Catal.*, **1998**, 175, 338-346.
- [127] Weckhuysen, B.M.; Wang, D.; Rosynek, M.P.; Lunsford, J.H. Conversion of methane to benzene over transition metal ion ZSM-5 zeolites: II. Catalyst characterization by X-ray photoelectron spectroscopy. *J. Catal.*, **1998**, 175, 347-351.
- [128] Ogunlaja, A.S.; Chidawanyika, W.; Antunes, E.; Fernandes, M.A.; Nyokong, T.; Torto, N.; Tshentu, Z.R. Oxovanadium(IV)-catalysed oxidation of dibenzothiophene and 4,6-dimethyldibenzothiophene. *Dalton Trans.*, **2012**, 41, 13908-13918.
- [129] Ogunlaja, A.S.; Khene, S.; Antunes, E.; Nyokong, T.; Torto, N.; Tshentu, Z.R. The development of catalytic oxovanadium(IV)-containing microspheres for the oxidation of various organosulfur compounds. *Appl. Catal., A*, **2013**, 462-463, 157-167.
- [130] González-García, O.; Cedeño-Caero, L. V-Mo based catalysts for oxidative desulfurization of diesel fuel. *Catal. Today*, **2009**, 148, 42-48.

- [131] Fedorova, E.V.; Zhirkov, N.P.; Tarakanova, A.V.; Ivanov, A.A.; Senyavin, V.M.; Anisimov, A.V.; Tulyakova, E.V.; Surin, S.A. Oxidative desulfurization of diesel fuel with hydrogen peroxide in the presence of vanadium peroxo complexes. *Pet. Chem.*, **2002**, 42, 253-256.
- [132] Bernal, H.G.; Cedeño-Caero, L.; Solvent effects during oxidation-extraction desulfurization process of aromatic sulfur compounds from fuels. *Int. J. Chem. Reactor Eng.*, **2005**, 3, 1542-6580.
- [133] Gómez-Bernal, H; Cedeño-Caero, L.; Gutiérrez-Alejandre, A. Liquid phase oxidation of dibenzothiophene with alumina-supported vanadium oxide catalysts: An alternative to deep desulfurization of diesel. *Catal. Today*, **2009**, 142, 227-233.
- [134] Ballhausen, C.J.; Harry, G.B. The electronic structure of vanadyl ion, *Inorg. Chem.* **1962**, 1, 111-122.
- [135] Maurya, M.R.; Arya, A.; Kumar, A.; Kuznetsov, M.L.; Avecilla, F.; Costa, P. Polymer-bound oxidovanadium(IV) and dioxidovanadium(V) complexes as catalysts for the oxidative desulfurization of model fuel diesel. *Eur. J. Inorg. Chem.*, **2010**, 49, 6586-6600.
- [136] Samuni, A.; Meisel, D.; Czapski, G. The kinetics of the oxidation of chromium(II), titanium(III), and vanadium(IV) by hydrogen peroxide and hydroxyl radicals. *J. Chem. Soc., Dalton Trans.*, **1972**, 1273-1277.
- [137] Rehder, D. Bioorganic vanadium chemistry; John Wiley and Sons Ltd.: West Sussex, **2008**.
- [138] Anderson, J.R.; Foger, K.; Mole, T.; Rajadhyaksha, R.A.; Saunders, J.V. Reactions on ZSM-5-type zeolite catalysts. *J. Catal.*, **1979**, 58, 114-130.
- [139] Delmon, B.; Grange, P.; Jacobs, P.A.; Poncelet, G. ed., 'Preparation of catalysts 11, Elsevier, Amsterdam, **1979**.
- [140] Zhao, X.S.; Bao, X.Y.; Guo, W.; Lee, F.Y. Immobilizing catalysts on porous materials. *Mater. Today*, **2006**, 9, 32-39.

- [141] Weckhuysen, B.M.; Keller, D.E. Chemistry, spectroscopy and the role of supported vanadium oxides in heterogeneous catalysis. *Catal. Today*, **2003**, 78, 25-46.
- [142] Bulushev, D.A.; Kiwi-Minsker, L.; Renken, A. Vanadia/titania catalysts for gas phase partial toluene oxidation spectroscopic characterisation and transient kinetics study. *Catal. Today*, **2000**, 57, 231-239.
- [143] Cedenõ, L.; Hernandez, E.; Pedraza, F.; Murrieta, F. Oxidative desulfurization of synthetic diesel using supported catalysts: Part I. Study of the operation conditions with a vanadium oxide based catalyst. *Catal. Today*, **2005**, 107, 564-569.
- [144] Gregori, F.; Nobili, I.; Bigi, F.; Maggi, R.; Predieri, G.; Sartori, G. Selective oxidation of sulfides to sulfoxides and sulfones using 30% aqueous hydrogen peroxide and silica-vanadia catalyst. *J. Mol. Catal. A: Chem.*, **2008**, 286, 124-127.
- [145] Cedenõ, L.C.; Navarro, J.F.A.; Gutierrez-Alejandre, A. Oxidative desulfurization of synthetic diesel using supported catalysts: Part II. Effect of oxidant and nitrogen-compounds on extraction-oxidation process. *Catal. Today*, **2006**, 116, 562-568.
- [146] José, L.G.G.; Gustavo, A. F.; Maria, E.; Hernández, T.; Florentino, M.; Juan, N.; Federico, J.C.; Ultra-deep oxidative desulfurization of diesel fuel with H<sub>2</sub>O<sub>2</sub> catalysed under mild conditions by polymolybdates supported on Al<sub>2</sub>O<sub>3</sub>. *Appl. Catal., A*, **2006**, 305, 15-20.
- [147] Maurya, M.R.; Arya, A.; Kumar, U.; Kumar, A.; Avecilla, F.; Pessoa, J.C. Polymer-bound oxidovanadium(IV) and dioxidovanadium(V) complexes: synthesis, characterization and catalytic application for the hydroamination of styrene and vinyl pyridine. *Dalton Trans.*, **2009**, 9555-9566.
- [148] Maurya, M.R.; Arya, A.; Kumarand, A.; Pessoa, J.C. Polystyrene bound oxidovanadium(IV) and dioxidovanadium(V) complexes of histamine derived ligand for the oxidation of methyl phenyl sulfide, diphenyl sulfide and benzoin. *Dalton Trans.*, **2009**, 2185-2195.

- [149] Maurya, M.R.; Kumar, M.; Kumar, A.; Pessoa, J.C. Oxidation of p-chlorotoluene and cyclohexene catalysed by polymer-anchored oxidovanadium(IV) and copper(II) complexes of amino acid derived tridentate ligands. *Dalton Trans.*, **2008**, 4220-4232.
- [150] Moad, G.; Solomon, D. H. The chemistry of free radical polymerization; Pergamon: Oxford; **1995**.
- [151] Harwood, L.M.; Moody, C.J. The practical approach in chemistry series, edited by Davis, F.J. Oxford University press, Great Britain, **2004**, p 43.
- [152] Alfrey, T., Jr. In copolymerisation; Ham, G. E., ed., Wiley: New York; **1964**.
- [153] Mayo, F.R.; Walling, C. Copolymerization. *Chem. Rev.*, **1950**, 46, 191-287.
- [154] Perrin, D.D.; Armarego, W. L. F. Purification of laboratory chemicals, 3<sup>rd</sup> edn. Pergamon Press: Oxford; **1988**.
- [155] Furniss, B.S.; Hannaford, A.J.; Smith, P.W.G.; Tatchell, A.R. Vogels's textbook of practical organic chemistry, 5th edn; Longman Scientific: Essex, UK; **1988**.
- [156] Casey, M.; Leonard, J.; Lygo, B.; Proctor, G. Advanced practical organic chemistry; Blackie: Glasgow; **1990**.
- [157] Canali, L.; Sherrington, D.C. Utilisation of homogeneous and supported chiral metal (salen) complexes in asymmetric catalysis. *Chem. Soc. Rev.*, **1999**, 28, 85-93.
- [158] Sherrington, D.C. Preparation, structure and morphology of polymer supports. *Chem. Commun.* **1998**, 2275-2286.
- [159] Lettieri, T.R.A.; Hartman, W.; Hembree, G.G.; Marx, E. Certification of SRM1960: Nominal 10  $\mu\text{m}$  diameter polystyrene spheres ("Space Microspheres"). *J. Res. Natl. Inst. Stand. Technol.*, **1991**, 96, 669-691.
- [160] Okay, O. Macroporous copolymer networks. *Prog. Polym. Sci.*, **2000**, 25, 711-779.
- [161] Benes. M.J.; Horak. D.; Svec. F. Methacrylate-based chromatographic media. *J. Sep. Sci.*, **2005**, 28, 1855-1875.

- [162] Arshady, R. Suspension, emulsion, and dispersion polymerization: a methodological survey. *Colloid Polym Sci.*, **1992**, 270, 717-732.
- [163] Serra, C.A.; Chang, Z. Microfluidic-assisted synthesis of polymer particles. *Chem. Eng. Technol.*, 2008, 31, 1099-1115.
- [164] Steinbacher, J.L.; McQuade, D.T. Polymer chemistry in flow: new polymers, microspheres, capsules, and fibers. *J. Polym. Sci. Part A: Polym. Chem.*, **2006**, 44, 6505-6533.
- [165] Dendukuri, D.; Doyle, P.S. The synthesis and assembly of polymeric microparticles using microfluidics. *Adv. Mater.*, **2009**, 21, 4071-4086.
- [166] Yan, M.; Ramstrom, O.; Dekker, M. Molecularly Imprinted Materials. *Science and Technology*, New York, **2005**.
- [167] Antonietti, M.; Tauer, K. 90 years of polymer latexes and heterophase polymerization: more vital than ever. *Macromol. Chem. Phys.* **2003**, 204, 207-219.
- [168] Zhang, J.L.; Han, B.X.; Zhang, C.X.; Li, W.; Feng, X.Y. Nanoemulsions induced by compressed gases. *Angew. Chem. Int. Ed.*, **2008**, 47, 3012-3015.
- [169] Li, W.H.; Stover, H.D.H. Porous monodisperse poly(divinylbenzene) microspheres by precipitation polymerization. *J. Polym. Sci Part A: Polym Chem.*, **1998**, 36, 1543-1551.
- [170] Li W.H.; Stover, H.D.H. Monodisperse cross-linked core-shell polymer microspheres by precipitation polymerization. *Macromolecules*, **2000**, 33, 4354-4360.
- [171] Saraçoğlu, B.; Ügüzdöğün, E.; Gölgeçlioğlu, C.; Tuncel, A. Synthesis of monodisperse glycerol dimethacrylate-based microgel particles by precipitation polymerization. *Ind. Eng. Chem. Res.*, **2009**, 48, 4844-4851.
- [172] Lai, J.P.; Yang, M.L.; Niessner, R.; Knopp, D. Molecularly imprinted microspheres and nanospheres for di(2-ethylhexyl)phthalate prepared by precipitation polymerization. *Anal. Bioanal. Chem.*, **2007**, 389, 405-412.

- [173] Watanabe, S.; Kobayashi, T.; Sumitomo, H.; Murata, M.; Masuda, Y. Preparation of monodisperse PMMA particles by dispersion polymerization of MMA using poly(styrene-co-methacrylic acid) copolymer as a steric stabilizer. *Polym. Bull.*, **2010**, 65, 543-550.
- [174] Minami, H.; Kimura, A.; Kinoshita, K.; Okubo, M.; Preparation of poly(acrylic acid) particles by dispersion polymerization in an ionic liquid. *Langmuir*, **2010**, 26, 6303-6307.
- [175] Kim, O.H.; Lee, K.; Kim, K.; Lee, B.H.; Choe, S. Effect of PVA in dispersion polymerization of MMA. *Polymer*, **2006**, 47, 1953-1959.
- [176] Kawaguchi, S.; Ito, K. Dispersion polymerization. *Adv. Polym. Sci.*, **2005**, 175, 299-328.
- [177] Kita, R.; Svec, F.; Frechet, J.M.J. Hydrophilic polymer supports for solid phase synthesis: preparation of poly(ethylene glycol) methacrylate polymer microspheres using “classical” suspension polymerization in aqueous medium and their application in the solid-phase synthesis of hydantoins. *J. Comb. Chem.*, **2001**, 3, 564-571.
- [178] Gokmen, M.T.; Du Prez, F.E. Porous polymer particles-a comprehensive guide to synthesis, characterization, functionalization and applications. *Prog. Polym. Sci.*, **2012**, 37, 365-405.
- [179] Ondarçuhu, T.; Joachim, C. Drawing a single nanofibre over hundreds of microns. *Europhys. Lett.*, **1998**, 42, 215-220.
- [180] Martin, C.R. Membrane-based synthesis of nanomaterials. *Chem. Mater.*, **1996**, 8, 1739-1746.
- [181] Feng, L.; Li, S.; Li, H.; Zhai, J.; Song, Y.; Jiang, L.; Zhu, D. Super-hydrophobic surface of aligned polyacrylonitrile nanofibers. *Angew. Chem. Int. Ed.*, **2002**, 41, 1221-1223.
- [182] Ma, P.X.; Zhang, R. Synthetic nano-scale fibrous extracellular matrix. *J. Biomed. Mater. Res.*, **1999**, 46, 60-72.
- [183] Liu, G.; Qiao, L.; Guo, A. Diblock copolymer nanofibers. *Macromolecules*, **1996**, 29, 5508-5510.
- [184] He, J.H.; Liu, Y.; Mo, L.F.; Wan, Y.Q.; Xu, L. Electrospun nanofibers and their applications; iSmithers: Shopshire, **2008**.



- [185] Subbiah, T.; Bhat, G.S.; Tock, R.W.; Parameswaran, S.; and Ramkumar, S.S. Electrospinning of nanofibers. *J. Appl. Polym. Sci.*, **2005**, 96, 557-569.
- [186] Huang, Z.M.; Zhang, Y.Z.; Kotaki, M.; Ramakrishna, S. A review on polymer nanofibers by electrospinning and their applications in nanocomposites. *Compos. Sci. Technol.*, **2003**, 63, 2223-2253.
- [187] Walmsley, R.S.; Ogunlaja, A.S.; Coombes, M.J.; Chidawanyika, W.; Litwinski, C.; Torto, N.; Nyokong, T.; Tshentu, Z.R. Imidazole-functionalized polymer microspheres and fibers – useful materials for immobilization of oxovanadium(IV) catalysts. *J. Mater. Chem.*, **2012**, 22, 5792-5800.
- [188] Cooley, J. F. Apparatus for electrically dispersing fluids, US Patent number 692631, **1902**.
- [189] Reneker, D.H.; Chun, I. Nanometre diameter fibres of polymer, produced by electrospinning. *Nanotechnology*, **1996**, 7, 216-223.
- [190] Doshi, J.; Reneker, D.H. Electrospinning process and applications of electrospun fibers. *J. Electrostat.*, **1995**, 35, 151-160.
- [191] Dzenis, Y. Spinning continuous fibers for nanotechnology. *Science*, **2004**, 304, 1917-1919.
- [192] Kumar, A. Nanofibers, Intech: Vukovar, **2010**.
- [193] Pham, Q.P.; Sharma, U.; Mikos, A.G. Electrospinning of polymeric nanofibers for tissue engineering applications: A review tissue engineering. *Tissue Eng.*, **2006**, 12 (5), 1197-1210.
- [194] Ki, C.S.; Baek, D.H.; Gang, K.D.; Lee, K.H.; Um, I.C.; Park, Y.H. Characterization of gelatin nanofiber prepared from gelatin-formic acid solution. *Polymer*, **2005**, 46, 5094-5102.
- [195] Jiang, H.L.; Fang, D.F.; Hsiao, B.S.; Chu, B.; Chen, W.L. Optimization and characterization of dextran membranes prepared by electrospinning. *Biomacromolecules*, **2004**, 5, 326-333.
- [196] Huang, L.; Nagapudi, K.; Apkarian, R.P.; Chaikof, E.L. Engineered collagen-PEO nanofibers and fabrics. *J. Biomater. Sci. Polym. Ed.*, **2001**, 12, 979-993.

- [197] Son, W.K.; Youk, J.H.; Lee, T.S.; Park, W.H. The effects of solution properties and polyelectrolyte on electrospinning of ultrafine poly(ethylene oxide) fibers. *Polymer*, **2004**, 45, 2959-2966.
- [198] Fong, H.; Chun, I.; Reneker, D.H. Beaded nanofibers formed during electrospinning. *Polymer*, **1999**, 40, 4585-4592.
- [199] Koski, A.; Yim, K.; Shivkumar, S. Effect of molecular weight on fibrous PVA produced by electrospinning. *Mater. Lett.*, **2004**, 58, 493-497.
- [200] Zhang, C.X.; Yuan, X.Y.; Wu, L.L.; Han, Y.; Sheng, J. Study on morphology of electrospun poly(vinyl alcohol) mats. *Eur. Polym. J.*, **2005**, 41, 423-432.
- [201] Lee, J.S.; Choi, K.H.; Do Ghim, H.; Kim, S.S.; Chun, D.H.; Kim, H.Y.; Lyoo, W.S. Role of molecular weight of a tactic poly(vinyl alcohol) (PVA) in the structure and properties of PVA nanofabric prepared by electrospinning. *J. Appl. Polym. Sci.*, **2004**, 94, 1638-1646.
- [202] Ding, B.; Kim, H.Y.; Lee, S.C.; Shao, C.L.; Lee, D.R.; Park, S.J.; Kwag, G.B.; Choi, K.J. Preparation and characterization of a nanoscale poly(vinyl alcohol) fiber aggregate produced by an electrospinning method. *J. Polym. Sci. B-Polym. Phys.*, **2002**, 40, 1261-1268.
- [203] Release, J.C.; Cha, D.I.; Kim, H.Y.; Lee, K.H.; Jung, Y.C.; Cho, J.W.; Chun, B.C. Electrospun nonwovens of shape-memory polyurethane block copolymers. *J. Appl. Polym. Sci.*, **2005**, 96, 460-465.
- [204] Demir, M.M.; Yilgor, I.; Yilgor, E.; Erman, B. Electrospinning of polyurethane fibers. *Polymer*, **2002**, 43, 3303-3309.
- [205] Mit-Uppatham, C.; Nithitanakul, M.; Supaphol, P. Ultrafine electrospun polyamide-6 fibers: effect of solution conditions on morphology and average fiber diameter. *Macromol. Chem. Phys.*, **2004**, 205, 2327-2338.
- [206] Chen, H.; Hsieh, Y.L. Ultrafine hydrogel fibers with dual temperature- and pH-responsive swelling behaviors. *J. Polym. Sci. A. Polym. Chem.*, **2004**, 42, 6331-6339.

- [207] Jun, Z.; Hou, H.Q.; Schaper, A.; Wendorff, J.H.; Greiner, A. Poly-L-lactide nanofibers by electrospinning– influence of solution viscosity and electrical conductivity on fiber diameter and fiber morphology. *E-Polymers*, **2003**, 9, 1-9.
- [208] Buchko, C.J.; Chen, L.C.; Shen, Y.; Martin, D.C. Processing and microstructural characterization of porous biocompatible protein polymer thin films. *Polymer*, **1999**, 40, 7397-7407.
- [209] Ryu, Y.J.; Kim, H.Y.; Lee, K.H.; Park, H.C.; Lee, D.R. Transport properties of electrospun nylon 6 nonwoven mats. *Eur. Polym. J.*, **2003**, 39, 1883-1889.
- [210] Lin, T.; Wang, H.X.; Wang, H.M.; Wang, X.G. The charge effect of cationic surfactants on the elimination of fibre microspheres in the electrospinning of polystyrene. *Nanotechnology*, **2004**, 15, 1375-1381.
- [211] Liu, J.; Kumar, S. Microscopic polymer cups by electrospinning. *Polymer*, **2005**, 46, 3211-3214.
- [212] Zuo, W.W.; Zhu, M.F.; Yang, W.; Yu, H.; Chen, Y.M.; Zhang, Y. Experimental study on relationship between jet instability and formation of beaded fibers during electrospinning. *Polym. Eng. Sci.*, **2005**, 45, 704-709.
- [213] Gupta, P.; Elkins, C.; Long, T.E.; Wilkes, G.L. Electrospinning of linear homopolymers of poly(methyl methacrylate): exploring relationships between fiber formation, viscosity, molecular weight and concentration in a good solvent. *Polymer*, **2005**, 46, 4799-4810.
- [214] Duan, B.; Dong, C.H.; Yuan, X.Y.; Yao, K.D. Electrospinning of chitosan solutions in acetic acid with poly(ethylene oxide). *J. Biomater. Sci. Polym. Ed.*, **2004**, 15, 797-811.
- [215] Jarusuwannapoom, T.; Hongroijanawiwat, W.; Jitjaicham, S.; Wannatong, L.; Nithitanakul, M.; Pattamaprom, C.; Koombhongse, P.; Rangkupan, R.; Supaphol, P. Effect of solvents on electro-spinnability of polystyrene solutions and morphological appearance of resulting electrospun polystyrene fibers. *Eur. Polym. J.*, **2005**, 41, 409-421.

- [216] Wannatong, L.; Sirivat, A.; Supaphol, P. Effects of solvents on electrospun polymeric fibers: preliminary study on polystyrene. *Polym. Int.*, **2004**, 53, 1851-1859.
- [217] Zong, X.H.; Kim, K.; Fang, D.F.; Ran, S.F.; Hsiao, B.S.; Chu, B. Structure and process relationship of electrospun bioabsorbable nanofiber membranes. *Polymer*, **2002**, 43, 4403-4412.
- [218] Yuan, X.Y.; Zhang, Y.Y.; Dong, C.H.; Sheng, J. Morphology of ultrafine polysulfone fibers prepared by electrospinning. *Polym. Int.*, **2004**, 53, 1704-1710.
- [219] Kim, H.S.; Kim, K.; Jin, H.J.; Chin, I.J. Morphological characterization of electrospun nanofibrous membranes of biodegradable poly(L-lactide) and poly(lactide-co-glycolide). *Macromol. Symp.*, **2005**, 224, 145-154.
- [220] Walmsley, R.S.; Hlangothi, P.; Litwinski, C.; Torto, N.; Nyokong, T.; Tshentu, Z.R. Catalytic oxidation of thioanisole using oxovanadium(IV)-functionalized electrospun polybenzimidazole nanofibers. *J. Appl. Polym. Sci.*, **2012**, 127(6), 4719-4725.
- [221] Shin, Y.M.; Hohman, M.M.; Brenner, M.P.; Rutledge, G.C. Experimental characterization of electrospinning: the electrically forced jet and instabilities. *Polymer*, **2001**, 42, 9955-9965.
- [222] Katta, P.; Alessandro, M.; Ramsier, R.D.; Chase, G.G. Continuous electrospinning of aligned polymer nanofibers onto a wire drum collector. *Nano. Lett.*, **2004**, 4, 2215-2218.
- [223] Sundaray, B.; Subramanian, V.; Natarajan, T.S.; Xiang, R.Z.; Chang, C.C.; Fann, W.S. Electrospinning of continuous aligned polymer fibers. *Appl. Phys. Lett.*, **2004**, 84, 1222-1224.
- [224] Theron, A.; Zussman, E.; Yarin, A.L. Electrostatic field-assisted alignment of electrospun nanofibers. *Nanotechnology*, **2001**, 12, 384-390.
- [225] Casper, C.L.; Stephens, J.S.; Tassi, N.G.; Chase, D.B.; and Rabolt, J.F. Controlling surface morphology of electrospun polystyrene fibers: effect of humidity and molecular weight in the electrospinning process. *Macromolecules*, **2004**, 37, 573-578.

- [226] Polyakov, M.V. Adsorption properties and structure of silica gel. *Zhur. Fiz. Khim.*, **1931**, 2, 799-805.
- [227] Polyakov, M.V.; Stadnik, P.; Paryckij, M.; Malkin, I.; Duchina, F. On the structure of silica. *Zhur. Fiz. Khim.*, **1933**, 4, 454-456.
- [228] Polyakov, M.V.; Kuleshina, L.; Neimark, I. On the dependence of silica gel adsorption properties on the character of its porosity. *Zhur. Fiz. Khim.*, **1937**, 10, 100-112.
- [229] Ekberg, B.; Mosbach, K. Molecular imprinting-a technique for producing specific separation materials. *Trends Biotechnol.*, **1989**, 7, 92-96.
- [230] Sellergren, B.; Nilsson, K.G.I. Molecular imprinting by multiple noncovalent host-guest interactions: synthetic polymers with induced specificity methods. *Mol. Cell Biol.*, **1989**, 31, 59-62.
- [231] Arshady, R. Functional monomers. *J. Macromo. Sci.-Rev. Macromol. Chem. Phys.*, **1992**, C32, 101-132.
- [232] Dandekar, T.; Argos, P. Drug assay using antibody mimics made by molecular imprinting. *Chemtracts. Biochem. Mol. Biol.*, **1993**, 4, 75-76.
- [233] Wulff, G. Molecular imprinting in synthetic-polymers-models for the receptor-site in enzymes. *Makromol. Chem. Macromol. Symp.*, **1993**, 70(1), 285-288.
- [234] Wulff, G. The role of binding-site interactions in the molecular imprinting of polymers. *Trends Biotechnol.*, **1993**, 11, 85-87.
- [235] Mosbach, K. Molecular imprinting. *Trends Biochem. Sci.*, **1994**, 19, 9-14.
- [236] Holmes, A.B.; Stephenson, G.R. Molecular imprinting. *Chem. Ind.*, **1994**, 18, 304.
- [237] Shea, K.J. Molecular imprinting of synthetic network polymers: synthesis of macromolecular binding and catalytic sites. *Trends Polym. Sci.*, **1994**, 2, 166-173.

- [238] Nicholls, I.A.; Andersson, L.I.; Mosbach, K.; Ekberg, B. Recognition and enantioselection of drugs and biochemical using molecularly imprinted polymer technology. *Trends Biotechnol.*, **1995**, 13, 47-51.
- [239] Kempe, M.; Mosbach, K. Molecular imprinting used for chiral separations. *J. Chromatogr. A*, **1995**, 694, 3-13.
- [240] Ansell, R.; Mosbach, K. Molecularly imprinted polymers-new tools for biomedical science. *Pharmaceut. News*, **1995**, 3, 16-20.
- [241] Steinke, J.; Sherrington, D.C.; Dunkin, I.R. Imprinting of synthetic polymers using molecular templates. *Adv. Polym. Sci.*, **1995**, 123, 81-125.
- [242] Holliger, P.; Hoogenboom, H. Artificial antibodies and enzymes: mimicking nature and beyond. *Trends Biotechnol.*, **1995**, 13, 7-9.
- [243] Wulff, G. Molecular imprinting in cross-linked materials with the aid of molecular templates-a way towards artificial antibodies. *Angew. Chem., Intl. Ed.*, **1995**, 34, 1812-1832.
- [244] Mosbach, K.; Ramström, O. The emerging technique of molecular imprinting and its future impact on biotechnology. *Bio/Technology*, **1996**, 14, 163-170.
- [245] Andersson, L.I.; Nicholls, I.A.; Mosbach, K. In biochemical technology, Part B, Advances in molecular and cell biology, Vol. 15B, Danielsson B, Bulow L (eds). Elsevier: Amsterdam, **1996**, p 651-670.
- [246] Muldoon, M.T.; Stanker, L.H. Plastic antibodies: molecularly- imprinted polymers. *Chem. Ind.*, **1996**, 204-207.
- [247] Takeuchi, T.; Matsui, J. Molecular imprinting: an approach to 'tailor-made' synthetic polymers with biomimetic functions. *Acta. Polym.*, **1996**, 47, 471-480.
- [248] Wulff, G. Molecular imprinting in crosslinked polymers-The role of the binding sites. *Mol. Cryst. Liq. Cryst.*, **1996**, 276, 1-6.

- [249] Mayes, A.G.; Mosbach, K. Molecularly imprinted polymers: useful materials for analytical chemistry. *TrAC Trends Anal. Chem.*, **1997**, 16, 321-332.
- [250] Muldoon, M.T.; Stanker, L.H. In immunochemical technology for environmental applications, ACS symposium series, Vol. 657, Aga DS, Thurman EM (eds). The American Chemical Society: Washington, DC, **1997**, p 314-330.
- [251] Murray, G.M.; Fish, R.H. Chemical slippers. *New Scientist*, **1997**, 34-37.
- [252] Andersson, H.S.; Nicholls, I.A. Molecular imprinting: recent innovations in synthetic polymer receptor and enzyme mimics. *Recent Res. Dev. Pure Appl. Chem.*, **1997**, 1, 133-157.
- [253] Sellergren, B. Imprinted polymers: stable, reusable antibody-mimics for highly selective separations. *Am. Lab*, **1997**, 29, 10A-10F.
- [254] Vulfson, E.N.; Alexander, C.; Whitcombe, M.J. Assembling the molecular cast. *Chem. Brit.*, **1997**, 33, 23-26.
- [255] Whitcombe, M.J.; Alexander, C.; Vulfson, E.N. Smart polymers for the food industry. *Trends Food Sci. Technol.*, **1997**, 8, 140-145.
- [256] Ramström, O.; Ansell, R.J. Molecular imprinting technology: challenges and prospects for the future. *Chirality*, **1998**, 10, 195-209.
- [257] Rimmer, S. Synthesis of molecular imprinted polymer networks. *Chromatographia*, **1998**, 47, 470-474.
- [258] Cormack, P.; Mosbach, K. Molecularly imprinted polymers for application in chemical analysis. *Am. Biotechnol.*, **1998**, 16, 47-48.
- [259] Wulff, G. Fitting molecules into polymeric receptors. *Chemtech.*, 1998, 28, 19-26.
- [260] Cormack, P.A.G.; Mosbach, K. Molecular imprinting: recent developments and the road ahead. *Reac. Func. Polym.*, **1999**, 41, 115-124.
- [261] Ensing, K.; deBoer, T. Tailor-made materials for tailor-made applications: application of molecular imprints in chemical analysis. *TrAC Trends Anal. Chem.*, **1999**, 18, 138-145.

- [262] Ratner, B.D.; Shi, H.Q. Recognition templates for biomaterials with engineered bioreactivity. *Curr. Opin. Solid State Mater. Sci.*, **1999**, 4, 395-402.
- [263] Chesnut, D.J.; Hagrman, D.; Zapf, P.J.; Hammond, R.P.; LaDuca, R.; Haushalter, R.C.; Zubieta, J. Organic/inorganic composite materials: the roles of organoamine ligands in the design of inorganic solids. *Coord. Chem. Rev.*, **1999**, 190-192, 737-769.
- [264] Brüggemann, O.; Haupt, K.; Ye, L.; Yilmaz, E.; Mosbach, K. New configurations and applications of molecularly imprinted polymers. *J. Chromatogr. A*, **2000**, 889, 15-24.
- [265] Dickert, F.L.; Hayden, O. Molecular fingerprints using imprinting techniques. *Adv. Mater.*, **2000**, 12, 311-314.
- [266] Asanuma, H.; Hishiya, T.; Komiyama, M. Tailor-made receptors by molecular imprinting. *Adv. Mater.*, **2000**, 12, 1019-1030.
- [267] Oral, E.; Peppas, N.A. Molecular imprinting in biological systems. *Stp. Pharma. Sciences*, **2000**, 10, 261-267.
- [268] Piletsky, S.A.; Alcock, S.; Turner, A.P.F. Molecular imprinting: at the edge of the third millennium. *Trends Biotechnol.*, **2001**, 19, 9-12.
- [269] Hentze, H.P.; Antonietti, M. Template synthesis of porous organic polymers. *Curr. Opin. Solid State Mater. Sci.*, **2001**, 5, 343-353.
- [270] Mosbach, K. Toward the next generation of molecular imprinting with emphasis on the formation, by direct molding, of compounds with biological activity (biomimetics). *Anal. Chim. Acta.*, **2001**, 435, 3-8.
- [271] Haupt, K.; Fradet, A. Molecularly imprinted polymers: concept and applications. *Actualité Chimique*, **2001**, 23-32.
- [272] Whitcombe, M.J.; Vulfson, E.N. Imprinted polymers. *Adv. Mater.*, **2001**, 13, 467-478.
- [273] Haupt, K. Creating a good impression. *Nat. Biotechnol.*, **2002**, 20, 884-885.



- [274] Spégel, P.; Schweitz, L.; Nilsson, S. Molecularly imprinted polymers. *Anal. Bioanal. Chem.*, **2002**, 372, 37-38.
- [275] Davidson, L.; Hayes, W. Molecular imprinting of biologically active steroidal systems. *Curr. Org. Chem.*, **2002**, 6, 265-281.
- [276] Shi, R.X.; Guo, C.H.; Zou, X.H.; Zhu, C.Y.; Zuo, Y.J.; Deng, Y.D. The development of research in molecular imprinting technique. *Prog. Chem.*, **2002**, 14, 182-191.
- [277] Haupt, K. Molecularly imprinted polymers: the next generation. *Anal. Chem.*, **2003**, 75: 376A-383A.
- [278] Striegler, S. Selective carbohydrate recognition by synthetic receptors in aqueous solution. *Curr. Org. Chem.*, **2003**, 7, 81-102.
- [279] Batra, D.; Shea, K.J. Combinatorial methods in molecular imprinting. *Curr. Opin. Chem. Biol.*, **2003**, 7, 434-442.
- [280] Bartels, H.; Prijs, B. Specifically adsorbing silica gel. *Adv. Chromatogr.*, **1974**, 11, 115-143.
- [281] Wulff, G.; Sarhan, A. In chemical approaches to understanding enzyme catalysis: Biomimetic chemistry and transition-state analogs, Green BS, Ashani Y, Chipman D (eds). Elsevier: Amsterdam; **1982**, p 106-118.
- [282] Wulff, G. In Polymeric reagents and catalysts, ACS symposium series, Vol. 308, Ford WT(ed.). The American Chemical Society: Washington, DC; **1986**, p 186-230.
- [283] Deng, G.; Markowitz, M.A.; Kust, P.R.; Gaber, B.P. Control of surface expression of functional groups on silica particles. *Mater. Sci. Eng.*, **2000**, C 11, 165-172.
- [284] Markowitz, M.A.; Deng, G.; Gaber, B.P. Effects of added organosilanes on the formation and adsorption properties of silicates surface-imprinted with an organophosphonate. *Langmuir*, **2000**, 16, 6148-6155.
- [285] Pérez-Moral, N.; Mayes, A.G. In molecularly imprinted materials-sensors and Other devices, MRS symposium proceedings, Vol. 723, Shea, K.J.; Yan, M.; Roberts, M.J.; Cremer, P.S.;

- Crooks, R.M.; Sailor, M.J. (eds). Materials Research Society: Warrendale, Pennsylvania; **2002**, p 61-66.
- [286] Matsui, J.; Miyoshi, Y.; Matsui, R.; Takeuchi, T. Rod-type affinity media for liquid-chromatography prepared by in-situ-molecular imprinting. *Anal. Sci.*, **1995**, 11, 1017-1019.
- [287] Pérez, N.; Whitcombe, M.J.; Vulfson, E.N. Molecularly imprinted nanoparticles prepared by core-shell emulsion polymerization. *J. Appl. Polym. Sci.*, **2000**, 77, 1851-1859.
- [288] Wulff, G.; Vesper, R.; Grobe-Einsler, R.; Sarhan, A. Enzyme-analogue built polymers-4: on the synthesis of polymers containing chiral cavities and their use for the resolution of racemates. *Makromol. Chem.*, **1977**, 178, 2799-2816.
- [289] Yoshizako, K.; Hosoya, K.; Iwakoshi, Y.; Kimata, K.; Tanaka, N. Porogen imprinting effects. *Anal. Chem.*, **1998**, 70, 386-389.
- [290] Svenson, J.; Nicholls, I.A. On the thermal and chemical stability of molecularly imprinted polymers. *Anal. Chim. Acta.*, **2001**, 435, 19-24.
- [291] Mullett, W.M.; Lai, E.P.C. Molecularly imprinted solid phase extraction micro-column with differential pulsed elution for theophylline determination. *Microchem. J.*, **1999**, 61, 143-155.
- [292] Ju, J.Y.; Shin, C.S.; Whitcombe, M.J.; Vulfson, E.N. Imprinted polymers as tools for the recovery of secondary metabolites produced by fermentation. *Biotechnol. Bioeng.*, **1999**, 64, 232-239.
- [293] Alexander, C.; Andersson, H.S.; Andersson, L.I.; Ansell, R.J.; Kirsch, N.; Nicholls, I.A.; O'Mahony, J.; Whitcombe, M.J. Molecular imprinting science and technology: a survey of the literature for the years up to and including 2003. *J. Mol. Recognit.*, **2006**, 19, 106-180.
- [294] Wulff, G.; Dederichs, R.; Grotstollen, R.; Jupe, C. In affinity chromatography and related techniques, Gribnau, T.C.J.; Visser, J.; Nivard, R.J.F. (eds). Elsevier scientific publishing company: Amsterdam; **1982**, p 207-216.

- [295] Wulff, G. Selective binding to polymers *via* covalent bonds-the construction of chiral cavities as specific receptor-sites. *Pure Appl. Chem.*, **1982**, 54, 2093-2102.
- [296] Wulff, G.; Biffis, A. In molecularly imprinted polymers: Man-made mimics of antibodies and their applications in analytical chemistry, techniques and instrumentation in analytical chemistry, Vol. 23, Sellergren, B. (ed.). Elsevier: Amsterdam; **2001**, p 71-111.
- [297] Shea, K.J.; Thompson, E.A. Template synthesis of macromolecules-selective functionalization of an organic polymer. *J. Org. Chem.*, **1978**, 43, 4253-4255.
- [298] Shea, K.J.; Thompson, E.A.; Pandey, S.D.; Beauchamp, P.S. Template synthesis of macromolecules. Synthesis and chemistry of functionalised macroporous polydivinylbenzene. *J. Am. Chem. Soc.*, **1980**, 102, 3149-3155.
- [299] Damen, J.; Neckers, D.C. Stereo-selective synthesis *via* a photochemical template effect. *J. Am. Chem. Soc.*, **1980**, 102, 3265-3267.
- [300] Damen, J.; Neckers, D.C. On the memory of synthesized vinyl polymers for their origins. *Tet. Lett.*, **1980**, 21, 1913-1916.
- [301] Damen, J.; Neckers, D.C. Memory of synthesized vinyl polymers for their origins. *J. Org. Chem.*, **1980**, 45, 1382-1387.
- [302] Arshady, R.; Mosbach, K. Synthesis of substrate selective polymers by host-guest polymerization. *Macromol. Chem. Phys.*, **1981**, 182, 687-692.
- [303] Sellergren, B. Noncovalent molecular imprinting: antibody-like molecular recognition in polymeric network materials. *TrAC Trends Anal. Chem.*, **1997**, 16, 310-320.
- [304] Mosbach, K.; Haupt, K. Some new developments and challenges in non-covalent molecular imprinting technology. *J. Mol. Recogn.*, **1998**, 11, 62-68.
- [305] Sellergren, B. In molecular and ionic recognition with imprinted polymers, ACS symposiumsSeries, Vol. 703, Bartsch RA, Maeda M (eds). The American Chemical Society: Washington, DC; **1998**, p 49-80.

- [306] Sellergren B. In molecularly Imprinted polymers: man-made mimics of antibodies and their applications in analytical chemistry, techniques and instrumentation in analytical chemistry, Vol. 23, Sellergren B (ed.). Elsevier: Amsterdam; **2001**, p 113-184.
- [307] Umpleby, R.J.; Bode, M.; Shimizu, K.D. Measurement of the continuous distribution of binding sites in molecularly imprinted polymers. *Analyst*, **2000**, 125, 1261-1265.
- [308] Wulff, G.; Sarhan, A. The use of polymers with enzyme-analogous structures for the resolution of racemates. *Angew. Chem. Intl. Ed.*, **1972**, 11, 341.
- [309] Lauer, M.; Böhnke, H.; Grotstollen, R.; Salehnia, M.; Wulff, G. On the chemistry of binding-sites-4: on an unusual increase in reactivity of arylboronic acids by neighboring groups. *Chem. Ber. Recl.*, **1985**, 118, 246-260.
- [310] Elementar Analysen Systeme GmbH, CHNS Elemental Analyzer Vario Micro-operating instruction, **2005**.
- [311] Rockenbauer, A.; Korecz, L. Automatic computer simulations of ESR spectra. *Appl. Magn. Reson.*, **1996**, 10, 29-43.
- [312] Fayemi, O.E.; Ogunlaja, A.S.; Kempgens, P.F.M.; Antunes, E.; Torto, N.; Nyokong, T.; Tshentu, Z.R. Adsorption and separation of platinum and palladium by polyamine functionalized polystyrene-based microspheres and nanofibers. *Miner. Eng.*, **2013**, 53, 256-265.
- [313] Standard test method for hydro peroxide number of aviation turbine fuels, gasoline and diesel fuels, ASTM D3703 - 07(**2012**).
- [314] Tshentu, Z.R.; Togo, C.; Walmsley, R.S. Polymer-anchored oxidovanadium(IV) complex for the oxidation of thioanisole, styrene and ethylbenzene. *J. Mol. Cat. A: Chem.*, **2010**, 318, 30-35.
- [315] World Health Organisation, *Reducing Risks, Promoting Healthy Life*, **2002**. (<http://www.who.int/whr/2002/en/>), date accessed: 09/09/2013.

- [316] World Health Organisation, *Effects of Air Pollution on Children's Health and; World Health Organisation*, WHO Air quality guideline for particulate matter, ozone, nitrogen dioxide, and sulfur dioxide, global update, **2005**. (<http://www.who.int/phe/air/aqg2006execsum.pdf>), date accessed: 09/09/2013.
- [317] Royston, H.F.; Gary, J.V.B. Geochemistry of metal complexes in petroleum, source rocks and coals. *American Chemical Society*, **1987**, 2-16.
- [318] Slotvinskii-Sidak N.P.; Andreev, V.K. Vanadium in the nature and technics. *Moscow*, **1979**, 10-24.
- [319] NRC, *Oil in the Sea: Inputs, Fates, and Effects*. National research council, National Academy Press, Washington, DC, **1985**.
- [320] Douglas, G.S.; Uhler, A.D. Optimizing EPA methods for petroleum-contaminated site assessments. *Environmental Testing and Analysis* May/June: **1993**, 1-6.
- [321] Christopher, M.R.; James G.Q. GC-MS analysis of total petroleum hydrocarbons and polycyclic aromatic hydrocarbons in seawater samples after the North Cape oil spill. *Mar. Pollut. Bull.*, **1999**, 38 (2), 126-135.
- [322] Douglas, G.S.; Bence, A.E.; Prince, R.C.; McMillen, S.J.; Butler, E.L. Environmental stability of selected petroleum source and weathering ratios. *Environ. Sci. Technol.*, **1996**, 30, 2332-2339.
- [323] Elirich, J.; Hirner, A.V.; Stark, H. Distribution of trace elements in crude oils from southern Germany. *Chem. Geol.*, **1985**, 48, 313-323.
- [324] Onojake, M.C.; Oforka N.C.; Osuji L.C. Trace metals geochemistry of crude oils from Umutu/Bomu fields in South West Niger Delta Nigeria. *Energy and Environment Research (EER)*., **2011**, 1, 139-146.

- [325] Oluwole, A.F.; Asubiojo, O.I.; Nwachukwu, J.I.; Ojo, J.A.; Ogunsola, A.; Filby, R.; Fitzgerald, S.; Grimmy, C. Neutron activation analysis of Nigerian crude oil. *J. Radioanal. Nuclear Chem.*, **1993**, 168 (1), 145-152.
- [326] Barwise, A.J.G. Role of nickel and vanadium in petroleum classification. *Energy Fuels*, **1990**, 4, 647-652.
- [327] Henry, E.K.; George, E.M. Analysis of petroleum for trace metals (I): Determination of Hg in petroleum oils and petroleum products. *Anal. Chem.*, **1975**, 47, 1263-1268.
- [328] Al-Swaidan, H.M. The determination of lead, nickel and vanadium in Saudi Arabian crude oil by sequential injection analysis/inductively coupled plasma-mass spectrometry. *Talanta*, **1996**, 43 (8), 1313-1319.
- [329] Akinlua, A.; Torto, N.; Ajayi, T.R. Determination of rare earth elements in Niger Delta crude oils by inductively coupled plasma-mass spectrometry. *Fuel*, **2008**, 87, 1469-1477.
- [330] Odebunmi, E.O.; Adeniyi, S.A. Characterization of crude oil and petroleum products for trace elements. *J. Chem. Soc. Nigeria*, **2004**, 29 (2), 149-154.
- [331] Olajire, A.A.; Oderinde, R.A. Trace metals in Nigerian crude oils and their heavy-end distillates. *Bull. Chem. Soc. Jpn.*, **1993**, 66, 1-3.
- [332] Boukir, A.; Aries, E.; Guiliano, M.; Asia, L.; Doumenq, P.; Mille, G. Subfractionation, characterization and photo-oxidation of crude oil resin. *Chemosphere*, **2001**, 43, 279-286.
- [333] Li, M.; Xu, M.; Ma, Y.; Wu, Z.; Christy, A.A. The effect of molecular parameters on the stability of water-in-crude oil emulsions studied by IR and UV spectroscopy. *Colloids Surf., A*, **2002**, 197, 193-201.
- [334] Jewell, D.M.; Weber, J.H.; Bungler, J.W.; Plancher, H.; Latham, D.R. Ion-exchange, coordination, and adsorption chromatographic separation of heavy-end petroleum distillates. *Anal. Chem.*, **1972**, 44, 1391-1395.

- [335] Ogunlaja, A.S.; Alade, O.S.; Odeunmi, E.O.; Majavu, A.; Torto, N.; Tshentu, Z.R. The ratios of vanadium-to-nickel and phenanthrene-to-dibenzothiophene as means of identifying petroleum source and classification of Nigeria crude oils. *Pet. Sci. Technol.*, **2013**, DOI: 10.1080/10916466.2013.795970.
- [336] Shi, Q.; Hou, D.; Chung, K.H.; Xu, C.; Zhao, S.; Zhang, Y. Characterization of heteroatoms in a crude oil and its saturates, aromatics, resins, and asphaltenes (SARA) and non-basic nitrogen fractions analysed by negative-ion electrospray fourier transform ion cyclotron resonance mass spectrometry. *Energy Fuels*, **2010**, *24*, 2545-2553.
- [337] Coates, J. Interpretation of infrared spectra, a practical approach, Meyers R.A. (Ed.) John Wiley & Sons Ltd, Chichester, **2000**, 10815-10837.
- [338] Gao, Y.Y.; Shen, B.X.; Liu, J.C. The structure identification of vanadium porphyrins in Venezuela crude oil. *Energy Sources Part A*, **2012**, *34*(24), 2260-2267.
- [339] Matava, T.; Rooney, M.A.; Chung, H.M.; Nwachukwu, B.C.; Unomah, G.I. Migration effects on the composition of hydrocarbon accumulations in the OML 67–70 areas of the Niger Delta. *AAPG Bull.*, **2003**, *87* (7), 1193-206.
- [340] Peters, K.E.; Walters, C.C.; Moldown, J.M. The Biomarker Guide; Cambridge University Press: Cambridge, U.K., **2005**, Vol. 2.
- [341] Ma, X.; Sakanishi, k.; Mochida, I. Hydrodesulfurization reactivities of various sulfur compounds in vacuum gas oil. *Ind. Eng. Chem. Res.*, **1996**, *35*, 2487-2494.
- [342] Ma, X.; Sakanishi, K.; Mochida, I. Hydrodesulfurization reactivities of various sulfur compounds in diesel fuel. *Ind. Eng. Chem. Res.*, **1994**, *33*, 218-222.
- [343] Ma, X.; Sakanishi, K.; Isoda, T.; Mochida, I. Quantum chemical calculation on the desulfurization reactivities of heterocyclic sulfur compounds. *Energy Fuels*, **1995**, *9*, 33-37.

- [344] William, B.H.; Albert, G.H.; Leon, I.P.D. The ratios of dibenzothiophene to phenanthrene and pristane to phytane as indicators of depositional environment and lithology of petroleum source rocks. *Geochim. Cosmochim. Acta.*, **1995**, 59 (17), 3581-3598.
- [345] Maurya, M.R.; Bisht, M.; Kumar, A.; Kuznetsov, M.L.; Avecilla, F.; Pessoa, J.C. Synthesis, characterization, reactivity and catalytic activity of oxidovanadium(IV), oxidovanadium(V) and dioxidovanadium(V) complexes of benzimidazole modified ligands. *Dalton Trans.*, **2011**, 40, 6968-6983.
- [346] Maurya, M.R.; Kumar, A.; Ebel, M.; Rehder, D. Synthesis, characterization, reactivity, and catalytic potential of model vanadium(IV, V) complexes with benzimidazole-derived ONN donor ligands. *Inorg. Chem.*, **2006**, 45, 5924-5937.
- [347] Da Silva, J.A.L.; da Silva J.J.R.F.; Pombeiro, A.J.L. Oxidovanadium complexes in catalytic oxidations. *Coord. Chem. Rev.*, **2011**, 255, 2232-2248.
- [348] Garcia-Gutierrez, J.L.; Fuentes, G.A.; Hernandez-Teran, M.E.; Garcia, P.; Murrieta-Guevara, F.; Jimenez-Cruz, F. Ultra-deep oxidative desulfurization of diesel fuel by the Mo/Al<sub>2</sub>O<sub>3</sub>-H<sub>2</sub>O<sub>2</sub> system: The effect of system parameters on catalytic activity. *Appl. Catal., A*, **2008**, 334, 366-373.
- [349] Sampanthar, J.T.; Xiao, H.; Dou, H.; Nah, T.Y.; Rong, X.; Kwan, W.P. Ultra-deep oxidative desulfurization of diesel fuel by the Mo/Al<sub>2</sub>O<sub>3</sub>-H<sub>2</sub>O<sub>2</sub> system: The effect of system parameters on catalytic activity. *Appl. Catal., B*, **2006**, 63, 85-93.
- [350] Nakayama, N.; Shinji, T.; Shojiro, O. Hydrocarbon oxidation with hydrogen peroxide and pentafluoriodosylbenzene catalysed by unusually distorted macrocycle manganese complexes. *J. Mol. Catal. A: Chem.*, **2007**, 277, 61-71.
- [351] Kong, L.Y.; Li, G.; Wang, X.S.; Wu, B. Oxidative desulfurization of organic sulfur in gasoline over Ag/TS-1. *Energy Fuels*, **2006**, 20, 896-902.



- [352] Ramin, M.; Jutz, F.; Jan-Dierk, G.; Baiker, A. Solventless synthesis of propylene carbonate catalysed by chromium–salen complexes: Bridging homogeneous and heterogeneous catalysis. *J. Mol. Catal. A: Chem.*, **2005**, 242, 32-39.
- [353] De, B. B.; Lohray, B. B.; Sivaram, S.; Dhal, P.K. Synthesis of catalytically active polymer-bound transition metal complexes for selective epoxidation of olefins. *Macromolecules*, **1994**, 27 (6), 1291-1296.
- [354] Canali, L.; Sherrington, D.C.; Deleuze, H. Synthesis of resins with pendently-bound chiral manganese-salen complexes and use as heterogeneous asymmetric alkene epoxidation catalysts. *React. Funct. Polym.*, **1999**, 40, 155-168.
- [355] Cedeno-Caero, L.; Gomez-Bernal, H.; Fraustro-Cuevas, A.; Guerra-Gomez, H.D.; Cuevas-Garcia, R. Oxidative desulfurization of synthetic diesel using supported catalysts Part III. Support effect on vanadium-based catalysts. *Catal. Today*, **2008**, 133-135, 244-254.
- [356] Gupta, K.C.; Sutar, A.K. Polymer anchored Schiff base complexes of transition metal ions and their catalytic activities in oxidation of phenol. *J. Mol. Catal. A: Chem.*, **2007**, 272, 64-74.
- [357] Tobiasz, A.; Walas, S.; Trzewik, B.; Grzybek, P.; Zaitz, M.M.; Gawin, M.; Mrowiec, H. Cu(II)-imprinted styrene–divinylbenzene microspheres as a new sorbent for flow injection-flame atomic absorption determination of copper. *Microchem. J.*, **2009**, 93, 87-92.
- [358] Claisen, L.; Eisleb, O. Über die umlagerung von phenolallyläthern in die isomeren allylphenole. *Liebigs Ann.*, **1914**, 401, 21-119.
- [359] (a) Bruker, APEX2.Version 1-0. Bruker AXS Inc., Madison, Wisconsin, USA, **2009**. (b) Bruker SAINT+. Version 7.60A. (includes XPREP and SADABS) Bruker AXS Inc., Madison, Wisconsin, USA, **2005**.
- [360] Bruker SHELXTL Version 5.1. (includes XS, XL, XP, XSHELL) Bruker AXS Inc., Madison, Wisconsin, USA. **1999**.

- [361] Spek, A.L. Single-crystal structure validation with the program PLATON. *J. Appl. Cryst.*, **2003**, 36, 7-13.
- [362] Addison, A.W.; Rao, T.N. Synthesis, structure, and spectroscopic properties of copper(II) compounds containing nitrogen–sulfur donor ligands; the crystal and molecular structure of aqua[1,7-bis(*N*-methylbenzimidazol-2'-yl)-2,6-dithiaheptane]copper(II) perchlorate. *J. Chem. Soc. Dalton. Trans.*, **1984**, 1349-1356.
- [363] Walmsley, R.S.; Tshentu, Z.R.; Fernandes, M.A.; Frost, C.L. Synthesis, characterization and anti-diabetic effect of bis[(1-*R*-imidazolyl)phenolato]oxidovanadium(IV) complexes. *Inorg. Chim. Acta.*, **2010**, 363, 2215-2221.
- [364] Nakamoto, K. Coordination compounds in infrared and raman spectra of inorganic and coordination compounds, 4th Ed.; *John Wiley & Sons, Inc.*: New York, **1986**.
- [365] Rehder, D. Bioinorganic vanadium chemistry, *John Wiley & Sons, Ltd*, UK, **2008**, 68.
- [366] White, L.K.; Chasteen, N.D. A Q-band electron paramagnetic resonance study of vanadyl(IV)-labeled human serotransferrin. *J. Phys. Chem.*, **1979**, 83, 279-284.
- [367] Buglyo, P.; Dessi, A.; Kiss, T.; Micera, G.; Sanna, D. Formation of tris-chelated vanadium(IV) complexes by interaction of oxidovanadium(IV) with catecholamines, 3-(3,4-dihydroxyphenyl)alanine and related ligands in aqueous solution. *Dalton Trans.*, **1993**, 2057-2063.
- [368] Paine, T.K.; Weyhermüller, T.; Slep, L.D.; Neese, F.; Bill, E.; Bothe, E.; Weighardt, K.; Chaudhuri, P. Nonoxidovanadium(IV) and oxidovanadium(V) complexes with mixed O, X, O-donor ligands (X = S, Se, P, or PO). *Inorg. Chem.*, **2004**, 43, 7324-7338.
- [369] Hagrman, D.J.; Finn, R.C.; Zubieta, J. Molecular manipulation of solid state structure: influences of organic components on vanadium oxide architectures. *Solid State Sci.*, **2001**, 3, 745-774.

- [370] Cornman, C.R.; Zovinka, E.P.; Boyajian, Y.D.; Geiser-Bush, K.M.; Boyle, P.D.; Singh, P. Structural and EPR studies of vanadium complexes of deprotonated amide ligands: effects on the  $^{51}\text{V}$  hyperfine coupling constant. *Inorg. Chem.*, **1995**, 34, 4213-4219.
- [371] Jakusch, T.; Hollender, D.; Enyedy, É.A.; Gonzalez, C.S.; Montes-Bayón, M.; Sanz-Medel, A.; Pessoa, J.C.; Kiss, I.T.T. Biospeciation of various antidiabetic  $\text{V}^{\text{IV}}\text{O}$  compounds in serum. *Dalton Trans.*, **2009**, 2428-2437.
- [372] Walmsley, R.S.; Tshentu, Z.R. Imidazole-based vanadium complexes as haloperoxidase models for oxidation reactions. *S. Afr. J. Chem.*, **2010**, 63, 95-104.
- [373] Mansuy, D.; Valadon, P.; Erdelmeier, I.; Lopez-Garcia, P.; Amar, C.; Girault, J.P.; Dansette, P.M. Thiophene S-Oxides as new reactive metabolites: formation by cytochrome P450 dependent oxidation and reaction with nucleophiles. *J. Am. Chem. Soc.*, **1991**, 113-20, 7825-7826.
- [374] Lingyan, K.; Gang, L.; Xiangsheng, W. Mild oxidation of thiophene over TS-1/ $\text{H}_2\text{O}_2$ . *Catal. Today*, **2004**, 93-95, 341-345.
- [375] Te, M.; Fairbride, C.; Ring, Z. Oxidation reactivities of dibenzothiophenes in polyoxometalate/ $\text{H}_2\text{O}_2$  and formic acid/ $\text{H}_2\text{O}_2$  systems. *Appl. Catal., A*, **2001**, 219, 267-280.
- [376] Lanju, C.; Shaohui, G.; Dishun, Z. Oxidation of thiophenes over silica gel in hydrogen peroxide/formic acid system. *Chin. J. Chem. Eng.*, **2006**, 14(6), 835-838.
- [377] Castillo, K.; Parsons, J.G.; Chavez, D.; Chianelli, R.R. Oxidation of dibenzothiophene to dibenzothiophene-sulfone using silica gel. *J. Catal.*, **2009**, 268, 329-334.
- [378] Gates, B.C.; Topsoe, H. Reactivities in deep catalytic hydrodesulfurization: challenges, opportunities, and the importance of 4-methyldibenzothiophene and 4,6-dimethyldibenzothiophene. *Polyhedron*, **1997**, 16, 3213-3217.
- [379] Hartmann, M.; Jung, D. Biocatalysis with enzymes immobilized on mesoporous hosts: the status quo and future trends. *J. Mater. Chem.*, **2010**, 20, 844-857.

- [380] Rosevear, A. Immobilized biocatalyst: A critical review. *J. Chem. Technol. Biotechnol.*, **1984**, 34, 127-150.
- [381] Xavier, F.; Malcata, H.; Reyes, H.; Garcia, C.; Hill, A.; Amundson, C. Immobilized lipase reactors for modification of fats and oils- A review. *J. Am. Oil. Chem. Soc.*, **1990**, 67, 890-910.
- [382] Bornscheuer, U.T. Immobilizing enzymes: How to create more suitable biocatalysts. *Angew. Chem. Int. Ed.*, **2003**, 42, 3336-3337.
- [383] Rao, N.N.; Lütz, S.; Würges, K.; Minör, D. Continuous biocatalytic processes. *Org. Process Res. Dev.*, **2009**, 13, 607-616.
- [384] Tomoi, M.; Ford, W.T. Importance of mass transfer and intraparticle diffusion in polymer-supported phase-transfer catalysis. *J. Am. Chem. Soc.*, **1980**, 102(23), 7140-7141.
- [385] Quimby, B.D.; Giarrocco, V.; Sullivan, J.J.; McCleary, K.A. Fast analysis of oxygen and sulfur compounds in gasoline by GC-AED. *J. High Resol. Chromatogr. Commun.*, **1993**, 15, 705-709.
- [386] Ogunlaja, A.S.; Walmsley, R.S.; du Sautoy, C.W.; Torto, N.; Tshentu, Z.R. Development of a continuous flow system for the oxidative desulfurization of refractory organosulfur compounds in hydrotreated diesel. *Energy Fuels*, **2013**, 27, 7714-7723.
- [387] Matsui, J.; Okada, M.; Tsuruoka, M.; Takeuchi, T. Solid-phase extraction of a triazine herbicide using a molecularly imprinted synthetic receptor. *Anal. Commun.*, **1997**, 34, 85-87.
- [388] Andersson, L.I.; Paprica, A.; Arvidsson, T. A highly selective solid phase extraction sorbent for pre-concentration of sameridine made by molecular imprinting. *Chromatographia*, **1997**, 46, 57-62.
- [389] Jorge, A.; Mendez-Orozco, A.; Le Borgne, S. Hydrogels as adsorbents of organosulfur compounds currently found in diesel. *Chem. Eng. Process.*, **2004**, 43, 1587-1595.

- [390] Ruiz, M.; Sastre, A.M.; Guibal, E. Palladium sorption on glutaraldehyde-crosslinked chitosan. *React. Funct. Polym.*, **2000**, 45, 155-173.
- [391] Fariba, G.; Vasheghani-Farahani, S.; Vasheghani-Farahani, E. Theoretical description of hydrogel swelling: a review. *Iran Polym. J.*, **2010**, 19 (5), 375-398.
- [392] Monteiro, O.A.C.; Airoidi, C. Some studies of crosslinking chitosan–glutaraldehyde interaction in a homogeneous system. *Int. J. Biol. Macromol.*, **1999**, 26(2), 119-128.
- [393] Kim, J.S.; Reneker, D.H. Mechanical properties of composites using ultrafine electrospun fibers. *Polym. Comp.*, **1999**, 20, 124 -131.
- [394] Kim, S.K.; Kim, T.H.; Jung, J.W.; Lee, J.C. Polybenzimidazole containing benzimidazole side groups for high-temperature fuel cell applications. *Polymer*, **2009**, 50, 3495-3502.
- [395] Miller, M.M.; Sherrington, D.C. Polybenzimidazole-supported molybdenum(VI) propene epoxidation catalyst. *J. Chem. Soc., Chem. Commun.*, **1994**, 55-56.
- [396] Miller, M.M.; Sherrington, D.C. Alkene epoxidations catalyzed by Mo(VI) supported on imidazole-containing polymers: I. synthesis, characterization, and activity of catalysts in the epoxidation of cyclohexene. *J. Catal.*, **1995**, 152, 368-376.
- [397] Mbeleck, R.; Ambroziak, K.; Saha, B.; Sherrington, D.C. Stability and recycling of polymer-supported Mo(VI) alkene epoxidation catalysts. *React. Funct. Polym.*, 2007, 67, 1448-1457.
- [398] Li, N.H.; Frechet, J.M.J. Polybenzimidazole-supported heterogeneous palladium catalysts. *J. Chem. Soc., Chem. Commun.*, **1985**, 1100-1101.
- [399] Magdalene, R.M.; Leelamani, E.G.; Nanje Gowda, N.M. Hydrogenation of nitroarenes using polybenzimidazole-supported rhodium catalyst. *J. Mol. Catal. A: Chem.*, **2004**, 223, 17-20.
- [400] D'Archivio, A.A.; Galantini, L.; Biffis, A.; Jerabek, K.; Corain, B. Polybenzimidazole as a promising support for metal catalysis: morphology and molecular accessibility in the dry and swollen state. *Chem. Eur. J.*, **2000**, 6, 794-799.

- [401] Kim, J.S.; Reneker, D. H. Polybenzimidazole nanofiber produced by electrospinning. *Polym. Eng. Sci.*, **1999**, 39, 849-854.
- [402] Xia, Y.Q.; Guo, T.Y.; Song, M.D.; Bang-hua, Z.; Bao-long, Z. Adsorption dynamics and thermodynamics of Hb on the Hb-imprinted polymer microspheres. *React. Funct. Polym.*, **2008**, 68, 63-69.
- [403] Kousaku, O.; Dongil, C.; Hakyong, K.; Ayako, N.; Hiroyuki, Y. Electrospinning of chitosan. *Macromol. Rapid Commun.*, **2004**, 25, 1600-1605.
- [404] Frank, R.S.; Downey, J.S.; Yu, K.; Stover, H.D.H. Poly(divinylbenzene-*alt*-maleic anhydride) microgels: intermediates to microspheres and macrogels in cross-linking copolymerization. *Macromolecules*, **2002**, 35, 2728-2735.
- [405] Greiner, A.; Wendorff, J. H. Electrospinning: a fascinating method for the preparation of ultrathin fibers. *Angew. Chem. Int. Ed.*, **2007**, 46, 5670-5703.
- [406] Hasegawa, M.; Isogai, A.; Onabe, F.; Usuda, M. Dissolving states of cellulose and chitosan in trifluoroacetic acid. *J. Appl. Polym. Sci.*, **1992**, 45, 1857-1863.
- [407] Marco, A.T.; Rodrigo, S.V.; Marisa, M.B.; Eduardo, J.A.; Cesar, C.S. Production of chemically modified chitosan microspheres by a spraying and coagulation method. *Mater. Res.*, **2007**, 10(4), 347-352.
- [408] Hudson, S.M.; Wei, Y.C.; Hudson, S.M.; Mayer, J.M.; Kaplan, D.L. The crosslinking of chitosan fibers. *J. Polym. Sci.*, **1992**, 30(10), 2187-2193.
- [409] Blout, E.R.; Fields, M.; Karplus, R. Absorption spectra. VI. The infrared spectra of certain compounds containing conjugated double bonds. *J. Am. Chem. Soc.*, **1948**, 70, 194-198.
- [410] Jouanneau, J.; Mercier, R.; Gonon, L.; Gebel, G. Synthesis of sulfonated polybenzimidazoles from functionalized monomers: preparation of ionic conducting membranes. *Macromolecules*, **2007**, 40, 983-990.

- [411] Sannigrahi, A.; Arunbabu, D.; Sankar, R.M.; Jana, T. Tuning the molecular properties of polybenzimidazole by copolymerization. *J. Phys. Chem. B.*, **2007**, 111, 12124-12132.
- [412] Lobato, J.; Canizares, P.; Rodrigo, M.; Linares, J.; Aguilar, J. Improved polybenzimidazole films for H<sub>3</sub>PO<sub>4</sub>-doped PBI-based high temperature PEMFC. *J. Membr. Sci.*, **2007**, 306, 47-55.
- [413] Gao, Z.; Nahrup, J. S.; Mark, J.E.; Sakr, A poly(dimethylsiloxane) coatings for controlled drug release. I. Preparation and characterization of pharmaceutically acceptable materials. *J. Appl. Polym. Sci.*, **2003**, 90, 658-666.
- [414] Enoki, T.; Tanaka, K.; Watanabe, T.; Oya, T.; Sakiyama, T.; Takeoka, Y.; Ito, K.; Wang, G.; Annaka, M.; Hara, K.; Du, R.; Chuang, J.; Wasserman, K.; Grosberg, A.Y.; Masamune, S.; Tanaka, T. Frustrations in polymer conformation in gels and their minimization through molecular imprinting. *Phys. Rev. Lett.*, **2000**, 85, 5000-5003.
- [415] Umpleby, R.J.; Baxter, S.C.; Bode, M. Application of the Freundlich adsorption isotherm in the characterization of molecularly imprinted polymers. *Anal. Chim. Acta.*, **2001**, 435, 35-42.
- [416] Wong, Y.C.; Szeto, Y.S.; Cheung, W.H. Equilibrium studies for acid dye adsorption onto chitosan. *Langmuir*, **2003**, 19, 7888-7894.
- [417] Yonghui, C.; Lei, Z.; Hanjie, Y.Z.L.; Hao, L.; Pingkai, O. Desulfurization of gasoline using molecularly imprinted chitosan as selective adsorbents. *Appl. Biochem. Biotechnol.*, **2010**, 160, 593-603.
- [418] Masel, R.I. in: Principles of adsorption and reaction on solid surfaces, Wiley, **1996**, p. 239–245, 299-301.
- [419] Treybal, E.R. Mass Transfer Operations, 3rd edition, McGraw Hill International editions, Chemical Engineering Series, Singapore, **1981**.
- [420] Rao, M.; Bhole, A.G. Chromium removal by adsorption using fly ash and bagasse. *Journal of Indian Water Works Association*, XXXIII **2001**, 1, 97-100.

- [421] Raji, C.; Shubha, K.P.; Anirudhan, T.S. Use of chemically modified sawdust in the removal of Pb(II) ions from aqueous media. *Indian J. Environ. Hlth.*, **1997**, 39 (3), 230-238.
- [422] Shotipruk, A.; Kiatsongserm, J.; Pavasant, P.; Goto, M.; Sasaki, M. Pressurized hot water extraction of anthraquinones from the roots of *Morinda citrifolia*. *Biotechnol. Prog.*, **2004**, 20, 1872-1875.
- [423] Miller, D.J.; Hawthorne, S.B.; Gizir, A.M.; Clifford, A.A. Solubility of polycyclic aromatic hydrocarbons in subcritical water from 298 K to 498 K. *J. Chem. Eng. Data*, **1998**, 43(6), 1043-1047.
- [424] Basile, A.; Jimenez-Carmona, M.M.; Clifford, A.A. Extraction of rosemary by superheated water. *J. Agric. Food Chem.*, **1998**, 46(12), 5205-5209.
- [425] Ong, E.S.; Len, S.M. Pressurized hot water extraction of berberine, baicalein and glycyrrhizin in medicinal plants. *Anal. Chim. Acta.*, **2003**, 482, 81-89.
- [426] Gelencser, A.; Kiss, G.; Krivacsy, Z.; Varga-Puchony, Z. A simple method for the determination of capacity factor on solid-phase extraction cartridges. I. *J. Chromatogr. A*, **1995**, 693, 217-225.
- [427] Liska, I.; Krupcik, J.; Leclercq, P.A. The use of solid sorbents for direct accumulation of organic compounds from water matrices-a review of solid-phase extraction techniques. *J. High Res. Chromatogr.*, **1989**, 12, 577-590.
- [428] Irving, H.M.N.H.; Freiser, H.; West, T.S. IUPAC Compendium of Analytical Nomenclature, Definitive Rules: Pergamon Press; Oxford, **1981**.
- [429] Giannozzi, P.; Baroni, S.; Bonini, N.; Calandra, M.; Car, R.; Cavazzoni, C.; Ceresoli, D.; Chiarotti, G.L.; Cococcioni, M.; Dabo, I.; Corso, A.D.; de-Gironcoli, S.; Fabris, S.; Fratesi, G.; Gebauer, R.; Gerstmann, U.; Gougoussis, C.; Kokalj, A.; Lazzeri, M.; Martin-Samos, L.; Marzari, N.; Mauri, F.; Mazzarello, R.; Paolini, S.; Pasquarello, A.; Paulatto, L.; Sbraccia, C.; Scandolo, S.; Sclauzero, G.; Seitsonen, A.P.; Smogunov, A.; Umari, P.; Wentzcovitch, R.M.



- QUANTUM ESPRESSO: a modular and open-source software project for quantum simulations of materials. *J. Phys. Condens. Matter.*, **2009**, 21, 395502-395519.
- [430] Dreizler, R.M.; Gross, E.K.U. Density functional theory (Berlin: Springer), **1990**.
- [431] Martin, R.M. Electronic structure: Basic theory and practical methods (Cambridge: Cambridge University Press), **2004**.
- [432] Frisch, M.J.; Trucks, G.W.; Schlegel, H.B.; Scuseria, G.E.; Robb, M.A.; Cheeseman, J.R.; Montgomery, Jr., J.A.; Vreven, T.; Kudin, K.N.; Burant, J.C.; Millam, J.M.; Iyengar, S.S.; Tomasi, J.; Barone, V.; Mennucci, B.; Cossi, M.; Scalmani, G.; Rega, N.; Petersson, G.A.; Nakatsuji, H.; Hada, M.; Ehara, M.; Toyota, K.; Fukuda, R.; Hasegawa, J.; Ishida, M.; Nakajima, T.; Honda, Y.; Kitao, O.; Nakai, H.; Klene, M.; Li, X.; Knox, J.E.; Hratchian, H. P.; Cross, J.B.; Bakken, V.; Adamo, C.; Jaramillo, J.; Gomperts, R.; Stratmann, R.E.; Yazyev, O.; Austin, A.J.; Cammi, R.; Pomelli, C.; Ochterski, J.W.; Ayala, P.Y.; Morokuma, K.; Voth, G.A.; Salvador, P.; Dannenberg, J.J.; Zakrzewski, V.G.; Dapprich, S.; Daniels, A.D.; Strain, M.C.; Farkas, O.; Malick, D.K.; Rabuck, A.D.; Raghavachari, K.; Foresman, J.B.; Ortiz, J.V.; Cui, Q.; Baboul, A.G.; Clifford, S.; Cioslowski, J.; Stefanov, B.B.; Liu, G.; Liashenko, A.; Piskorz, P.; Komaromi, I.; Martin, R.L.; Fox, D.J.; Keith, T.; Al-Laham, M.A.; Peng, C.Y.; Nanayakkara, A.; Challacombe, M.; Gill, P.M.W.; Johnson, B.; Chen, W.; Wong, M.W.; Gonzalez, C.; Pople, J.A. Gaussian 03, Revision E.01. Gaussian, Inc., Wallingford CT, **2004**.
- [433] Hehre, W.J.; Burke, L.D.; Shusterman, A.J.; Pietro, W.J. Experiments in computational organic chemistry, wave function Inc., CA, USA, **1993**.
- [434] Yun, G.N.; Lee, Y.K. Beneficial effects of polycyclic aromatics on oxidative desulfurization of light cycle oil over phosphotungstic acid (PTA) catalyst. *Fuel Process. Technol.*, **2013**, 114, 1-5.
- [435] Caldwell, T.E.; Land, D.P. Desulfurization, deoxygenation and denitrogenation of heterocycles by a palladium surface: a mechanistic study of thiophene, furan and pyrrole on

- Pd(III) using laser-induced thermal desorption with Fourier-transform mass spectrometry. *Polyhedron*, **1997**, 16(18), 3197-3211.
- [436] Fletcher, P.D.I.; Haswell, S.J.; Pombo-villar, E.; Warrington, B.H.; Watts, P.; Wong, Y.F.; Zhang, X. Micro reactors: principles and applications in organic synthesis. *Tetrahedron*, **2002**, 58(609), 4735-4757.
- [437] Gunn, D.J. An analysis of convective dispersion and reaction in the fixed-bed reactor. *Int. J. Heat Mass Transfer*, **2004**, 47(12-13), 2861-2875.
- [438] Liu, W.; Roy, S. Effect of channel shape on gas/liquid catalytic reaction performance in structured catalyst/reactor. *Chem. Eng. Sci.*, **2004**, 59(22-23), 4927-4939.
- [439] Kashid, M.N.; Renken, A.; Kiwi-Minsker, L. Microstructured reactors and supports for ionic liquids. *Chem. Eng. Sci.*, **2012**, 66(7), 1480-1489.
- [440] Kashid, M.N.; Kiwi-Minsker, L. Microstructured reactors for multiphase reactions: state of the art. *Ind. Eng. Chem. Res.*, **2009**, 48(14), 6465-6485.
- [441] Wiles, C.; Watts, P. Recent advances in synthetic micro reaction technology. *Chem. Commun.*, **2011**, 47, 6512-6535.